HOT COMPRESSION OF ARMCO IRON AND SILICON STEEL

bу

Jaromir Lev Uvira

A thesis submitted to the Faculty of Graduate Studies and Research in partial fulfilment of the requirements for the degree of Doctor of Philosophy.

Department of Metallurgical Engineering, McGill University, Montreal, Canada.

October 1967.

A B S T R A C T

Equipment was constructed which permitted the hot compression of Armco iron and silicon steel at constant true strain rates of 0.05 to 1/sec over the temperature range 600° to 1,000°C. A maximum true strain of 1.9 could be attained, followed by immediate quenching or by isothermal annealing.

True stress-true strain curves were obtained, and the steady-state flow stress (G), strain rate ($\dot{\epsilon}$) and temperature (T) were found to fit the following expression: $\dot{\mathcal{E}} = A \left[\sinh\left(\alpha G\right)\right]^{n'} \exp\left(-\frac{\Delta H}{RT}\right)$. The constants (A, α , n' and Δ H) were determined for the two materials. The substructural changes occurring during hot compression were investigated by optical and transmission electron microscopy. Under steady-state conditions, repolygonization occurred and the subgrains remained equiaxed at all strains. The mean subgrain diameters were found to be related to the strain rate and temperature by (d⁻¹) = a + b log Z, where $Z = \left[\dot{\epsilon} \exp\left(\frac{\Delta H}{RT}\right)\right]$, and to the flow stress by (d⁻¹) = a' + b' log sinh (α G), where a, a', b and b' are constants.

The room temperature microhardness was proportional to the $(subgrain\ diameter)^{-\frac{1}{2}}$ and dependent on the deformation temperature, the strain rate, and the extent of recovery following hot compression.

ACKNOWLEDGEMENTS

The writer expresses his gratitude and appreciation to Dr. J.J. JONAS, director of this research, for his constant encouragement and advice.

Thanks are also due to Dr. D.R. AXELRAD for his suggestions and for the use of his experimental facilities.

Assistance from the following organizations and persons is gratefully acknowledged: Messrs. E. JONES, M. KNOEPFEL, L. VROOMEN and A.J. WARD for their skilled help in the construction of the equipment; the Armco Steel Corporation and the Allegheny Ludlum Corporation for the provision of experimental materials; the Steel Company of Canada Ltd., especially Mr. D. RICHARDSON, and the Dominion Steel and Coal Corporation Ltd., especially Mr. P. MUDRY, for assistance in chemical analysis; his fellow graduate students Messrs. G. GAGNON and W.A. WONG for helpful discussions.

The author would like to express his particular gratitude to Mr. S.L. GERTSMAN of the Physical Metallurgy Division of the Department of Energy, Mines and Resources, Ottawa, for providing facilities for electron microscopy, and to Drs. H.J. McQUEEN, R. PACKWOOD and E. SMITH for helpful suggestions in specimen preparation and the techniques of electron microscopy.

The writer also acknowledges the receipt of the following awards: the Steel Company of Canada Ltd. Bursary, the Women's Association of the Montreal Branch, C.I.M.M. Bursary, the William Henry Howard Scholarship, the Sir William Dawson Fellowship, and the Aluminium Laboratories Ltd. Fellowship. He is also grateful to the Defence Research Board of Canada for supporting the work under Grant No. 9535-34.

TABLE OF CONTENTS

		Page
ACKNOW	LEDGEMENTS	i
LIST O	FIGURES	vi
LIST O	F TABLES	жi
1	INTRODUCTION	. 1
1.1	Comparison of Industrial Hot Working and Experimental Testing Methods	1
1.2	Survey of Previous Creep and Hot Working Investigations	. 3
2	THEORIES OF DEFORMATION WITH SPECIAL ATTENTION TO THERMALLY ACTIVATED PROCESSES	6
2.1	Dislocation Reactions in Bcc Metals	6
2.2	The Flow Curve at Room Temperature	8
2.2.1	Work Hardening of Single Crystals	8
2.2.2	Work Hardening of Polycrystals	10
2.3	The Flow Curve at High Temperature	11
2.3.1	Flow Curves	11
2.3.2	The Theory of Activated Complexes	13
2.3.3	The Importance of Diffusion	14
2.4	Static and Dynamic Recovery	16
2.4.1	The Kinetics of Static Recovery	17
2.4.2	Recovery Mechanisms and Changes of Microstructure	19
2.5	Rate Controlling Mechanisms in Hot Deformation	21
3	EXPERIMENTAL MATERIALS AND EQUIPMENT	24
3.1	Materials	24
3 1 1	Preparation of Specimens	24

3.1.2	Annealing	26
3.1.3	Straining	27
3.1.4	Lubricants for Hot Compression	27
3.2	Modification of the Extrusion Press for Hot Compression	. 29
3.2.1	General Requirements of Equipment for Hot Compression Testing	29
3.2.2	Modified Extrusion Press	31
3.2.3	Strain Rate Controlling Mechanism	34
3.2.4	Temperature Control	35
3.2.5	Experimental Capabilities of the Equipment	36
3.3	Modified High Temperature Creep Equipment	36
3.3.1	General Layout of the Equipment	36
3.3.2	Strain Rate Controlling Mechanism	40
3.3.3	Experimental Capabilities of the Equipment	40
4	EXPERIMENTAL PROCEDURE	42
4.1	Preparation of Specimens for Microhardness Tests and Optical Metallography	42
4.1.1	Sectioning and Mounting of Specimens	42
4.1.2	Grinding and Mechanical Polishing	44
4.1.3	Electrolytic Polishing	44
4.1.4	Chemical and Electrolytic Etching	45
4.2	Preparation of Specimens for Transmission Electron Microscopy	45
4.3	Optical and Electron Metallography	47
4.4	Determination of Subgrain Size	47
4.4.1	Planimetric Procedure	47
4.4.2	Comparison Procedure	48

4.5	Determination of Subgrain Misorientation	49
4.6	Calculation of True Stress-True Strain Curves	49
4.7	Microhardness Measurements	52
5 .	EXPERIMENTAL RESULTS	57
5.1	True Stress-True Strain Curves	57
5.1.1	The Effect of Friction	58
5.1.2	The Stored Energy and the Flow Stress	60
5.1.3	Temperature Rise During Deformation	61
5.1.4	True Stress-True Strain Curves with Corrected Stress	63
5.2	A Stress/Strain Rate/Temperature Relationship for Hot Compression	63
5.2.1	Determination of (∞) and (n')	76
5.2.2	Activation Energies for Hot Compression	80
5.3	Microstructural Observations	83
5.3.1	Transient Region Microstructures	85
5.3.2	Equiaxed and Steady-State Substructures	88
5.4	Static Recovery After Hot Deformation	111
5.4.1	Effect of Static Recovery on Microhardness	112
5.4.2	Effect of Static Recovery on Substructure	114
5.4.3	Effect of Annealing Time on Recrystallization	119
5.5	Mean Subgrain Size and Misorientation	128
5.6	Microhardness Results	136
5.6.1	Microhardness Dependence on Subgrain Size	136
6	DISCUSSION	139
6.1	True Stress-True Strain Curves	139
6.2	Material Constants and Activation Energies for Hot Compression	142

6.3	Substructure Formation During High Temperature Compression	148
6.4	Recovery and Recrystallization	151
6.4.1	Dynamic Recovery During Hot Compression	152
6.4.2	Static Recovery After Hot Compression	154
6.4.3	Recrystallization After Hot Compression	157
6.5	Subgrain Size as a Function of Stress, Strain Rate and Temperature	160
6.6	The Introduction of Substructure Parameters into the Stress/Strain Rate/Temperature Equation	174
6.7	Microhardness Measurements	177
6.8	Room Temperature Properties in Terms of Hot Working Strain Rates and Temperatures	178
7.	CONCLUSIONS	180
	True Stress-True Strain Curves	180
	Strain Rate Equations and Material Constants	180
	Substructural Results	181
	Recovery and Recrystallization After Hot Working	182
	Microhardness Results	183
STATE	MENT OF ORIGINAL WORK AND CONTRIBUTION TO KNOWLEDGE	184
प्रयास प्र	FNCES	186

·

LIST OF FIGURES

		Page
Fig. 1	Grooved specimen faces	28
Fig. 2	Layout of the hot compression equipment	32
Fig. 3	Arrangement of the hot compression furnace	33
Fig. 4	Modified high temperature creep equipment	37
Fig. 5	Arrangement for hot compression testing in modified high temperature creep furnace	39
Fig. 6	Specimen mounting practice	43
Fig. 7	Polishing fixture	43
Fig. 8	Transmission electron diffraction pattern (Armco iron)	50
Fig. 9	Transmission electron diffraction pattern (silicon steel)	50
Fig. 10	Hot compression record (extrusion press)	53
Fig. 11	Hot compression record (creep furnace)	54
Fig. 12	Location of microhardness impressions	55
	True_stress-true_strain_curves :	
Fig. 13	Armco iron; (a) uncorrected; (b) 600°C, corrected	64
Fig. 14	Armco iron; (a) uncorrected; (b) 700°C, corrected	65
Fig. 15	Armco iron; (a) uncorrected; (b) 800°C, corrected	66
Fig. 16	Armco iron-Mn; (a) uncorrected; (b) 650°C, corrected	67
Fig. 17	Armco iron-Mn; (a) uncorrected; (b) 750°C, corrected	68
Fig. 18	Armco iron-Mn; (a) uncorrected; (b) 800°C, corrected	69
Fig. 19	Silicon steel; (a) uncorrected; (b) 650°C, corrected	70
Fig. 20	Silicon steel; (a) uncorrected; (b) 700°C, corrected	71
Fig. 21	Silicon steel; (a) uncorrected; (b) 750°C, corrected	72

True stress-true strain curves - cont.

•	00	Silicon steel; (a) uncorrected; (b) 800°C, corrected	73
Fig.	22		
Fig.	23	Silicon steel; (a) uncorrected; (b) 900°C, corrected	74
Fig.	24	Silicon steel; (a) uncorrected; (b) 1,000°C, corrected	75
Fig.	25	Graphical determination of constants (α) and (n ')	79
Fig.	26	The stress/strain rate relationship in Armco iron	81
Fig.	27	The stress/strain rate relationship in silicon steel	82
Fig.	28	The stress/temperature relationship in Armco iron	84
Fig.	29	The stress/temperature relationship in silicon steel	84
		Substructures (Photomicrographs):	
 -	20	Silicon steel; 560°C; &= 0.11	86
Fig.			86
Fig.	31	Silicon steel; 700°C; &= 0.17	
Fig.	32	Armco iron; 750° C; $\varepsilon = 0.38$; $\dot{\varepsilon} = 0.40/\text{sec}$	87
Fig.	33	Armco iron; 750°C ; $\varepsilon = 0.38$; $\dot{\varepsilon} = 0.60/\text{sec}$	87
Fig.	34	Silicon steel; 650° C; $\varepsilon = 0.085$	88
Fig.	. 35	Silicon steel; 800° C; $\varepsilon = 0.15$	88
Fig	. 36	Silicon steel; 800° C; $\varepsilon = 0.75$	89
Fig	. 37	Armco iron; 750° C; $\varepsilon = 0.27$	92
Fig	. 38	Armco iron; 800° C; $\varepsilon = 0.19$	92
Fig	. 39	Armco iron; 750° C; $\varepsilon = 0.70$	93
Fig	. 40	Armco iron; 700° C; $\varepsilon = 1.45$	93
Fig	. 41	Silicon steel; 700° C; $\mathcal{E} = 0.17$	94
Fig	. 42	Silicon steel; 750° C; $\dot{\varepsilon} = 0.075/\text{sec}$	95
Fie	, 43	Silicon steel; 800° C; $\dot{\varepsilon} = 0.26/\text{sec}$	95
Fig	s. 44	Silicon steel; 750° C; $\dot{\mathcal{E}} = 0.06/\text{sec}$	96

Substructures (Photomicrographs) - cont.

Fig. 45	Silicon steel; 750° C; $\dot{\mathcal{E}} = 0.25/\text{sec}$	96
Fig. 46	Armco iron; 800° C; $\dot{\mathcal{E}} = 0.075/\text{sec}$	97
Fig. 47.	Armco iron; 800° C; $\dot{\epsilon} = 0.13/\text{sec}$	97
Fig. 48	Silicon steel; 900° C; $\dot{\varepsilon} = 0.06/\text{sec}$	98
Fig. 49	Silicon steel; $900^{\circ}C$; $\dot{\varepsilon} = 0.20/\text{sec}$	99
Fig. 50	Silicon steel; $1,000^{\circ}C$; $\dot{\varepsilon} = 0.05/\text{sec}$	100
Fig. 51	Silicon steel; 1,000°C; $\dot{\mathcal{E}}$ = 0.15/sec	100
Fig. 52	Silicon steel; 560°C; 220 X	101
Fig. 53	Silicon steel; 750°C; 220 X	101
Fig. 54	Silicon steel; 800°C; 220 X	102
Fig. 55	Silicon steel; 900°C; 220 X	102
Fig. 56	Silicon steel; 1,000°C; 220 X	103
Fig. 57	Armco iron; 600°C; 950 X	104
Fig. 58	Silicon steel; 650°C; 680 X	104
Fig. 59	Silicon steel; 800°C; 585 X	105
Fig. 60	Silicon steel; 900°C; 585 X	105
Fig. 61		106
Fig. 62	Silicon steel; 650° C; $\mathcal{E} = 0.49$; $\dot{\mathcal{E}} = 0.09/\text{sec}$	107
Fig. 63	Silicon steel; 650° C; $\varepsilon = 1.55$; $\dot{\varepsilon} = 0.5/\text{sec}$	107
Fig. 6	Silicon steel; 1,000°C; 5,700 X	108
Fig. 6	5 Armco iron; 600°C; 7,150 X	108
Fig. 6	6 Armco iron; 600°C; 14,300 X	109
Fig. 6	7 Armco iron; 700°C; 10,000 X	109
Fig. 6	8 Change of microhardness with delay before quenching	113

Substructures (Photomicrographs):

Fig.	69	Silicon steel; 1,000°C; delay 1 sec; 220 X	115
Fig.	70	Silicon steel; 1,000°C; delay 40 sec; 220 X	115
Fig.	71	Silicon steel; 1,000°C; delay 1 sec; 585 X	116
Fig.	72	Silicon steel; 1,000°C; delay 40 sec; 585 X	116
Fig.	73	Silicon steel; 900°C; delay 5 sec; 220 X	117
Fig.	74	Silicon steel; 900°C; delay 90 sec; 220 X	117
Fig.	75	Silicon steel; 900°C; delay 5 sec; 585 X	118
Fig.	76	Silicon steel; 900°C; delay 90 sec; 585 X	118
Fig.	77	Silicon steel; 800°C; delay 18 sec; 220 X	120
Fig.	78	Silicon steel; 800°C; delay 35 sec; 220 X	120
Fig.	79	Silicon steel; 800°C; delay 13 sec; 585 X	121
Fig.	80	Silicon steel; 800°C; delay 35 sec; 585 X	121
Fig.	81	Silicon steel; 800°C; delay 1 sec; 11,400 X	122
Fig.	82	Silicon steel; 800°C; delay 5 sec; 11,400 X	122
Fig.	83	Silicon steel; 800°C; delay 35 sec; 11,400 %	123
Fig.	84	Silicon steel; 800°C; delay 40 sec; 2,850 X	124
Fig.	85	Silicon steel; 800°C; delay 40 sec; 11,400 X	124
Fig.	86	Silicon steel; 800°C; delay 40 sec; 28,600 X	125
Fig.	87	Isothermal recrystallization data for Armco iron	126
		Isothermal recrystallization data for silicon steel	127
		- · · · · · · · · · · · · · · · · · · ·	
		Progress of Recrystallization (Photomicrographs):	
Fig.	89	Silicon steel; 560°C; delay 25 min	129
Fig.	90	Silicon steel; 650°C; delay 10 min	129
Fig.	91	Silicon steel; 650°C; delay 25 min	130

		Graphical representation of equation (23)	
Fig.	92	Microhardness vs. (subgrain diameter) 2; Armco iron	138
Fig.	93	Microhardness vs. (subgrain diameter) ; silicon steel	138
Fig.	94	Time of 50% recrystallization as a function of temperature	159
<u>G</u>	raphi	cal representation of equations (24) to (29), (32) and (33)	
Fig.	95	The temperature corrected strain rate vs. sinh stress	161
Fig.	96	(Subgrain diameter) -1 vs. log sinh stress	163
Fig.	97	Subgrain diameter vs. stress	164
Fig.	98a	(Subgrain diameter) vs. stress; Armco iron	165
Fig.	98ъ	(Subgrain diameter) ⁻¹ vs. stress; silicon steel	165
Fig.	99a	(Subgrain diameter) 1 vs. (stress); Armco iron	166
Fig.	99ъ	(Subgrain diameter) ⁻¹ vs. (stress) ⁿ ; silicon steel	166
Fig.	100	(Subgrain diameter) ⁻¹ vs. (sinh stress) ^N	167
Fig.	101	Three (subgrain diameter) -1/stress relationships	169
Fig.	102	(Subgrain diameter) ⁻¹ vs. log Z; Armco iron	171
Fig.	103	(Subgrain diameter) ⁻¹ vs. log Z; silicon steel	171
Fig.	104	(Subgrain diameter) ⁻¹ vs. (Z) ^q	173

LIST OF TABLES

		Page
Table I C	Chemical Composition of Materials Investigated	25
Table II S	Specimen Preparation Procedure	26
Table III I	Dimensions of Grooves on the Specimen Faces	28
Table IV (Composition of Lubricants	30
	Temperature Increases for the Maximum Compressive Strains Attained	62
Table VI	Hot Deformation Investigations of Steels	77
Table VII	Material Constants for Hot Compression	83
	Subgrain Sizes Determined in Iron Deformed at High Temperatures	131
	Experimental Mean Subgrain Size and Misorientation (Armco iron)	133
Table X	Experimental Mean Subgrain Size and Misorientation (Silicon steel)	134
Table XI	Experimental Values of the Material Constants	143
Table XII	Activation Energies for Hot Deformation	145
Table XIII	Activation Energies for Self-Diffusion	146
Table XIV	Experimental Values of Equation Constants	174

1 INTRODUCTION

1.1 COMPARISON OF INDUSTRIAL HOT WORKING AND EXPERIMENTAL TESTING METHODS

Hot working processes play an important role in the fabrication of metals and alloys. This is because much less force is required to effect equal reductions at elevated temperatures than at homologous temperatures below 0.5. Furthermore, the ductility of most metals is also higher during hot working than during cold working. The term hot working commonly refers to high temperature deformation occurring at strain rates ranging from about 10^{-3} to $10^3/\text{sec}^{1}$. This distinguishes it from creep, which takes place at strain rates below $10^{-3}/\text{sec}$, and from very high strain rate deformations, such as explosive forming, which occur at strain rates in excess of $10^3/\text{sec}$. The present investigation was limited to hot working strain rates and temperatures, although frequent reference will be made to creep mechanisms and equations.

Industrial deformation processes are not generally used for fundamental research work. This is because of the complexity of flow in these processes (e.g. extrusion, rolling and forging) and also because of the difficulty of maintaining a uniform and constant temperature in the test material. For these reasons, simpler testing methods, such as hot torsion, hot tension and hot compression, have been developed for experimental investigation. These methods will now be compared briefly.

Hot torsion has the advantage that the experimental torque data need not be corrected for friction and redundant work, while deformations to high values of strain can be achieved. Also, arrangements can easily be made for the rapid quenching of samples after completion of the

deformation. On the other hand, the variation of the strain rate from zero at the center to a maximum at the surface²⁾ causes difficulties in the calculation of the flow stress from the torque data, and in the correlation of the structure with the deformation variables.

The advantages of hot tension testing are the following. It is based on room temperature tensile testing, equipment for which is commonly available. Furthermore, no corrections are necessary for friction, and the geometry of flow is easily understood. The main disadvantage is that these tests are limited to maximum strains ranging from 10 to 30%. This is because of the incidence of necking, which leads to non-uniform deformation and eventual fracture. Also expensive accessories are required to produce constant true strain rates. For the latter reason, and particularly because of the maximum strain limitation, this method of testing does not have wide application.

The main problem associated with hot compression testing is the provision of constant true strain rates. A simple testing machine producing constant anvil speeds is unsuitable, because the true strain rate increases as the specimen gets shorter. Constant true strain rates can, however, be produced mechanically or hydraulically. The mechanical means for achieving this is the cam plastometer 3,4) which is a somewhat elaborate and expensive device. Constant true strain rates can also be produced hydraulically, using open or closed loop servo systems. The latter means was the one employed in the present investigation. Unlike the other two test methods considered above, hot compression testing does involve corrections for friction, and these will be discussed later. Compression tests are, however, more representative of important industrial

working processes such as extrusion, forging and rolling, in which the forming forces are primarily compressive.

1.2 SURVEY OF PREVIOUS CREEP AND HOT WORKING INVESTIGATIONS

Prior to describing the present investigation, a brief survey of recent research on high temperature deformation will be presented. Although the strain rates in creep are several orders of magnitude lower than those of hot working, the survey will begin with creep, as hot working is similar in many respects to creep. Also, data for steady-state creep are more readily available in the literature than the results of hot working experiments. Two aspects of creep testing are of particular interest with regard to hot working. These are: the equations relating strain rate, stress and temperature; and the microstructural changes taking place during creep.

Creep Equations. Strain rate equations have been reported both for steels investigated in the ferritic region 5,6,7) and for austenitic steels 8,9), as well as for other bcc metals, (e.g. W¹⁰⁾ and Ta¹¹⁾). In these investigations, the stress-dependence of the strain rate has been given by a power term 10,11) or a hyperbolic sine term 5,6,7,8,9). Also, the activation energy for creep has been found to be approximately equal to that for self-diffusion 7,11,12). Thus it is generally accepted that creep is a diffusion-controlled thermally-activated process, although the same conclusion has not yet been applied to hot working.

<u>Microstructural Changes During Creep</u>. Formation of stable subgrains during steady-state creep was observed in steels tested at temperatures in the ferritic range 12,13,14,15,16). The establishment of this well-developed substructure was due to extensive dynamic recovery,

where the subgrains remained unchanged throughout steady-state creep 13,15). Similar substructures were not observed in ferritic steels tested in the austenitic range, since the networks were destroyed by the phase change that took place during cooling.

Hot Working. Hot working tests on steel have been carried out by hot torsion 12 , 17 to 23 , hot tension 12 , 13 , 14 , 19 , 20 , 25 , 26 , and hot compression 3,4,14,27 to 31,32,33). These investigations will be discussed in greater detail in the appropriate sections below. Before proceeding, however, some general remarks will be made concerning the present state of the accumulated data and of inadequacies in the general picture obtained to date. The most obvious one is the following. Separate investigations concerning either the flow stress during deformation, the structure produced by the deformation, or the mechanical properties as a function of the deformation conditions have been carried out. However, the interdependence of flow stress, structure and properties does not seem to have been investigated in detail in a single experiment. Another lack is that many of the previous investigations were carried out over small ranges of temperature and strain rate. Furthermore, the study of the structural changes occurring during deformation, and of their relationship to the deformation variables, was generally performed by optical microscopy. These studies are therefore incomplete, and somewhat unreliable with respect to the dislocation substructure. No data at all were uncovered concerning static recovery after hot working.

Regarding the structural changes associated with hot working, the following important problems remain to be thoroughly investigated:

(a) In the transient region, the process of substructure development and its relationship to work hardening;

- (b) in steady-state hot working, the dislocation mechanisms involved, and the relationship between the microstructures produced and the deformation variables;
- (c) during isothermal annealing after hot working, the structural changes caused by static recovery on the one hand and by recrystallization on the other.

Outline of the Project. The present project was mainly concerned with steady-state hot working. The transient region of hot working, as well as isothermal recovery and recrystallization after hot working, were also investigated, but to a lesser extent. An outline of the aims of the investigation follows:

- 1. To determine flow curves for the hot working of Armco iron and silicon steel in the ∞ -region, and to establish the extent of the steady-state region.
- 2. To determine the temperature and stress dependence of the strain rate and to calculate material constants for hot working.
- 3. To study substructure formation during hot compression, and to investigate the relationship between substructure, mechanical properties, and the deformation variables.
- 4. To examine the structure and properties of Armco iron and silicon steel as a function of annealing time after hot compression.

2 THEORIES OF DEFORMATION, WITH SPECIAL ATTENTION TO THERMALLY ACTIVATED PROCESSES

2.1 <u>DISLOCATION REACTIONS IN BCC METALS</u>

Less attention has so far been paid to dislocation mechanisms in bcc metals than in fcc metals, as the geometry of slip of the former is more complicated than that of the latter. Unlike the case of fcc metals, there are no close-packed planes in bcc metals. There are close-packed directions, however, which are the slip directions, and these are the <111> . Some recent work on dislocation reactions, work hardening, and recovery, will be reviewed briefly in the paragraphs below.

Slip occurs in the <111> directions ^{34,35)}, as already mentioned above, as these are the directions of closest atomic approach. It is normally assumed that {112}, {110} and {123} are possible slip planes, but which of them is operative depends on the homologous temperature. They change successively from {112} to {110} and to {123} as the temperature increases from -185° to 20°C. In iron, however, all three planes seem to be operative at once ^{34,36)}.

In a recent paper, KROUPA and VÍTEK³⁵⁾ concluded that the above-mentioned slip planes are only the "macroscopic" ones, as observed by optical or electron microscopy, and that there are other (as yet undetected) "microscopic" or elementary slip planes concerned with the motion of individual dislocations. For example, non-crystallographic slip has been observed in 3% silicon iron at low strain rates ³⁷⁾, although at high strain rates and low temperatures, slip was confined to {110} planes ^{38,39)}.

The stacking fault energy of bcc metals is thought to be high, since extended dislocations have not been commonly observed 40,41). Some evidence has been accumulated to support the view that the plane of dissociation of dislocations is a function of the impurity content 42). This result is in agreement with other reports 40) which propose that dislocations probably dissociate when particular alloying elements are present (for example, Si). These elements presumably lower the stacking fault energy. The presence of impurities might therefore be the reason why extended dislocations are sometimes observed on $\{110\}$ 35,40) and {112} planes 43,44,45). The stacking fault energy, however, can also be influenced by the different types of stress present. The influence of the mode of deformation on the stacking fault energy has recently been investigated by testing at 77°K⁴⁶). In this work it was found that an applied tensile stress increased the stacking fault energy on {110} planes, whereas a compressive stress caused its reduction. It has also been reported that screw dislocations can dissociate onto { 110} and {112} planes at the same time 35). From the above-mentioned results it can be seen that stacking fault energies in bcc metals are generally high, and that the partial dislocations are not widely separated. Hence cross-slip in bcc metals is relatively easy. On the other hand, the stacking fault energy can be reduced by the presence of impurities or compressive stress, so that the width of the extended dislocations increases, making cross-slip more difficult.

Besides the splitting of dislocations, another important dislocation reaction occurs in bcc metals which is concerned with work hardening mechanisms. This reaction occurs when two 2a <111> dislocations

combine to form a <100> sessile dislocation 47). This attractive interaction presumably contributes substantially to the flow stress. It probably plays an important role in the work hardening of bcc metals, much as LOMER-COTTRELL locks do in the work hardening of fcc metals 34).

2.2 THE FLOW CURVE AT ROOM TEMPERATURE

2.2.1 WORK HARDENING OF SINGLE CRYSTALS

The plastic flow of fcc single crystals has been extensively investigated 1,34,48,49,50) and is commonly divided into the following three stages: easy glide or laminar flow (stage I), linear hardening or turbulent flow (stage II) and dynamic recovery (stage III). Whether this scheme could also be applied to bcc metals was not clear until recent investigations in which a certain degree of parallelism between fcc and bcc behavior was demonstrated 51). Although similarities have been found in the three-stage scheme, the detailed work hardening behavior of bcc metals has not yet been fully established due largely to difficulties arising from the sensitivity of the plastic properties to the presence of carbon, nitrogen and oxygen in interstitial solid solution 34). Some of the flow stress theories for bcc metals will now be briefly described, with particular reference to the behavior of iron.

The typical stress-strain curve of a bcc single crystal starts at higher stresses than that of a typical fcc metal³⁴⁾. After stage I is complete, the curve for Fe is roughly parabolic⁵²⁾, as it is for other bcc metals. The initial flow stress has been found to increase sensitively with decreasing temperature⁵³⁾. The flow stress is believed to consist of the following components³⁴⁾:

- (a) the flow stress associated with the intrinsic resistance of the lattice to dislocation motion (i.e. the Peierls-Nabarro force),
- (b) the stress attributed to the presence of impurities,
- (c) the stress connected with the presence of dislocations (structural hardening).

Opinions of some investigators about the relative importance of the first two above-mentioned flow stress components at low temperatures will now be described briefly.

CONRAD⁵⁴⁾ pointed out that the intrinsic lattice resistance arising from the Peierls-Nabarro force is responsible for the strong temperature and strain rate dependence of the yield and flow stresses at low temperatures. However, some objections have been raised against this theory. For example, MORDIKE and HAASEN⁵²⁾ have suggested that the increase in the temperature and strain rate sensitivities of the flow stress is due to the breaking up of the larger insurmountable precipitates into small thermally surmountable fragments as the strain increases. Another objection to the theory proposed by CONRAD has been raised by STEIN et al 55). They conducted an investigation of iron single crystals containing less than 5×10^{-3} ppm carbon and proposed that the dependence of yield stress on temperature in α -iron of commercial purity is due primarily to the interaction of mobile dislocations with interstitial impurities in solid solution. Although the Peierls mechanism is not too important in fcc metals, NABARRO, BASINSKI and HOLT 34) concluded that in bcc lattices it appears to play a much more significant role, especially at low temperatures and strains. As far as structural hardening is concerned, it seems that the basic mechanisms here are very

similar to those operating in fcc lattices; an interaction leading to the formation of a sessile dislocation takes the place of the LOMER-COTTRELL interaction, as already mentioned in section 2.1³⁴).

2.2.2 WORK HARDENING OF POLYCRYSTALS

Commercial metals are polycrystalline and the polycrystalline flow curves differ from those of single crystals because of the constraining effect of neighbouring grains. In particular, stage I is absent as single slip cannot take place in constrained deformation. The work hardening of polycrystals at homologous temperatures below 0.5 has been studied by many investigators ⁵⁶ to ⁶¹), and some of the more important of these results will now be described.

In stage II, the hardening rate of polycrystals is higher than in single crystals ⁴⁸⁾, which can also be accounted for by the constraining effect of neighbouring grains. The stress-strain curve of polycrystalline iron shows a rapid fall-off in the capacity to work harden at low temperatures ⁵⁸⁾. The temperature and strain rate dependence of the flow stress in polycrystalline iron is also affected by the presence of alloying elements. At low temperatures silicon decreases the temperature sensitivity of the flow stress in contrast to manganese and chromium ⁵⁸⁾. Most of the previous investigations were concerned with the dependence of flow stress on dislocation density, and with dislocation configurations at lower stresses ^{60,61)}. The work hardening behavior of different metals subject to large plastic strains has recently been investigated by EMBURY, KEH and FISHER ⁵⁹⁾. They proposed that for large plastic strains the work hardening process cannot be explained in terms of any elementary dislocation theory. However, the process may be

described in terms of the reduction of substructural-barrier spacing during deformation. The above-mentioned investigators studied a wide range of polycrystalline materials which enabled comparisons to be made of the properties of both fcc and bcc metals. Fcc metals do not harden as extensively during cold working as do bcc metals; also the decrease in cell size with strain during cold working is less marked in the former than in the latter case. The rate of dynamic recovery, which is indicated by the slope of the stress-strain curve in stage III, is smaller in bcc than in fcc metals. This behavior is presumably associated with the presence of interstitials in bcc materials.

2.3 THE FLOW CURVE AT HIGH TEMPERATURE

2.3.1 FLOW CURVES

Hot working investigations are usually concerned with the relationship between the main deformation variables: i.e. strain (\mathcal{E}), strain rate ($\dot{\mathcal{E}}$), flow stress ($\dot{\mathcal{G}}$) and temperature ($\dot{\mathcal{E}}$). The interdependence of these variables is described by sets of flow curves in which the true stress is given as a function of true strain at various constant strain rates and temperatures. The main features of the true stress-true strain curves reported by previous investigators will now be discussed, and special attention will be given to the shapes of the curves obtained from the hot compression testing of steel.

The shape of the flow curve is related to the deformation mechanism operating in each region of strain. The important features of stress-strain curves have been discussed by previous investigators 21,62,63,64) and some of their conclusions will now be introduced. It is generally

known that high temperature stress-strain curves exhibit a transient and a steady-state stress region $\hat{\Sigma}$. The slope in the transient region is a measure of the network hardening rate; the steady-state region is established when a balance is reached between the rates of work hardening and of dynamic recovery. Under steady-state conditions, the flow stress is constant and independent of strain. Some of the metals, such as Ni, Cu and Y-Fe, when tested in hot torsion, exhibit pronounced stress peaks just before steady-state deformation sets in, even at high temperatures 21). In Fe-25% Cr and in silicon steels, on the other hand, a more gradual transition is observed 21). Stress peaks have also been observed during the hot torsion and hot tension of ferritic steels $^{19,20)}$. In contrast, compression curves for these materials exhibit a maximum only at high temperatures and low strain rates 4,30). These results suggest that not only the choice of material, but also the mode and conditions of deformation are responsible for the shape of the stress-strain curve. The strain at the maximum stress for a particular metal is believed to be somewhat strain rate and temperature dependent $^{62,63)}$. The maximum moves towards higher strains as the temperature drops and the strain rate increases $^{62)}$.

So far only a few investigators have presented data concerning the hot compression of iron or steel in the α -region 29,30,31 . Some of the curves presented 31 did not exhibit a steady-state region; in other curves the stress rose after large strains. These departures from steady-state conditions occurred at extremely high strain rates and at lower temperatures. The lack of explanation for some of the features of the flow curves is due to the fact that the mechanisms governing hot working processes are not yet completely understood.

2.3.2 THE THEORY OF ACTIVATED COMPLEXES

As hot working is a thermally activated process which involves both stress and thermal energy, the principles of activated complexes or rate processes 65) will be described in the following paragraphs.

When a unit of flow consisting of a group of atoms passes over another group by shear, it has to be excited to an activated state 65). The driving force for this event is supplied by thermal activation 66). The free energy of the activated atoms increases from the initial state to a maximum (the transition or activated state) and decreases again to another level. To get from the initial energy level to the final one, the atoms have to overcome this "energy barrier" and the difference between the initial and the maximum energy levels is called the free energy of activation or simply the activation energy. Since the volume changes in condensed systems are negligible, and also the lowering of the free energy by entropy changes is insignificant 68) or not known, the change of internal energy is commonly used rather than the change of free energy for the activation energy. It provides a reasonable estimate of the free energy change and is also approximately equal to the change of enthalpy.

However, not all the atoms in the body have the required activation energy at the same time. This is due to the non-uniform distribution of the thermal energy in the body. The fraction of atoms having the required thermal energy is proportional to the exp $(\frac{-\Delta H}{RT})$, where (ΔH) is the activation energy, (R) is the universal gas constant and (T) is the absolute temperature.

The simultaneous action of stress is believed to decrease the energy barriers $^{69)}$. During plastic deformation the thermal energy can,

however, activate only a relatively small number of atoms. Thermal energy is not capable of causing movement of long dislocation segments. When stress is applied simultaneously with thermal activation, the energy barrier will be lowered or raised depending upon whether the strain is in the same direction (\mathfrak{S}_1) or opposite to the stress (\mathfrak{S}_2) . The strain rate of the process is then proportional to the difference between the forward and reverse frequencies (\mathfrak{V}_1) and (\mathfrak{V}_2) , and can be expressed by the following equation:

$$\dot{\mathcal{E}} = v_1 - v_2 \approx \mathbb{E}\left[\exp\left(-\frac{\Delta H - v \delta_1}{RT}\right) - \exp\left(-\frac{\Delta H + v \delta_2}{RT}\right)\right] \tag{1}$$

where(v) is a constant. This can be simplified by assuming that $c_1 = c_2 = c_3$

$$\dot{\mathcal{E}} = B' \exp \left(-\frac{\Delta H}{RT}\right) \sinh \frac{\sqrt{G}}{RT}$$
 (2)

where (B') is a constant 69).

The rate of a single thermally activated process is proportional to the frequency with which the atoms attempt to overcome the barrier (in solids it is equivalent to the Debye or vibration frequency) and to the above-mentioned temperature dependence and stress dependence terms. When several mechanisms are involved at the same time, the process becomes more complicated and it is very difficult to establish the rate controlling mechanism.

2.3.3 THE IMPORTANCE OF DIFFUSION

Diffusion is an important thermally activated process. Some of the main principles of diffusion will now be described briefly, especially those related to hot working.

The thermally activated transport of atoms through matter can

occur by means of the following four processes: 66)

- (a) movement within regions of perfect lattice (bulk diffusion);
- (b) movement of diffusing atoms along an external surface (surface diffusion);
- (c) movement along internal surfaces, such as grain boundaries (boundary diffusion); and
- (d) movement along dislocations (pipe diffusion).

Diffusion in pure metals is referred to as self-diffusion in contrast to chemical diffusion, which occurs in heterogeneous matter. Although, from a technical point of view, the latter is the more important, it has not yet been completely understood in fundamental terms ⁶⁶⁾. However, the self-diffusion process is also complex, and in cubic metals it can occur by four distinct mechanisms:

- (1) ring diffusion, where the atoms exchange places by means of "musical chairs" movements;
- (2) interstitial diffusion, where the atoms move through interstitial spaces;
- (3) vacancy diffusion, which is based on position interchanges between atoms and vacant lattice sites; and
- (4) relaxation diffusion, which is associated with the movement of atoms in locally disordered regions.

Of the four mechanisms described above, vacancy diffusion is thought to be the dominant one in metallic self-diffusion 70).

The activation energy for self-diffusion in metals can be approximated from the following relationship:

$$\Delta H_{S.D.} = 34 T_{m}$$
 (3)

where T_m is the melting point temperature (°K), and ($\Delta H_{S.D.}$) is given in cal/mole. This relation is believed to be accurate to $\pm 20\%^{71}$. It has been observed for some time that the activation energy for creep is approximately equal to that for self-diffusion^{7,11,12)}, which has already been mentioned in section 1.2.

Thus it is fairly generally accepted that creep is a diffusion controlled process. It is not as well known that hot working is also diffusion controlled. This is one of the conclusions of the present work and is based on the observation that the experimental activation energies for hot working are also approximately equal to those for self-diffusion, as in the case of creep. The activation energies for hot working and for creep and self-diffusion will be compared in more detail in the Discussion.

2.4 STATIC AND DYNAMIC RECOVERY

It has generally been observed that metals with high stacking fault energies do not recrystallize during hot working^{2,72)}; the extensive "softening" occurring during high temperature deformation is produced by dynamic recovery instead. Also, after deformation is complete, and while the specimen is cooling down to room temperature, static recovery can take place. Recovery kinetics and mechanisms will therefore be reviewed briefly in the following paragraphs.

A distinction has first to be made between:

- (a) static recovery, which is associated with the internal stresses produced by the deformation, and with thermal activation; and
- (b) dynamic recovery, which results from the combined influence of external and internal stresses, and from thermal activation.

 Both kinds of recovery lead to changes in physical and mechanical properties,

and to changes in the dislocation structure. Their effect can be evaluated quantitatively by the dependence of these properties on temperature and time or strain rate.

By means of static recovery, the properties can never be restored completely to their pre-deformation values. Even in deformed single crystals, static recovery still leaves some non-recoverable residual stresses ⁶⁸⁾. In aluminum, the softening which can be produced by static recovery after cold working has been reported to be not higher than 30 to 40% ⁷³⁾, or even only 20% ^{68,74)} of the hardness increase produced by cold working. Comparable values for steels of commercial purity deformed to large strains are not available. However, it seems likely that the fractional restoration of properties by static recovery is as low for iron as it is for aluminum.

On the other hand, it has recently been shown that <u>dynamic</u> recovery during the hot extrusion of aluminum⁷⁵⁾ can lead to much lower final hardnesses than can be obtained by static recovery after cold working. The occurrence of extensive dynamic recovery can result in almost complete softening during hot working. The progress of recovery during hot working can reduce the density of dislocations in the subboundaries and within the subgrains to a very low level. Thus the material can resist recrystallization on subsequent heating because of the low driving force ⁷⁵⁾.

2.4.1 THE KINETICS OF STATIC RECOVERY

The investigation of static recovery after cold working has uncovered the following features (68,76): recovery does not require an incubation period; the recovery rate decreases with time, and increases

with increasing annealing temperature. The recovery rate increases also with decreasing deformation temperature (below 0° C)⁷⁷⁾ and with strain⁷⁷⁾. No data were uncovered for static recovery after hot working.

The activation energies for static recovery are believed to be lower than those for recrystallization (78). It has not yet been established whether the activation energy during recovery is constant, or whether it changes with the instantaneous value of the recoverable property (68). In a recent investigation of static recovery in zone-refined iron (79), it was found that the activation energy increased during annealing in the following way: at the beginning of the annealing cycle the activation energy was about 1/3 of the self-diffusion value, and at the end of the cycle it was about the same as the activation energy for self-diffusion. The latter result is in general agreement with the estimate that the activation energy for self-diffusion reduced by the stored energy of the deformation (68).

Although recovery kinetics cannot be completely satisfactorily described by simple functions 78), over limited time periods, the change of a selected property can be expressed by the following equation:

where: X = the intensity of the lattice imperfections responsible for the instantaneous property change,

A = a constant dependent on the intensity of the lattice imperfections at the start of the recovery treatment.

B = a temperature-dependent constant, and

t = the time of recovery.

This equation is valid for constant temperatures and is subject to the

condition that the activation energy remain constant during recovery.

Equation (4) can also be given in its exponential form, which is:

$$X = X_0 \exp(-B t)$$
 (5)

where (Xo) is the value of the property after cold working.

If the activation energy is assumed to be a function of the instantaneous value of the recovering property, the following equation can be written $^{68)}$:

$$X = A' - B' \ln t ag{6}$$

where: A' = a constant dependent on the initial intensity of the lattice imperfections, the activation energy at the start of the recovery process, and on temperature, and B' = a constant dependent on temperature,

The application of equation (6) is, however, limited to an intermediate range of annealing times since, as (t) approaches zero, (X) becomes infinite.

2.4.2 RECOVERY MECHANISMS AND CHANGES OF MICROSTRUCTURE

t = time.

Recovery Mechanisms. Various mechanisms are involved in recovery after plastic deformation, although the determination of the specific mechanism which is rate controlling is very difficult. From recovery experiments on iron it has been proposed that vacancy migration is controlling at the start and self-diffusion is controlling towards the end 68).

Changes of Microstructure Due to Recovery. Structural changes are a consequence of the rearrangement of lattice imperfections during recovery. The most important structural changes are the following: the

formation of subgrains from cells, and the growth of subgrains. These will now be described briefly.

It has been commonly observed that cell walls consist of dislocation tangles. During static recovery, the cell walls become narrower and better defined, which is due to the partial annihilation and rearrangement of the dislocations within them. Also the dislocation density in the cell interiors decreases as the cells are transformed into subgrains. The average subgrain size remains about the same as that of the cells, although it can increase slightly late in the recovery process ⁶⁸⁾.

At present, the mechanisms of subgrain growth are not fully understood. It has not yet been determined, for example, whether boundary migration or coalescence is the more important process ⁶⁸⁾. Theories proposing boundary migration ⁶⁸⁾ as the nucleation mechanism for recrystallization are based on the mechanism of grain growth at the expense of adjacent subgrains ^{80,81,82)} in locally highly deformed regions. The alternative coalescence theory ⁸³⁾ proposes that the common boundary between some subgrains is eliminated by the movement of dislocations out of the disappearing sub-boundary. It can be concluded from this brief survey that subgrain growth probably occurs by coalescence as well as by boundary migration.

In contrast to the process of <u>static</u> recovery, which is associated with a continuous decrease in dislocation density, <u>dynamic</u> recovery during steady-state hot deformation leads to an equilibrium between the rate of dislocation generation and the rate of internal annihilation. Hence the substructural phenomena will be different in each case. During steady-state hot deformation a constant dislocation density

is maintained, and the overall geometry of the subgrains remains constant. This has already been reported both for creep 13,15,84) and for hot working 85,86). In addition to coalescence and grain boundary migration, which are operative during static recovery, dynamic recovery is accompanied by the continuous creation of new subgrains as the material is being deformed. The net result is that the subgrains are continually being destroyed and reformed at an equilibrium spacing. Presumably a limited amount of subboundary migration is also taking place, which is associated with the climb of dislocations in the networks. This climb is enhanced by high concentrations of vacancies, which are produced by the hot working. The term "repolygonization" has been proposed by McQUEEN et al 86) for this process.

2.5 RATE CONTROLLING MECHANISMS IN HOT DEFORMATION

Steady-state hot working is similar to steady-state creep in that, after a transient period, the stress and strain rate remain constant at a given temperature. The substructural changes taking place in both creep and hot working are also substantially similar. These two observations suggest that the rate controlling mechanisms in hot working are similar to those in creep.*

SCHOECK has suggested that the rate controlling mechanism for steady-state creep could be one of the following dislocation mechanisms:

^{*} The above remarks exclude grain boundary sliding and Nabarro-Herring creep, which occur during low strain rate and very high temperature creep, respectively. These mechanisms are not expected to be significant at the strain rates involved in hot working.

- (a) The generation of dislocations;
- (b) The movement of dislocations through the lattice;
- (c) The annihilation or rearrangement of dislocations in a recovery process.

These mechanisms will now be briefly discussed with respect to hot working.

- (a) The flow stress in hot working is temperature dependent and therefore the rate controlling mechanism must be thermally activated; that means, it must have an activation energy less than about 50 to 100 RT, so that appreciable numbers of thermally activated events can occur⁷²⁾. Thermal energy can aid an applied stress in the activation of dislocation sources; however, the generation of dislocations by the operation of sources probably involves too much energy for thermal activation, so that it is probably dependent almost entirely on the external stress⁷²⁾.
- (b) In the second case two further mechanisms are possible: forest intersection and the diffusion-controlled motion of jogged screw dislocations. Both mechanisms are important for creep for two reasons. First, the forcing of a dislocation through the stress field of another dislocation involves a certain amount of work, and second, the movement of jogged dislocations (produced by intersection) can be thermally aided for latter mechanism has been proposed as rate controlling for several metals for several including ferritic steels.
- (c) The third group of mechanisms involves both cross-slip and climb. Climb can release blocked edge dislocations so that they can overcome obstacles. Climb can also lead to decreases in dislocation

density by the annihilation of segments of opposite dislocations. The concept of climbing over obstacles has been used in the models proposed by WEERTMAN 89,90,91 .

Although both the model based on the non-conservative motion of jogged screw dislocations and the other one based on the climb of edge dislocations represent important mechanisms in creep, it has not yet been possible to determine which of them is the more important 90,92). On the other hand, the activation energies for creep and hot working are similar, and are approximately equal to the activation energy for self-diffusion. This implies that both creep and hot working are diffusion-controlled and thermally activated, and that recovery mechanisms are of paramount importance in both processes.

3. EXPERIMENTAL MATERIALS AND EQUIPMENT

3.1 MATERIALS

The investigation was carried out with three different ferrous materials obtained from five commercial heats, as follows:

- 1) Armco iron two heats.
- 2) Armco iron with increased manganese one heat.
- 3) Silicon steel two heats.

The first four shipments were utilized for investigations performed in the temperature range 600°C to 800°C; the last one was used for tests at temperatures from 600°C to 1,000°C. The materials were of commercial purity supplied by the following companies:

- Item 1: A.D. MACKAY, Inc., New York 38, N.Y., as 1 in. rod.
- Ttem 2: ARMCO STEEL CORPORATION, Middletown, Ohio, as 2 in. rod.
- Item 3: ALLEGHENY LUDLUM STEEL CORPORATION, Dunkirk, N.Y. as 5/8 in. and ½ in. rod.

Chemical analyses were obtained from the suppliers and were checked through the courtesy of the STEEL COMPANY OF CANADA LTD. and the DOMINION STEEL AND COAL CORPORATION LTD. The averaged results are listed in Table I.

In addition, some preliminary tests were made on samples of spectrographically pure iron. However, no full scale tests were carried out on the latter material, as strain-annealing did not produce a reliable grain structure.

3.1.1 PREPARATION OF SPECIMENS

Substructure free cylinders of five different sizes, suitable

Table I. Chemical Composition of Materials Investigated (in percent)

ELEMENT	ARMCO IRON 1 a	ARMCO IRON 1 b	ARMCO IRON 2	SILICON STEEL a	SILXCON STEEL b	
С	0.02	0.02	0.03	0.03	0.03	
P	0.004	0.003	0.005	0.004	0.008	
s	0.009	0.010	0.010	0.020	0.020	
Mn	0.03	0.06	0.26	0.45	0.39	
Si	0.003	0.002	0.15	2.80	2.70	
Cu	0.08	0.08	0.13	0.05	0.07	
Cr	0.01	0.01	0.01	0.02	0.02	
Ni.	0.02	0.02	0.05	0.03	0.05	
Al	0.01	0.01	0.00	0.05	0.06	
N	0.003	0.006	0.007	0.010	0.010	

for hot compression with the available facilities, were prepared by strain-annealing. Different ratios of diameter/length enabled the determination of the coefficient of friction. The resulting mean grain diameter in 1 in. Armco iron was 4 mm, and 3 mm in the other sizes and grades. The procedure concerning specimen preparation is given in Table II. The facing of the specimens was carried out on a horizontal grinding machine fitted with a magnetic chuck.

Table II. Specimen Preparation Procedure

OPERATI ON		ARMCO la,lb	ARMCO IRON 2		SILICON STEEL a		SILICON STEEL b			
Turning	Dia.(in.)	0.98	0.378		0.59	0.378				
	Length	1.38	0.63	0.32	0.88	0.44	0.63	0.32		
Facing	Length (in.)	1.36	0.622	0.311	0.872	0.436	0.622	0.311		
Pre- annealing	T°C Time Cooling	950 5 hours air quench			1,100 2 hours air quench					
Straining by Com- pression	3	0.038	0.03	35	0.038					
Grooving the Faces		See Fig. 1 and Table III								
Strain Annealing	T°C Time Cooling Rate	850 100 hours 40°C/hour			1,020 10 hours 50°C/hour					

3.1.2 ANNEALING

Annealing both before and after straining was performed in a BURRELL high temperature furnace with automatic temperature control. To

prevent oxidation, the specimens were sealed in containers made of thin, low-carbon seamless steel tube and purged with argon gas. Chromelalumel thermocouples were mounted in a few of these containers to check the temperature inside the container. Prior to any of the annealing cycles, the specimens were very carefully degreased with acetone, washed in alcohol and dried. After annealing, the samples were pickled for 15 minutes in 10% HCl to remove small amounts of dirt from the surfaces, although shiny and oxide-free exteriors were obtained by the use of the controlled atmospheres, as described above. The sealed containers were exposed to the annealing temperature without preheating.

3.1.3 STRAINING

The specimens were strained using the ram of a 150-ton vertical hydraulic extrusion press, between two flat highly polished dies, with lanolin as lubricant. The strains used are indicated in Table II. Barreling was absent. Prior to the final annealing cycle, the specimen faces were provided with grooves, which were recommended by previous investigators 33,93), to increase the effectiveness of the lubricant during hot compression. The grooves are shown in Fig. 1 and their dimensions are listed in Table III.

3.1.4 LUBRICANTS FOR HOT COMPRESSION

Powdered glass lubricants were applied to the samples before hot compression to decrease friction and barreling, following the practice of previous investigators 3,4,33,94). The most suitable compositions for the glass powders were determined by the present author by experiment and adjusted according to the temperature range used.

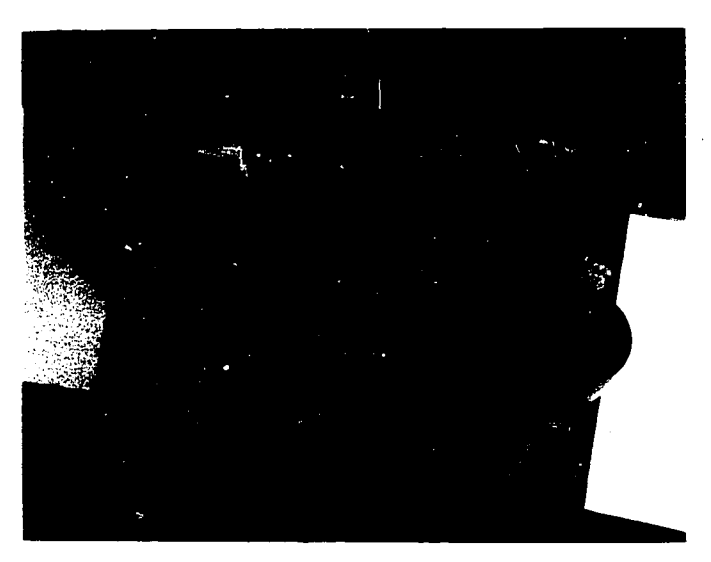


Fig. 1 - Grooved Specimen Faces; 1.35 X

Table III. Dimensions of Grooves on the Specimen Faces (in inches)

SIZE OF SPECIMEN	SPACING BETWEEN GROOVES	DEPTH OF GROOVES		
1 dia. x 1.3	0.04	0.006		
0.6 dia. x 0.84	0.03	0.004		
0.6 dia. x 0.4	0.03	0.004		
0.385 dia. x 0.6	0.02	0.003		
0.385 dia. x 0.3	0.02	0.003		



Fig. 1 - Grooved Specimen Faces; 1.35 X

Table III. Dimensions of Grooves on the Specimen Faces (in inches)

SIZE OF SPECIMEN	SPACING BETWEEN GROOVES	DEPTH OF GROOVES		
1 dia. x 1.3	0.04	0.006		
0.6 dia. x 0.84	0.03	0.004		
0.6 dia. x 0.4	0.03	0.004		
0.385 dia. x 0.6	0.02	0.003		
0.385 dia. x 0.3	0.02	0.003		

(=)

Compositions used by previous workers as well as the ones employed in the present work are compared in Table IV. The powders were applied to the specimens by two methods: 1 in. and 0.6 in. dia. specimens, by dipping at the working temperature; 0.385 in. dia. specimens, by dipping at ambient temperature prior to heating after the samples had been coated on their faces with aerosol spray³³⁾.

3.2 MODIFICATION OF THE EXTRUSION PRESS FOR HOT COMPRESSION

3.2.1 GENERAL REQUIREMENTS OF EQUIPMENT FOR HOT COMPRESSION TESTING

Hot compression tests were carried out on an adapted 150-ton vertical hydraulic extrusion press and also on a modified high temperature creep machine. The modifications had to be carried out for the following reasons.

The compression of metals at high temperatures requires equipment which has five characteristics:

- (a) The ability to provide a constant working temperature over a wide range.
- (b) The ability to vary the force during the testing cycle so as to maintain constant strain rates.
- (c) The availability of a wide range of speeds which can be continuously decreased during the compression cycle so as to produce different constant true strain rates.
- (d) An arrangement for the rapid release of load and for fast quenching of specimens after compression has been accomplished.
- (e) A means of recording the load, strain, and temperature against time.

 The equipment on hand could at best meet only part of the first

Table IV. Composition of Lubricants Used by Other Investigators and by Present Author

		COMPOSITION (%)								
TEMPERATURE RANGE (°C)	USED BY	SiO ₂	B ₂ O ₃	A1203	Ca0	MgO	Na ₂ 0	к ₂ 0	РЬО	Window glass
450 - 600	ALDER and PHILLIPS 3)	-	20	-	-	-	-	-	80	_
600 - 750	PHILLIPS	27.3	-	-	-	-	_	1.5	71	-
850 - 1,000		69	1.2	3.4	6.1	3.2	16.2	0.7	-	-
900 - 1,000	COOK ⁴⁾	-	20	-	-	-	-	-	80	-
560 - 600	Present Work	-	20	_	-	-	-	-	80	-
650 - 700	WOLK	-	15	-	-	-	-	-	75	10
750 - 800		-	15	-	-	-	-	-	70	15
900		5,-	10	-	-	-	10	-	50	25
1,000		10	10	-	-	-	5	-	25	50

and last of these requirements. Furthermore, the extensive financial resources required for the construction of a cam plastometer were not available. The following modifications were therefore designed in all details and constructed in the laboratory. Some novel ideas are described below, which enabled the inexpensive realization of apparatus to provide constant true strain rate testing with an arrangement for rapid quenching.

3.2.2 MODIFIED EXTRUSION PRESS

Figures 2 and 3 show the arrangement of the extrusion press as modified for hot compression testing at temperatures up to 800°C.

The accessories utilized for adaptation were the following: a high temperature furnace with built-in upper and lower platens and a transmission assembly which permitted the attainment of logarithmically decreasing crosshead speeds. The accessories are designated with heavier lines in Fig. 3.

Specimens were heated to the working temperature for 45 minutes in an antimony-lead bath placed in the pre-heating furnace (F), (Fig. 2). After coating with the powdered glass lubricant, they were transferred to the hot compression furnace (R) and reheated for several minutes in a protective atmosphere of argon gas admitted at a flow rate of 1/2 cu.ft./min. The specimens were then placed on the lower platen (15) in the hot compression furnace and the pressure of the ram was transmitted to them via the upper platen (11), suspended on the ram of the extrusion press (Fig. 3). Contact of the specimens with the cool ram was thus prevented. After compression, the load was released, and the top of the furnace was raised at the same time by means of flange (2),

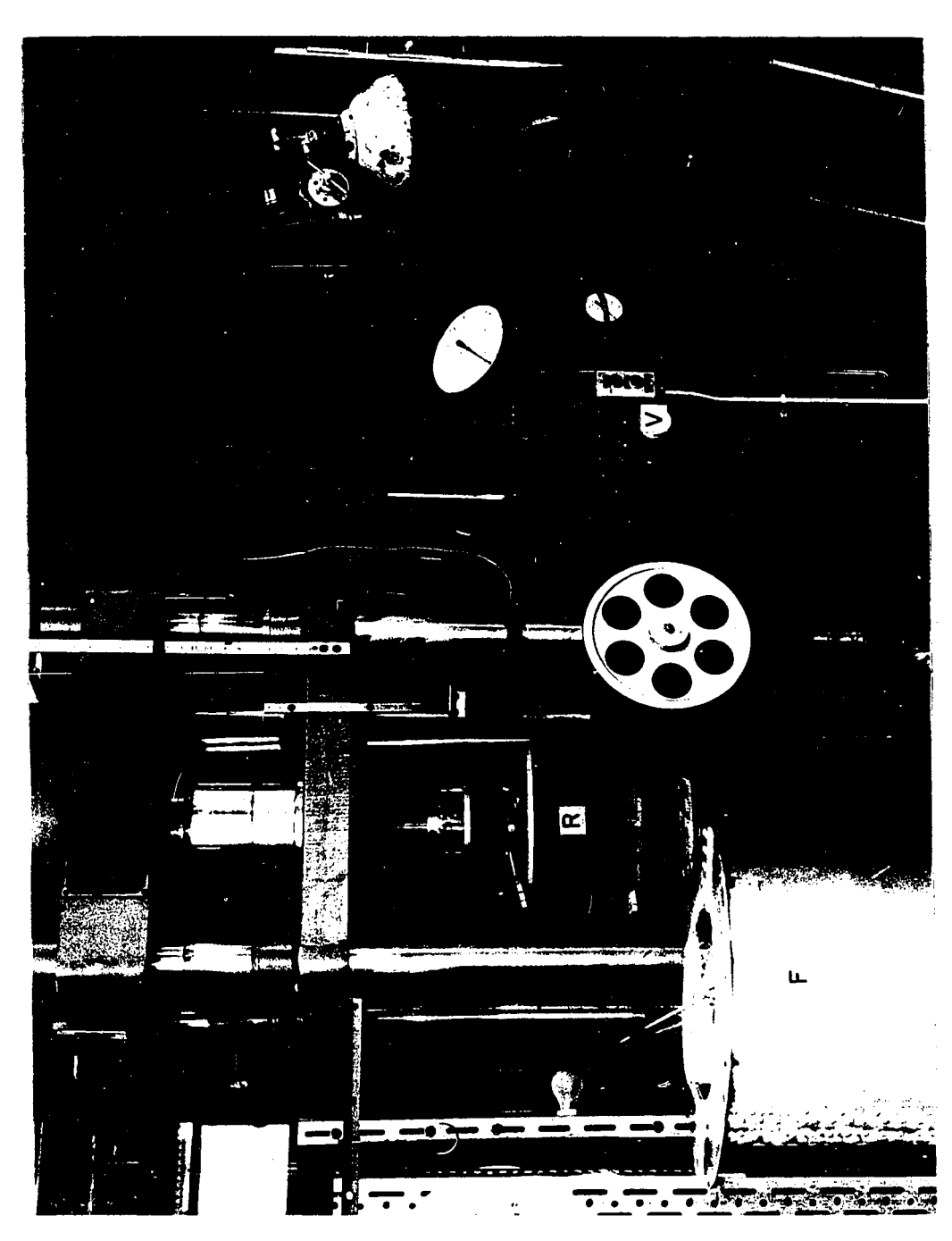
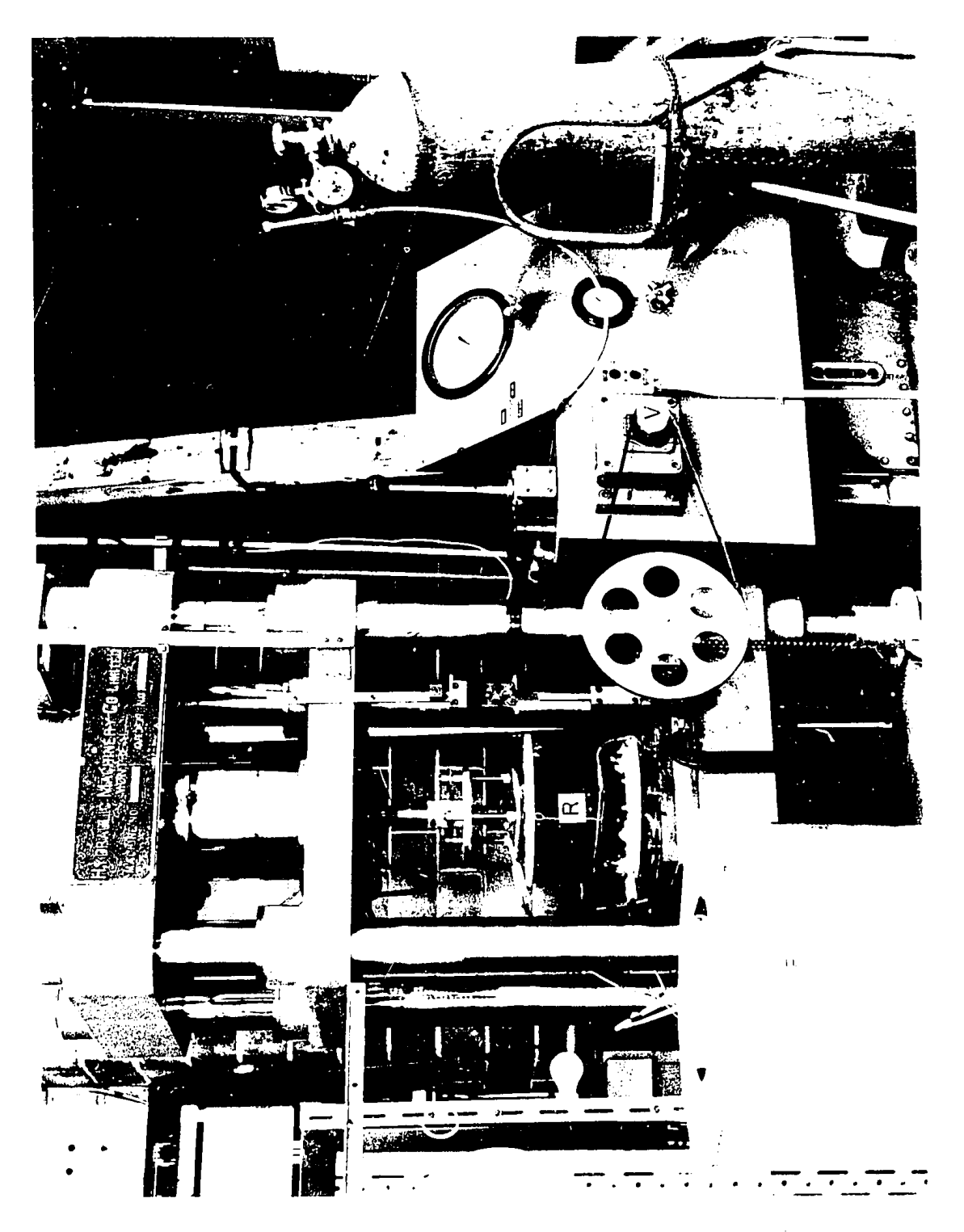


Fig. 2 - General layout of the hot compression equipment using the extrusion press.



and the second of the second of the stock of the second of

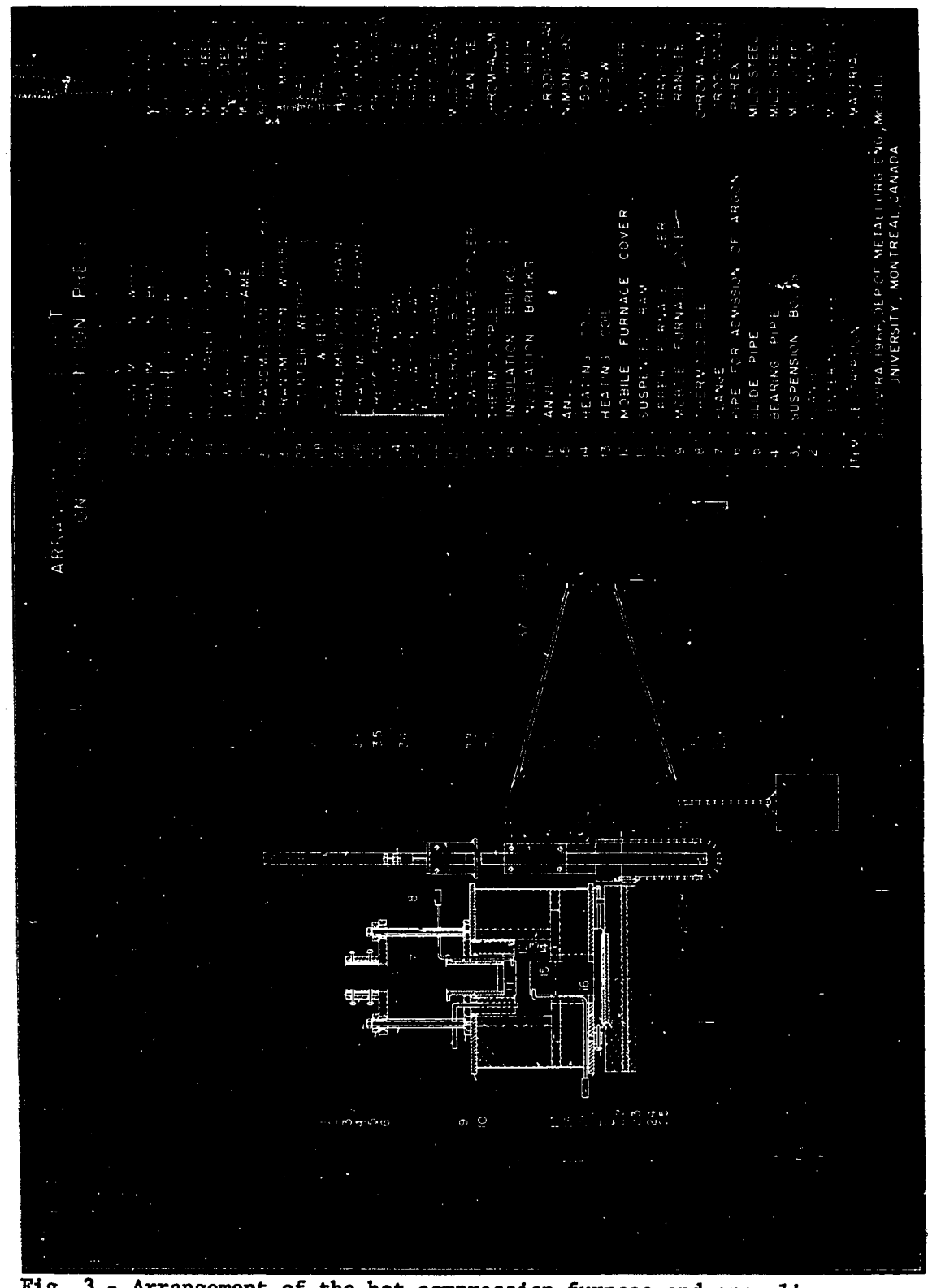
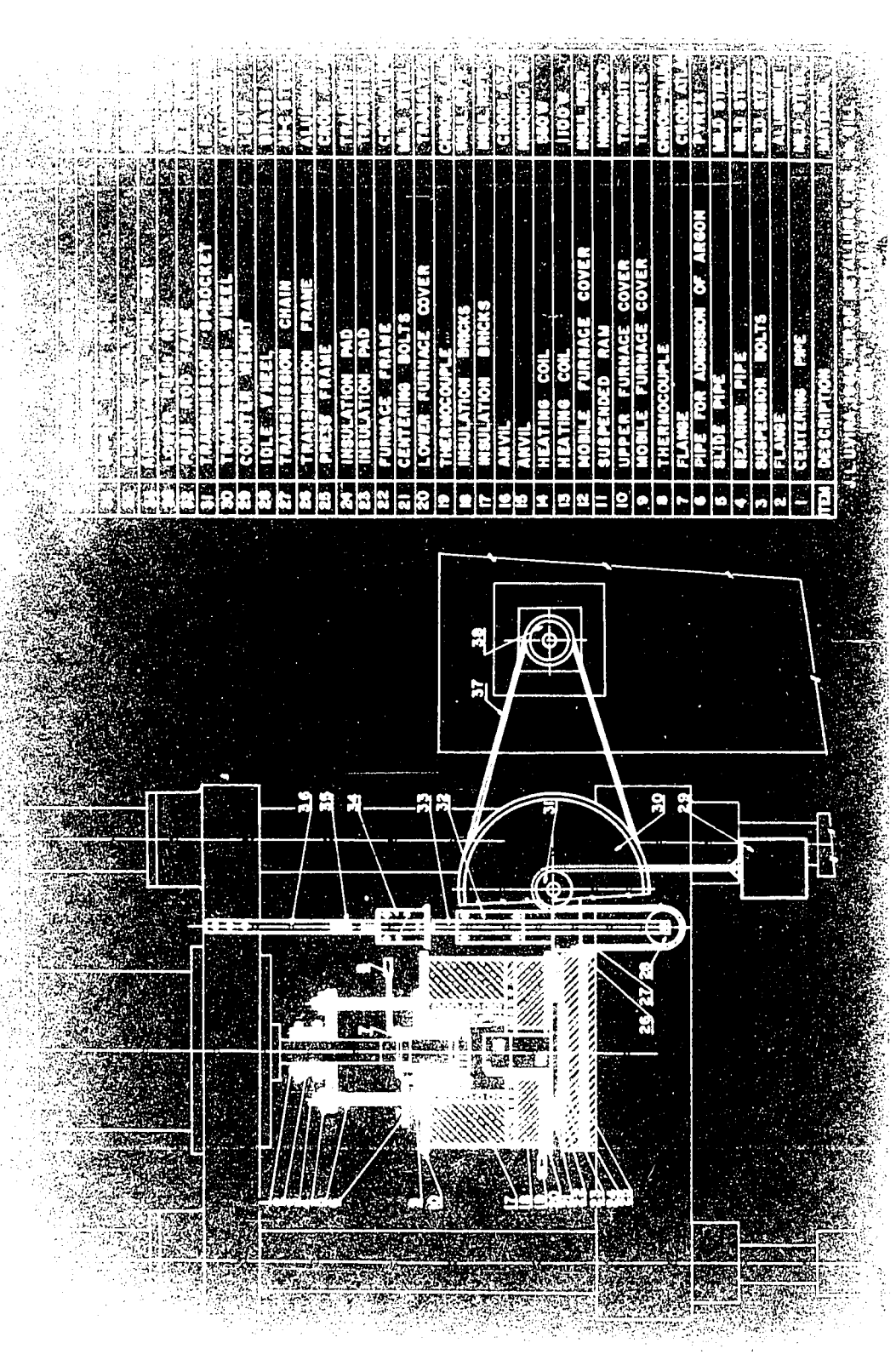


Fig. 3 - Arrangement of the hot compression furnace and annealing equipment.

Decreased for reproduction 2.5X



fixed on the extrusion ram and sliding over pipe (5). The specimens were discharged using crucible tongs and quenched in water.

3.2.3 STRAIN RATE CONTROLLING MECHANISM

A constant true strain rate was provided during the compression cycle by arranging that the instantaneous crosshead velocity of the extrusion press be proportional to the instantaneous specimen height. The reason for doing so can be seen from the following argument.

The strain & at any moment of a right cylinder undergoing compression is

$$\mathcal{E} = -\ln \frac{h_0}{h} \tag{7}$$

where (h_o) is the initial height of the cylinder and (h) is the instantaneous height.

By differentiation with respect to time, the strain rate can be expressed as

$$\dot{\mathcal{E}} = \frac{\mathrm{d}\ln h}{\mathrm{d}t} \tag{8}$$

However, $\dot{\mathcal{E}}$ = constant $\dot{\mathcal{E}}_c$ during constant true strain rate testing.

$$\frac{1}{h} dh = \dot{\mathcal{E}}_c dt$$

and
$$\frac{dh}{dt} = \dot{\mathcal{E}}_c h$$

However,
$$\frac{dh}{dt} = v$$
, the crosshead velocity (10)

Thus constant true strain rate testing can be achieved by decreasing the crosshead velocity as the specimen height decreases; that

is by making

$$v = \dot{\mathcal{E}}_{c} \cdot h \tag{11}$$

The steps required to do this mechanically were the following. As an approximation, the crosshead position during compression was taken to represent the instantaneous specimen height. This neglected the very small change in length of the upper ram during the cycle due to elastic compression. It also neglected the time constant of the hydraulic system, which was much smaller than the period of the compression cycle. Under normal extrusion conditions, the crosshead velocity was set on the flow control valve (V) at the beginning of an experiment, and left unchanged. Fortunately, the flow control valve had a linear angular displacement/ crosshead velocity characteristic. Thus a linear linkage between the crosshead position and the angular position of the control valve could be used to produce a constant true strain rate during hot compression.

There were two further requirements. One was that the initial crosshead speed not change during the free travel of the ram, but only when actual compression of the specimen had begun. This was achieved by the use of a friction clutch which engaged the linkage at the appropriate instant.

The other requirement was that the geometry of the linkage be appropriate to the actual constant true strain ${\rm rate}(\dot{\mathcal{E}}_c)$ being used. Thus suitable combinations of gears (30) and (38) had to be employed in order to produce different strain rates (Fig. 3).

3.2.4 TEMPERATURE CONTROL

The temperature of the cycle was controlled by thermocouples (8) and (19), situated under the surface of the platens, very close to

the specimen faces (Fig. 3). Each thermocouple operated one of the two independent heating elements (13) and (14) in the hot compression furnace (R), Fig. 2. The furnace temperature, ram force, and position of the ram were recorded as functions of time during each test.

The temperature inside the specimens was checked by the use of small thermocouples during the heating cycle. The thermocouples were inserted into a hole drilled in a few specimens up to the center line. These were afterwards placed into the furnace and the extension wires were passed through the argon jet (6), Fig. 3. The differences in the readings of the thermocouples recording the temperatures inside and outside the specimens, were less than 8°C at 800°C.

3.2.5 EXPERIMENTAL CAPABILITIES OF THE EQUIPMENT

As modified, the hot compression equipment was used up to 800° C and permitted quenching after a time lapse of 8 sec following the completion of compression. Constant true strain rates ranging from $\dot{\mathcal{E}} = 7.5 \text{x} 10^{-2}/\text{sec}$ up to $5 \text{x} 10^{-1}/\text{sec}$ were attained at maximum forces of 90,000 lb. The maximum true strain was limited to 1.9 by the size of the platens and by incidence of barreling.

Actual recorded strain rates were found to differ from the desired constant true strain rates by less than 15%. In view of the inexpensive equipment used, this would seem to be a satisfactory result.

3.3 MODIFIED HIGH TEMPERATURE CREEP EQUIPMENT

3.3.1 GENERAL LAYOUT OF THE EQUIPMENT

The general layout of the equipment as finally used is shown in Fig. 4 and the high temperature furnace itself has been described in



Fig. 4 - Experimental apparatus for hot compression using the modified high temperature creep equipment.

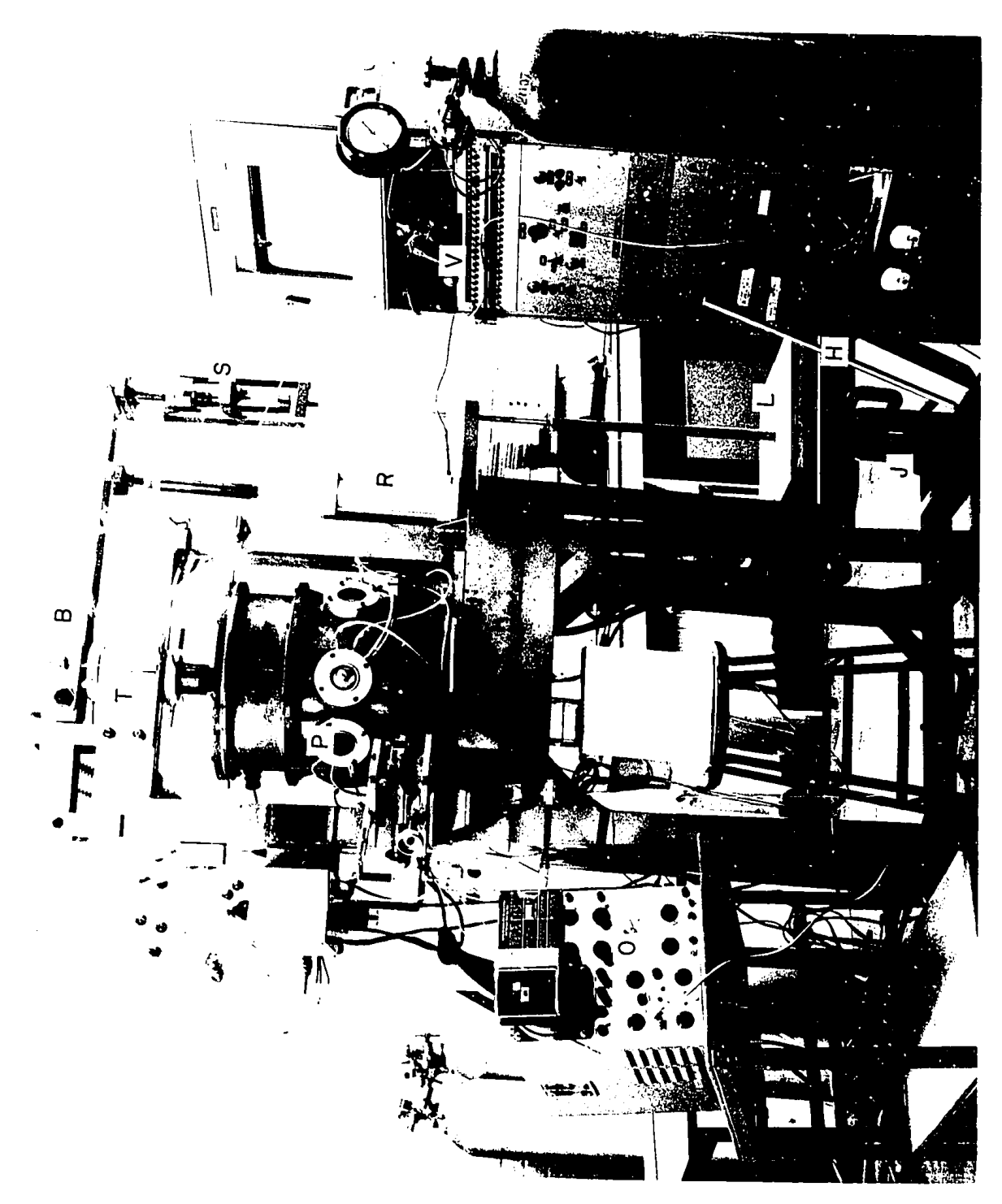


Fig. 4 - Experimental apparatus for hot compression using the modified high temperature creep equipment.

detail by AXELRAD 95,96). The details of the modifications to the high temperature furnace are shown in Fig. 5, where the changed or added parts are distinguished from the original equipment by heavier lines. The accessories are described in the schedule on the drawing. Further parts of the adapted equipment consisted of the strain gauges (S), the displacement transducer (T) and the pneumatic jack (R), and can be seen in Fig. 4.

The specimens to be compressed were inserted into the high temperature furnace through the port (P) Fig. 4 and placed by means of specially designed crucible tongs onto the anvil (15) Fig. 5. After the furnace had been purged with dry argon, the specimen was heated up to temperature by two separate electric elements. These were controlled by two thermocouples, which contacted the cylindrical surface of the specimens at the top and at the bottom of each specimen. Force was exerted on the ram by an adjustable load (L) Fig. 4, suspended on the beam (B) and supported by the hydraulic jack (J), which was released by the handle (H). After the compression had been accomplished, the load was released by the pneumatic jack (R), which was operated by the valve (V) and powered by compressed air. The forward motion of the jack (R) released the push-rod lock (14) Fig. 5, shooting the compressed specimen from the anvil (15) into the basket (7). The specimen dropped through the hollow anvil (15), the tubular support (16) and the distance flange (19) onto the hopper (22). Releasing the counterbalanced hopper by its weight, the specimen fell into the water tank (25) and was quenched. The mobile lock (23) was released during the compression cycle and the counter weight (20) kept the hopper closed preventing air from intruding

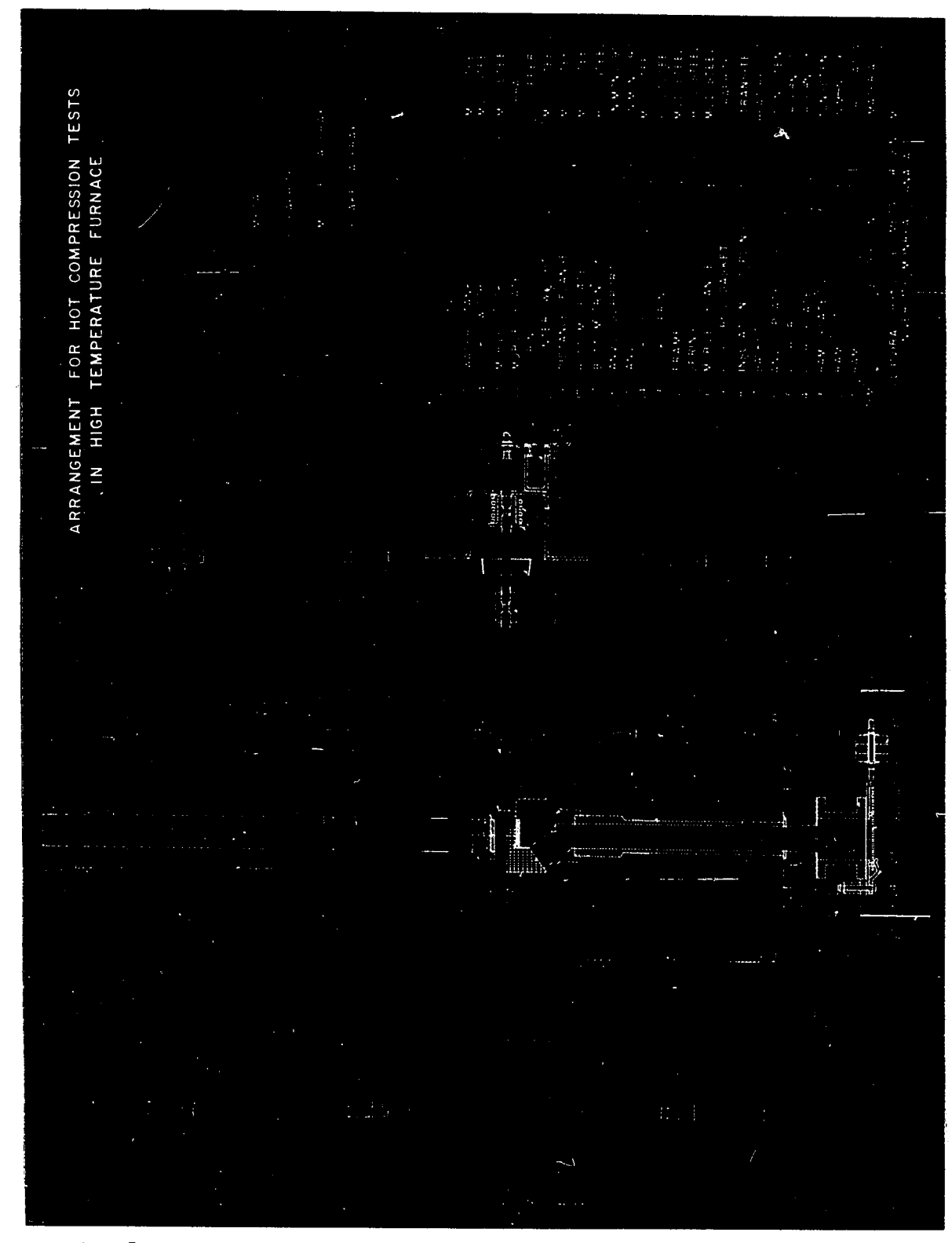
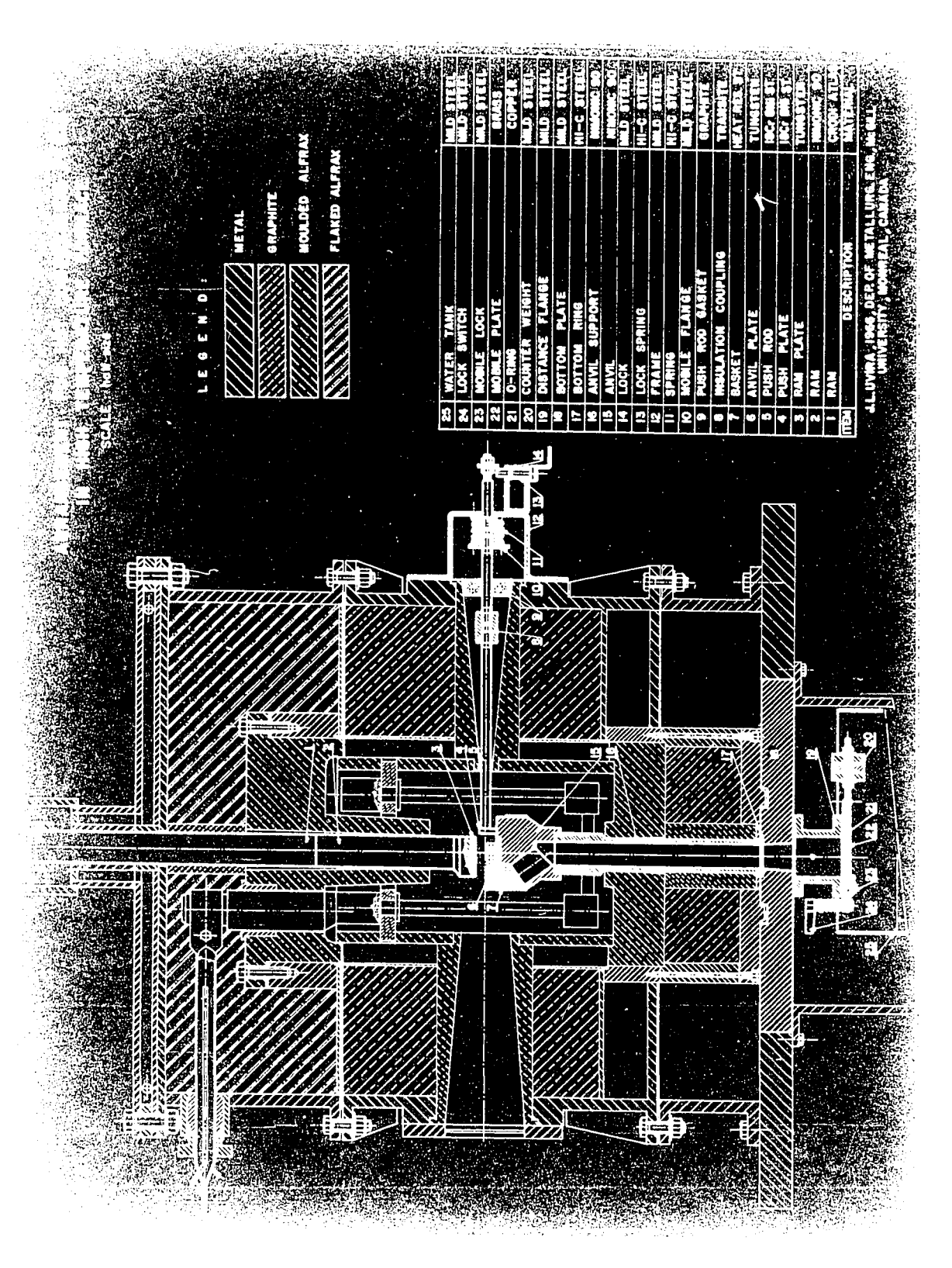


Fig. 5 - Arrangement for hot compression testing in modified high temperature creep furnace.



into the furnace.

The strain-time cycle was recorded on a suitable chart by means of a displacement transducer (T) type 7DCDT-1,000, supplied by the HEWLETT PACKARD CO., Sanborn Division, Waltham, Mass. The change of load with time was detected by a strain gauge bridge (S) and recorded on POLAROID prints by an OSCILLOSCOPE TYPE 531 fitted with a Q-type PLUG-IN UNIT (O) produced by TEKTRONIC INC., Portland, Oregon.

3.3.2 STRAIN RATE CONTROLLING MECHANISM

In this case, the constant true strain rate was produced by means of an open loop control system, with the operator closing the loop by following a programmer or strain pacer. For each constant strain rate, an appropriate strain-time curve was prepared and mounted on the strain recorder. The operator attempted to release the jack (J) in such a way as to reproduce the desired strain-time curve on the recorder as closely as possible. After a certain amount of practice, fairly good constant true strain rates were achieved, although not in every test. Only those specimens which had compressive strain rates varying no more than ± 15% from the desired values were selected for further investigation.

3.3.3 EXPERIMENTAL CAPABILITIES OF THE EQUIPMENT

The modified creep equipment enabled compression tests to be conducted at temperatures up to 1,000°C and at constant true strain rates ranging from $\dot{\mathcal{E}}=5\times 10^{-2}/\mathrm{sec}$ to about 1/sec. An important feature of the equipment was that quenching was possible within about 1 sec of the completion of the deformation. The maximum force used was about 8,000 lb., and the maximum strain was limited to $\mathcal{E}=1$ by the size of

the platen and of the tubular passages inside the furnace required for quenching.

4 EXPERIMENTAL PROCEDURE

4.1 PREPARATION OF SPECIMENS FOR MICROHARDNESS TESTS AND OPTICAL METALLOGRAPHY

Several different methods were tried to prepare the specimens for optical observation of the substructure and for microhardness examination. Neither mechanical polishing using diamond paste ³³⁾, nor electropolishing in acetic-perchloric acid solutions ⁹⁷⁾ was completely satisfactory. Difficulties were also encountered during etching because of overetching around the numerous impurities present in the commercial material. The best results were obtained by following the practice developed by MORRIS ⁹⁸⁾, which was modified as described in the following section. Both the source of direct current and the electropolishing equipment were designed and constructed by the present author.

4.1.1 SECTIONING AND MOUNTING OF SPECIMENS

Compressed specimens were sectioned by hand along planes containing the compression axis. One half of each of the sectioned cylinders was mounted in a conductive mount 1 1/4 in. in diameter, following the practice developed by MORRIS⁹⁸⁾. The moulding powder was produced in the laboratory by mixing three untapped volumes of black bakelite with one untapped volume of iron dust, both sieved to 60-mesh. However, the mounting technique was modified as follows. To decrease the conductivity of the mount face contacting the electrolyte, the bottom face of the mount was provided with a thin layer of plain bakelite as shown in Fig. 6. Satisfactory contact was thus maintained between the specimen body and the conductive part of the mount. This arrangement decreased not only the overall heating of the solution due to the large currents involved,

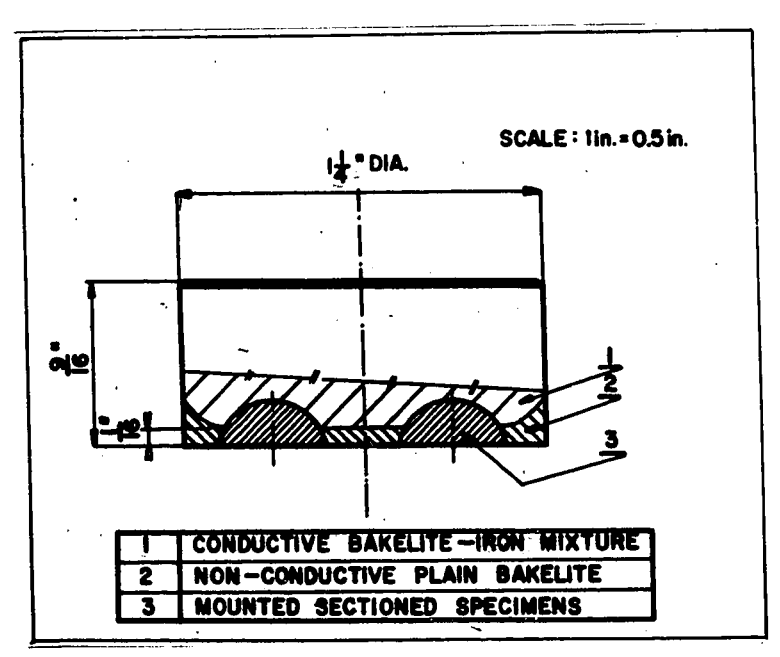


Fig. 6 - Specimen mounting practice

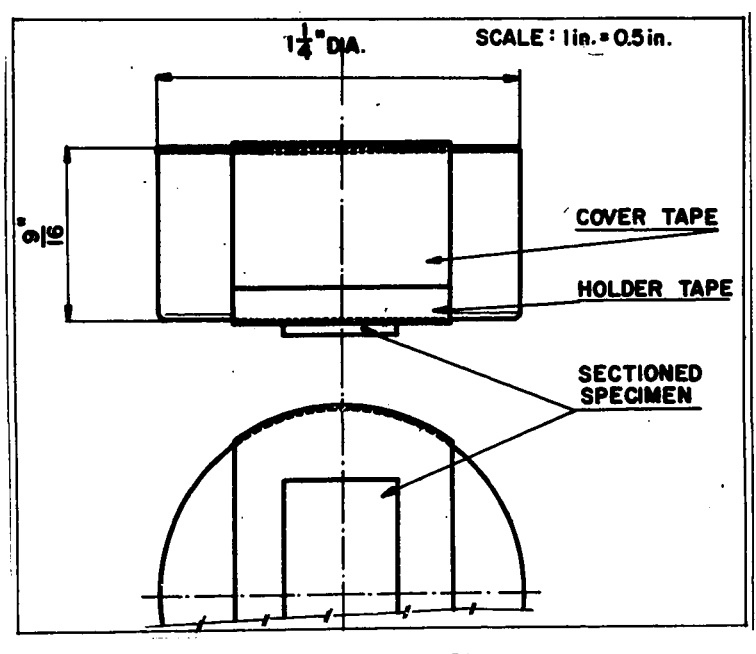


Fig. 7 - Polishing fixture



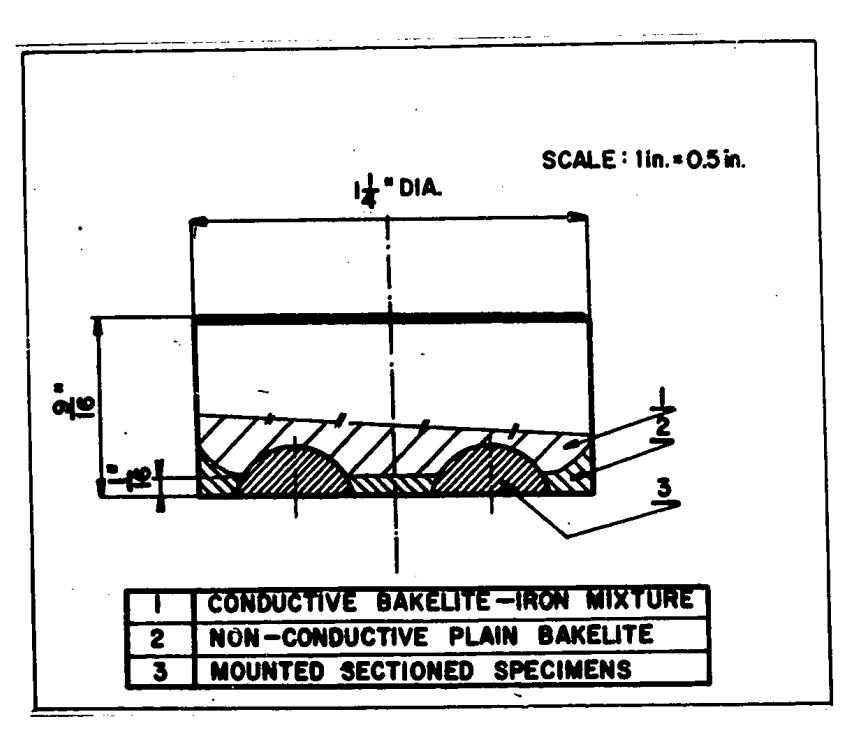


Fig. 6 - Specimen mounting practice

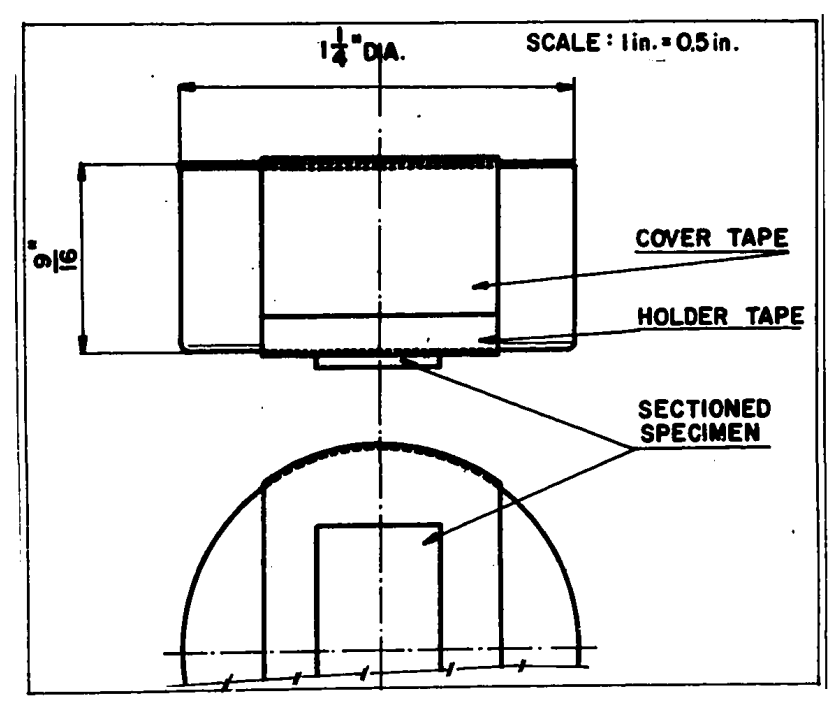


Fig. 7 - Polishing fixture



but local overheating, causing non-uniform polishing, was also prevented. After mounting, the surfaces of the mounted specimens were prepared for surface grinding by passing them through 320-mesh grit to 600-A-mesh emery papers.

4.1.2 GRINDING AND MECHANICAL POLISHING

During electropolishing the distance between the specimen surface and the electrode plays a very important role and affects the uniformity of electrochemical attack. A practice was therefore developed of surface grinding all the mounted specimens to the same height. This also removed the unwanted thin layer of plain bakelite on the top of the mount preventing electrical contact with the mount holder.

Prior to electropolishing, the specimen surface was conditioned by grinding on polishing wheels using 15 μ diamond paste. Afterwards the specimen surface was degreased with acetone, washed in methanol, and dried.

4.1.3 ELECTROLYTIC POLISHING

This operation was carried out in a cell as recommended by MORRIS 98 . The cell consisted of a stainless steel dish cooled by water circulating in stainless steel coils. The conductive bakelite-iron mount containing the specimen was fixed in a rotating stainless steel jig driven at a constant 100 ± 2 rpm. The composition of the electrolyte was as follows:

133 ml glacial acetic acid (99.5% by wt. min.)

25 g chromium trioxide CrO₃

7 ml water

The specimen, which was fixed in the rotating jig, was held at a constant distance of 1/4 in. from the bottom of the stainless steel dish, which served as the cathode. The operating temperature was maintained between 17°C and 19°C. The voltage applied across the cell was 20 V. In general, the polishing time did not exceed 6 min.

4.1.4 CHEMICAL AND ELECTROLYTIC EICHLING

After polishing, the Armco iron specimens were rinsed with acetic acid, washed with methyl alcohol and dried. The silicon steel specimens were subsequently etched in the same electrolyte for 0.5 to 2.5 minutes at a decreased voltage of 10 V.

The Armco iron specimens were etched in 1% nital for 3 to 5 minutes followed by a rinse in methyl alcohol. If the polishing electrolyte was carefully removed, and the etching followed immediately after polishing, the substructure was clearly brought out. Etching with nital was tried on some of the silicon steel specimens and a few Armco iron specimens were submitted to electrolytic etching at different voltages. However, no satisfatory results were ever obtained with any of these alternatives. Other reagents, such as saturated picral or Fry's reagent, did not reveal the substructure better than 1% nital carefully applied. This result confirms the reports of previous investigators 17). The electrolytic etching of silicon steel gave satisfatory results and was found to be very sensitive to the voltage and the etching time used.

4.2 PREPARATION OF SPECIMENS FOR TRANSMISSION ELECTRON MICROSCOPY

Specimens of both Armco iron and silicon steel were prepared for examination by transmission electron microscopy as follows. Sections

containing the compression axis approximately 0.1 in. thick were sawn by hand from the compressed cylinders. These had previously been carefully pickled in a 5% hydrofluoric acid solution containing hydrogen peroxide so as to remove the surface layer which was contaminated with traces of lubricant. Further decreases of thickness down to 0.05 in. were produced by grinding the specimen on a surface grinding machine fitted with magnetic chuck.

The rough surface after grinding was polished by hand on emery papers under water, starting with a 320-mesh grit and going through to a 600-A-mesh grit. A simple contrivance, which is shown in Fig. 7, was constructed to keep the surface flat during grinding. The specimen thickness was decreased to about 0.04 in. by this method. A rinse with acetone and with methyl alcohol followed this operation.

The final thinning of the specimens was performed chemically in a solution suggested by PACKWOOD⁹⁹⁾ having the following ingredients: 80 ml $_{2}O_{2}$ (30%), 5 ml HF acid (48%), 15 ml $_{2}O_{3}$.

The area selected for examination was cut out under an optical microscope and placed into the specimen holder of the electron microscope. The tiny piece was located between two copper mesh grids, the positions of which were fixed by a spring washer.

An alternative thinning procedure, that of jet-machining followed by electrolytic thinning, did not yield satisfactory results. This was attributed to the preferential attack of the areas around inclusions, so that the adjacent areas were unsatisfactorily thinned. Another possibility was the deflection of the electron beam due to the magnetic field of the relatively massive rim of the dished specimen.

4.3 OPTICAL AND ELECTRON METALLOGRAPHY

The optical investigation of the microstructure was carried out on a VICKERS projection microscope at magnifications ranging from 130 X to 1,550 X. Photomicrographs were taken both on 4 x 5 in. KODAK M-plates and on 200 ASA POLAROID films. The magnifications were determined using a stage micrometer.

Transmission electron micrographs of the substructure and diffraction patterns were taken on SIEMENS ELMISKOP I (100 kv) electron microscope fitted with a tilting stage at magnifications ranging from 2,000 X to about 50,000 X. Photomicrographs were taken on standard 6.5 x 9 cm KODAK plates.

4.4 DETERMINATION OF SUBGRAIN SIZE

Subgrain sizes were determined by areal analysis of micrographs taken optically and by transmission electron microscopy. The use of polarized light was tried in an attempt to accentuate the subgrains observed optically; however, the results were unsatisfactory. Following the practice used for the determination of austenitic grain size 100 and the ASTM recommendations for subgrain size measurement, both comparison and counting procedures were used for the determination of the average subgrain size.

4.4.1 PLANIMETRIC PROCEDURE (ASTM Standard No. E 112-63 section 8)

The magnifications of the optical micrographs were selected so that each field contained at least 50 subgrains. The sum of all the complete subgrains plus one half of the subgrains intersected by the perimeter of the area, was taken as the number of equivalent whole sub-

grains within the area. Instead of circles, rectangular frames were used for subgrain counting on both the optical and the electron micrographs. As regards the electron micrographs, when fewer than 50 subgrains were present on a given plate, plates of adjacent areas were used to increase the subgrain count to at least 50.

As the magnifications were not standardized, the ASTM formulae were adapted to suit, and the following equation was used:

$$d = \frac{1,000 \sqrt{A/N}}{M}$$
 (12)

where d = the "diameter" of the average subgrain [microns];

A = the plate area over which the size measurement was
made [sq.mm];

N = the equivalent number of whole subgrains;

M = the magnification used.

4.4.2 COMPARISON PROCEDURE (ASTM Standard No. E 112-63 section 6)

Subgrain sizes were compared with the standard network charts published in the ASM METALS HANDBOOK 1948, pp. 402-403, Figs. 3 to 8. The resulting ASTM numbers were corrected by the factor Q = 6.64 $\log \frac{M}{M_{\rm L}}$ to allow for the fact that the specimens were viewed at the magnification (M) instead of the basic magnification (M_b). The ASTM numbers resulting from the comparison were rounded off to the nearest approximate unit listed in Table II. — (Micro-grain size relationships), ASTM Book of Standards, Part 31, p. 231, and the "diameter" of the average subgrain was thus obtained.

4.5 DETERMINATION OF SUBGRAIN MISORIENTATION

Diffraction patterns of neighbouring subgrains were taken from nearly every specimen examined, using the method described by 102 and others 103 . The electron diffraction patterns were produced in two alternative ways:

- (a) The beam was directed in turn towards the center of two adjacent subgrains, so that two separately exposed patterns were superimposed on the $film^{104}$ (Fig. 8).
- (b) The beam was directed towards a sub-boundary which separated two adjacent subgrains and the diffraction pattern of the entire area was then obtained in one exposure 77) (Fig. 9).

The rotation of the patterns about an axis parallel to the electron beam was then determined. The angles obtained correspond to the tilt component of the misorientation for general boundaries which are parallel to the electron beam. The misorientation components about axes normal to the beam were estimated to be of the same order as the measured misorientation. This estimation is based on the fact that the longitudinal sections were taken at random azimuth angles to the specimen exterior.

No misorientation measurements were made on transverse sections.

4.6 CALCULATION OF TRUE STRESS-TRUE STRAIN CURVES

<u>Deformation Variables</u>. As mentioned in section 3.2 above, the following variables were measured in the course of the compression cycles:

- 1. Load, recorded with respect to time as follows:
 - (a) on a 10 in. wide chart running at a constant speed of 0.345 in./sec(modified extrusion press);

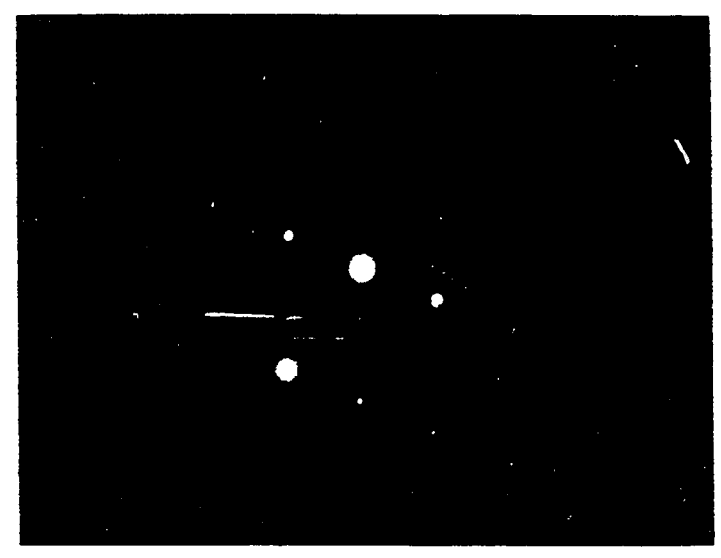


Fig. 8 - Superimposed transmission electron diffraction patterns of 2 adjacent subgrains. Armco iron; 600°C ; ϵ = 0.56.

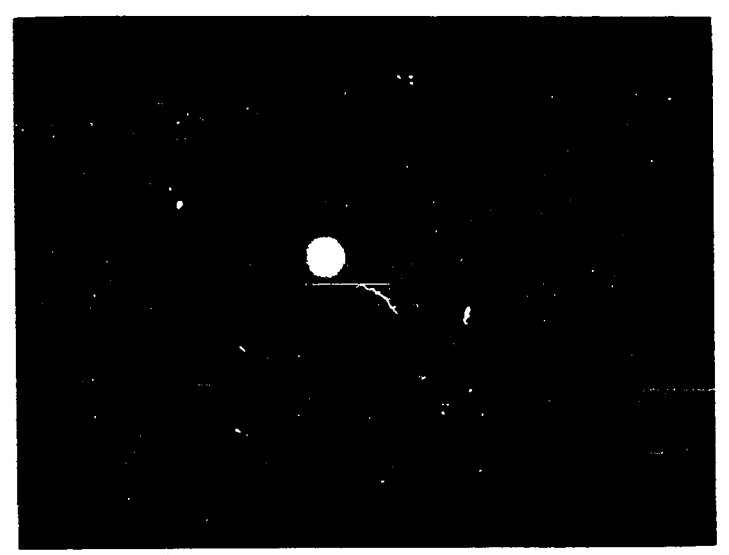


Fig. 9 - Transmission electron diffraction pattern of area with 3 subgrains. Silicon steel; 900°C ; $\varepsilon = 0.30$.

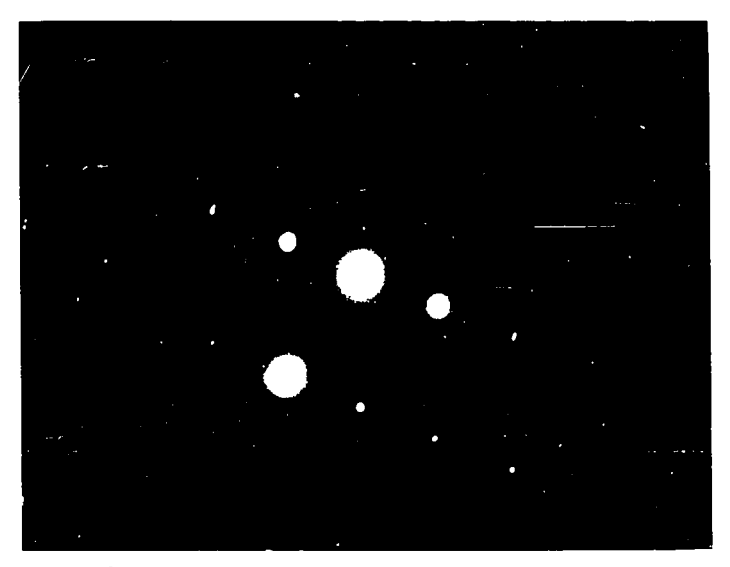
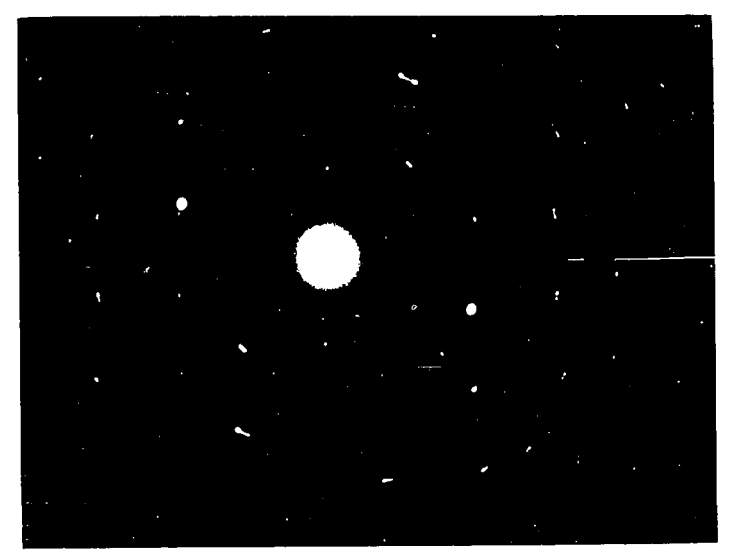


Fig. 8 - Superimposed transmission electron diffraction patterns of 2 adjacent subgrains. Armco iron; 600°C ; $\epsilon=0.56$.



ř.

Fig. 9 - Transmission electron diffraction pattern of area with 3 subgrains. Silicon steel; 900°C ; \mathcal{E} = 0.30.

- (b) on a POLAROID print by means of a camera fixed to the screen of an oscilloscope recording the cycle. The adjustable scanning sensitivity of the oscilloscope ranged from 0.1 to 100 sec/cm (modified creep machine).
- 2. Axial contraction, recorded against time as follows:
 - (a) on the same chart as mentioned in 1(a), by means of a ten-turn position potentiometer and a two-pen recorder;
 - (b) on a 11 in. wide chart running at a constant speed of 0.266 in./sec, registered by means of a linear displacement transducer.
- 3. Temperature, measured by contact thermocouples.

The arrangement described under 1(a) and 2(a) supplied data for the compression cycles of 1 in. dia. Armco iron and 0.6 in dia. silicon steel. The 1(b) and 2(b) arrangement was used to control and to record the compression cycles of Armco iron and silicon steel specimens 0.385 in. in diameter.

<u>Calculation of True Stress and True Strain.</u> The true strain (&) was calculated from the axial contraction as follows:

$$\mathcal{E} = -\ln\frac{h_0}{h} \tag{7}$$

where: h_o = specimen height prior to compression,

h = specimen height at any instant.

The corresponding true stress (\circ) induced by a uniaxial force (F) is given by:

$$6 = \frac{F}{A_i} \tag{13}$$

where: A_i = the instantaneous cross-sectional area of the specimen, which is related to the original area A_0 as follows:

$$A_{i} = A_{o} \frac{h_{o}}{h}.$$

It should be pointed out that the compressive load (F) includes a contribution due to friction and barreling, as well as the energy stored during work hardening. Thus it is higher than in the ideal case of frictionless, homogeneous deformation. Corrections were therefore made for friction and barreling, and the procedure used will be described later in the Results. Figs. 10 and 11 show typical experimental records, which were used for calculation of the true stress-true strain curves. The load - time graph in Fig. 11 is a trimmed POLAROID print of the original record.

4.7 MICROHARDNESS MEASUREMENTS

The microhardness tests were carried out on a TUKON hardness tester designed for the determination of KNOOP and 136° diamond pyramid hardness numbers.

According to the literature, a range of loads has been used for DPH tests of cold worked and annealed Armco iron and silicon steel. These include the following: $10~{\rm kg}^{109}$, $1~{\rm kg}^{83,105,106}$, $100~{\rm g}^{107}$, $50~{\rm g}^{108}$. Most of the test results using loads lower than 100 g have been presented in the form of distribution curves rather than as single values.

Accordingly, in the present investigation, loads of 100 g and 1 kg were used, and hardness measurements were made on every second specimen. Impressions were taken on three rows lying parallel to the compression axis and at different distances from it. Prior to examination the specimens were electrolytically polished. The location pattern of indentations is represented in Fig. 12. Occasionally large variations were found in the size of adjacent impressions. When the microhardness

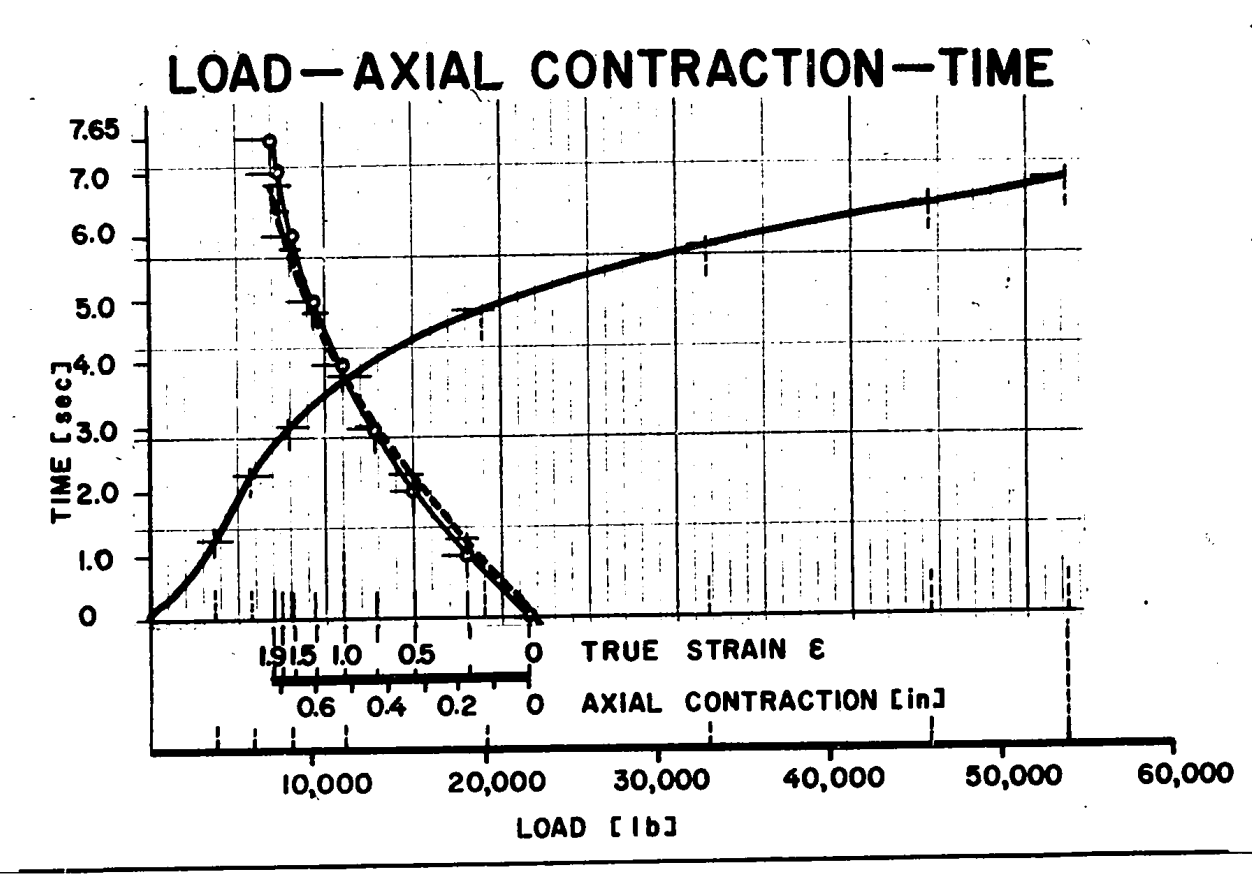
Typical

extrusion press.

hot

compression using the

ram of

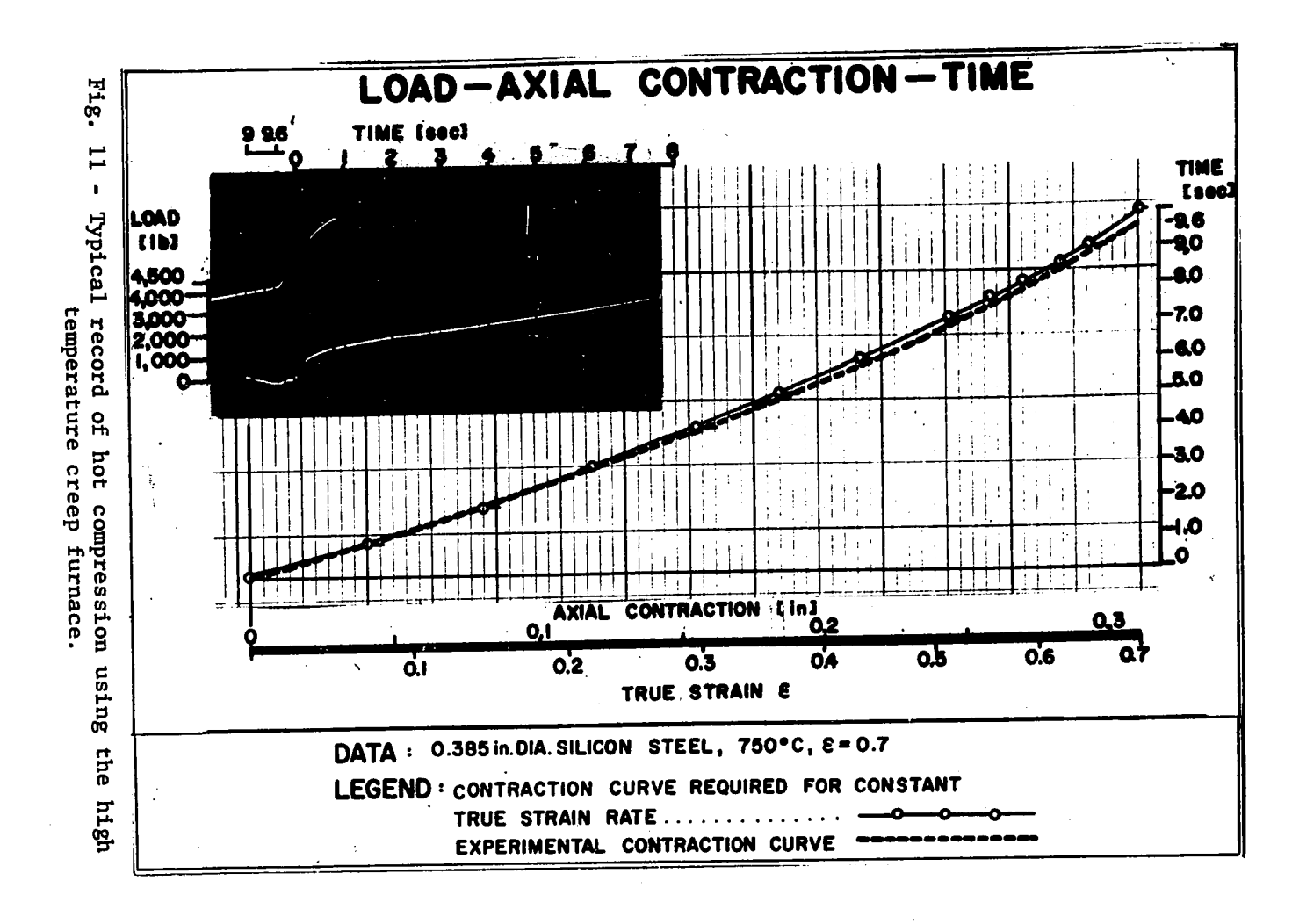


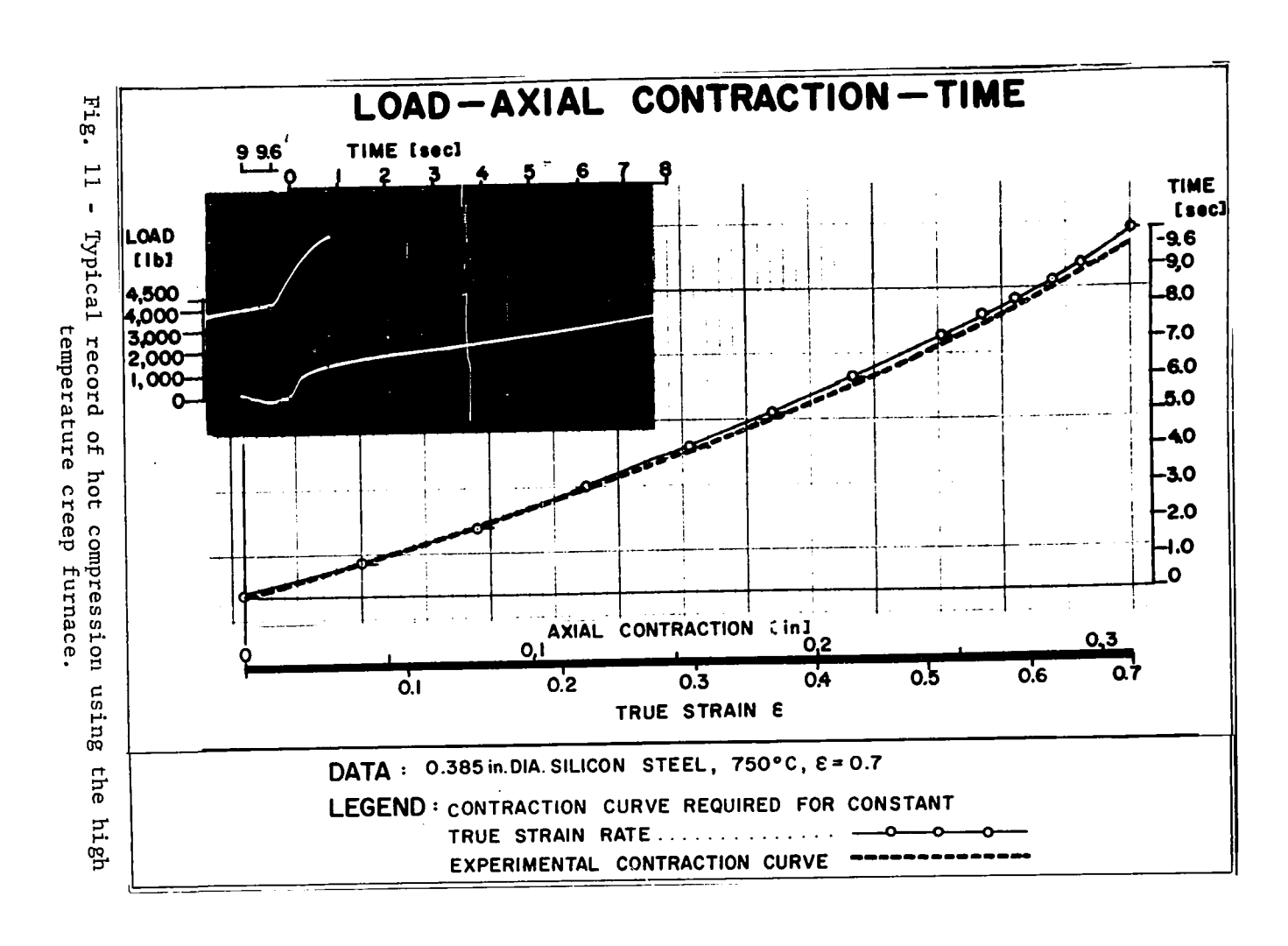
DATA: O.6 in.DIA. SILICON STEEL, 800°C, E = 1.91

LEGEND: CONTRACTION CURVE REQUIRED FOR CONSTANT

TRUE STRAIN RATE.

EXPERIMENTAL CONTRACTION CURVE.





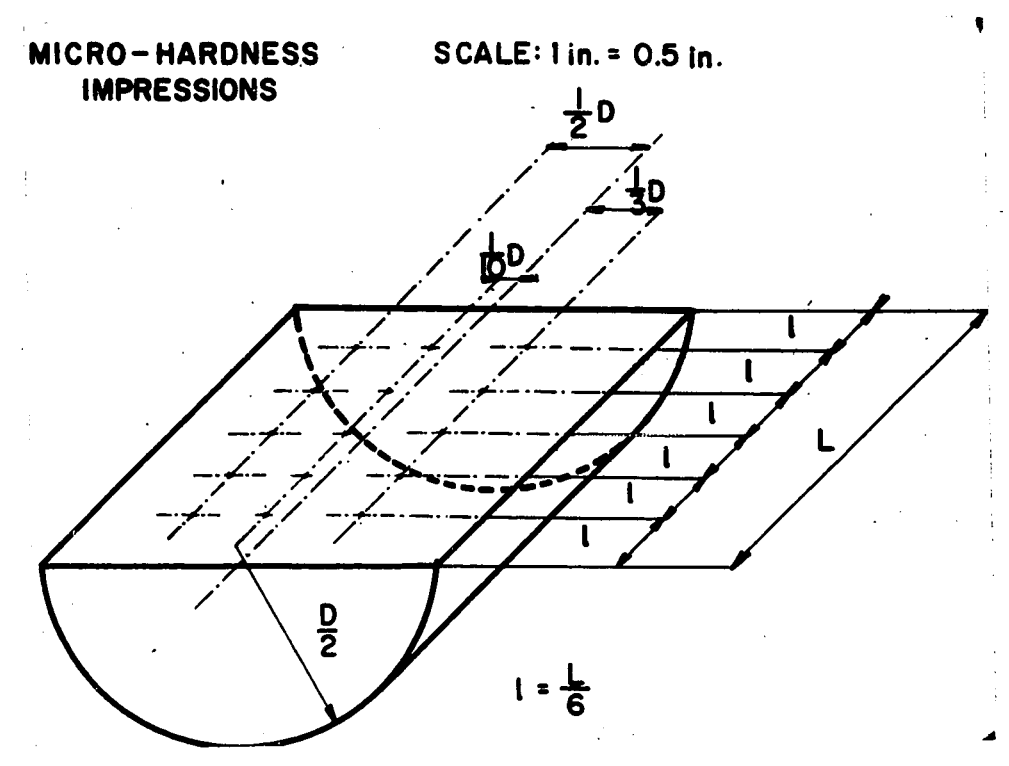


Fig. 12 - Location of microhardness impressions.

difference was more than 10%, a new impression was made in each area and the average value of the four readings taken. The microhardness of a specimen was usually determined by averaging 12 impressions. In some cases, when the microhardness was uniformly distributed, only 9 impressions were used. However, 15 or even more tests were done on specimens which exhibited a large scatter of results.

The diagonals of the indentations were measured at 750 X magnification and objective factors were determined by the use of a stage micrometer. For each group of tests, the machine was checked by the use of a standardized test block. About 700 indentations using a load of 100 g were carried out on 64 specimens, and 18 of them were rechecked with a load of 1 kg. The differences resulting from the application of two different loads were not substantial.

5 <u>EXPERIMENTAL RESULTS</u>

5.1 TRUE STRESS-TRUE STRAIN CURVES

The true stress-true strain curves shown in Figs. 13a to

24a represent the stresses as calculated from the total work done during hot compression, plotted against the true strains. These curves are only approximate, however, because the total work done during hot compression is greater than the work of homogeneous deformation. The total energy expended during hot compression is composed of the following:

- (a) the energy required for homogeneous deformation;
- (b) the energy required to overcome friction between the specimen and the anvils;
- (c) the energy for the inhomogeneous deformation associated with barreling;
- (d) the energy stored in the lattice during work hardening. (This is usually considered as part of (a) or (c), but will be discussed separately below).

In order to derive a general stress, strain rate, temperature relationship for hot compression, the flow stress with respect to homogeneous deformation must be obtained. There are two ways in which such a condition can be approximated, one experimental, and the other analytical. The first is to eliminate friction as completely as possible by the use of suitable lubricants and thus to prevent barreling. The second is to allow barreling to take place and to calculate suitable correction factors. As it is impossible to eliminate friction completely, especially at large strains, both these methods were used in the present work and will be described briefly.

5.1.1 THE EFFECT OF FRICTION

Friction and barreling can be substantially decreased by the application of appropriate lubricants 3,4,33), especially when these maintain a continuous layer on the contact surfaces. Lubrication breakdown is also prevented to a certain extent by grooves 33,93) on the specimen faces. The machining of the grooves and the composition of the lubricants used have already been described in section (3.1). Other arrangements leading to decreased friction, e.g. the shaping of the interface, and interrupted "multiple controlled compression", have been discussed in previous extensive studies 110), but were not used by the author.

Given that a certain amount of inhomogeneous deformation has taken place, the following methods have been proposed to correct the flow stress for the effect of friction and barreling.

- (a) Extrapolation of the data obtained for different ratios of specimen radius/specimen height to R/h = zero¹¹¹. This is valid because the effect of friction becomes negligible when either (R) approaches zero or (h) increases to infinity.
- (b) Derivation of a stress distribution satisfying the equations of plasticity and giving zero normal stress on the cylindrical part of the specimen surface¹¹²⁾. This approach to the problem is based on the idea that barreling in compression can be compared to necking in tension.
- (c) Application of empirical formulae concerning correction factors for friction and barreling 112). These formulae are dependent on data obtained from tests carried out with different lubricants.

The stress data in the present investigation were corrected for the effect of friction by using the equations of SCHROEDER and WEBSTER¹¹³⁾, which fall in category (b) above. These equations were derived for the forging of round blanks and were adapted by DIETER⁴⁸⁾ for the evaluation of compression data for cylinders in plane strain. The coefficient of friction for use in this equation was determined by compressing a range of cylinders with different R/h ratios. The results of the tests were evaluated by means of an equation proposed by SIEBEL⁴⁾.

The above-mentioned equations are quoted below.

SCHROEDER and WEBSTER:

$$\frac{\mathcal{G}_{AV}}{\mathcal{G}} = \frac{2}{C^2} \left[\exp (C) - C - 1 \right]$$
 (14)

SI EBEL:

$$\frac{G_{AV}}{G} = \left(1 + \frac{2}{3} \varphi \times \frac{R}{h}\right) \tag{15}$$

where: G_{AV} = the average stress for a cylinder loaded in compression;

6 = the flow stress;

 $C = 2 \varphi \frac{R}{h} ;$

 φ = the coefficient of friction;

R = the radius of the specimen;

h = the height of the specimen.

The coefficient of friction determined in the present investigation was found to be about 0.1 for all temperatures and materials. The same value was obtained by $COOK^4$ in the hot compression of steels in the γ -region.

Equation (14) may be used when both the coefficient of friction and the ratio of radius to height are small. If the coefficient

of friction increases to 0.577 or over, the spreading of the material proceeds by shear deformation within the specimen rather than by the relative motion of the specimen face to the platen surface. This usually occurs during hot compression with no lubricants. Inspection of both equations indicates that, unless the R/h ratio exceeds 3, there is little difference in the interpretation of the data by either equation.

5.1.2 THE STORED ENERGY AND THE FLOW STRESS

Most of the energy expended during the deformation of metals is converted into heat. A small remainder is stored in the crystal lattice. The amount of energy stored in steels after cold working by compression has been reported to be less than 1% 114). Another investigator 115) has proposed that the total energy stored during very rapid compression (10³/sec) is about 10%. No data concerning energy storage during the hot compression of steels has yet been reported. However, an estimate can be made as follows. The stresses involved in hot working to a given strain are about a fifth or a tenth of the cold working stress for the same material and the same strain. Thus the work done during hot working is an order of magnitude smaller than the work done during cold working. The dislocation density increases produced by cold working are around 10¹¹ to 10¹³ lines/cm². An estimate of the dislocation densities in unrecrystallized hot worked material suggests that they are close to those of creeped or polygonized material, and of the order of 10^8 to 10^{10} lines/cm² 5). The density increases during hot working are thus two or three orders of magnitude below those for cold working, and the ratio of the density increase to the total work done can be expected to be lower during hot working than cold working by as much as one or

two orders of magnitude. Thus, only a negligible part of the total work done can be stored in the lattice during hot working, and it can be concluded that the first stress during hot working is little affected by the energy being stored as distortions in the lattice. It also follows that the work of homogeneous deformation, inhomogeneous deformation and friction are converted almost entirely into heat.

It should be added that the stored energy contribution to the flow stress can in any event only have an effect during the work hardening part of the stress/strain curve, as once steady-state hot working is achieved, the rate of energy storage in the form of dislocations is matched by the rate of energy release by dynamic recovery.

5.1.3 TEMPERATURE RISE DURING DEFORMATION

As described above, the mechanical energy of hot working is converted almost entirely into heat. This produces a temperature rise which can be detected at high strain rates, but not easily at low strain rates, because there is enough time for the heat to escape into the surrounding medium. For adiabatic compression, the temperature increase of the specimen is given by the following equation:

$$\Delta T = \frac{w}{\text{const. } \delta \cdot c_{y}}$$
 (16)

where: $w = \text{the mechanical work per unit volume } \left[\frac{g \cdot cm}{cm^3} = \frac{g}{cm^2} \right]$;

const. = the mechanical equivalent of heat $[1 \text{ gcm} = 2.35 \times 10^{-5} \text{ cal}]$;

 δ = the average density over the given temperature range $\left[\frac{g}{cm^3}\right]$;

c_v = the average specific heat over the given temperature
 range [cal/g°C];

 ΔT = the temperature increment [°C];

The temperature rises corresponding to the applied strain rates and temperatures used in the present investigation were calculated for non-adiabatic and some of them also for adiabatic compression testing. For the non-adiabatic case, coefficients for the temperature increase of steel during hot torsion testing were used, as reported by REYNOLDS and TEGART¹⁷⁾. These were converted for compression and for the strain rates involved in the present investigation. The initial compression temperatures, the calculated temperature rises during the tests and the temperatures used in the calculations are given in Table V.

Table V. Temperature Increases for the Maximum Compressive Strains Attained at the Strain Rates and Temperatures Used

MATERIAL	TEMPERATINI TI AL		STRAIN E	STRAIN RATE É [&/sec]	TEMPERATURE INCRE CALCULATED FOR CO ADIABATIC	ASES AT [°C] MPRESSION ACTUAL
Armco iron	590 600 690 800 800	600 600 700 800 800	0.85 0.80 1.45 0.40 0.60	0.25 0.075 0.25 0.90 0.075	26 21 not calculated 8 5.5	8 4 9.5 6.5
Silicon steel		650 650 650 700 750 800 1,000	1.55 1.64 1.35 1.30 1.25 1.75 0.50 0.30	0.50 0.25 0.075 0.25 0.25 0.25 0.25 0.075	not calculated not calculated not calculated not calculated not calculated 4.5	36 18 2.5 14 9.5 11.5 1

Lowered initial temperatures were only used for a few specimens, as indicated in Table V. For the other specimens, where the calculated increases were less than 7°C, temperature corrections were neglected.

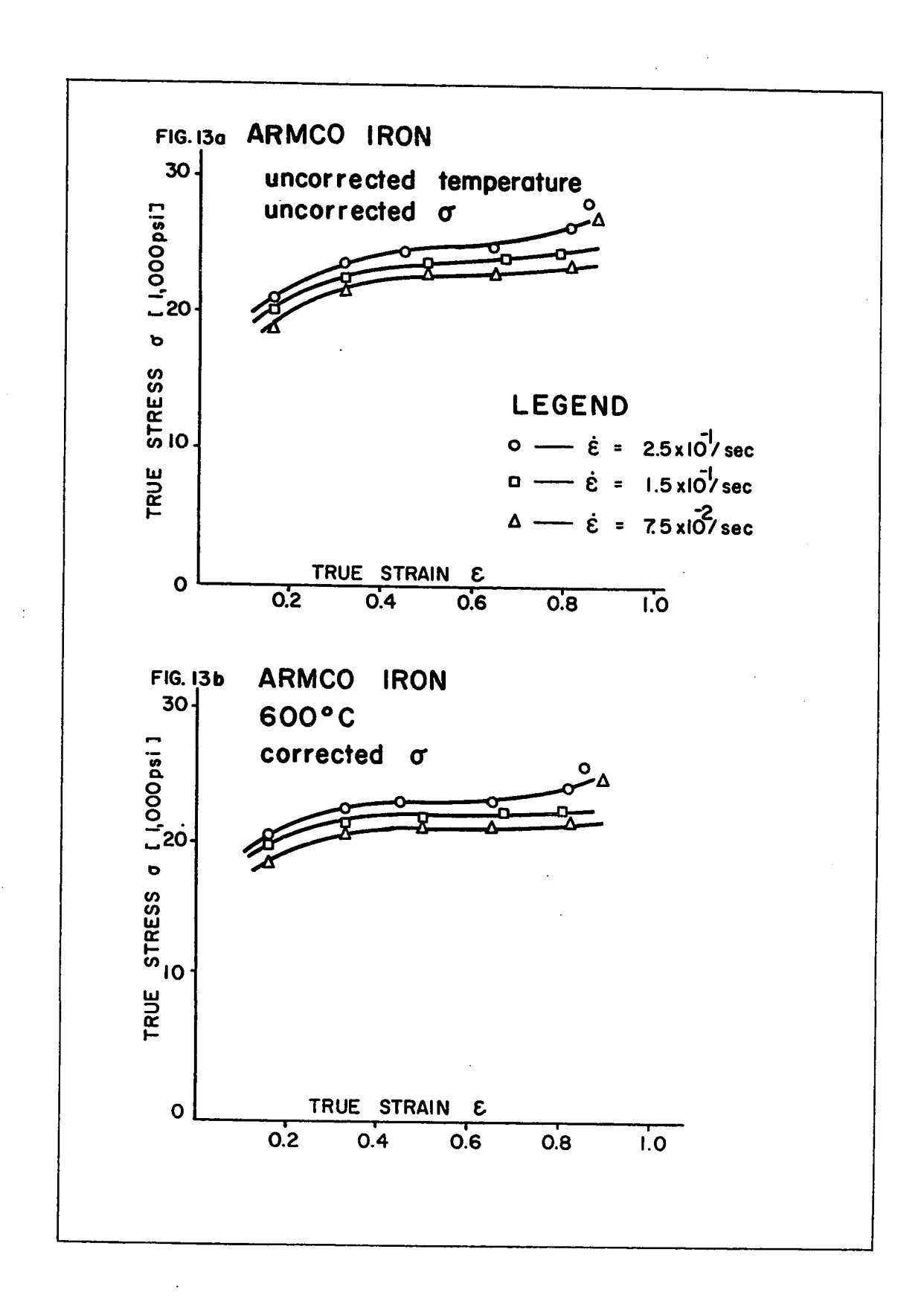
5.1.4 TRUE STRESS-TRUE STRAIN CURVES WITH CORRECTED STRESSES

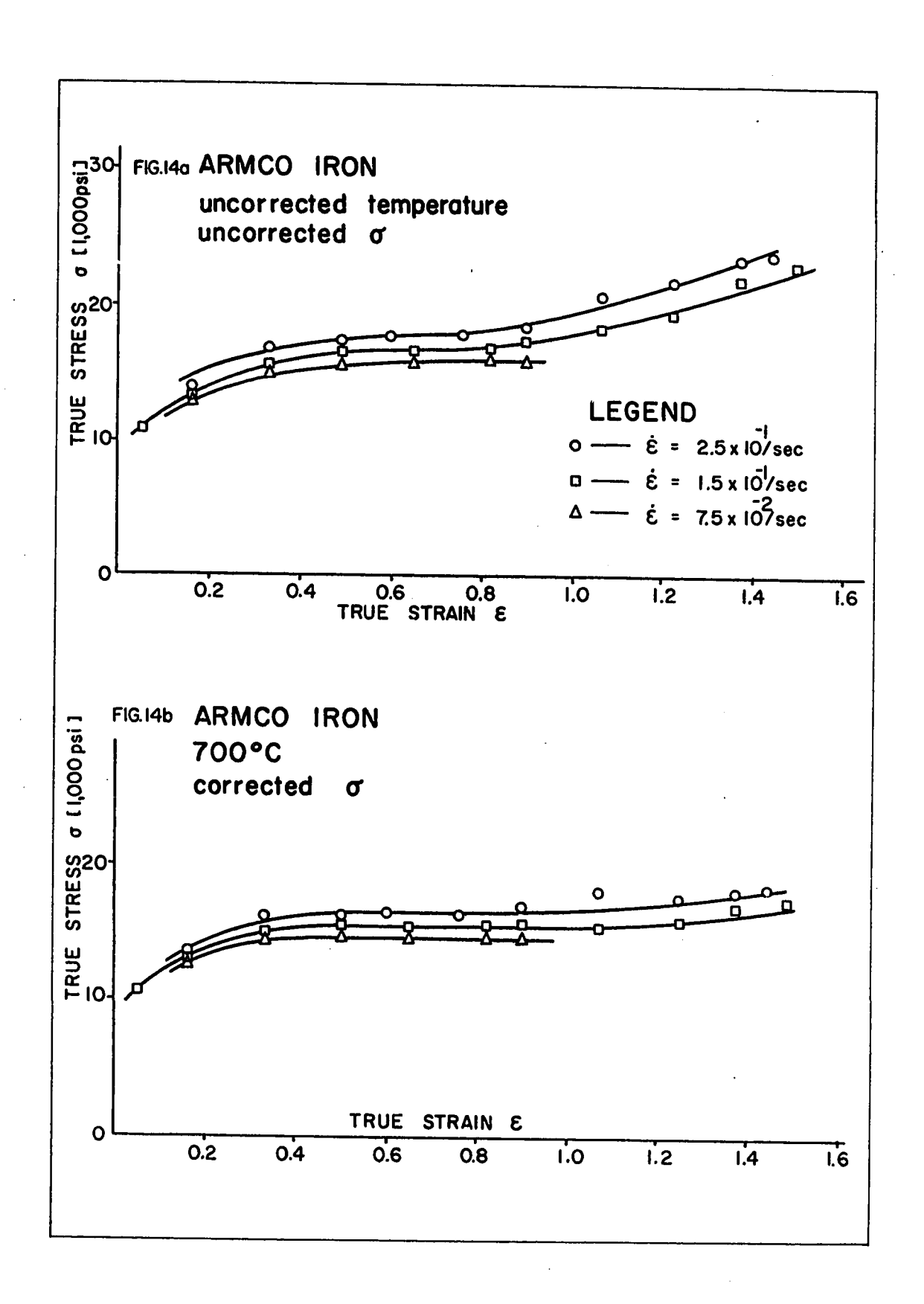
These curves were plotted after the stresses were corrected for friction and some of them also for temperature rise; they are presented in Figs. 13b to 24b. Most of the points in the curves represent from 2 to 7 specimens, the true stresses for which were averaged at the values of true strain, temperature and strain rate indicated. A few of the points are for single specimens only. Certain specimens were omitted from Figs. 21a, 23a and 24a, as they had very different R/h ratios from the rest. However, corrected stresses resulting from the deformation of these specimens were included in the corrected graphs (Figs. 21b, 23b and 24b).

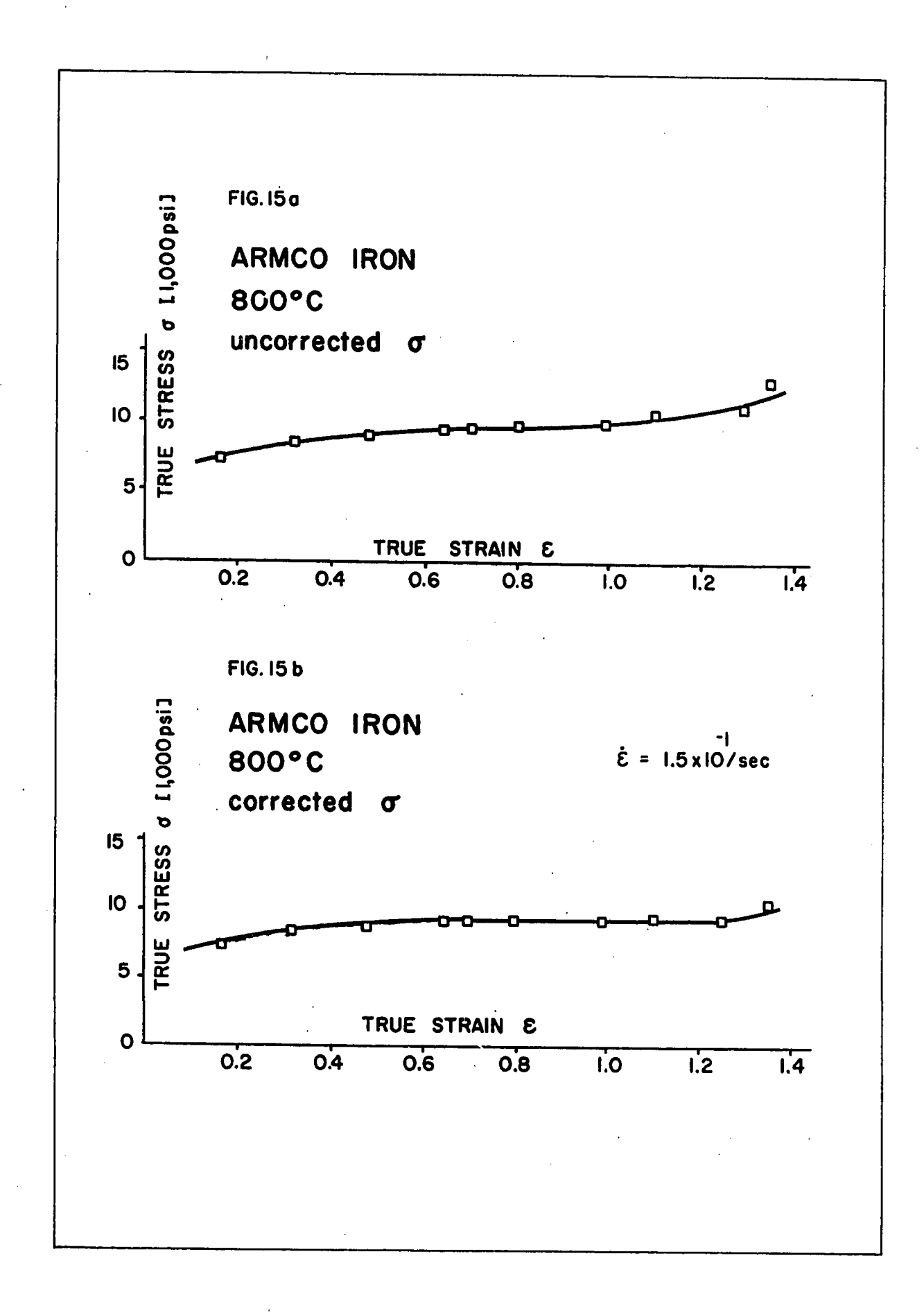
5.2 A STRESS/STRAIN RATE/TEMPERATURE RELATIONSHIP FOR HOT COMPRESSION

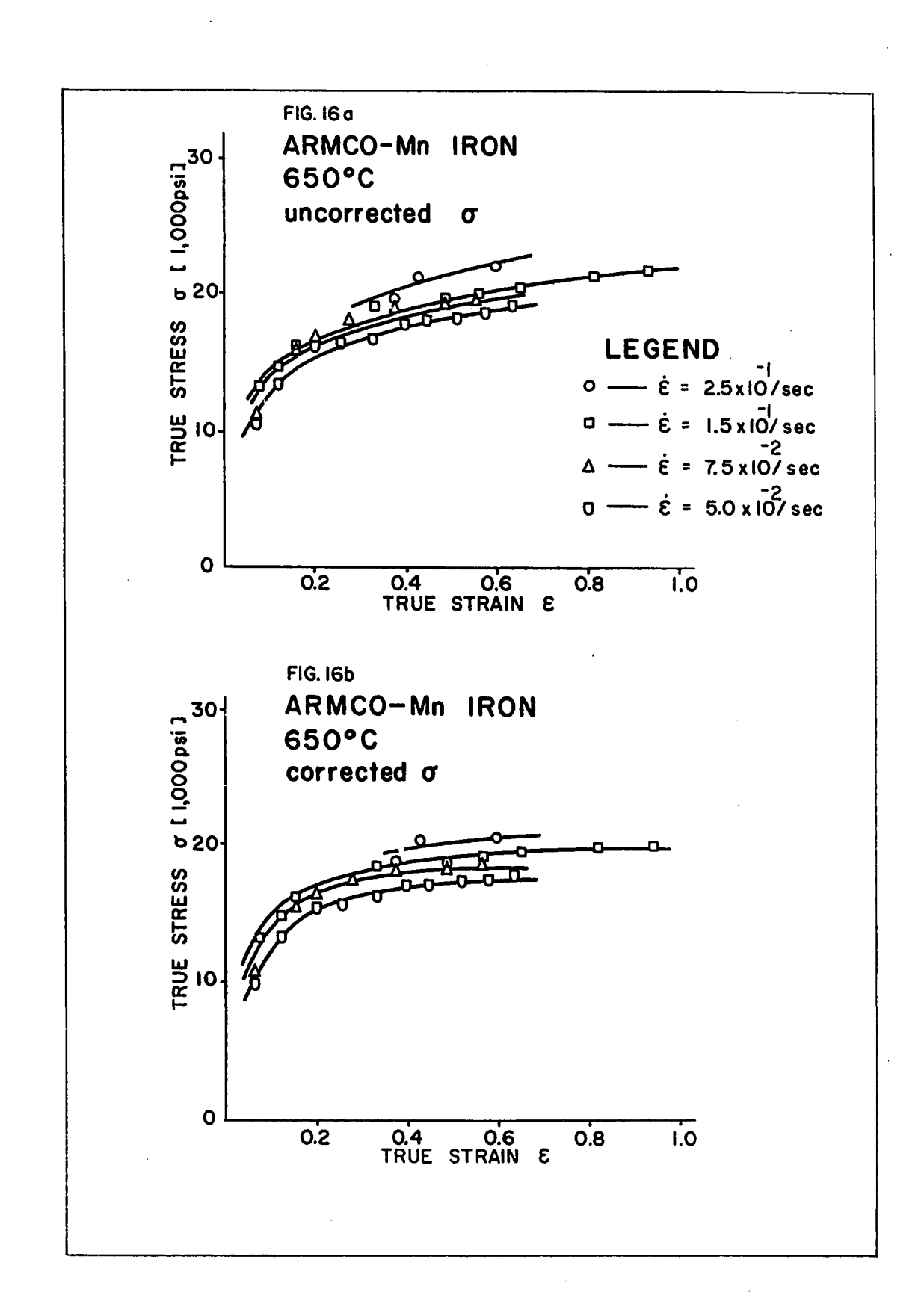
High temperature deformation is a thermally activated process in which the four main variables are the following: flow stress, strain, strain rate, temperature. Once steady-state hot working is achieved, that is, when the rate of work hardening is zero, the strain is no longer a significant variable, leaving only three, any two of which can be considered as independent. Given a set of experimental values of the three variables over a range of temperatures, strain rates and flow stresses, an equation linking the variables can be obtained. The values of the constants in this equation, which can be called "material constants", give an indication of the mechanisms acting during hot working. The determination of a suitable equation and the calculation of material constants will now be described.

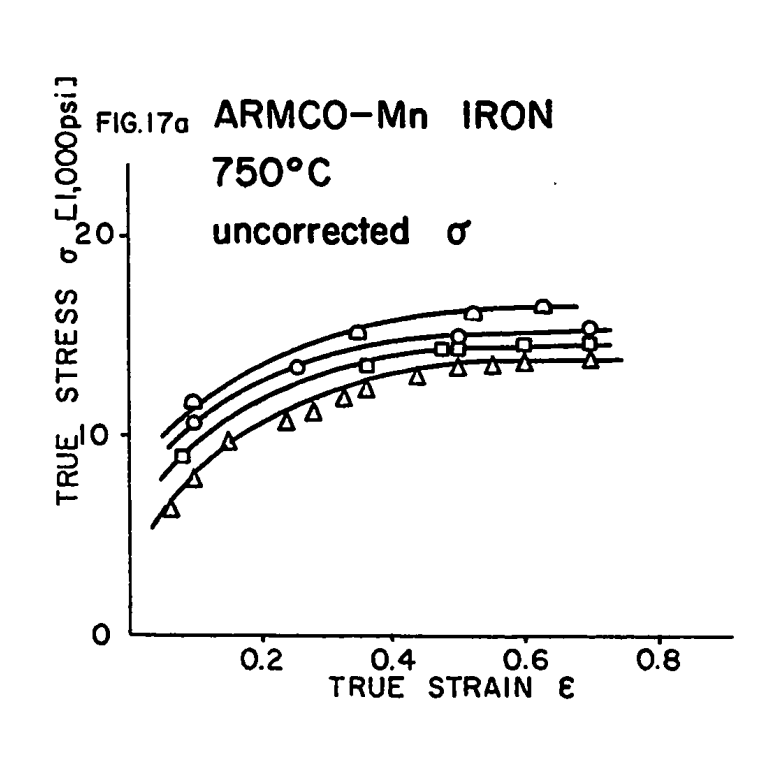
The true stresses acting under steady-state conditions, when work hardening is counteracted by recovery, were determined from the

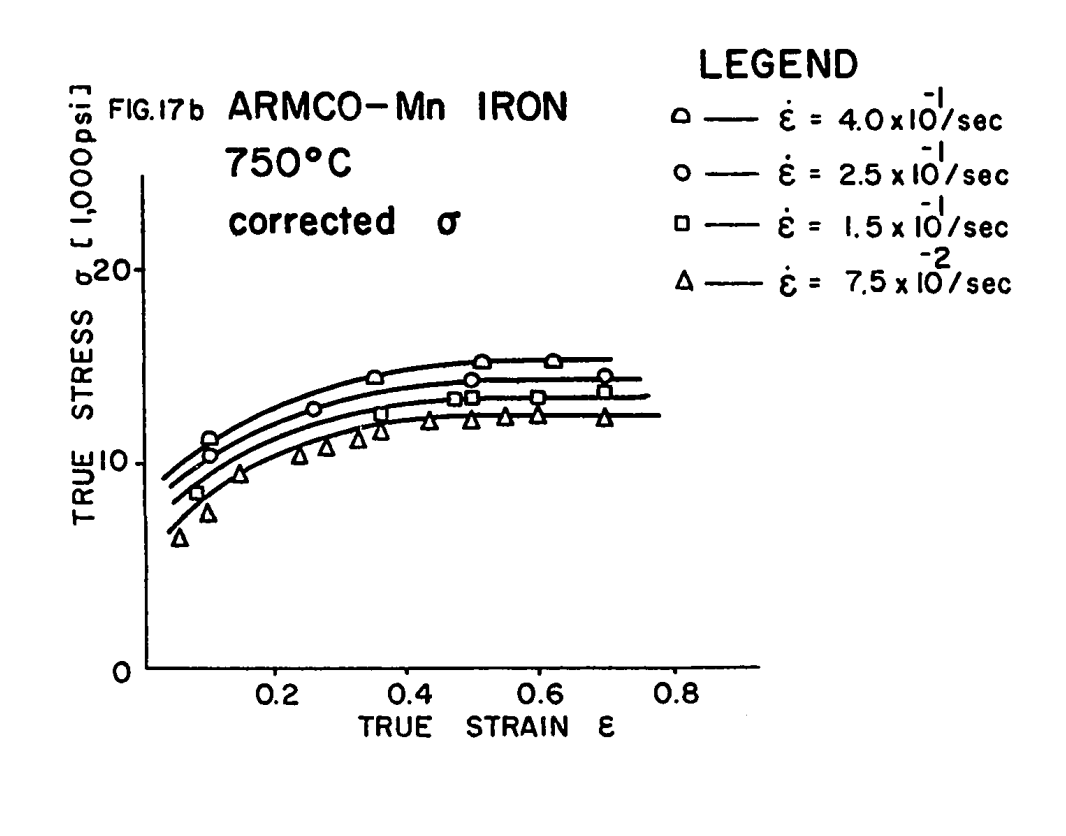


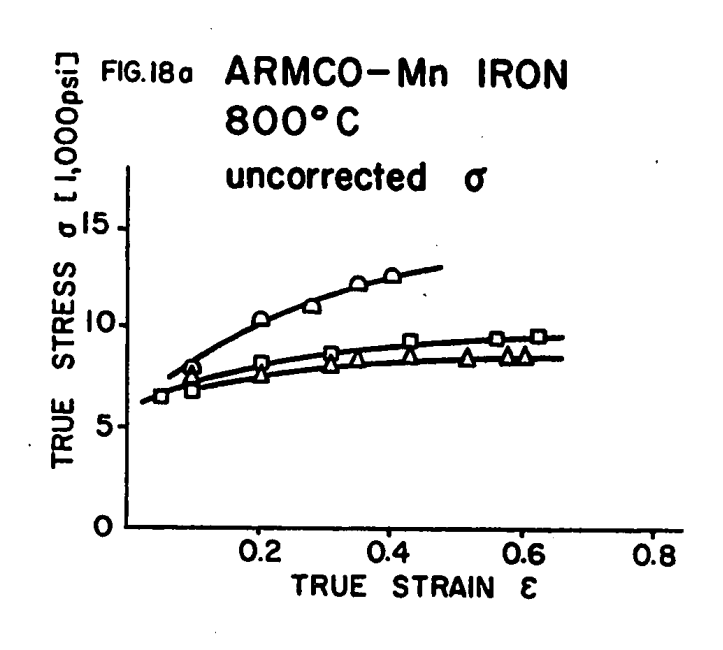


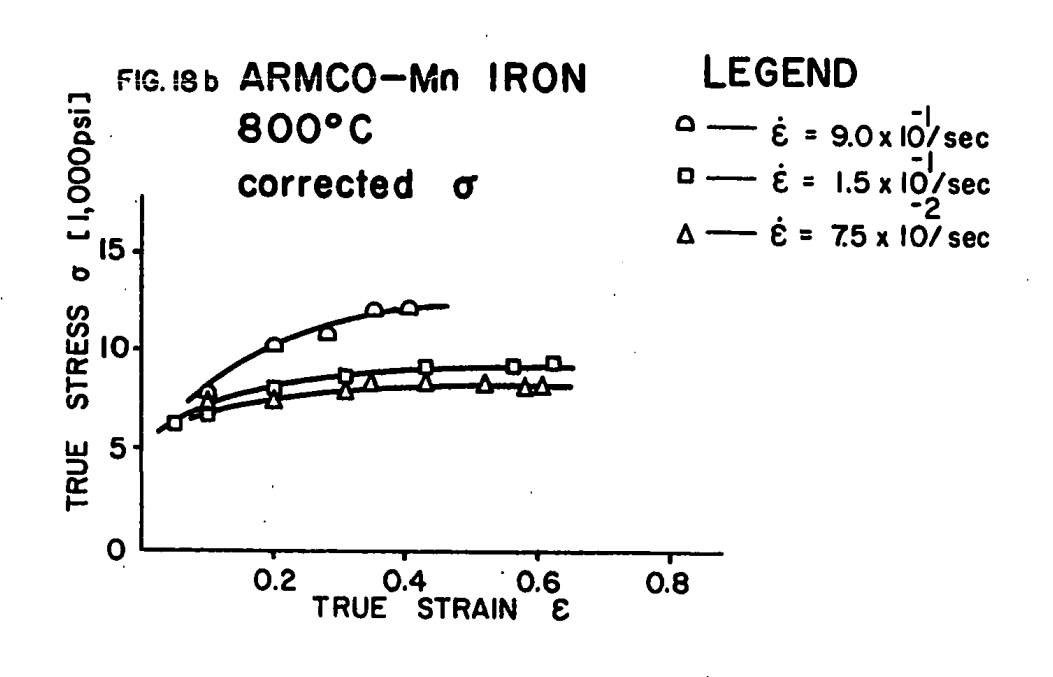


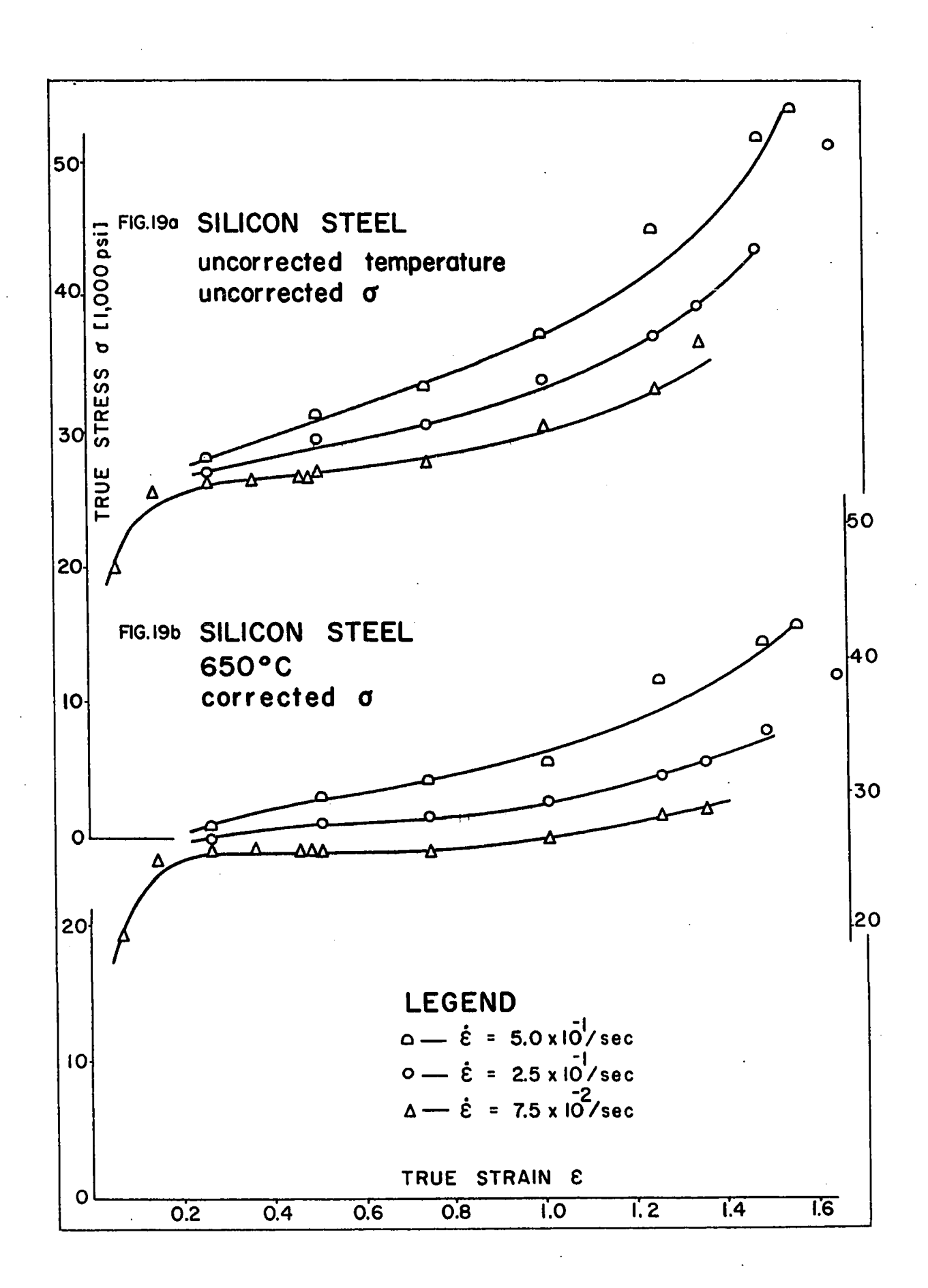


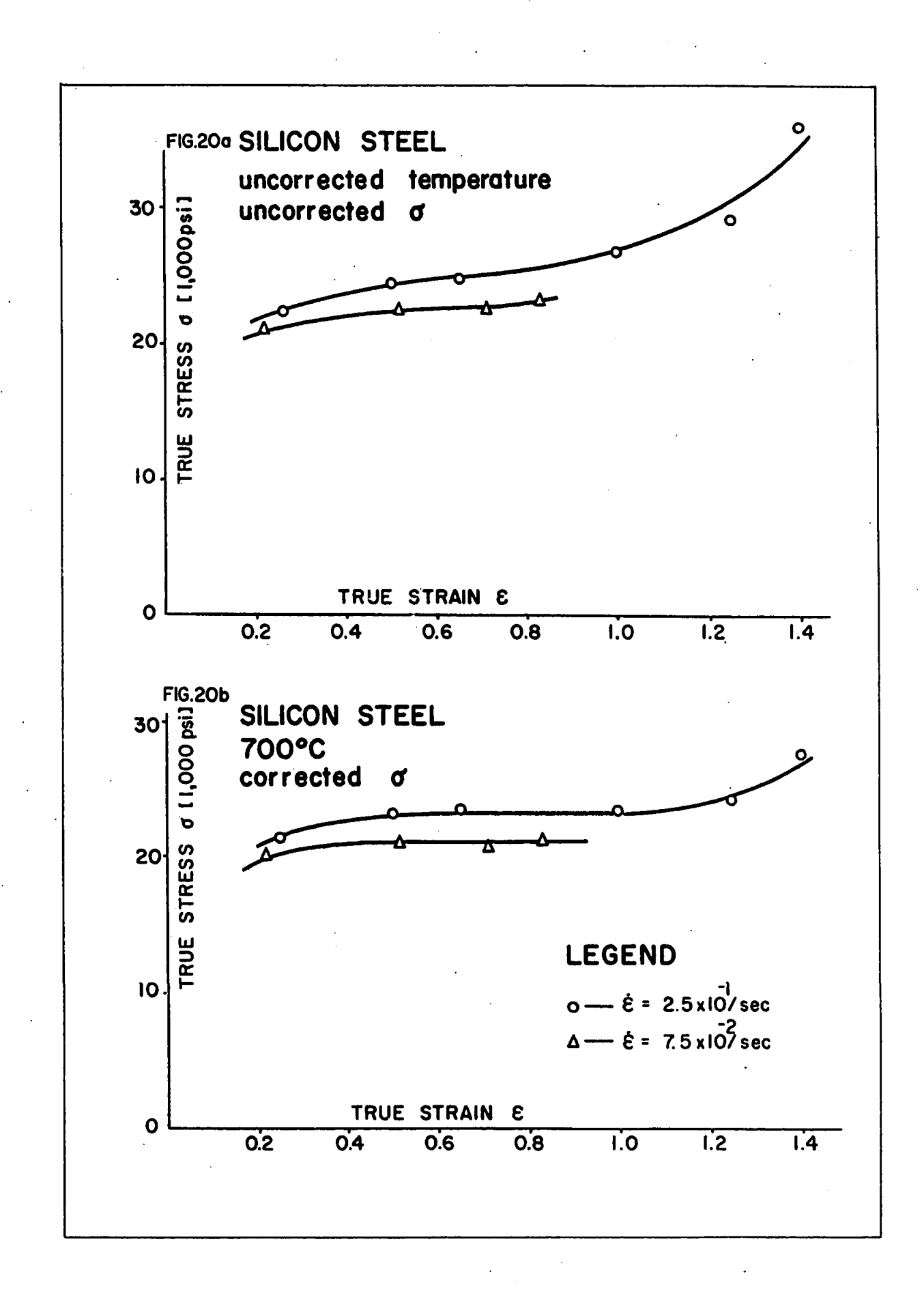


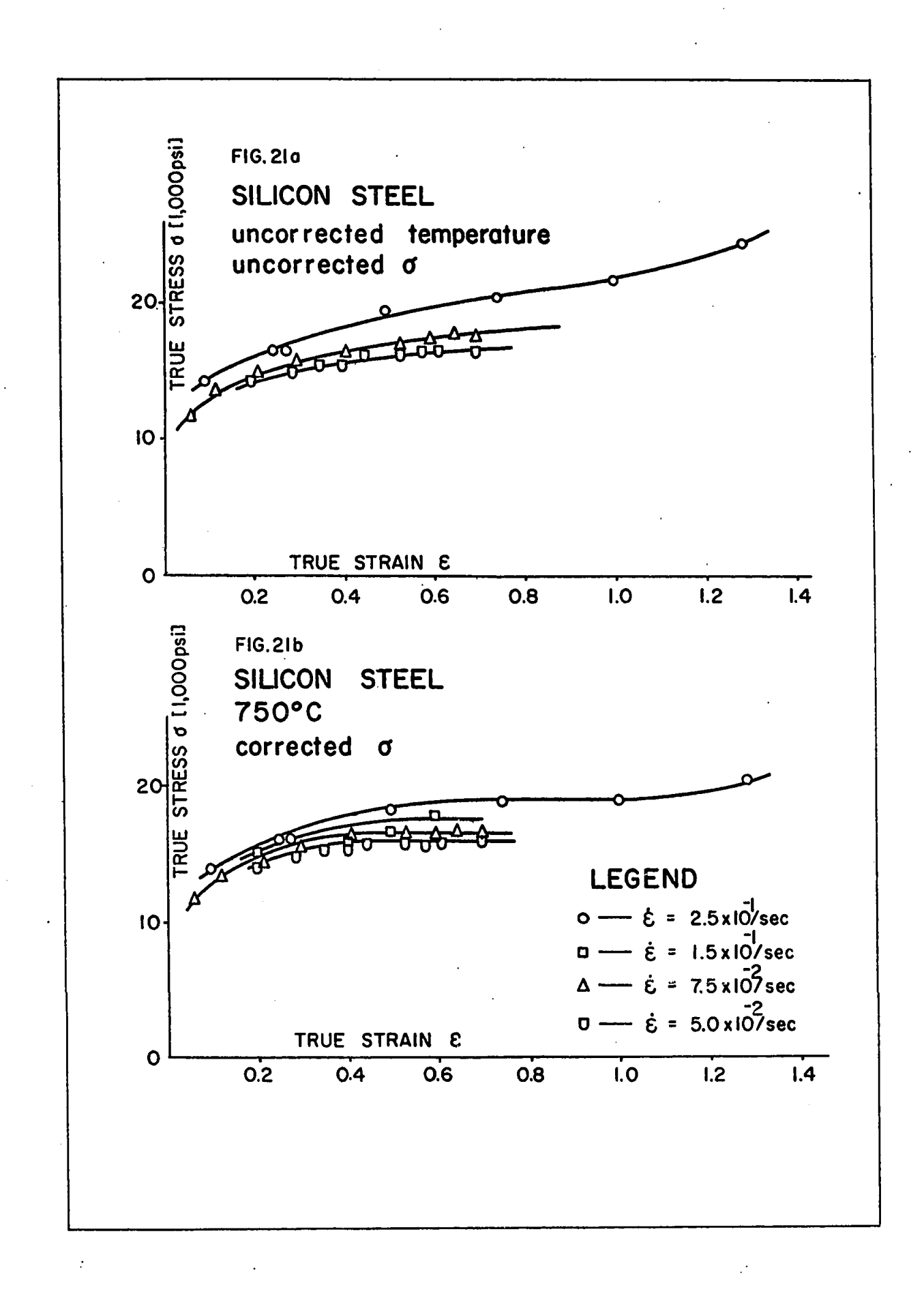


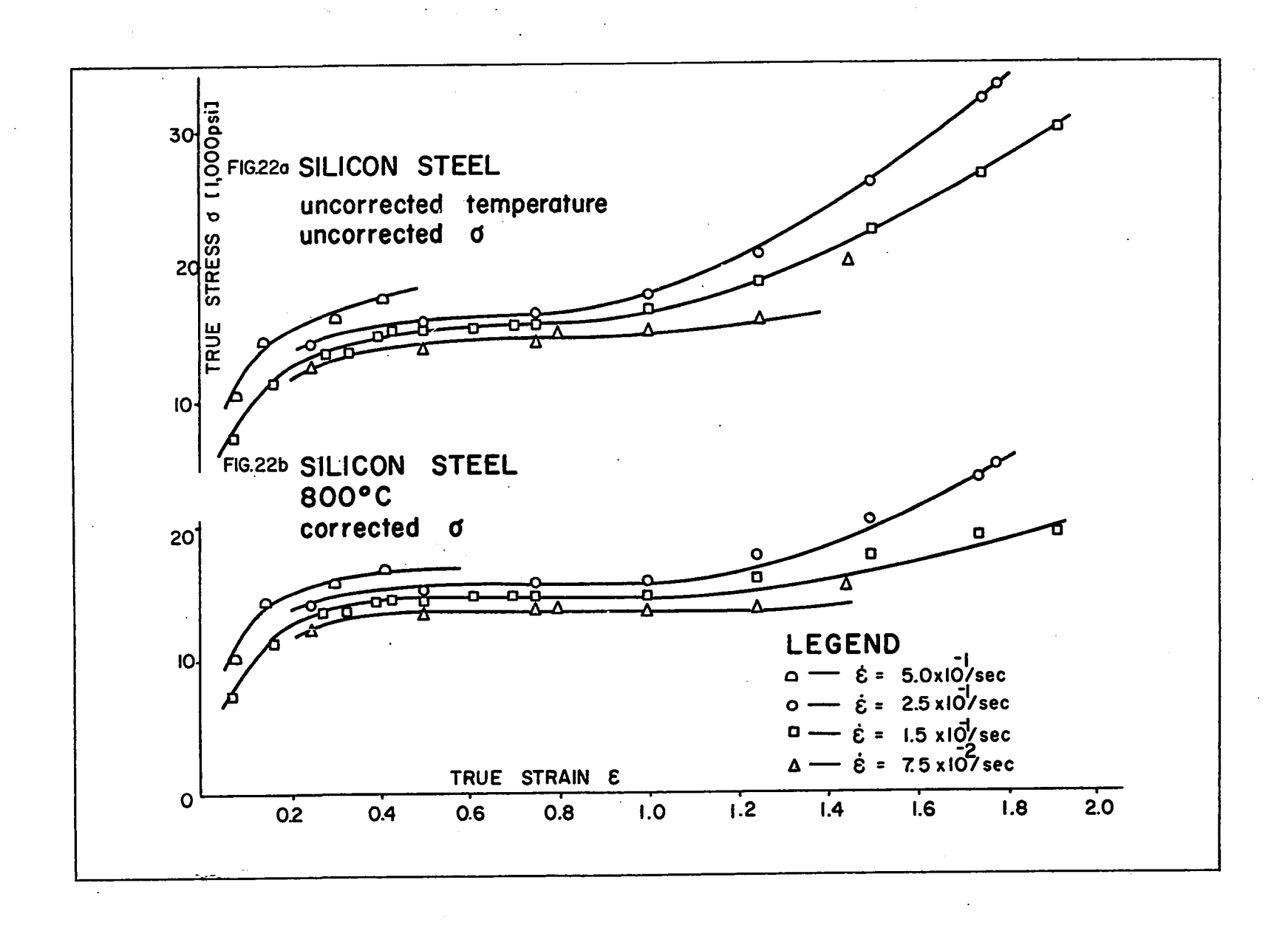


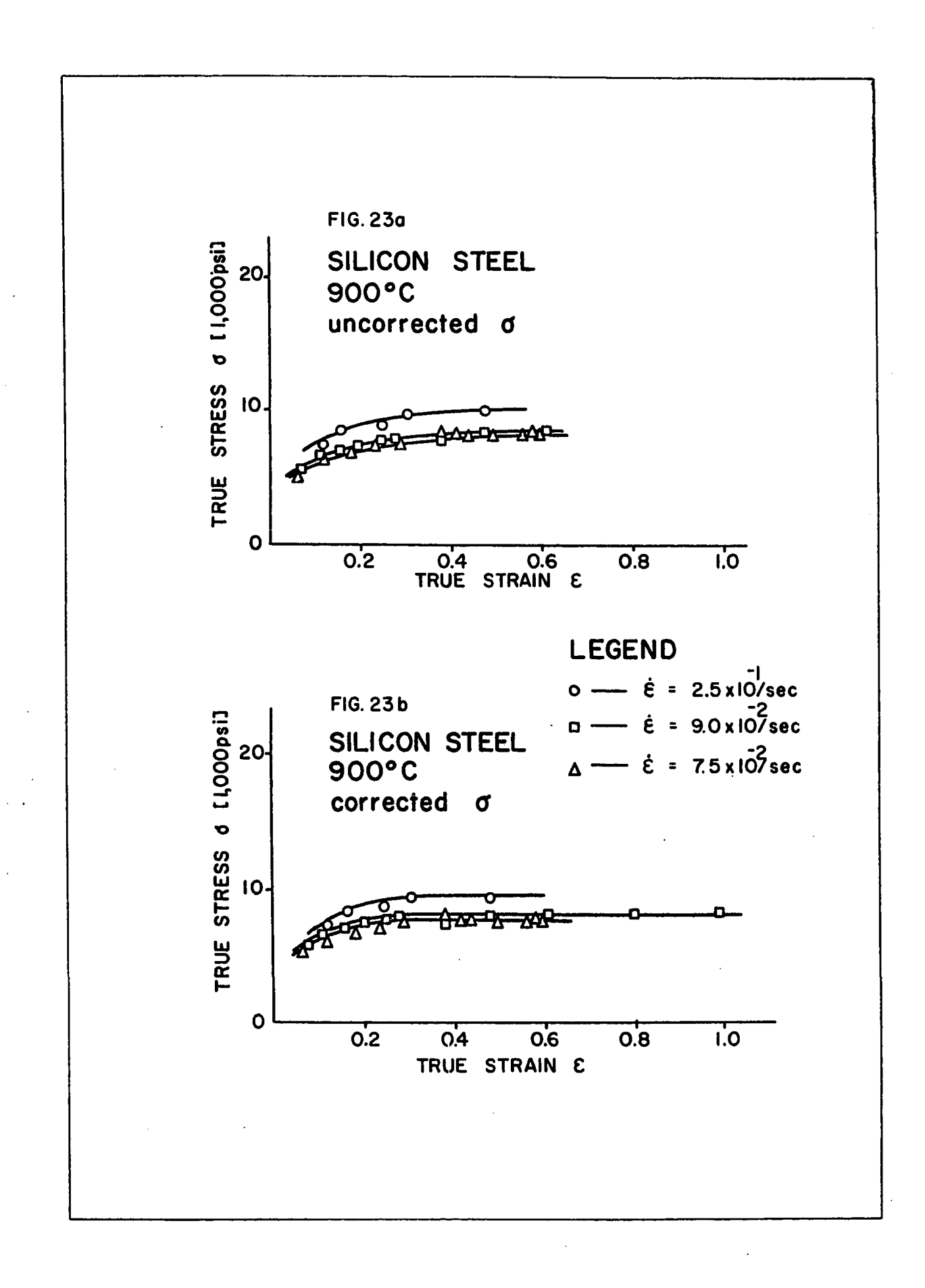


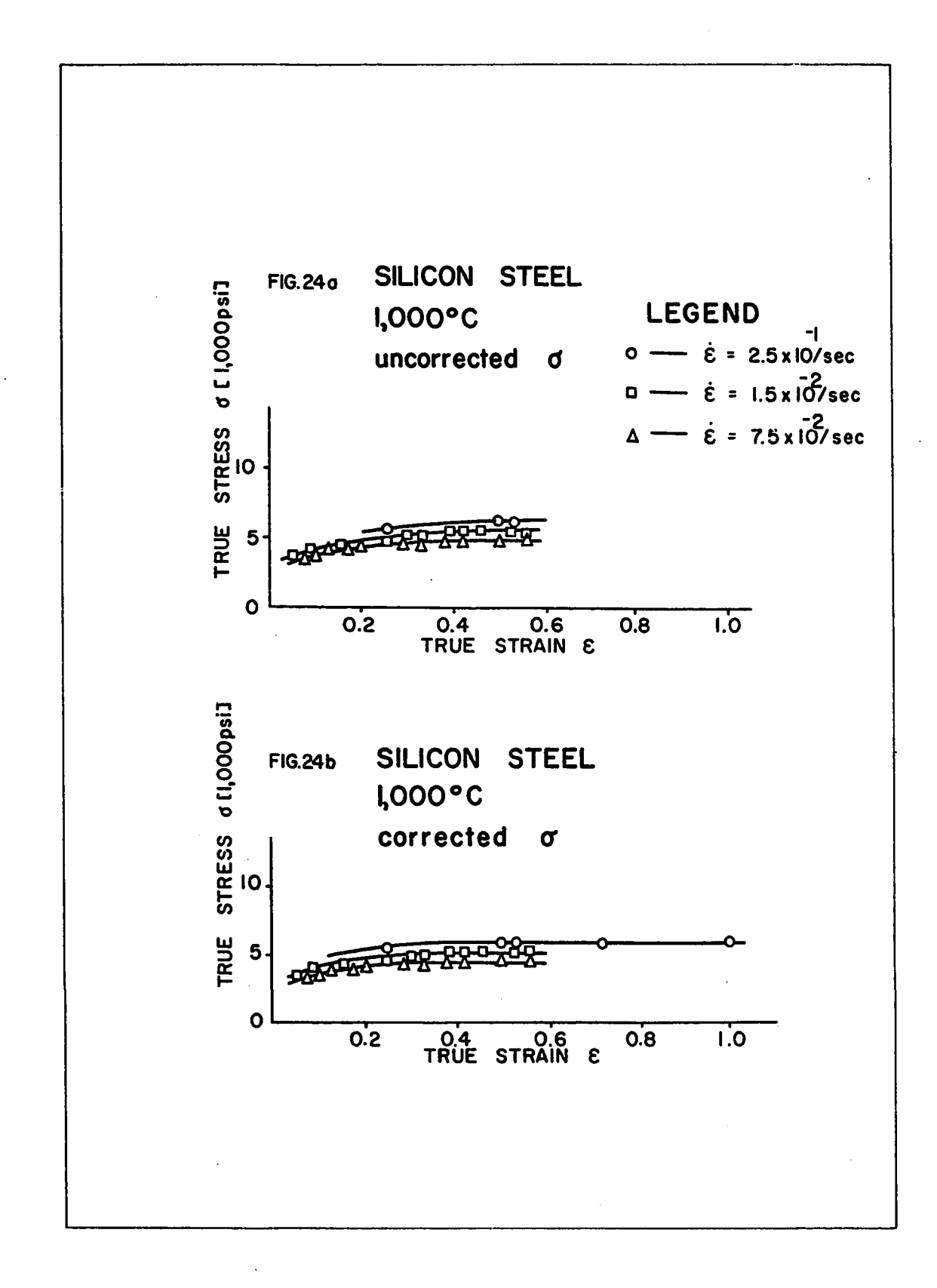












corrected curves presented in Figs. 13b to 24b. The corrected values of the true stresses were taken as flow stresses for the compression cycles investigated. The resulting data were evaluated using the following equation, first proposed by SELLARS and TEGART⁸⁵⁾ for hot torsion.

$$\dot{\varepsilon} = A. \left[\sinh (\omega \phi) \right]^{n'} \cdot \exp \left(-\frac{\Delta H}{RT} \right)$$
 (17)

where: $\dot{\varepsilon}$ = the strain rate [sec⁻¹];

 $A, \infty, n' = \text{material constants independent of temperature};$

6 = the flow stress [psi];

 ΔH = the activation energy for hot deformation [cal/mole];

R = the universal gas constant = 1.987 [cal/mole°K];

T = the deformation temperature [°K].

Inspection of equation (17) indicates that it approximates to a power law with a constant power (n') at low stresses [i.e. when (&6) < 0.23], whereas it approaches an exponential stress law, when the stress is high [i.e. when (&6) > 2.3] 72,85). These approximations permit a first estimate to be made of the four material constants, because creep data for power and exponential law fits are sometimes available, whereas comparable information for hot working is not as plentiful.

The only data uncovered to date on the high temperature deformation of Armco iron and silicon steel in the ferritic region are summarized in Table VI, and these investigations did not include the use of power, exponential or hyperbolic sine terms.

5.2.1 DETERMINATION OF (∞) AND (n')

The following practice was therefore developed to determine the most appropriate values of the material constants (∞) and (n') from

Table VI. Hot Deformation Investigations of Steels in the Ferritic Region

REF.	MATERIAL	MODE OF HOT DEFORMATION	STRESS/STRAIN RATE/TEMPERATURE DATA				
18	Armco Iron 99.7%	Torsion	T [°C] ÿ [sec ⁻¹] T _{max} [psi]	700 0.47 13,000	750 0.47 9,000	800 0.47 7,000	850 0.47 5,400
17	Armeo Iron 99.65%	Torsion	T [°C] ŷ [sec ⁻¹] [[lb-in]	807 0.8 78	851 0.8 62		
12	Armeo Iron 99.9%	Creep	Τ [°C] έ[hour ⁻¹] 6 [kg/mm ²]	550 8x10-3 3	650 7x10 ⁻ 2 2	700 6x10 ⁻² 1	
22	Steel: 0.58% C, 0.53% Mn, 0.16% Si	Torsion	T [°C] @[RPM] Tmax[kg/mm ²]	700 31.5 13.5	700 213 19	700 840 25	
30	Steel 0.45% C of commercial purity	Compression	T [°C] &[sec ⁻¹] &[kg/mm ²]	700 1.0 25.9	750 1.0 25.6		
19	Silicon steel 4% Si	Torsion	T [°C] ORPM] P[kg.cm]	1,100 316 9.5	1,100 18.2 4.5	1,100 4.97 3.4	

the present work. Considering the activation energy and the parameter (A) to be constant over the range of strain rates and temperatures involved, the relation between (∞) and (n') was found by the use of equation (17) in the following form:

$$\ln\dot{\hat{\epsilon}}_1 - n' \ln \left[\sinh \left(\mathcal{C} \mathcal{O}_1 \right) \right] + \frac{\Delta H}{RT_1} = \ln\dot{\hat{\epsilon}}_2 - n' \ln \left[\sinh \left(\mathcal{C} \mathcal{O}_2 \right) \right] + \frac{\Delta H}{RT_2}$$
 (18)

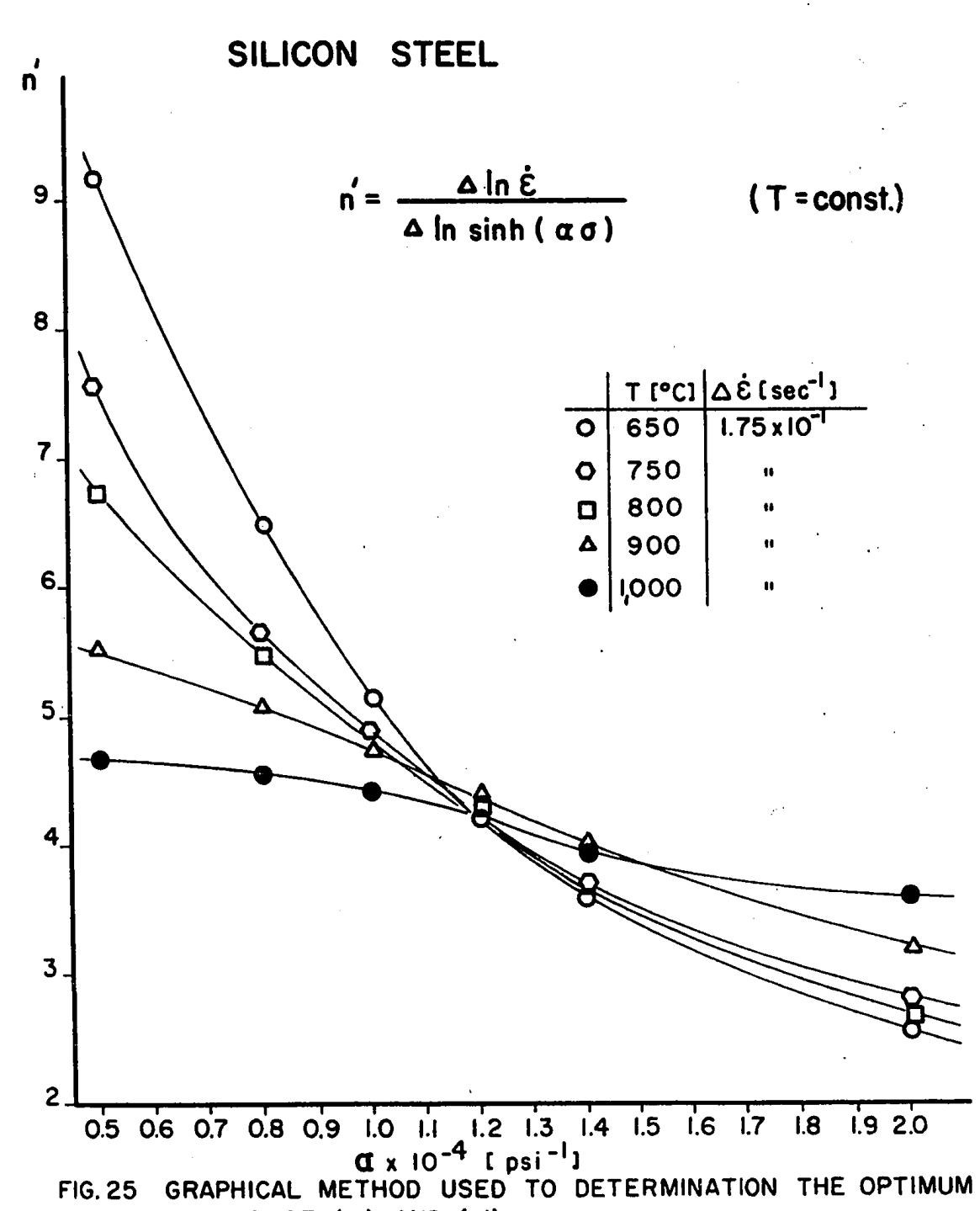
For a constant temperature the term $\Delta H/RT$ is eliminated, so that

$$\ln \dot{\hat{\epsilon}}_1 - n' \ln \left[\sinh \left(\omega \hat{c}_1 \right) \right] = \ln \dot{\hat{c}}_2 - n' \ln \left[\sinh \left(\omega \hat{c}_2 \right) \right]$$
 (19)

and the material constant (n') can be expressed in terms of (\mathcal{K}) as follows:

$$n' = \frac{\ln \dot{\hat{c}}_1 - \ln \dot{\hat{c}}_2}{\ln \left[\sinh \left(\partial \hat{c}_1\right)\right] - \ln \left[\sinh \left(\partial \hat{c}_2\right)\right]}$$
 (20)

The most suitable value of (\mathcal{L}) for correlation of the hot compression data over the full range of temperatures and strain rates was determined in the following way. A tentative range of (\mathcal{L}) values was selected on the basis of the material constants determined for soft steels deformed by hot torsion in the γ -region. The work on which these values were based is listed as reference 85) in Table XI in the Discussion. The selected (\mathcal{L}) 's which were in the range $5\times10^{-4.5}$ to 2×10^{-4} (psi)⁻¹, were then substituted into equation (20), together with the experimental stresses and $(\dot{\mathcal{E}}$'s). A range of values of (n') was thus obtained, corresponding to the full range of stresses, strain rates and temperatures involved. The resulting (n') values were plotted against (\mathcal{L}) in the graph shown in Fig. 25, and a set of curves was obtained, each of which represented the dependence of (n') on (\mathcal{L}) at a particular temperature. It can be seen from the graph that as (\mathcal{L}) increases above 5×10^{-5} (psi)⁻¹, the differences between the various values of (n')



VALUES OF (a) AND (n')

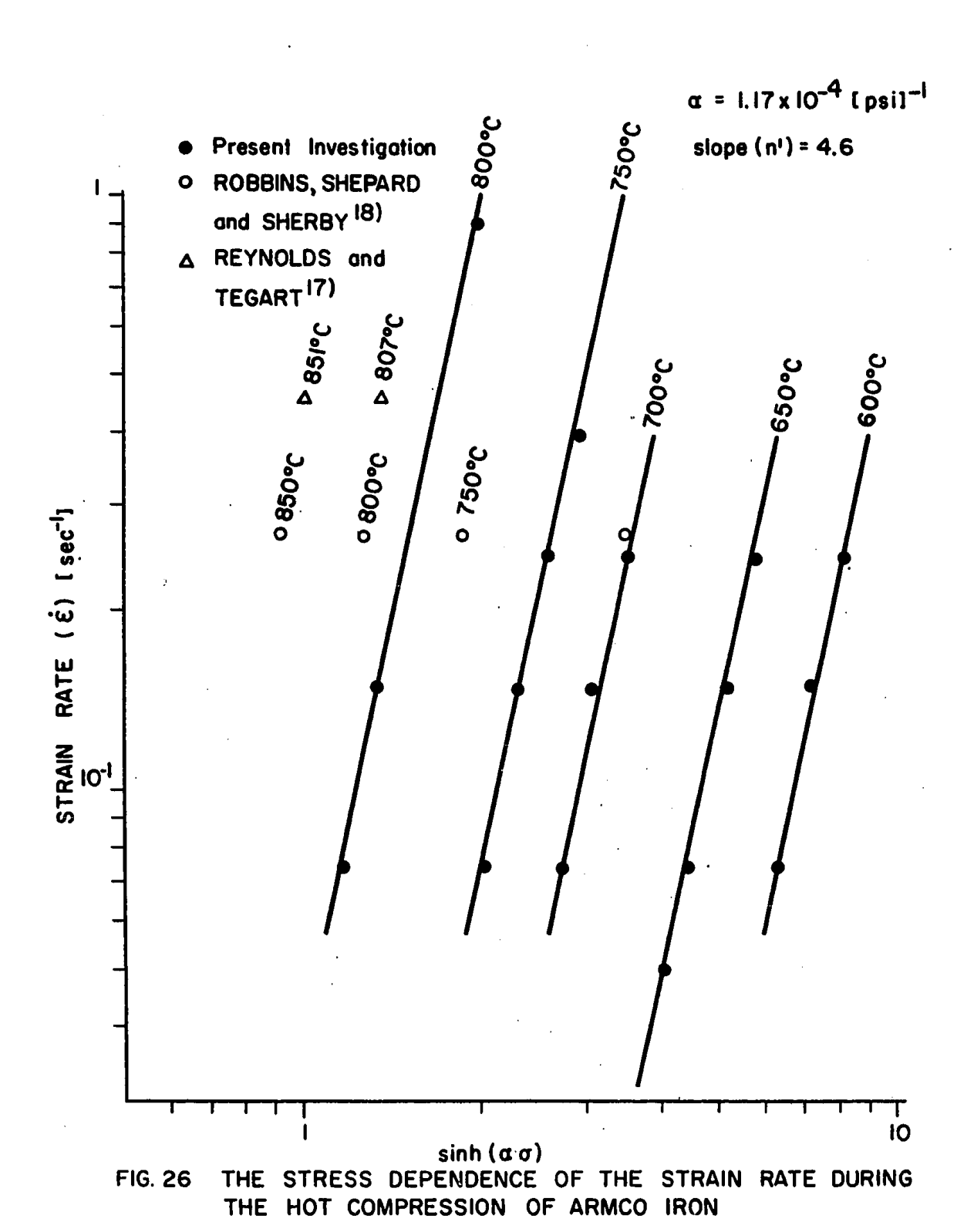
decrease to a minimum, and then become larger again. There is a range of (\mathcal{L}) between 1.1×10^{-4} to $1.25 \times 10^{-54} (\text{psi})^{-1}$, where the various values of (n') do not differ greatly. The final value of (\mathcal{L}) was selected by calculating the effect on (n') of variations in (\mathcal{L}) over the narrow range 1.1×10^{-4} to 1.25×10^{-4} $(\text{psi})^{-1}$. The most suitable value $\mathcal{L} = 1.15 \times 10^{-4} (\text{psi})^{-1}$ was the one which led to the minimum standard deviation in (n'), 5.2% over the full range investigated.

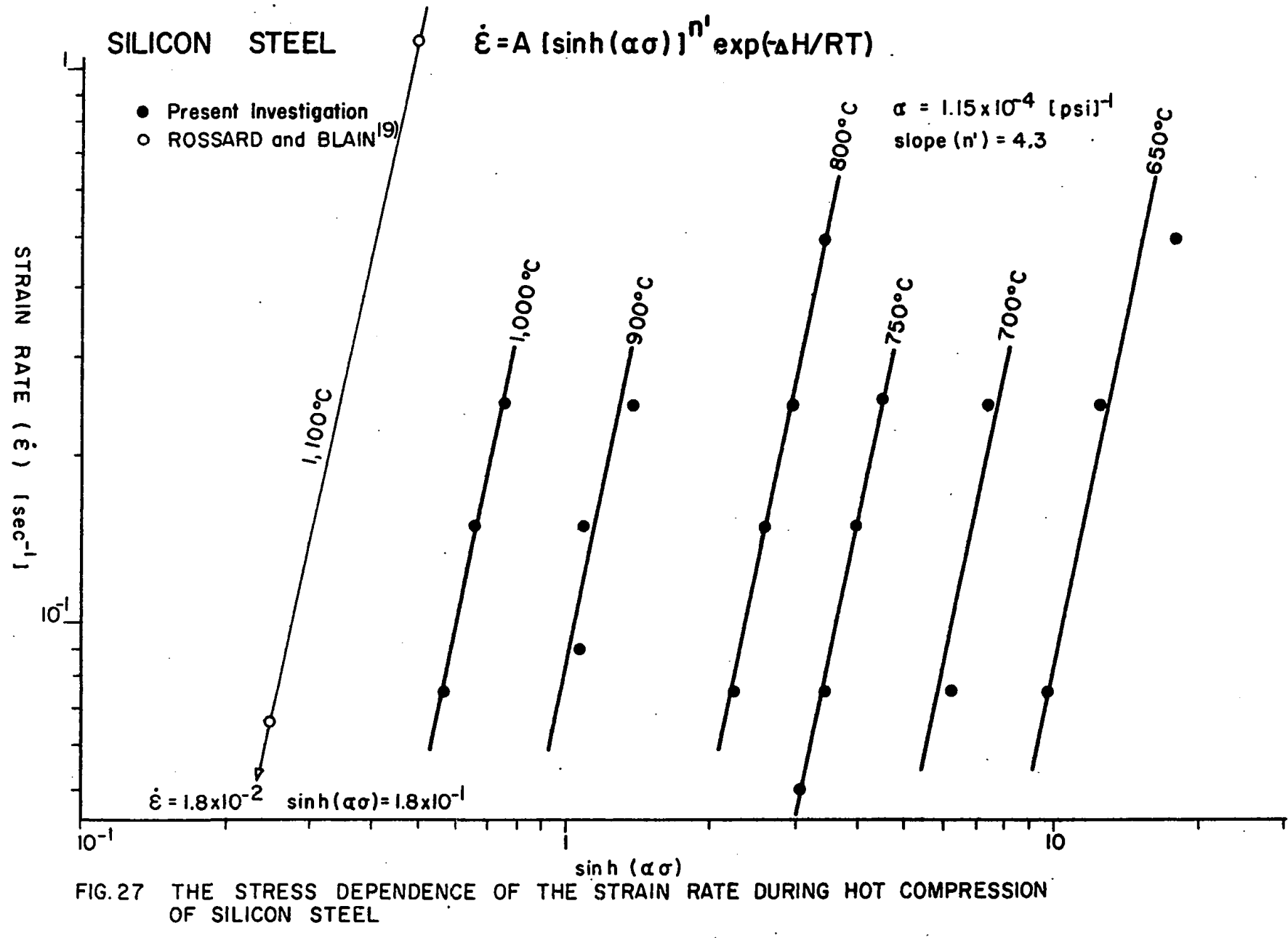
The above description concerns the method used to fix values for (\mathcal{X}) and (n') in silicon steel. A similar procedure was followed for the determination of (\mathcal{X}) and (n') for Armco iron. In this case the standard deviation in (n') was found to be only 1.4%.

Figs. 26 and 27 show the stress/strain rate/temperature relationship given by equation (17) for the values of (\mathcal{L}) determined as described above. The slopes represent the values of (\mathcal{L}) is (\mathcal{L}) in sinh (\mathcal{L}) investigators (\mathcal{L}) investigators (\mathcal{L}) in sinh (\mathcal{L}) investigators (\mathcal{L}) investigators (\mathcal{L}) investigators investigators (\mathcal{L}) in the selected values of (\mathcal{L}) in the selected values of (\mathcal{L}) investigators investigators (\mathcal{L}) in the selected values of (\mathcal{L}) investigation of the present results by the application of the coefficient (\mathcal{L}) and are shown in Figs. 26 and 27. The constants (\mathcal{L}) in and (\mathcal{L}) suggested by these results differ slightly from those of the present investigation. However, such differences as are shown can be attributed to slightly different material purities, and to the fact that the limited data abstracted from these authors do not permit the plotting of curves with any degree of confidence.

5.2.2 ACTIVATION ENERGIES FOR HOT COMPRESSION

Having determined suitable values for (\mathcal{L}) and (n'), the activation energies for hot compression were calculated using equation (18)





as follows:

$$\Delta H = 2.3 R \frac{\log \dot{\epsilon}_2 - \log \dot{\epsilon}_1 + n' [\log \sinh (\mathcal{C}_1) - \log \sinh (\mathcal{C}_2)]}{\frac{1}{T_1} - \frac{1}{T_2}}$$
(21)

At any constant strain rate the above equation will simplify to the following form:

$$\Delta H = 2.3 R n' \frac{d \left[\log \sinh (\mathcal{LG})\right]}{d \left[\frac{1}{T}\right]}$$
 (22)

The activation energy can then be calculated from the slope of the lines in Figs. 28 and 29, that is from plots of log sinh (∞ 6) against $(\frac{1}{T})$ at constant strain rate. In both diagrams the plotted points were fitted by a straight line. The single point off the line in the case of Armco iron is thought to be due to a change of activation energy associated with the (∞) to (β) transformation, as will be discussed in more detail below. The material constants obtained from the present calculations are collected and shown in Table VII.

Table VII. Material Constants for the Hot Compression of Armco Iron and Silicon Steel

MATERIAL	HOMOLOGOUS TEMPER- ATURE RANGE	n'	<pre></pre>	log A	ACTIVATION ENERGY [cal/mole]
Armco iron	0.48 - 0.58	4.6	1.17	11.65	66,000
silicon steel	0.55 - 0.70	4.3	1.15	13.78	80,000

5.3 MICROSTRUCTURAL OBSERVATIONS

Extensive microscopic examination was carried out on the samples with particular regard to substructure formation and to the

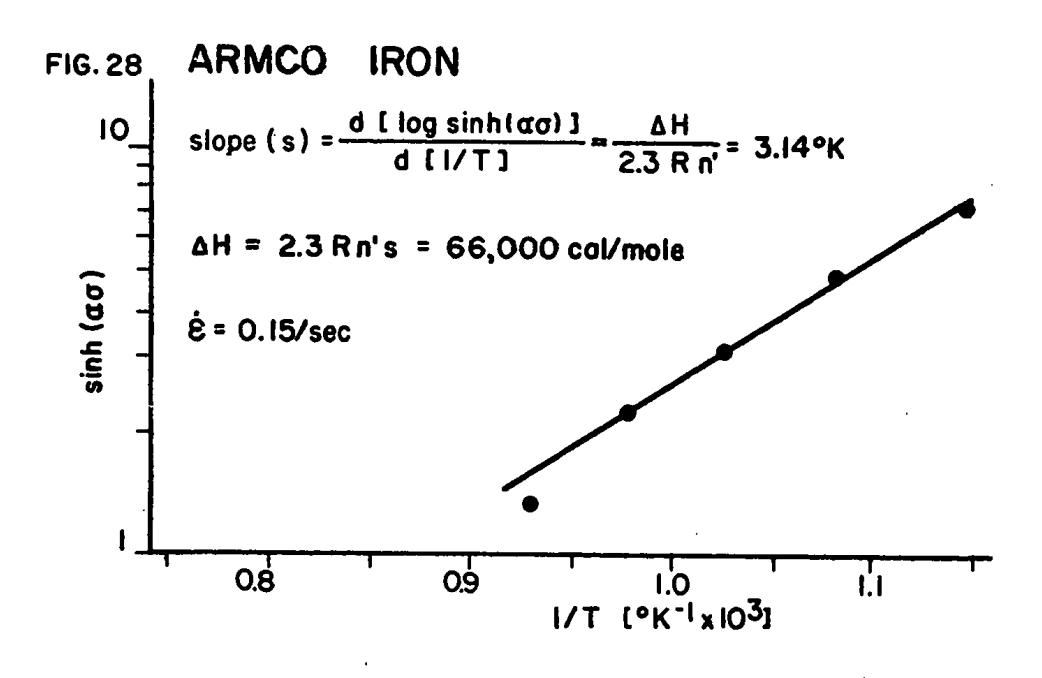
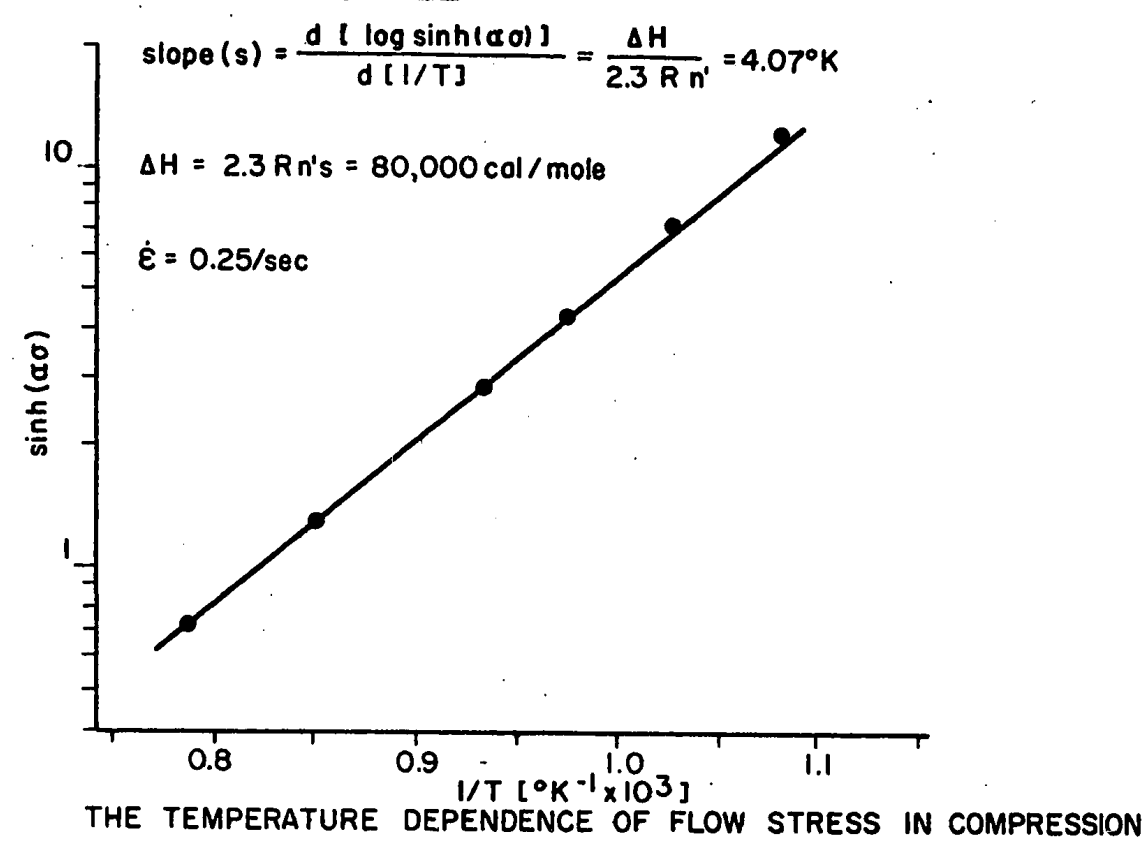


FIG. 29 SILICON STEEL



relationship between the substructure geometry and the deformation variables (6), (\mathcal{E}) , $(\dot{\mathcal{E}})$, (T). Recrystallization was prevented, and the as-worked substructure was preserved for examination, by quenching the samples within seconds of deformation. Most of the microscopic work was concerned with the steady-state region; the transient region was given less attention, as it was not of central interest in this study, and an investigation of the latter is proposed for future work.

5.3.1 TRANSIENT REGION MICROSTRUCTURES

Banded Dislocation Substructure. In both steels the presence of a band-type substructure was frequently detected by optical examination. The bands were identified as traces of two slip systems. In silicon steel the bands were closer together than in Armco iron and their spacing appeared to be temperature dependent (Figs. 30 to 33). With increasing deformation temperature, the spacing increased. The broad slip line spacing and the tangled appearance of the substructure in Fig. 31 were probably due to the dislocation rearrangement taking place during the time lapse between the end of compression and quenching. Slip lines were usually more pronounced in the middle of the grains than at the grain boundaries, which agrees with BARRETT et al 13 who pointed out that the formation of deformation bands near grain boundaries is more difficult because stress concentration at the grain boundaries activates slip on more than two systems. Slip bands were virtually absent at temperatures over 900°C.

Extended Tilt Boundaries. These were seldom detected optically and were limited to the regions adjacent to high-angle boundaries (Figs. 34, 35 and 36). Their appearance indicated that they had been created

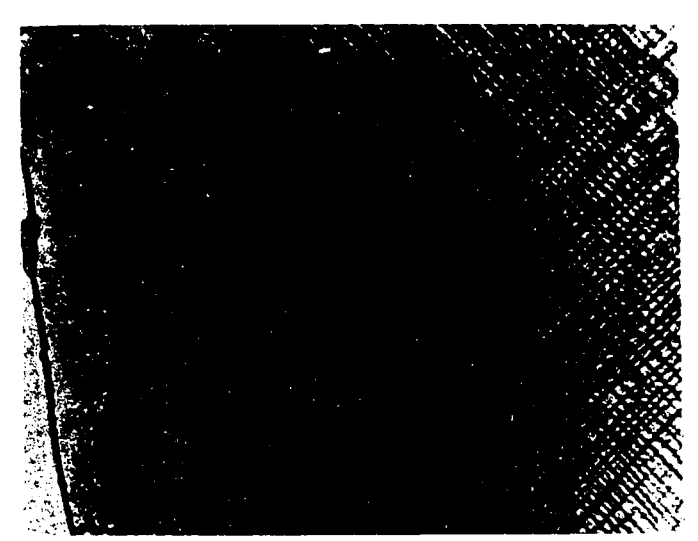


Fig. 30 - Silicon steel; 560°C; ε = 0.11; ε = 0.20/sec; delay 6 sec; electrolytically polished and etched*); 585 X.
*) In the optical microphotographs which follow, this will be abbreviated as EPE.



Fig. 31 - Silicon steel; 700° C; $\varepsilon = 0.17$; $\dot{\varepsilon} = 0.25/\text{sec}$; delay 60 min; EPE; 585 X.



Fig. 32 - Armco iron; 750° C; $\varepsilon = 0.38$; $\dot{\varepsilon} = 0.40/\text{sec}$; delay 5 min; electrolytically polished, etched with 1% nital**) 220 X **) In the optical microphotographs which will follow, this will be abbreviated as EPNE.

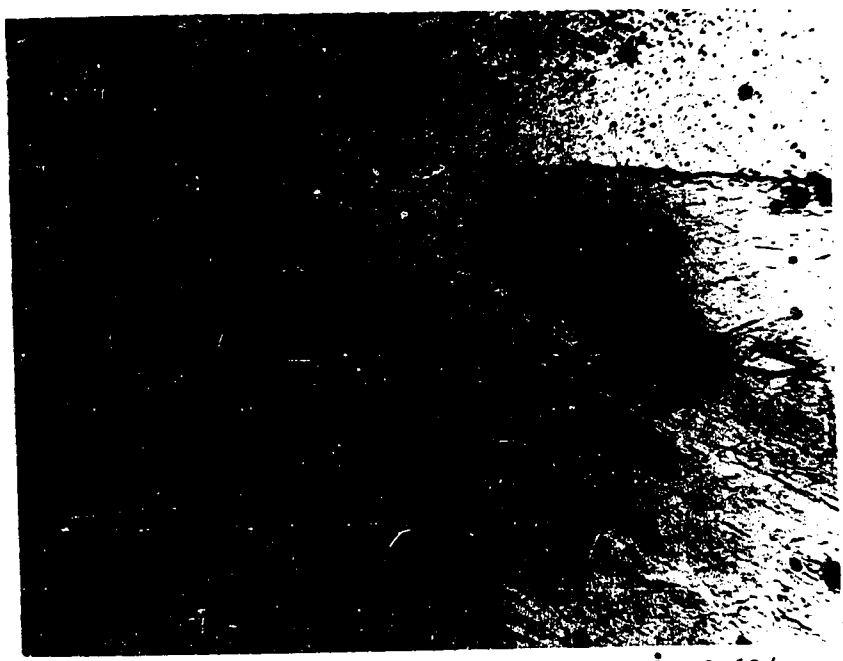
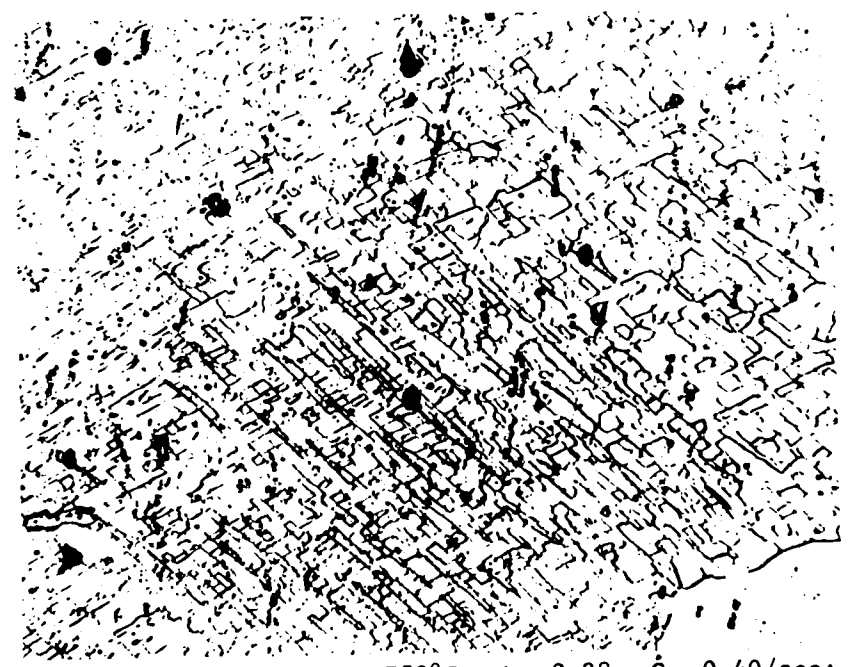


Fig. 33 - Armco iron; 750°C; &= 0.38; &= 0.60/sec; delay 1 sec; EPNE; 220 X.



 $(\underline{\cdot},\underline{\cdot})$

Fig. 32 - Armco iron; 750° C; $\varepsilon = 0.38$; $\dot{\varepsilon} = 0.40/\text{sec}$; delay 5 min; electrolytically polished, etched with 220 X 1% nita1**) **) In the optical microphotographs which will follow, this will be abbreviated as EPNE.

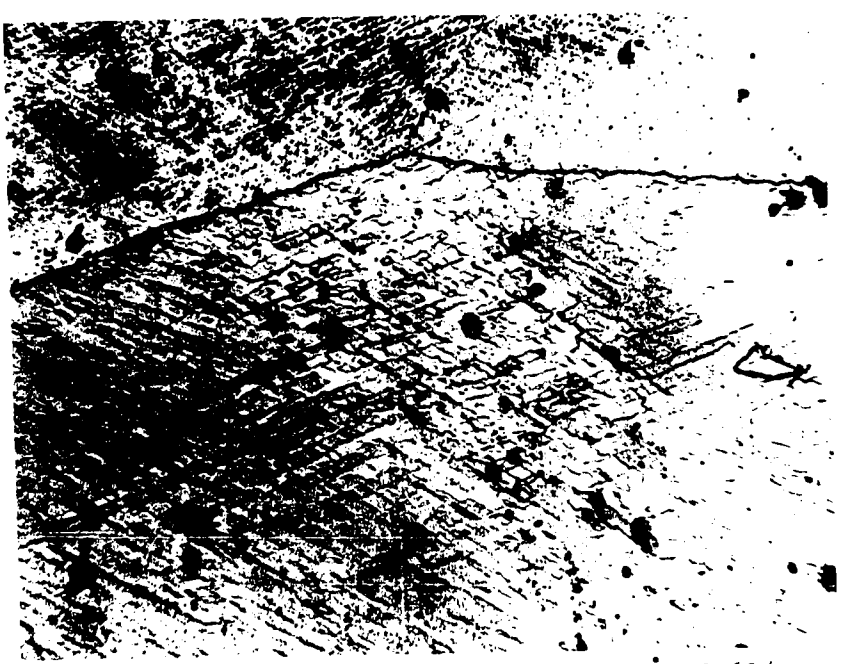


Fig. 33 - Armco iron; 750° C; $\mathcal{E} = 0.38$; $\dot{\mathcal{E}} = 0.60/\text{sec}$; delay 1 sec; EPNE; 220 X.

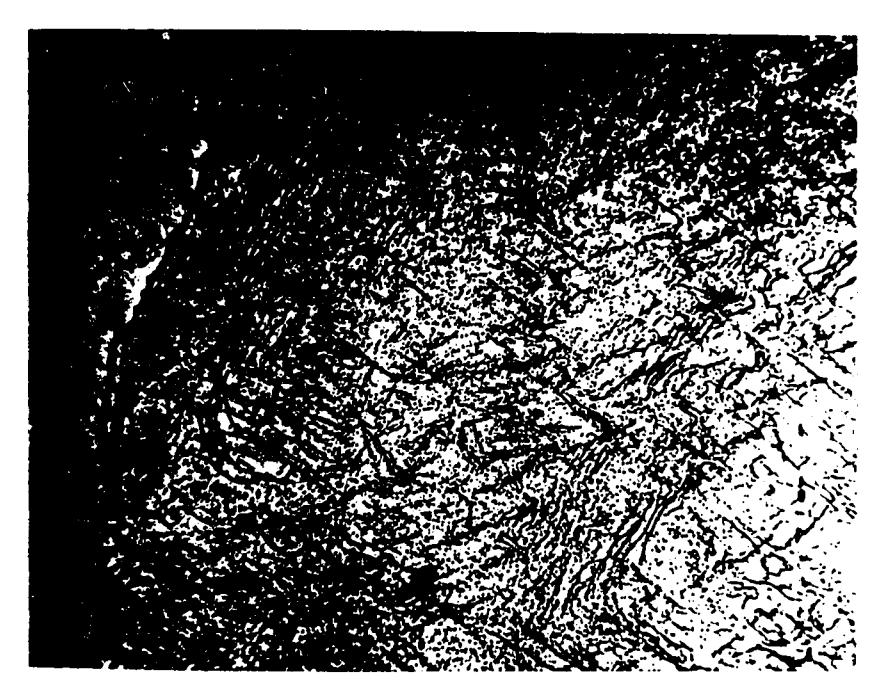


Fig. 34 - Silicon steel; 650°C; ε = 0.085; $\dot{\varepsilon}$ = 0.25/sec; delay 90 min; EPE; 220 X.

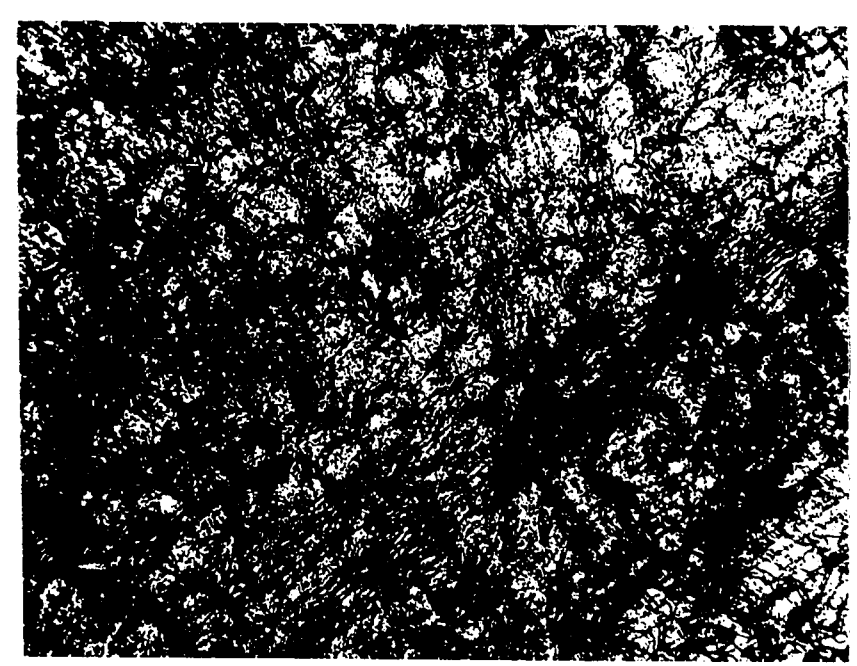


Fig. 35 - Silicon steel; 800° C; $\mathcal{E} = 0.15$; $\dot{\mathcal{E}} = 0.24/\text{sec}$; delay 40 min; EPE; 220 X.



Fig. 34 - Silicon steel; 650° C; $\varepsilon = 0.085$; $\dot{\varepsilon} = 0.25/\text{sec}$; delay 90 min; EPE; 220 X.

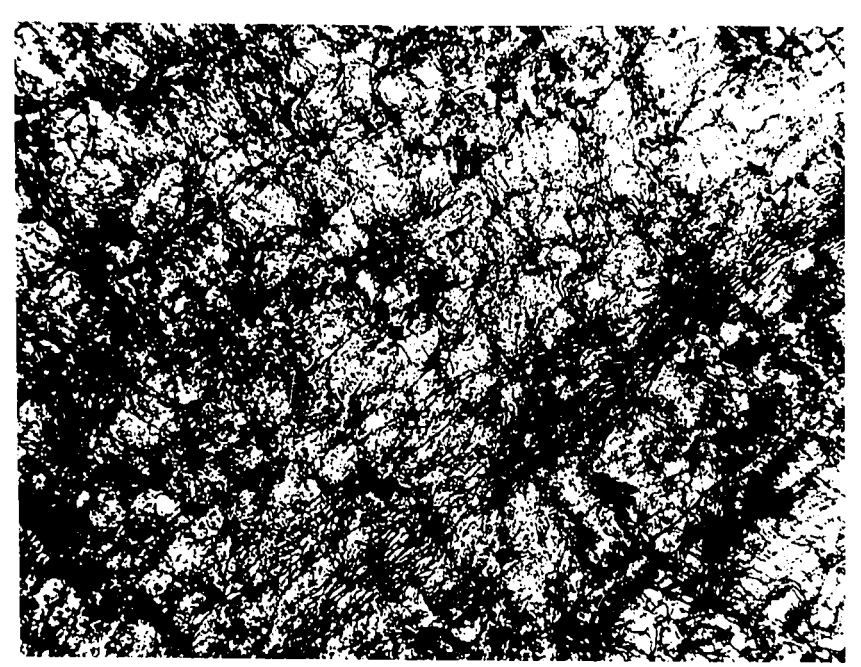


Fig. 35 - Silicon steel; 800° C; $\mathcal{E} = 0.15$; $\dot{\mathcal{E}} = 0.24/\text{sec}$; delay 40 min; EPE; 220 X.

1.1.29.20.17

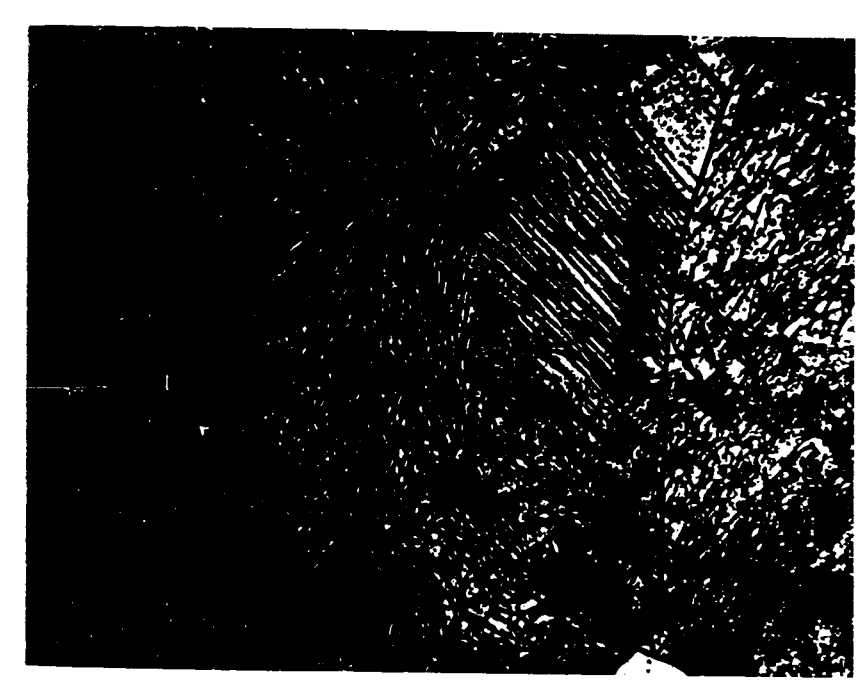


Fig. 36 - Silicon steel; 800° C; &= 0.75; &= 0.15/sec; delay 10 sec; EPE; 485 X.



Fig. 36 - Silicon steel; 800° C; $\mathcal{E} = 0.75$; $\dot{\mathcal{E}} = 0.15/\text{sec}$; delay 10 sec; EPE; 485 X.

by the glide of individual edge dislocations of the same sign, which then climbed into walls normal to their Burgers vector and revealed themselves as groups of almost parallel lines. This mechanism has previously been discussed by BYRNE⁶⁸⁾. The distance between the polygonized boundaries appeared to be the same, or smaller than that of the slip lines. Stress concentration in the regions adjacent to high-angle boundaries, affecting the flow and the shape of polygonized groups, is evident in Fig. 36. Extended tilt boundaries were never detected by optical microscopy after deformation to high strains.

5.3.2 EQUIAXED AND STEADY-STATE SUBSTRUCTURES

Most of the substructures observed were composed of equiaxed subgrains, and their low-angle boundaries contained both screw and edge dislocations. Transmission electron micrographs of specimens examined after deformation under different conditions, enabled the dependence of the substructure geometry on the strain rate, temperature and delay after deformation to be determined. The relationship will be discussed in more detail later. It is worth pointing out that the average subgrain size did not change with strain during deformation under steady-state conditions.

Effect of Strain. The present investigation demonstrated that the formation of equiaxed substructure began in the transient region and that fairly well-formed subgrains were present at strains as low as $\mathcal{E} = 0.19$. It was also evident that the size of the subgrains did not change with increasing strain in the steady-state region. This remained true unless the constant rate of strain was interrupted and replaced by a different strain rate, or by a period of recovery. The progress of sub-

structure development with strain is shown in Figs. 37 to 40 for Armco iron and in Figs. 41, 42 and 43 for silicon steel. Similar results were obtained using electron microscopy.

Effect of Strain Rate. The decrease of subgrain size with increasing strain rate was expected, because hot deformation is a thermally activated process and the flow stress increases with the strain rate. This effect has been observed before by other investigators 13,86), and can be seen in Figs. 46 and 47 and also in the transmission electron micrographs in Figs. 44 and 45 and 48 to 51. The quantitative effect of strain rate on average subgrain size will be discussed in more detail later.

Effect of Temperature. The influence of temperature on the subgrain size was marked, as the range of temperatures involved was considerable. As already discussed in previous sections, and demonstrated on the true stress-true strain curves, the flow stress decreased as the temperature was increased. By contrast, the subgrain size increased with the temperature of deformation. The influence of the working temperature on the substructure was observed even at very low magnifications, as shown in Figs. 52 to 56. Substructure size differences due to temperature are presented at higher magnifications in Figs. 57 to 61. Transmission electron micrographs of silicon steel specimens are shown in Figs. 62, 63 and 64. Typical substructures in Armco iron hot compressed at different temperatures are shown in Figs. 65, 66 and 67.

Equiaxed Subgrains in the Transient Region. The transient region was given less attention than the steady-state region; however, the following observations may be worth noting. Photomicrographs 37, 38

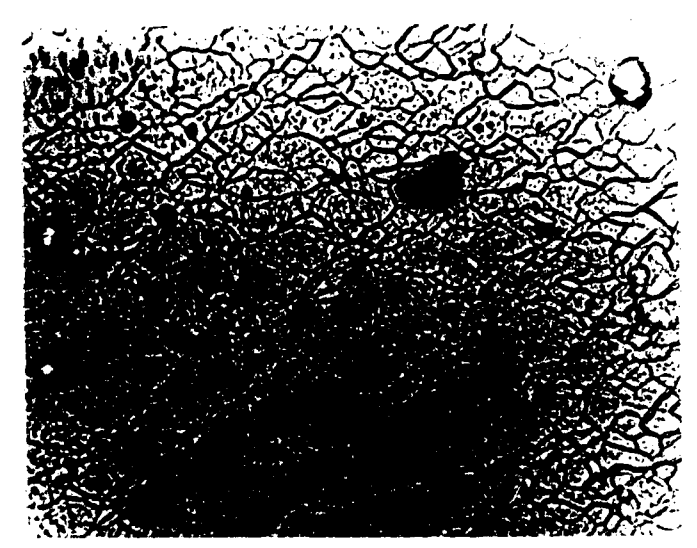


Fig. 37 - Armco iron; 750° C; $\varepsilon = 0.27$; $\dot{\varepsilon} = 0.25/\text{sec}$; delay 1 sec; EPNE; 585 X.



Fig. 38 - Armco iron; 800° C; $\varepsilon = 0.19$; $\dot{\varepsilon} = 0.25/\text{sec}$; delay 3 sec; EPNE; 585 X.



Fig. 37 - Armco iron; 750° C; $\varepsilon = 0.27$; $\dot{\varepsilon} = 0.25/\text{sec}$; delay 1 sec; EPNE; 585 X.

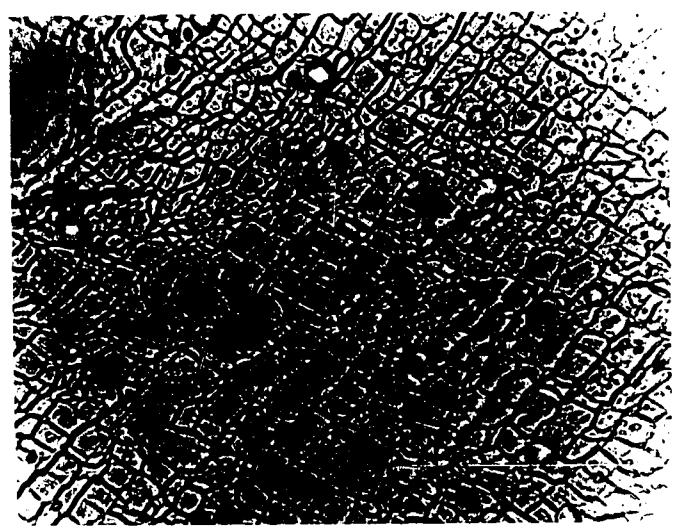


Fig. 38 - Armco iron; 800° C; $\mathcal{E} = 0.19$; $\dot{\mathcal{E}} = 0.25/\text{sec}$; delay 3 sec; EPNE; 585 X.

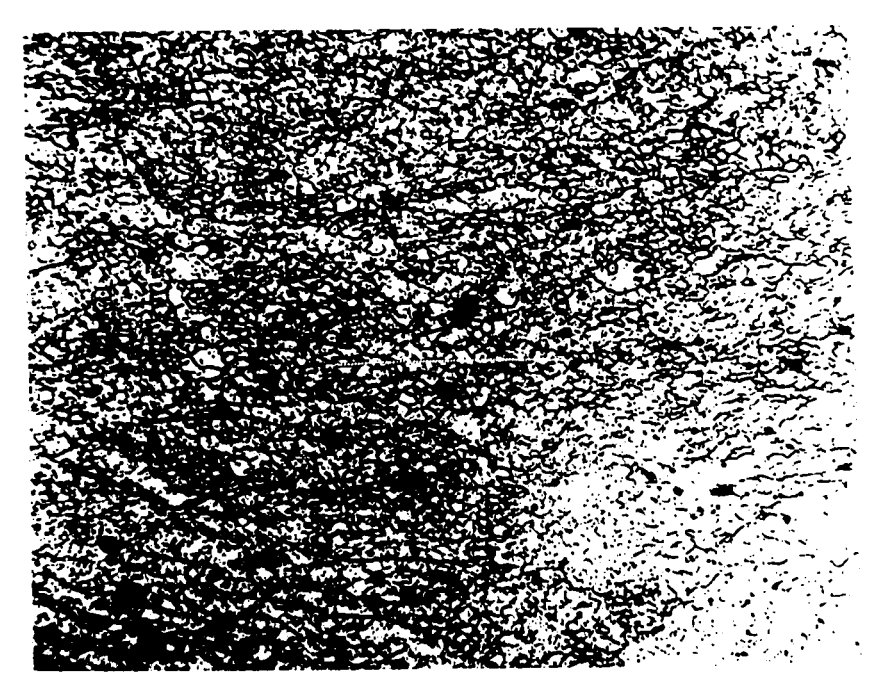


Fig. 39 - Armco iron; 750° C; $\varepsilon = 0.70$; $\dot{\varepsilon} = 0.25/\text{sec}$; delay 1 sec; EPNE; 220 X.

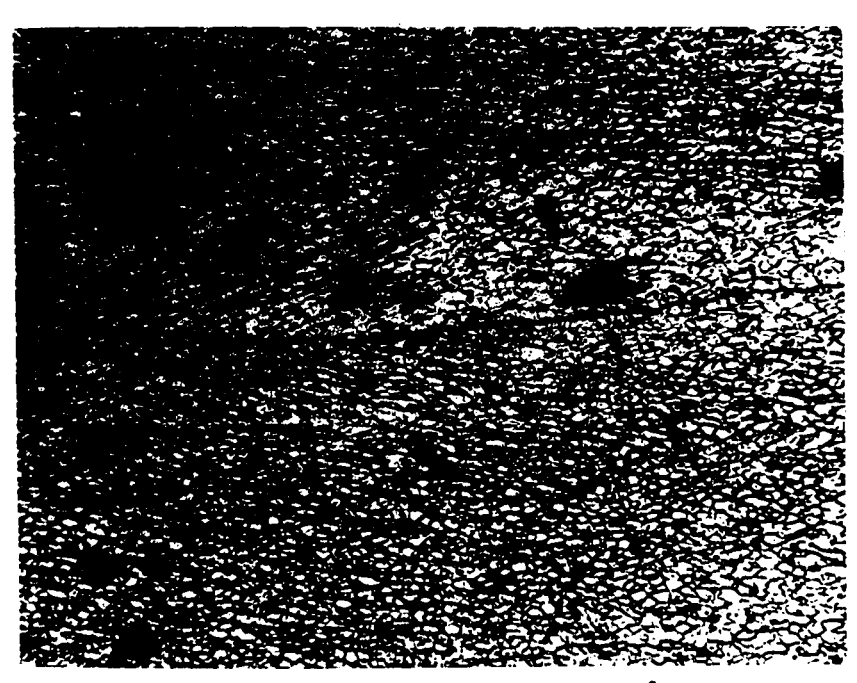


Fig. 40 - Armco iron; 700° C; $\varepsilon = 1.45$; $\dot{\varepsilon} = 0.27/\text{sec}$; delay 15 sec; EPNE; 220 X.

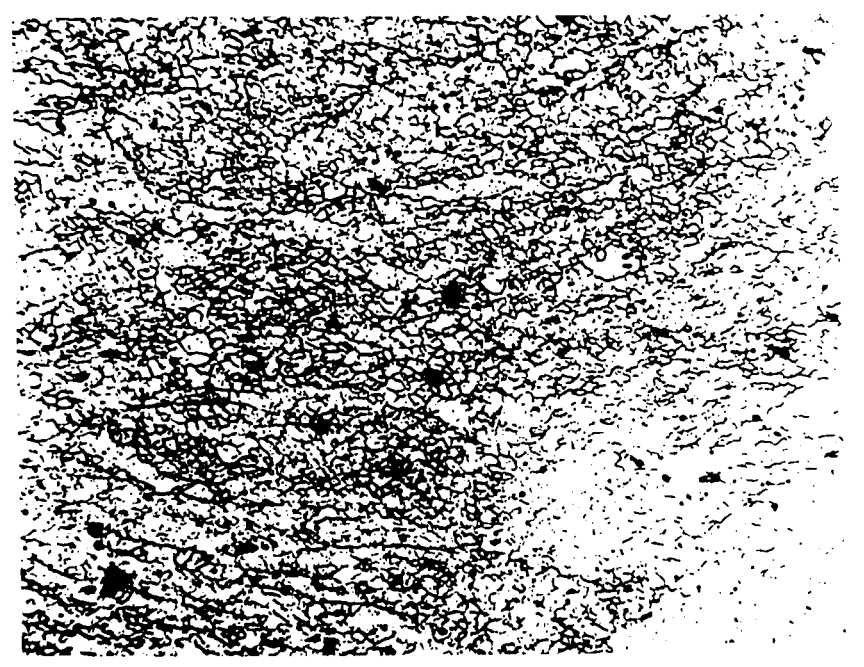


Fig. 39 - Armco iron; 750° C; $\varepsilon = 0.70$; $\dot{\varepsilon} = 0.25/\text{sec}$; delay 1 sec; EPNE; 220 X.

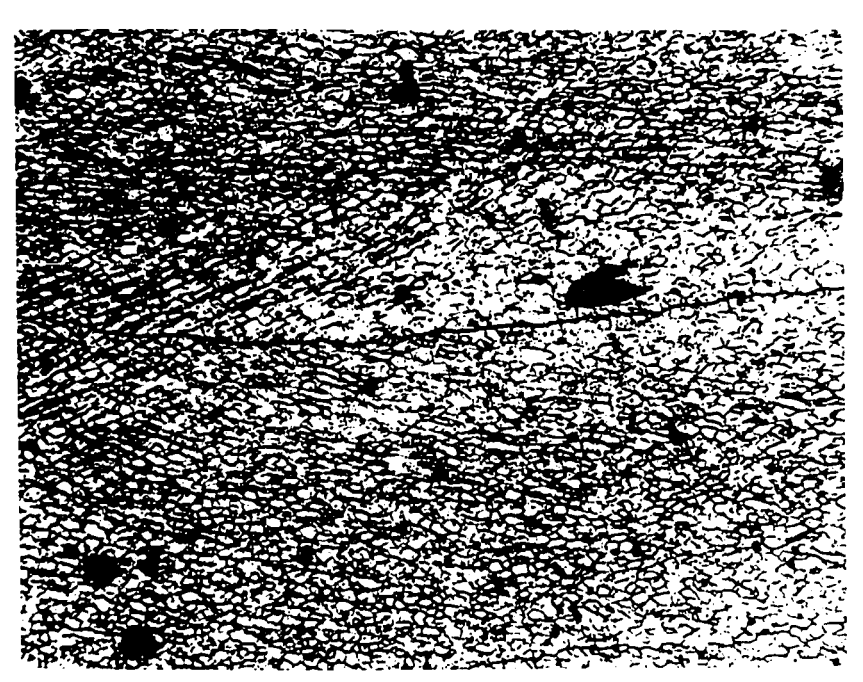


Fig. 40 - Armco iron; 700° C; $\varepsilon = 1.45$; $\dot{\varepsilon} = 0.27/\text{sec}$; delay 15 sec; EPNE; 220 X.

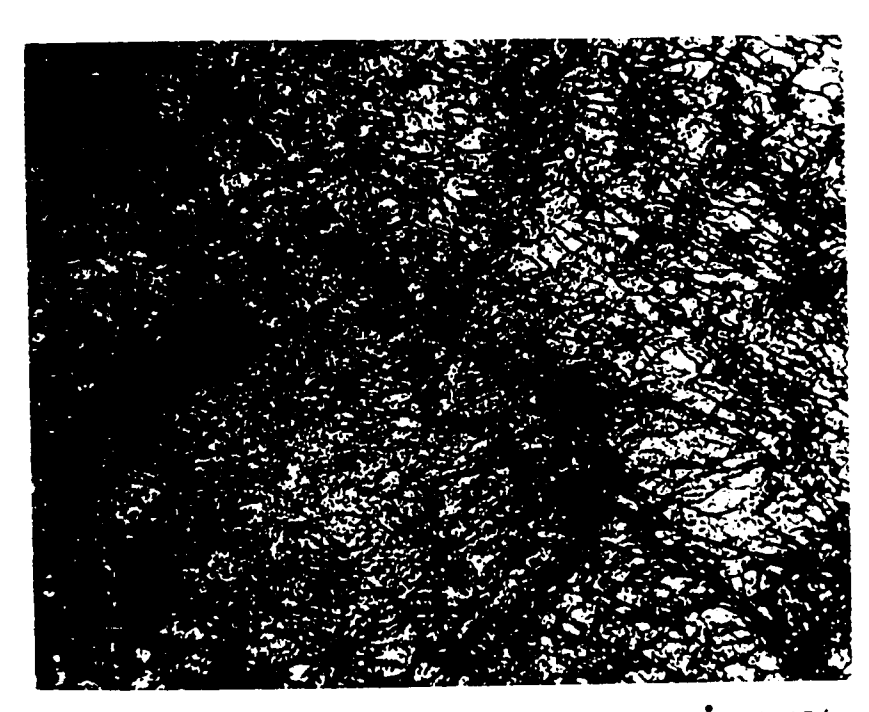


Fig. 41 - Silicon steel; 700° C; $\mathcal{E} = 0.17$; $\dot{\mathcal{E}} = 0.25/\text{sec}$; delay 60 min; EPE; 460 X.

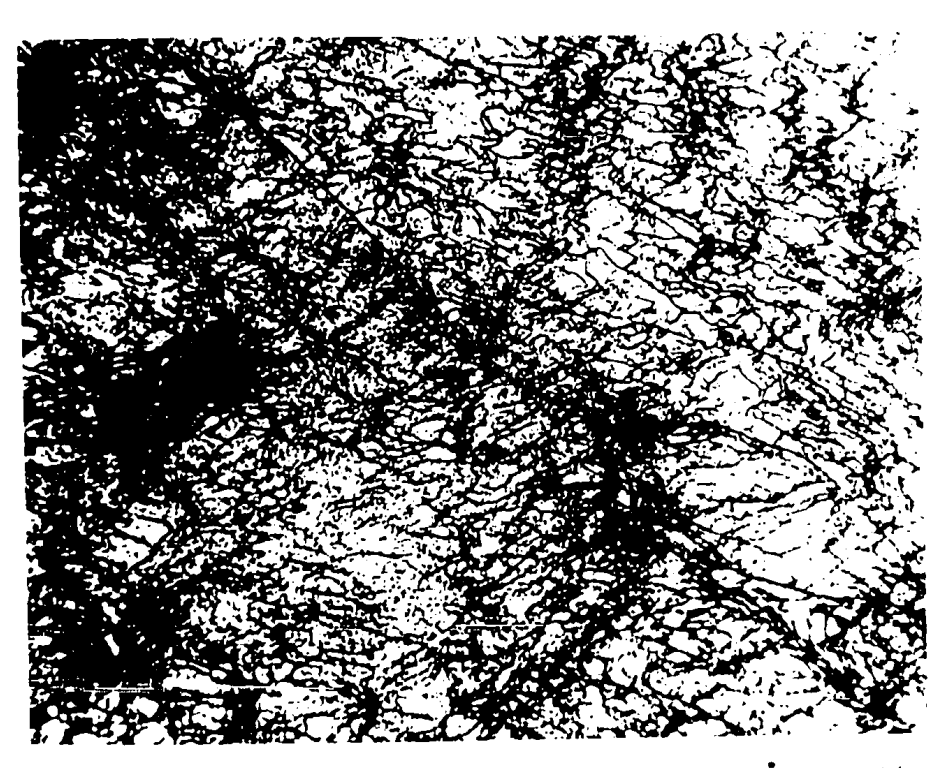


Fig. 41 - Silicon steel; 700° C; $\mathcal{E} = 0.17$; $\dot{\mathcal{E}} = 0.25/\text{sec}$; delay 60 min; EPE; 460 X.

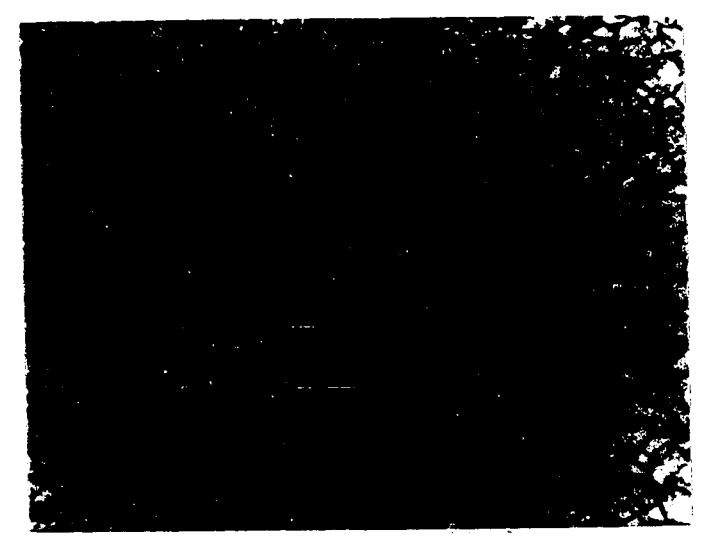
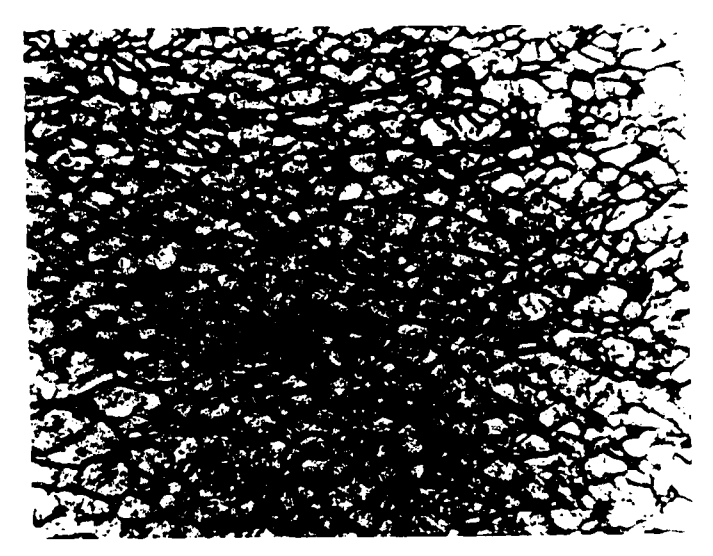


Fig. 42 - Silicon steel; 750° C; $\varepsilon = 0.70$; $\dot{\varepsilon} = 0.075/\text{sec}$; delay 1 sec; EPE; 585 X.



Fig. 43 - Silicon steel; 800° C; $\varepsilon = 1.8$; $\dot{\varepsilon} = 0.26/\text{sec}$; delay 18 sec; EPE; 585 X.



()

Fig. 42 - Silicon steel; 750° C; $\varepsilon = 0.70$; $\dot{\varepsilon} = 0.075/\text{sec}$; delay 1 sec; EPE; 585 X.

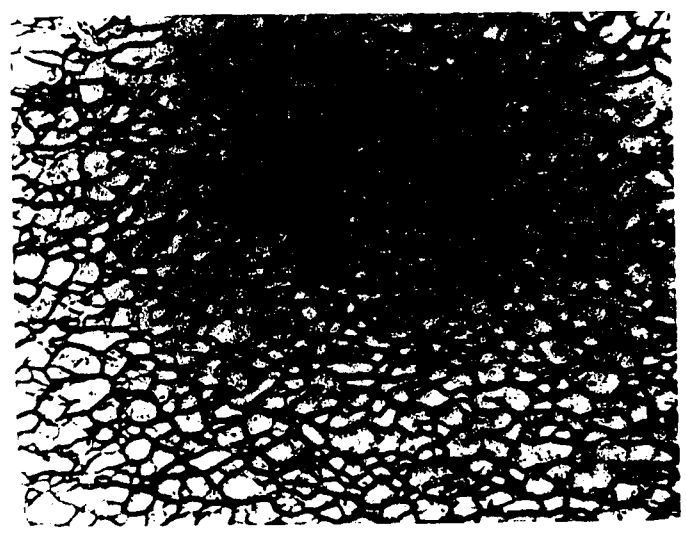


Fig. 43 - Silicon steel; 800° C; $\varepsilon = 1.8$; $\dot{\varepsilon} = 0.26/\text{sec}$; delay 18 sec; EPE; 585 X.



Fig. 44 - Transmission electron micrograph †). Silicon steel; 750°C; ε = 0.40; $\dot{\varepsilon}$ = 0.06/sec; delay 1 sec; 5,700 X.

†) In all the transmission electron micrographs which follow, this will be abbreviated as TEM.



Fig. 45 - Silicon steel; 750° C; $\mathcal{E} = 1.80$; $\dot{\mathcal{E}} = 0.25/\text{sec}$; delay 10 sec; TEM; 5,700 X.



Fig. 44 - Transmission electron micrograph †). Silicon steel; 750°C; $\varepsilon = 0.40$; $\dot{\varepsilon} = 0.06/\text{sec}$; delay 1 sec; 5,700 X.

†) In all the transmission electron micrographs which follow, this will be abbreviated as TEM.



Fig. 45 - Silicon steel; 750° C; $\mathcal{E} = 1.80$; $\dot{\mathcal{E}} = 0.25/\text{sec}$; delay 10 sec; TEM; 5,700 X.

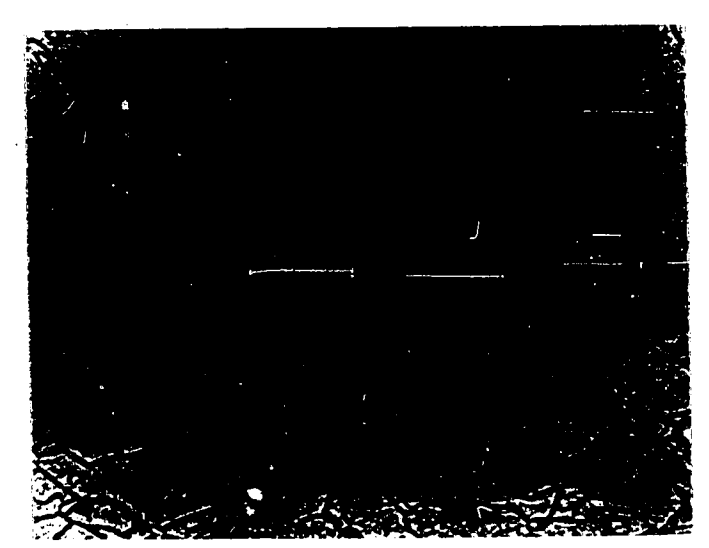


Fig. 46 - Armco iron; 800° C; $\varepsilon = 0.60$; $\dot{\varepsilon} = 0.075/\text{sec}$; delay 15 sec; EPNE; 585 X.

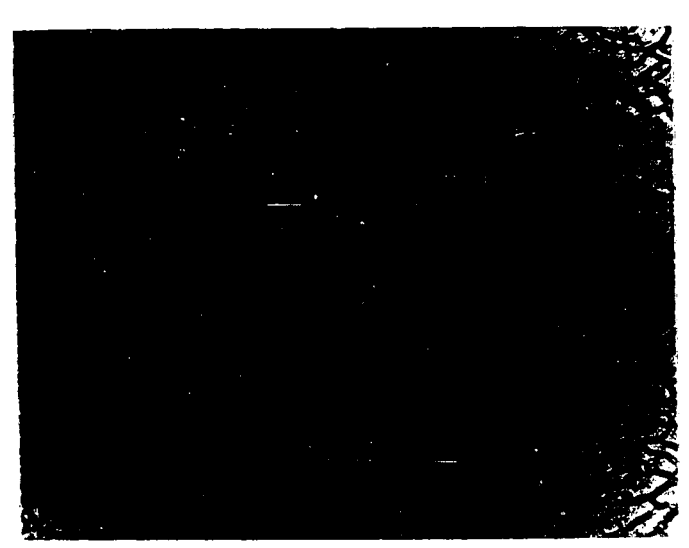
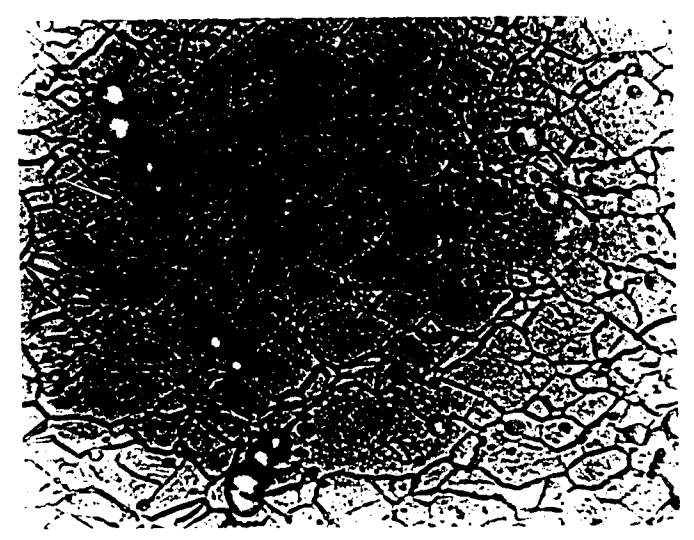


Fig. 47 - Armco iron; 800° C; $\mathcal{E} = 0.61$; $\dot{\mathcal{E}} = 0.13/\text{sec}$; delay 1 sec; EPNE; 585 X.



 \mathbf{C}

Fig. 46 - Armco iron; 800° C; $\varepsilon = 0.60$; $\dot{\varepsilon} = 0.075/\text{sec}$; delay 15 sec; EPNE; 585 X.

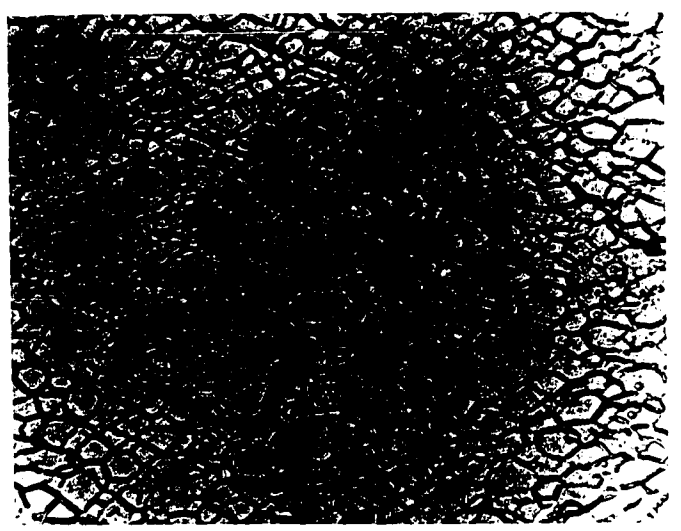


Fig. 47 - Armco iron; 800° C; $\mathcal{E} = 0.61$; $\dot{\mathcal{E}} = 0.13/\text{sec}$; delay 1 sec; EPNE; 585 X.

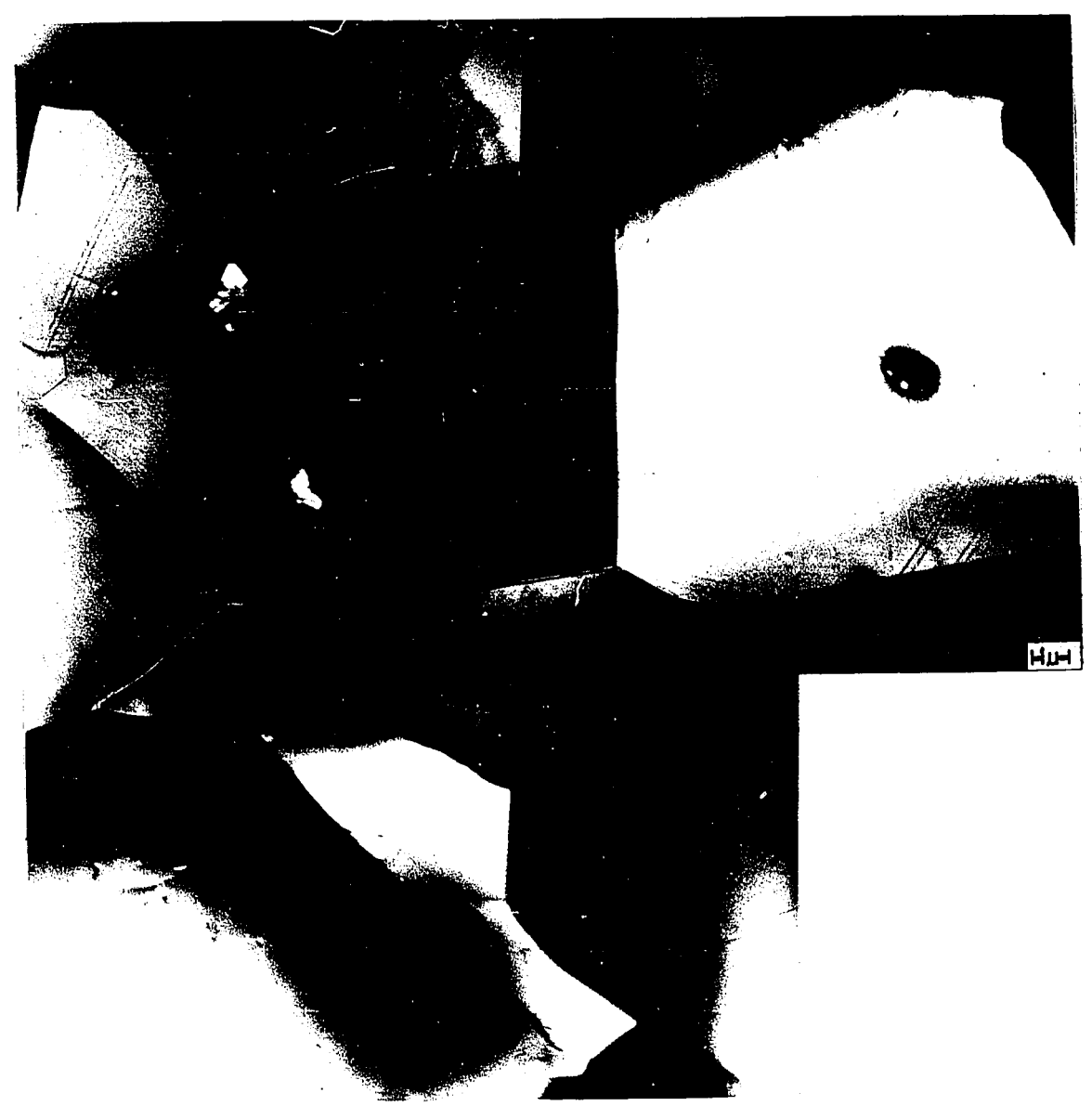


Fig. 48 - Silicon steel; 900° C; $\varepsilon = 0.60$; $\dot{\varepsilon} = 0.06/\text{sec}$; delay 1 sec; TEM; 5,700 X.



Fig. 48 - Silicon steel; 900°C; $\varepsilon = 0.60$; $\dot{\varepsilon} = 0.06/\text{sec}$; delay 1 sec, TEM; 5,700 X.

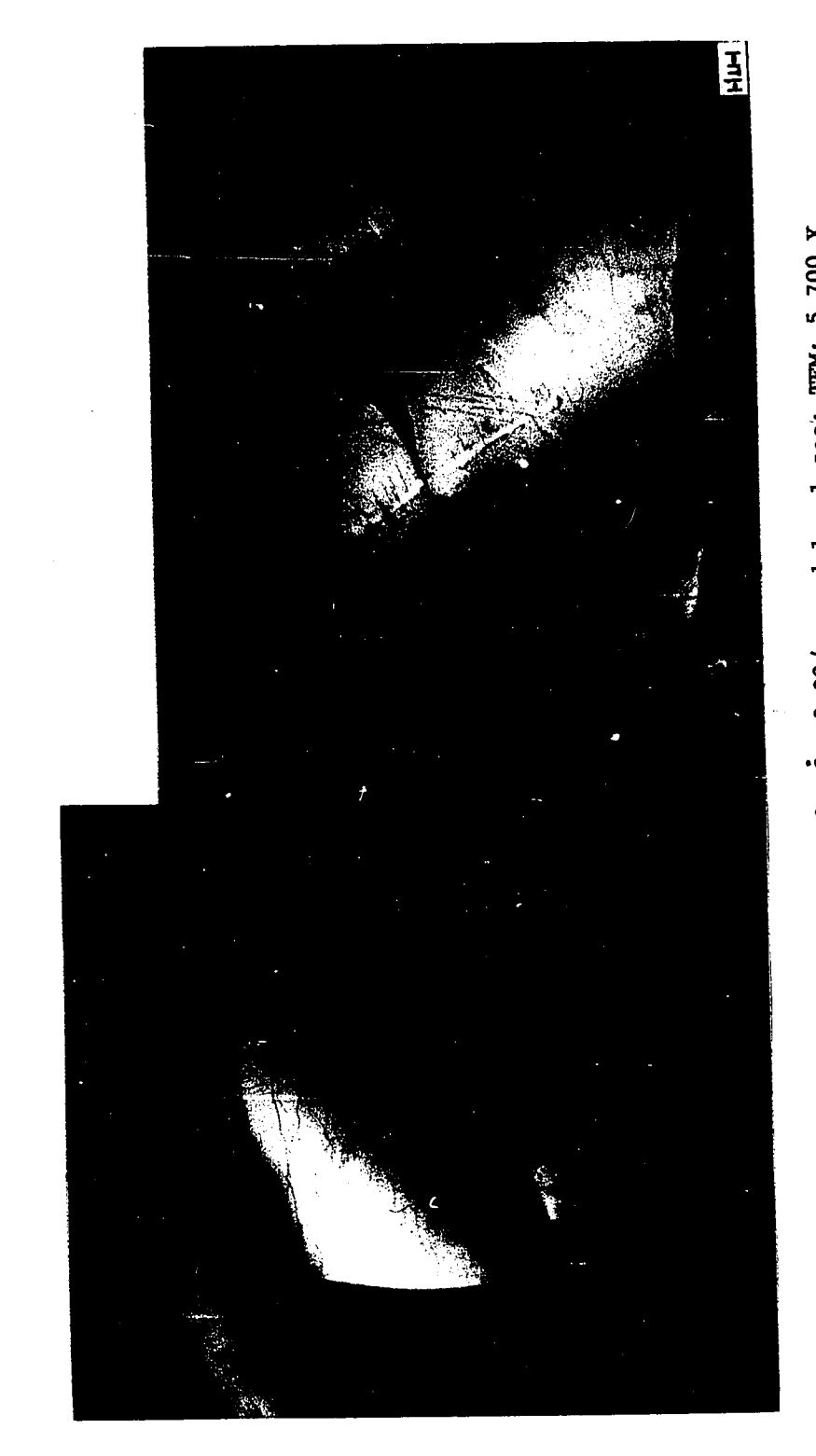


Fig. 49 - Silicon steel; 900°C; &= 0.28; &= 0.20/sec; delay l sec; TEM; 5,700 X.



Fig. 49 - Silicon steel; 900° C; $\mathcal{E} = 0.28$; $\dot{\mathcal{E}} = 0.20/\text{sec}$; delay 1 sec; TEM; 5,700 K.



Fig. 50 - Silicon steel; 1,000°C; ε = 0.29; $\dot{\varepsilon}$ = 0.05/sec; delay 1 sec; TEM; 5,700 X.



Fig. 51 - Silicon steel; $1,000^{\circ}$ C; $\varepsilon = 0.31$; $\dot{\varepsilon} = 0.15/\text{sec}$; delay 1 sec; TEM; 5,700 X.

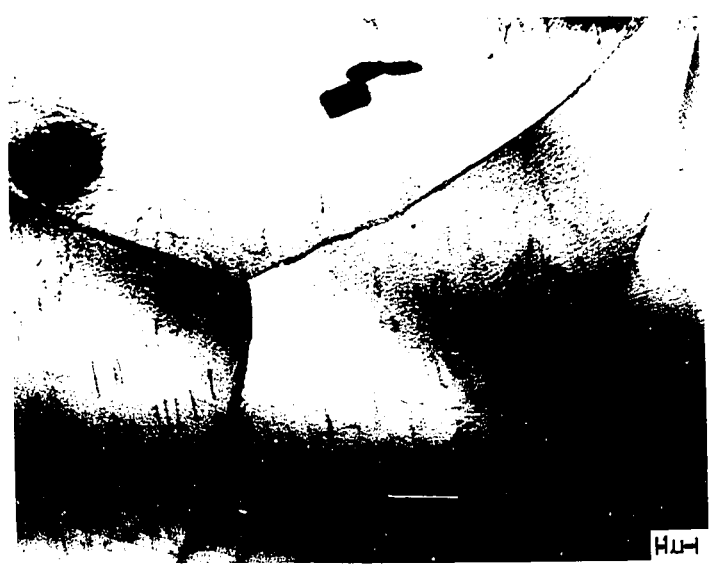


Fig. 50 - Silicon steel; 1,000°C; ε = 0.29; $\dot{\varepsilon}$ = 0.05/sec; delay 1 sec; TEM; 5,700 X.



Fig. 51 - Silicon steel; 1,000°C; ε = 0.31; $\dot{\varepsilon}$ = 0.15/sec; delay 1 sec; TEM; 5,700 X.



Fig. 52 - Silicon steel; 560° C; $\mathcal{E} = 1.67$; $\dot{\mathcal{E}} = 0.42/\text{sec}$; delay 20 min; EPE; 220 X.

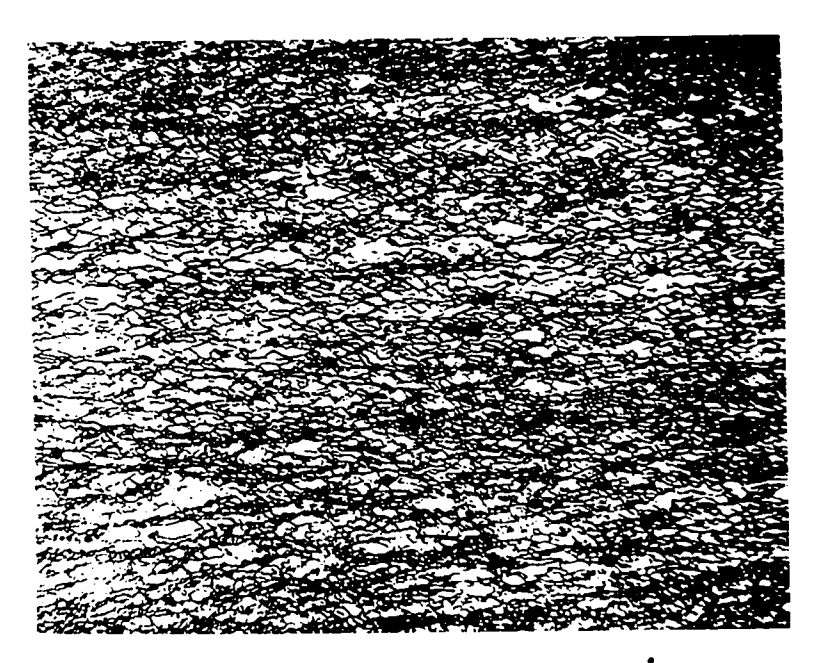


Fig. 53 - Silicon steel; 750°C; $\mathcal{E} = 0.57$; $\dot{\mathcal{E}} = 0.15/\text{sec}$; delay 1 sec; EPE; 220 X.



Fig. 52 - Silicon steel; 560° C; $\mathcal{E} = 1.67$; $\dot{\mathcal{E}} = 0.42/\text{sec}$; delay 20 min; EPE; 220 X.

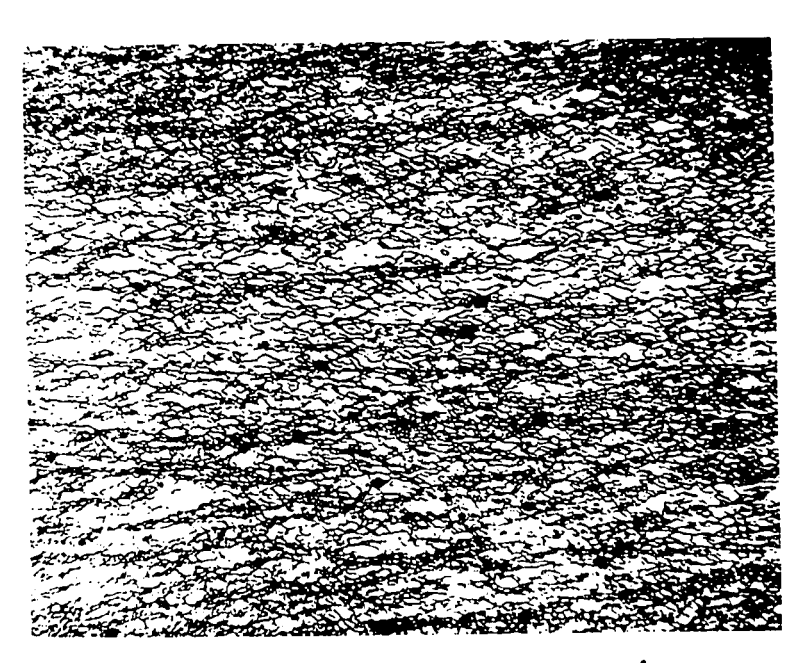


Fig. 53 - Silicon steel; 750° C; & = 0.57; & = 0.15/sec; delay 1 sec; EPE; 220 X.

 $(\cdot \)$

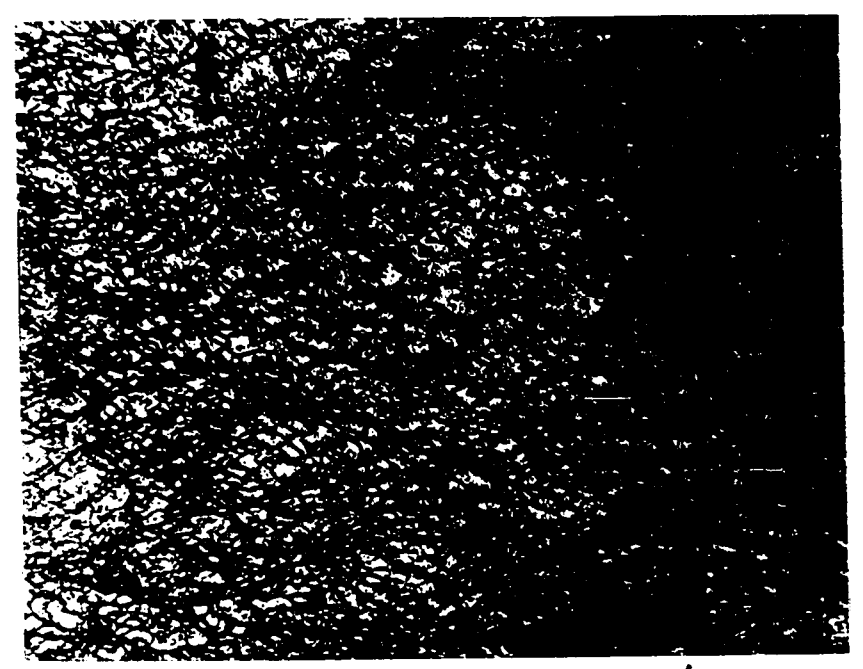


Fig. 54 - Silicon steel; 800° C; $\mathcal{E} = 1.46$; $\dot{\mathcal{E}} = 0.075/\text{sec}$; delay 15 sec; EPE; 220 X.

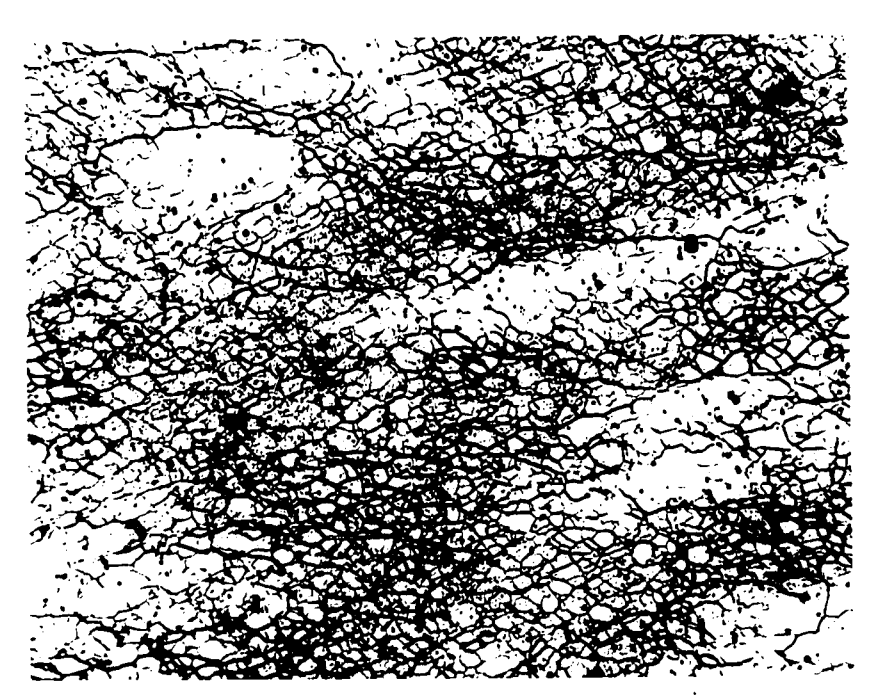


Fig. 55 - Silicon steel; 900° C; $\mathcal{E} = 0.48$; $\dot{\mathcal{E}} = 0.24/\text{sec}$; delay 1 sec; EPE; 220 X.



Fig. 54 - Silicon steel; 800° C; $\mathcal{E} = 1.46$; $\dot{\mathcal{E}} = 0.075/\text{sec}$; delay 15 sec; EPE; 220 X.

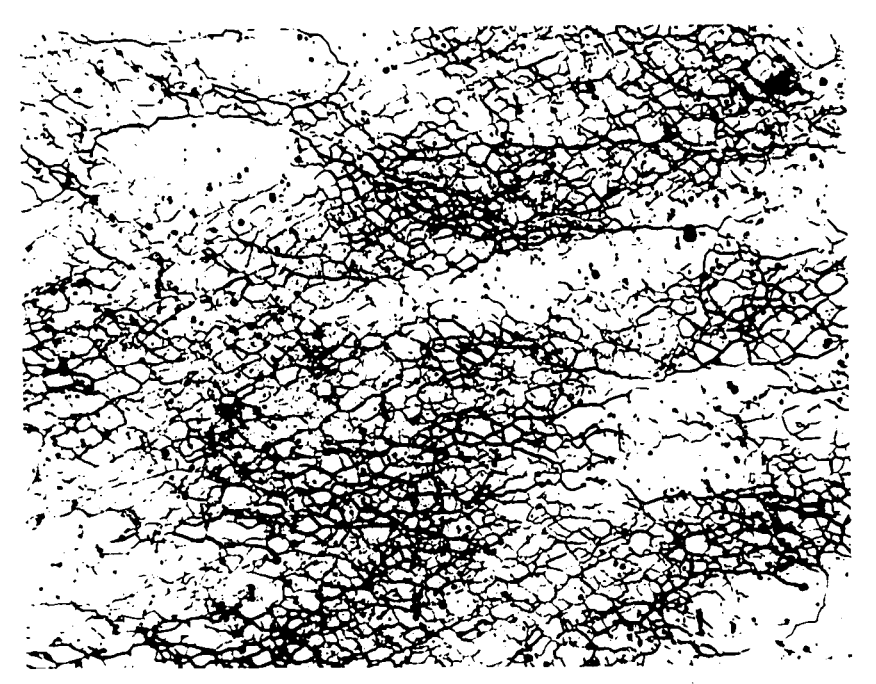


Fig. 55 - Silicon steel; 900° C; &= 0.48; &= 0.24/sec; delay 1 sec; EPE; 220 X.

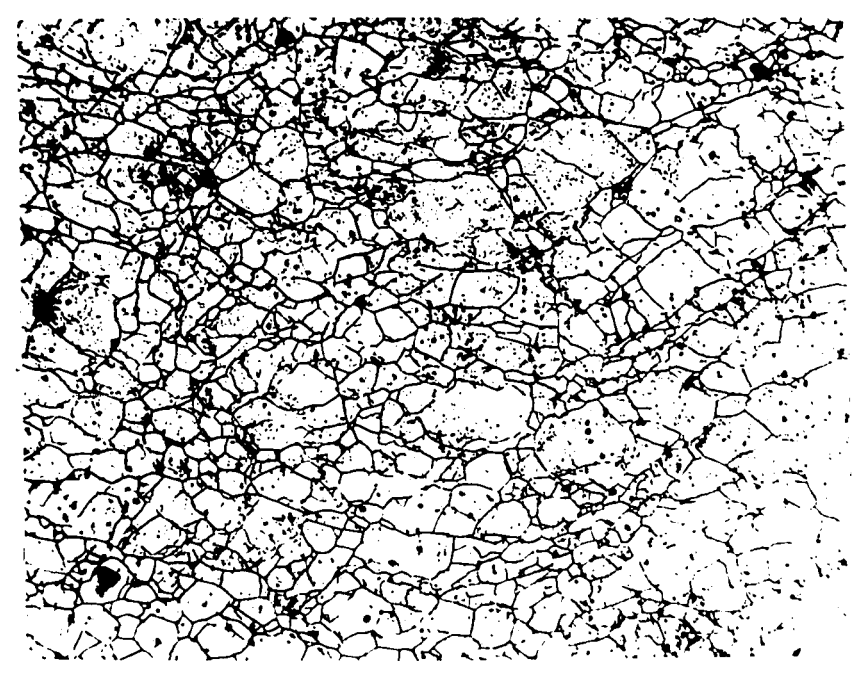


Fig. 56 - Silicon steel; 1,000°C; $\mathcal{E}=0.31; \dot{\mathcal{E}}=0.15/\text{sec};$ delay 1 sec; EPE; 220 X.



Fig. 57 - Armco iron; 600° C; $\mathcal{E}=1.29$; $\dot{\mathcal{E}}=0.16/\text{sec}$; delay 10 sec; EPNE; 950 X.



Fig. 58 - Silicon steel; 650° C; $\mathcal{E} = 1.32$; $\dot{\mathcal{E}} = 0.25/\text{sec}$; delay 5 sec; EPE; 680 X.



Fig. 57 - Armco iron; 600° C; $\mathcal{E}=1.29$; $\dot{\mathcal{E}}=0.16/\text{sec}$; delay 10 sec; EPNE; 950 X.

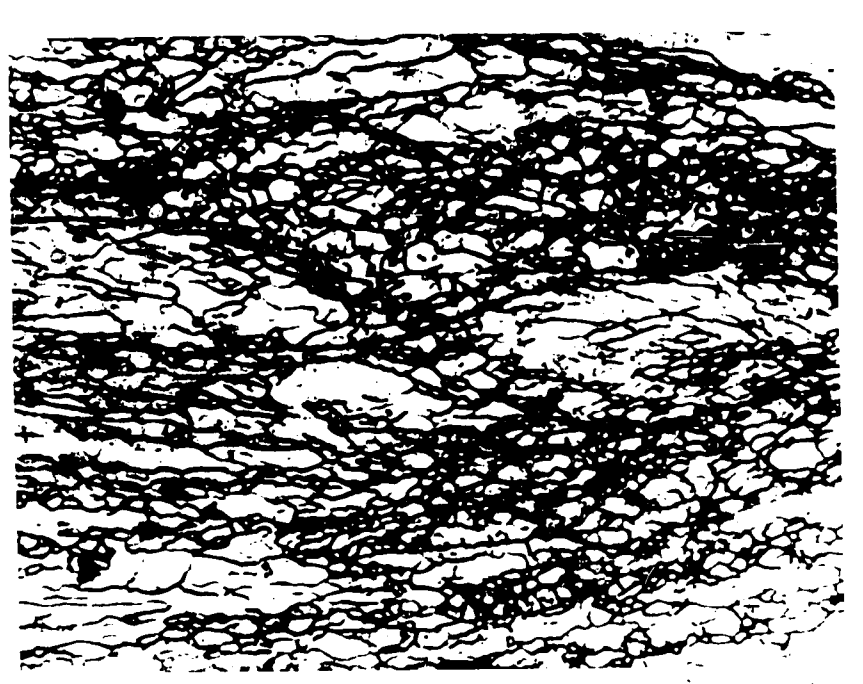


Fig. 58 - Silicon steel; 650°C; \mathcal{E} = 1.32; $\dot{\mathcal{E}}$ = 0.25/sec; delay 5 sec; EPE; 680 X.



Fig. 59 - Silicon steel; 800° C; $\mathcal{E} = 1.70$; $\hat{\mathcal{E}} = 0.26/\text{sec}$; delay 18 sec; EPE; 585 X.



Fig. 60 - Silicon steel; 900°C; $\mathcal{E} = 0.48$; $\dot{\mathcal{E}} = 0.24/\text{sec}$; delay 1 sec; EPE; 585 X.

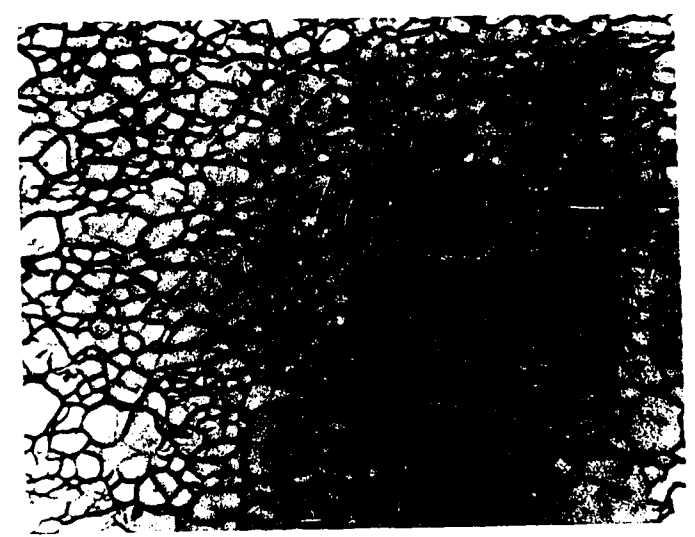


Fig. 59 - Silicon steel; 800° C; $\mathcal{E} = 1.70$; $\hat{\mathcal{E}} = 0.26/\text{sec}$; delay 18 sec; EPE; 585 X.

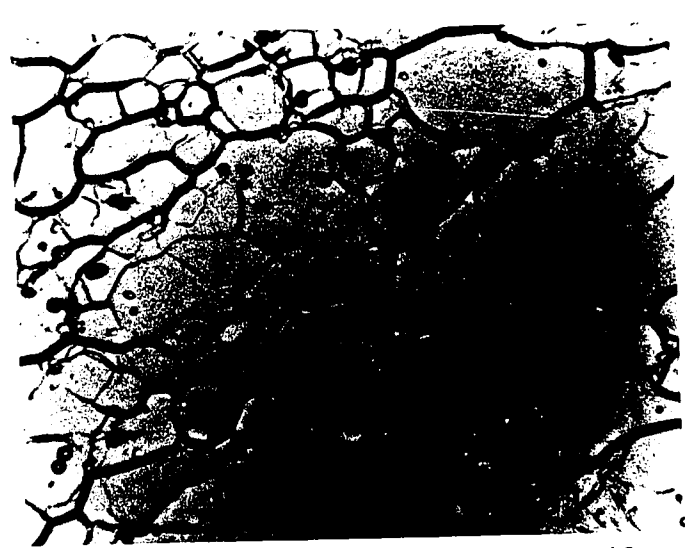


Fig. 60 - Silicon steel; 900°C; $\mathcal{E} = 0.48$; $\dot{\mathcal{E}} = 0.24/\text{sec}$; delay 1 sec; EPE; 585 X.

Fig. 61 - Silicon steel; 1,000°C; ε = 0.30; $\dot{\varepsilon}$ = 0.05/sec; delay 1 sec; EPE; 585 X.

Fig. 61 - Silicon steel; $1,000^{\circ}$ C; $\mathcal{E}=0.30$; $\dot{\mathcal{E}}=0.05/\text{sec}$; delay 1 sec; EPE; 585 X.

(



Fig. 62 - Silicon steel; 650°C; \mathcal{E} = 0.49; $\dot{\mathcal{E}}$ = 0.09/sec; delay 2 sec; TEM; 5,700 X.

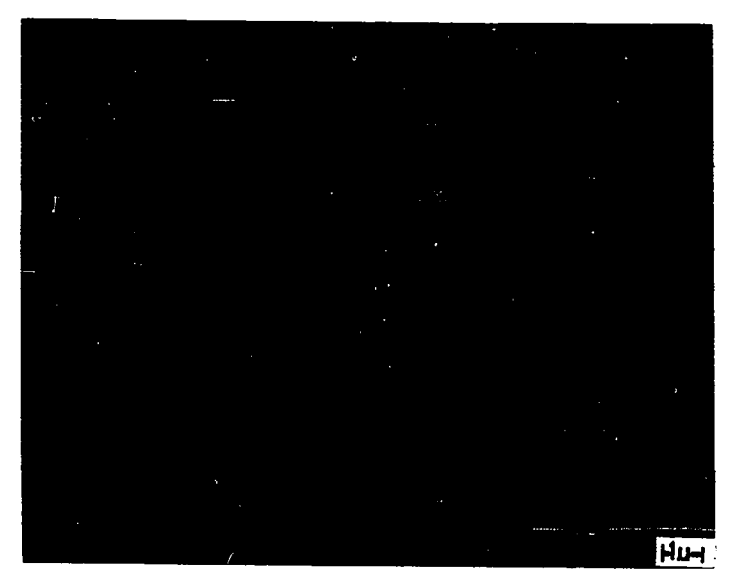


Fig. 63 - Silicon steel; 650° C; $\mathcal{E} = 1.55$; $\dot{\mathcal{E}} = 0.50/\text{sec}$; delay 10 sec; TEM; 5,700 X.



Fig. 62 - Silicon steel; 650°C; \mathcal{E} = 0.49; $\dot{\mathcal{E}}$ = 0.09/sec; delay 2 sec; TEM; 5,700 X.



Fig. 63 - Silicon steel; 650°C; $\mathcal{E}=$ 1.55; $\dot{\mathcal{E}}=$ 0.50/sec; delay 10 sec; TEM; 5,700 X.

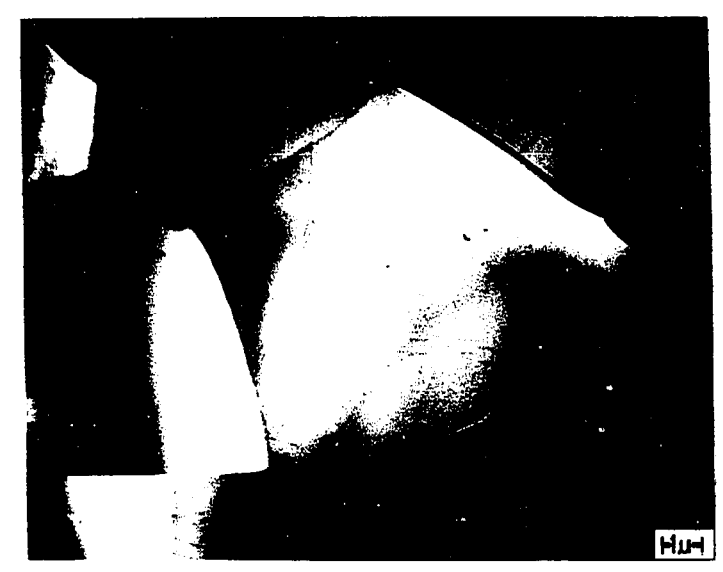


Fig. 64 - Silicon steel; 1,000°C; \mathcal{E} = 0.42; $\dot{\mathcal{E}}$ = 0.15/sec; delay 1 sec; TEM; 5,700 X.



Fig. 65 - Armco iron; 600° C; $\varepsilon = 0.85$; $\dot{\varepsilon} = 0.15/\text{sec}$; delay 10 sec; TEM; 7,150X.

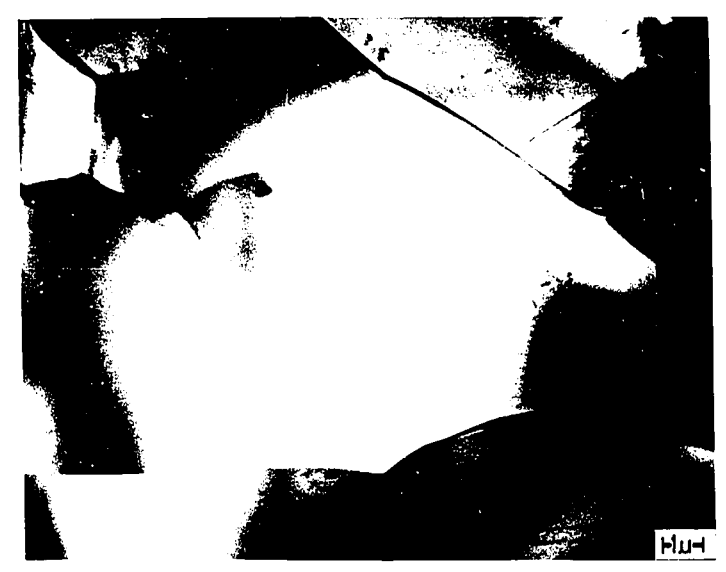


Fig. 64 - Silicon steel; 1,000°C; \mathcal{E} = 0.42; $\dot{\mathcal{E}}$ = 0.15/sec; delay 1 sec; TEM; 5,700 X.



Fig. 65 - Armco iron; 600° C; $\varepsilon = 0.85$; $\dot{\varepsilon} = 0.15/\text{sec}$; delay 10 sec; TEM; 7,150X.

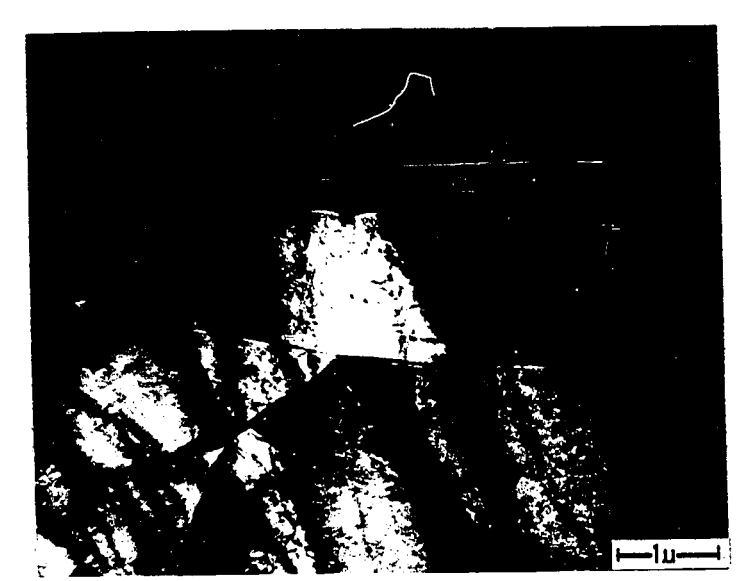


Fig. 66 - Armco iron; 600° C; &= 1.30; &= 0.16/sec; delay 13 sec; TEM; 14,300 X.



Fig. 67 - Armco iron; 700° C; $\hat{\epsilon} = 1.52$; $\dot{\hat{\epsilon}} = 0.23/\text{sec}$; delay 5 sec; TEM; 10,000 X.



Fig. 66 - Armco iron; 600° C; $\hat{c} = 1.30$; $\dot{c} = 0.16/\text{sec}$; delay 13 sec; TEM; 14,300 X.

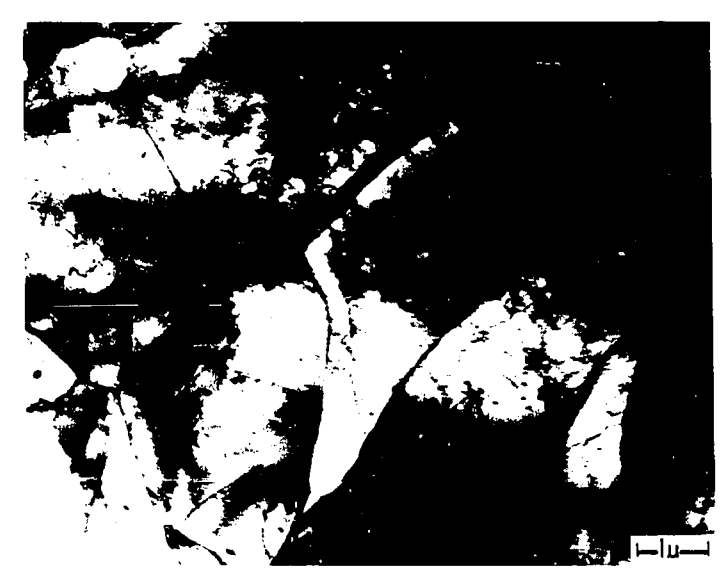


Fig. 67 - Armco iron; 700° C; $\hat{\epsilon}$ = 1.52; $\dot{\hat{\epsilon}}$ = 0.23/sec; delay 5 sec; TEM; 10,000 X.

and 41 characterize the substructure formed at early stages of hot compression. They suggest that, at similar strains, the average subgrain size becomes smaller as the temperature is increased. This contradicts the observations in the steady-state region and can be explained by the fact that the actual sub-boundaries are not as well defined at lower temperatures, and probably do not all show up after electrolytic etching.

Observations of the substructure formed in the late transient region, at strains near to those in the steady-state region, were carried out at different temperatures. It was observed that, at high temperatures, there was virtually no difference between the subgrain size corresponding to the late transient region and that well on in the steady-state.

Equiaxed Subgrains in the Steady-State Region. The onset of a steady-state of flow stress can be detected from the true stress-true strain curves (Figs. 13b to 24b). Microscopic examination confirmed the existence of a steady-state as regards the microstructure as well, beginning at the same strains indicated by the afore-mentioned curves.

The subgrain size established at the onset of the steady-state region did not change with increasing strain. Also the shape of the subgrains did not change with strain within the steady-state region. This can be observed in Figs. 43 and 44 and also in Figs. 45 and 63, where the subgrains remain equiaxed after strains ranging up to $\mathcal{E}=1.8$. The substructure, even after deformation to a strain of $\mathcal{E}=1.55$ at $650^{\circ}\mathrm{C}$, and at strain rates as high as $0.5/\mathrm{sec}$, remains approximately equiaxed. The individual subgrains appear as if they were created from

elongated units by the continuous introduction of new sub-boundaries, thus dividing the deformed units into equiaxed subgrains. The subgrains shown in the latter figure are slightly elongated, which was a general property of subgrains formed at homologous temperatures below 0.50.

The subgrain walls did not seem to form rigid barriers restricting the extension of dislocation loops within the subgrains, as postulated by STUWE⁶²⁾. In many cases, e.g. Figs. 49 and 51, dislocations were observed to move in long lines across the subgrain boundaries.

5.4 STATIC RECOVERY AFTER HOT DEFORMATION

Static recovery after hot deformation is closely connected to hot deformation and proceeds subsequent to dynamic recovery after the load is released, and while the specimen is cooling. To date, little attention has been paid to recovery phenomena following hot deformation 108). Most of the investigations described in the literature have concerned the progress of recrystallization after hot deformation 27,33,116).

In the present investigation, specimens were held for different times at the working temperature after hot compression and then quenched. Changes both of microhardness and of substructure were observed, as well as the progress of recrystallization during isothermal annealing. The results, however, can only be regarded as tentative, as only a limited number of specimens was examined, and the microhardness readings were somewhat scattered.

5.4.1 EFFECT OF STATIC RECOVERY ON MICROHARDNESS

The change of microhardness with time lapse after hot working and before quenching was measured and evaluated as shown in Fig. 68. A simple exponential recovery law was assumed, in which the activation energy is not a function of the microhardness, but remains constant. This law was introduced in section 2.4.1.

In Fig. 68, DPH values obtained after different time lapses following hot deformation are plotted against time on a semilogarithmic basis. The advantage of using the exponential recovery law and semilogarithmic paper can be seen from this graph. Microhardness can be extrapolated back to zero time, even though the fastest quenches were no shorter than one second. Using the logarithmic law and semi-logarithmic paper, extrapolation to shorter and shorter delay times leads to continuously increasing microhardnesses, which are clearly incorrect.

From Fig. 68 it can be seen that approximately straight lines having different slopes can be fitted to the microhardness values obtained after various time lapses. Although some scatter was obtained, which is inevitable in microhardness testing, values determined after long delays enables the determination of the decay slopes at the different temperatures. It can also be seen that the softening during hot working due to dynamic recovery alone (microhardness at zero delay time) is very pronounced, and at high temperatures can be almost complete.

It should be noted that the microhardness decreased more quickly when the temperature of working was increased, and when the strain rate and the accompanying work hardening were increased. This was observed both in Armco iron and in silicon steel. It is also of interest

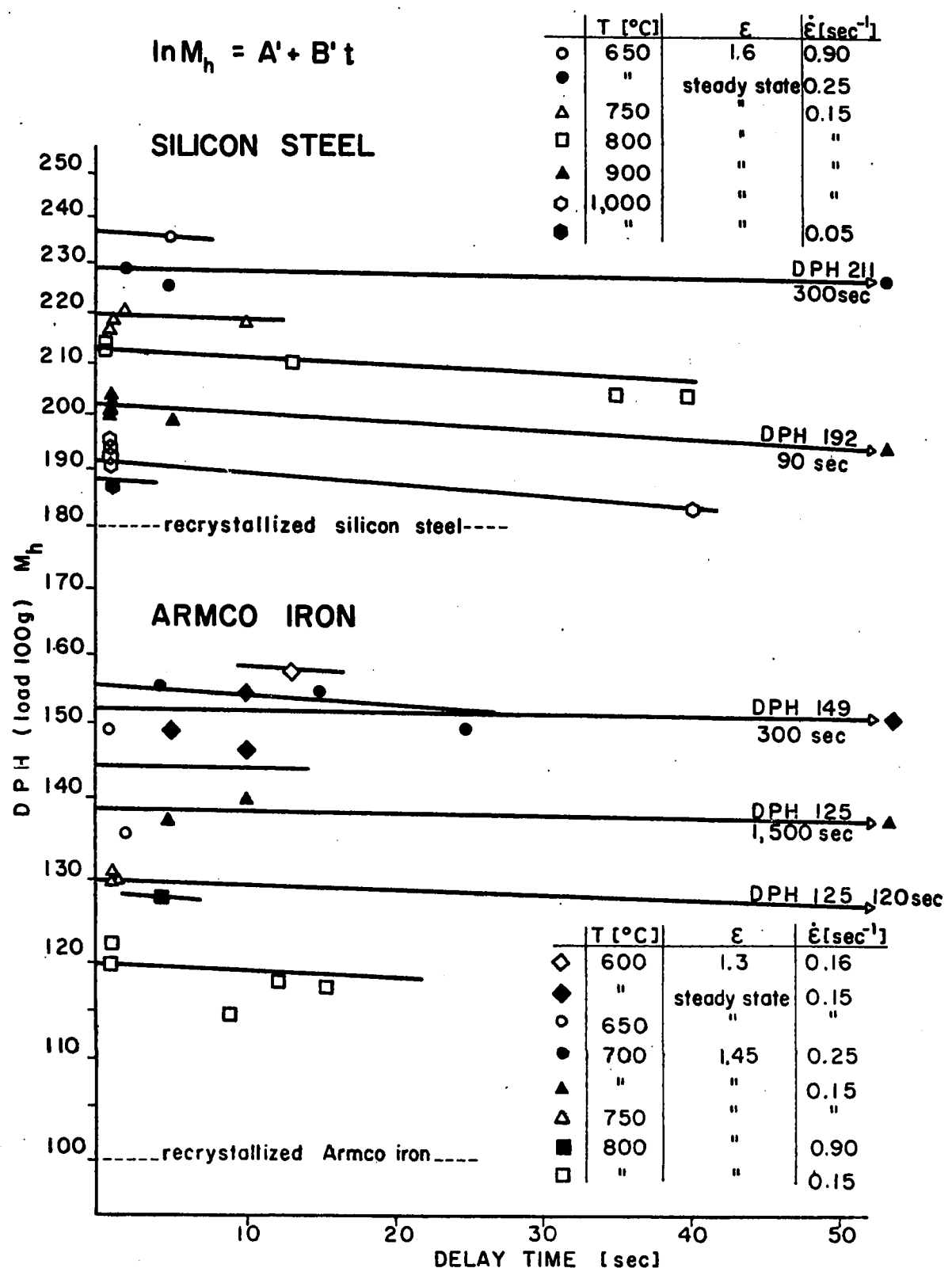


FIG. 68 CHANGE OF MICROHARDNESS WITH DELAY BEFORE QUENCHING. EACH POINT REPRESENTS AN AVERAGE OF ABOUT 12 READINGS

that the activation energy of static recovery after hot compression can be estimated from the above results, with the aid of the exponential equation. Calculation led to values of 25,000 ± 5,000 cal/mole for silicon steel and of 22,000 ± 2,000 cal/mole for Armco iron. The changes of slope suggest that the activation energies increase by about 10% as the deformation temperature is raised. The Armco iron value is in agreement with that obtained for the onset of recovery in zone-melted iron by MICHALAK and PAXTON⁷⁹⁾. The activation energies for the onset of static recovery represent approximately one third of the values of the activation energies for self diffusion and for dynamic recovery.

5.4.2 EFFECT OF STATIC RECOVERY ON SUBSTRUCTURE

At high temperatures static recovery after hot deformation proceeded very quickly, followed by recrystallization. Figs. 71 and 72 show the decrease in the dislocation density in some of the subboundary networks arising from the dislocation rearrangement taking place due to recovery. The distinction between clearly and slightly visible low-angle boundaries is probably due to the different susceptibility to electrochemical attack of the well-defined as opposed to the disintegrating sub-boundary networks. The dull lines in these photographs represent low-angle boundaries partially decomposed. After a sufficient time lapse, some sub-boundaries disappeared completely and recrystallization was nucleated (Fig. 72).

As the deformation temperature was decreased, the disintegration of the sub-boundaries due to recovery also proceeded more slowly. In Figs. 73 to 76, the recovering subgrains can be observed at 900°C in the presence of already recrystallized areas. Figs. 75 and 76 show

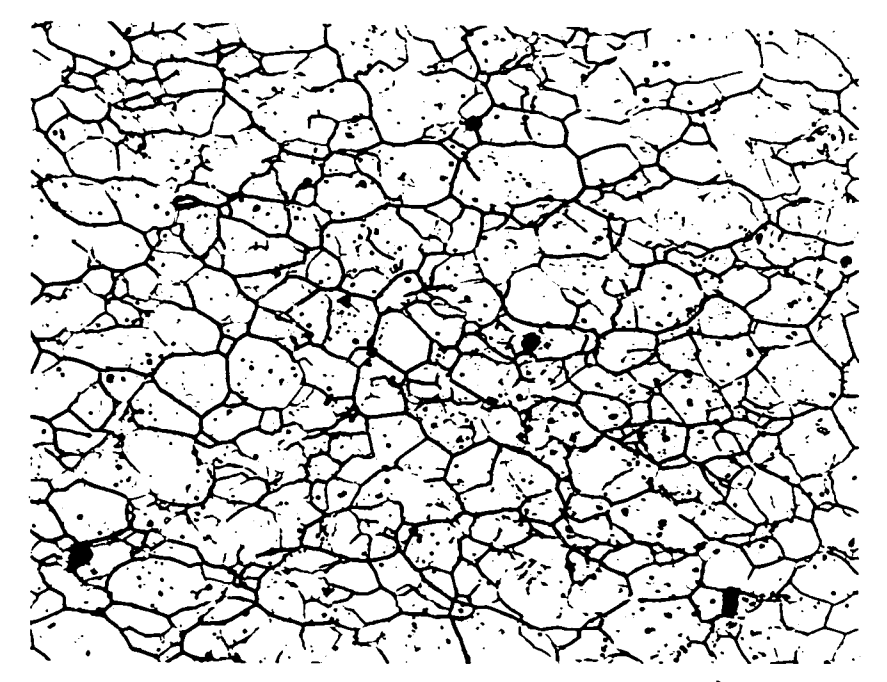


Fig. 69 - Silicon steel; 1,000°C; $\mathcal{E} = 0.53$; $\dot{\mathcal{E}} = 0.08/\text{sec}$; delay 1 sec; EPE; 220 X.

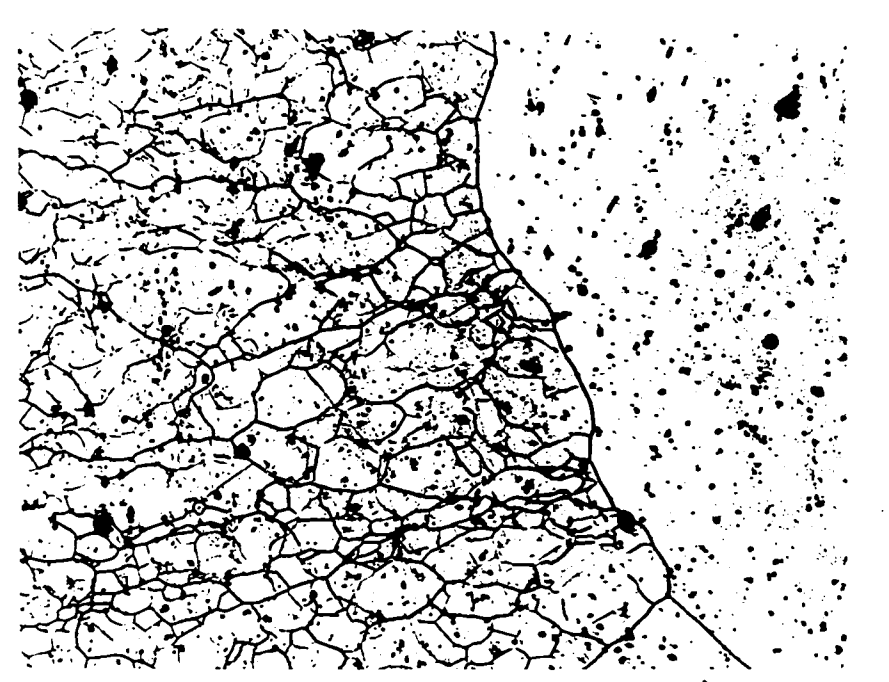


Fig. 70 - Silicon steel; 1,000°C; ε = 0.56; $\dot{\varepsilon}$ = 0.15/sec; delay 40 sec; EPE; 220 X.

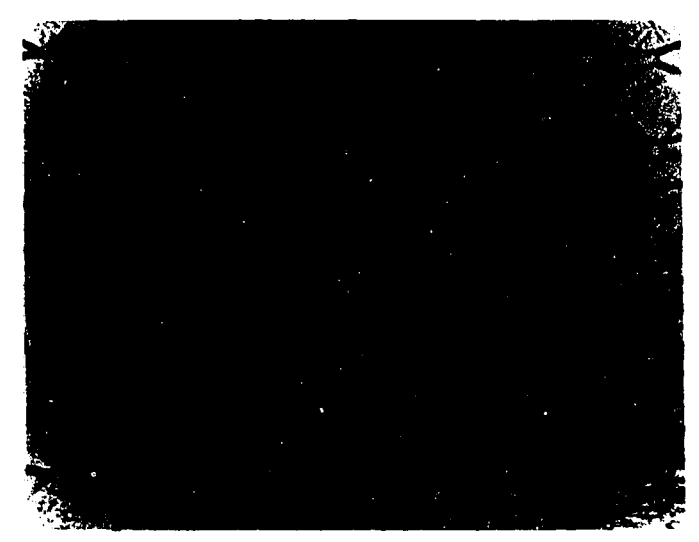


Fig. 71 - Silicon steel; 1,000°C; \mathcal{E} = 0.53; $\dot{\mathcal{E}}$ = 0.08/sec; delay 1 sec; EPE; 585 X.



Fig. 72 - Silicon steel; 1,000°C; \mathcal{E} = 0.56; $\dot{\mathcal{E}}$ = 0.15/sec; delay 40 sec; EPE; 585 X.



()

Fig. 71 - Silicon steel; 1,000°C; \mathcal{E} = 0.53; $\dot{\mathcal{E}}$ = 0.08/sec; delay 1 sec; EPE; 585 X.

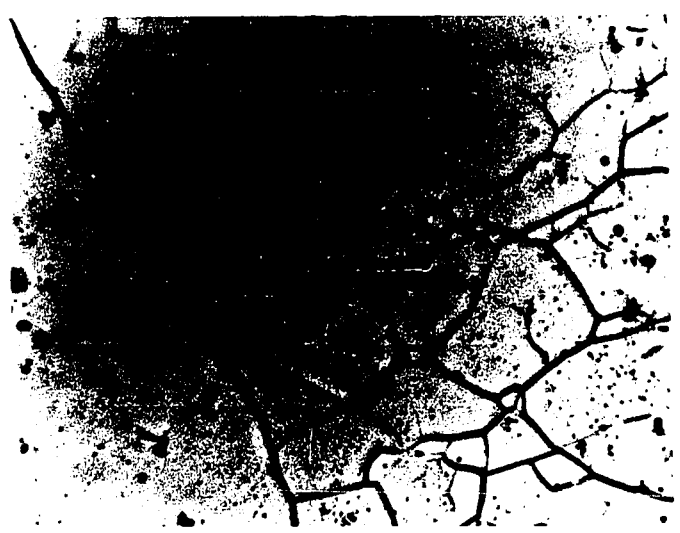


Fig. 72 - Silicon steel; 1,000°C; \mathcal{E} = 0.56; $\dot{\mathcal{E}}$ = 0.15/sec; delay 40 sec; EPE; 585 X.

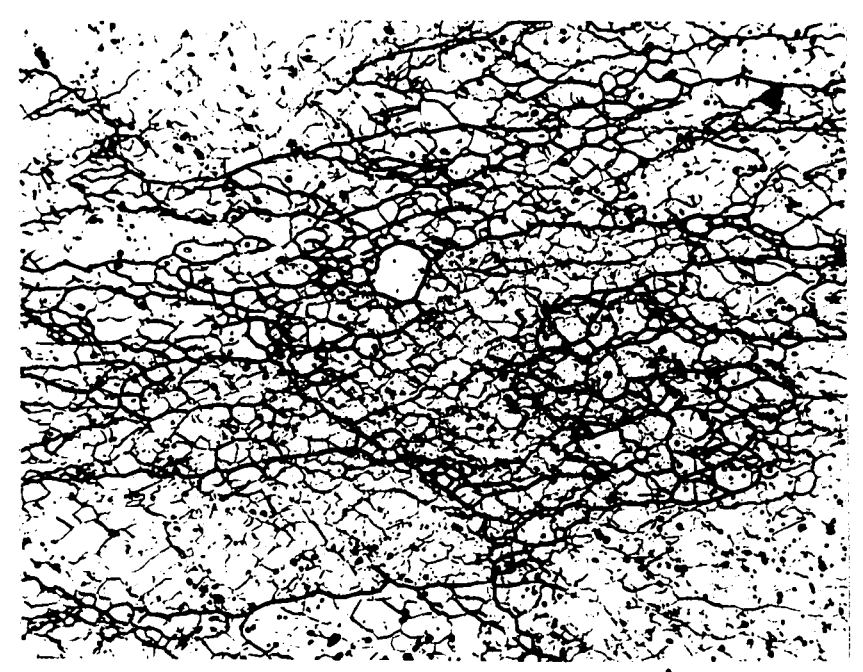


Fig. 73 - Silicon steel; 900° C; &= 0.48; &= 0.19/sec; delay 5 sec; EPE; 220 X.

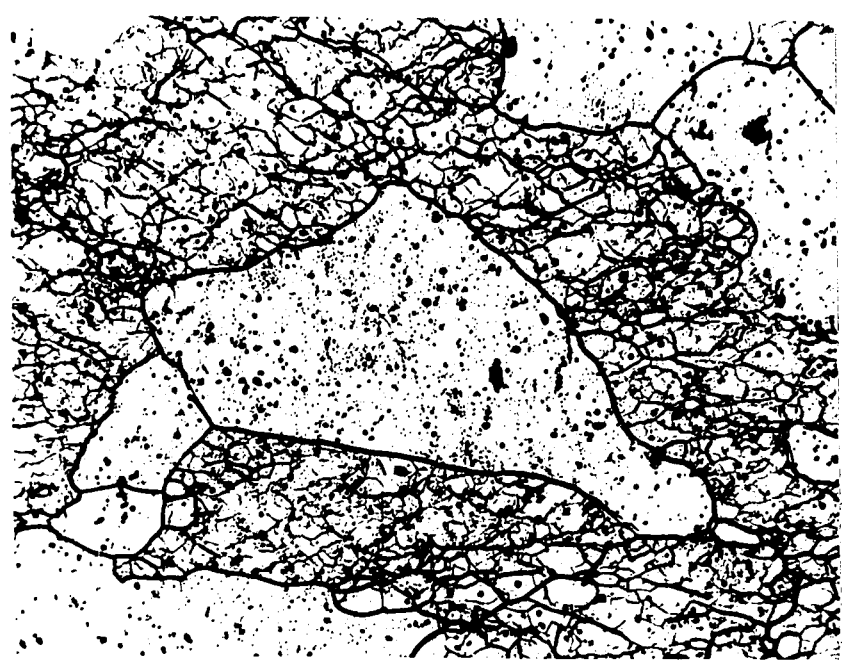


Fig. 74 - Silicon steel; 900° C; &= 0.48; &= 0.10/sec; delay 90 sec; EPE; 220 X.



Fig. 75 - Silicon steel; 900° C; & = 0.48; & = 0.19/sec; delay 5 sec; EPE; 585 X.

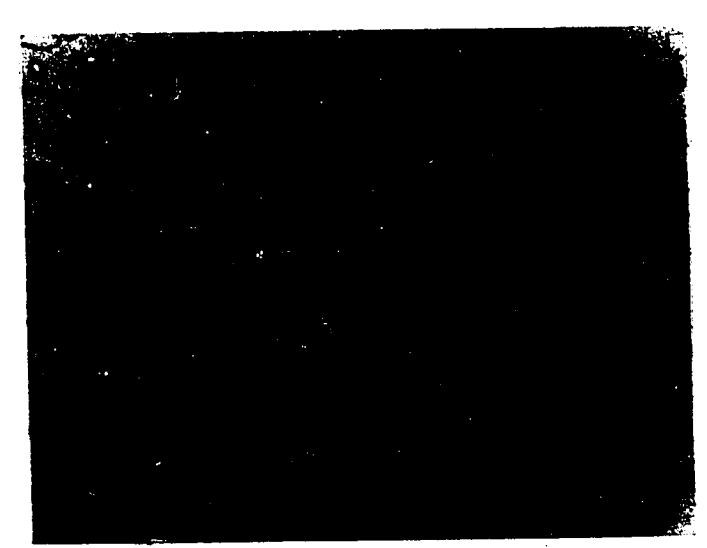


Fig. 76 - Silicon steel; 900° C; $\varepsilon = 0.48$; $\dot{\varepsilon} = 0.10/\text{sec}$; delay 90 sec; EPE; 585 X.



Fig. 75 - Silicon steel; 900° C; & = 0.48; $\dot{\mathcal{E}}$ = 0.19/sec; delay 5 sec; EPE; 585 X.



Fig. 76 - Silicon steel; 900° C; $\varepsilon = 0.48$; $\dot{\varepsilon} = 0.10/\text{sec}$; delay 90 sec; EPE; 585 X.

at higher magnifications the substructures presented in Figs. 73 and 74. The progress of substructural changes associated with static recovery after compression at 800°C, is represented in Figs. 77 to 80.

At the onset of recovery after hot working, the higher was the initial dislocation density, the larger was the driving force and the faster recovery progressed. The higher dislocation densities were produced at the higher steady-state flow stresses and the higher values of the ZENER-HOLLOMON parameter.

The disintegration of low-angle boundaries during static recovery after hot working is connected with dislocation rearrangement and results in an increase in the average subgrain size. This can be observed in the transmission electron micrographs in Figs. 81 to 86.

Evidence of coalescence during recovery can be seen in Fig. 82, where the disappearance of a sub-boundary probably led to the formation of the neck shown in the centre of the micrograph. Another neck in the process of forming can be seen in Fig. 83. Fig. 84 shows an example of another phenomenon observed in a number of samples after 30 or more seconds of delay before quenching. In this micrograph, general sub-boundary disintegration can be seen in progress over a fairly large area.

5.4.3 THE EFFECT OF ANNEALING TIME ON RECRYSTALLIZATION

The relative times of recrystallization in Armco iron and in silicon steel over a range of strains and holding temperatures can be seen in Figs. 87 and 88. The volume fraction recrystallized was determined by quantitative metallography, as described by HILLIARD and CAHN 117,118). The grid method of point counting 119) was applied for

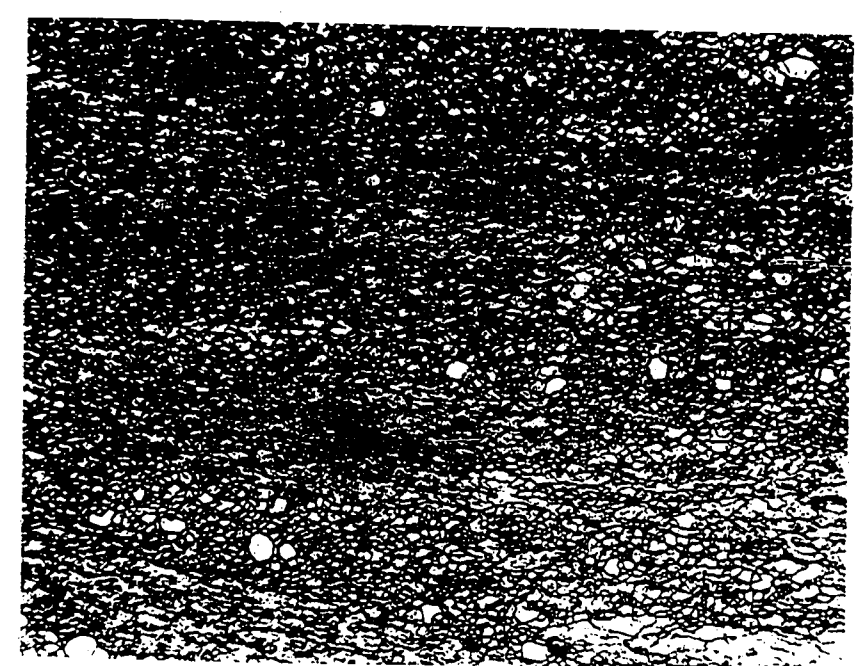


Fig. 77 - Silicon steel; 800° C; $\mathcal{E} = 1.75$; $\dot{\mathcal{E}} = 0.26/\text{sec}$; delay 18 sec; EPE; 220 X.



Fig. 78 - Silicon steel; 800°C; &= 1.75; &= 0.26/sec; delay 35 sec; EPE; 220 X.

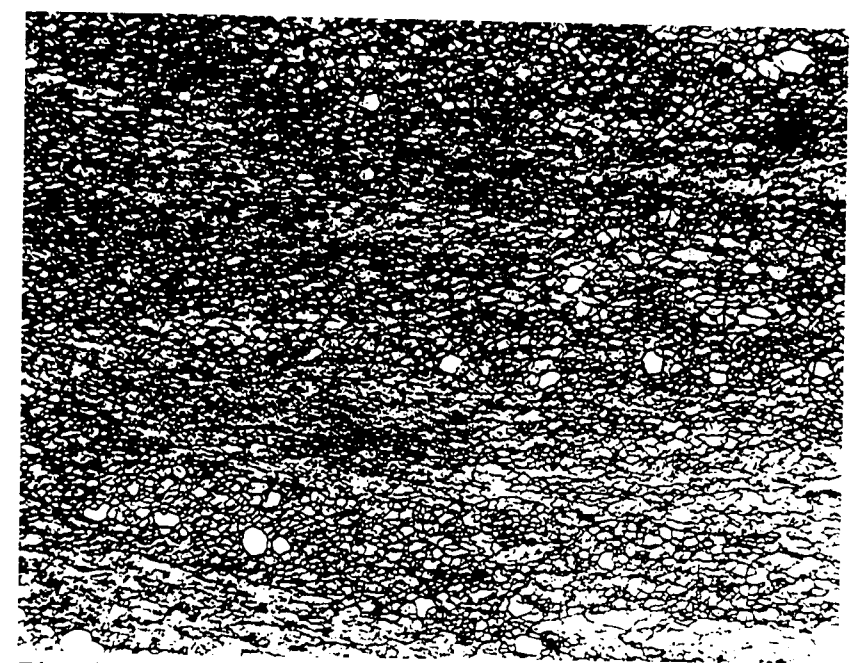


Fig. 77 - Silicon steel; 800° C; $\mathcal{E} = 1.75$; $\dot{\mathcal{E}} = 0.26/\text{sec}$; delay 18 sec; EPE; 220 X.



Fig. 78 - Silicon steel; 800° C; &= 1.75; &= 0.26/sec; delay 35 sec; EPE; 220 X.

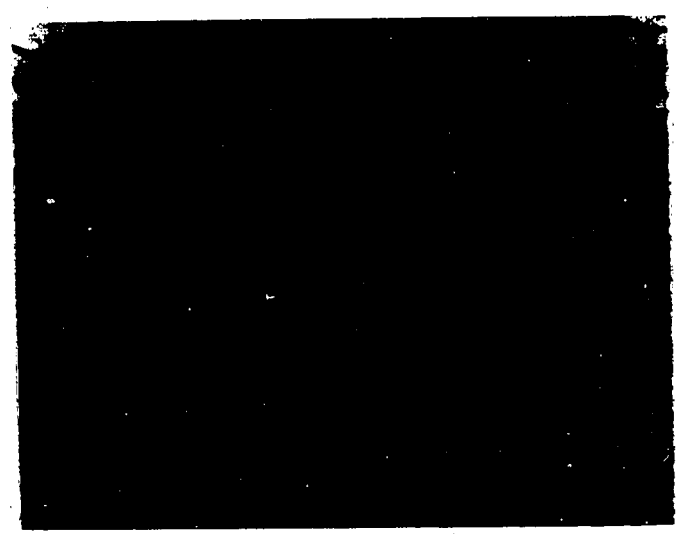


Fig. 79 - Silicon steel; 800° C; $\mathcal{E} = 1.92$; $\dot{\mathcal{E}} = 0.26/\text{sec}$; delay 13 sec; EPE; 585 X.

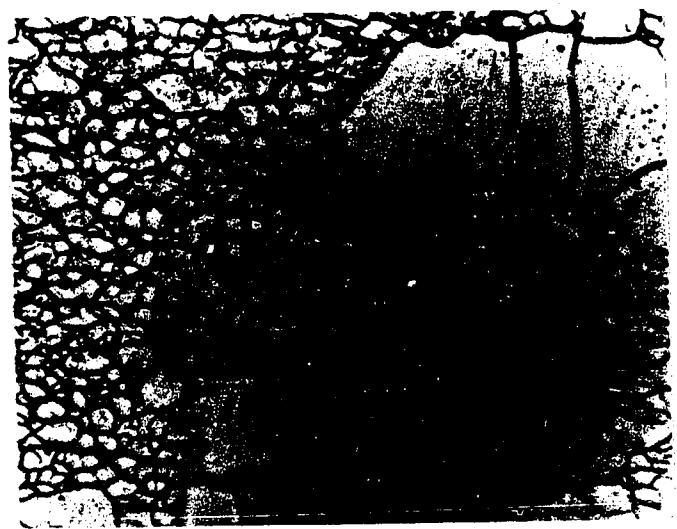


Fig. 80 - Silicon steel; 800° C; $\varepsilon = 1.75$; $\dot{\varepsilon} = 0.26/\text{sec}$; delay 35 sec; EPE; 585 X.

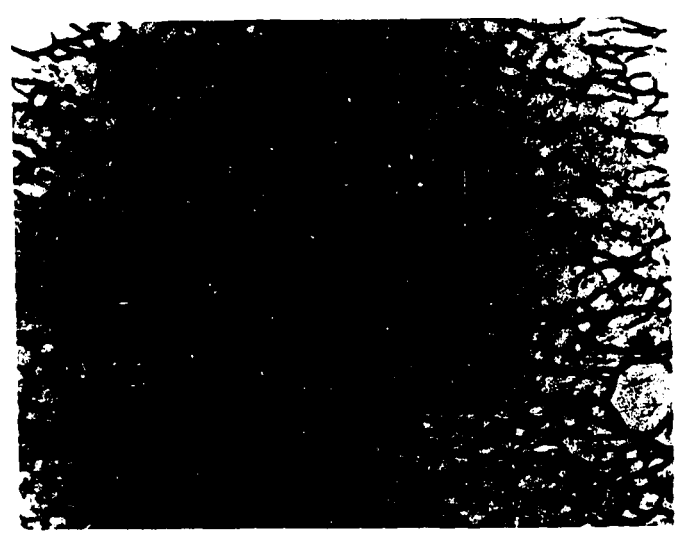


Fig. 79 - Silicon steel; 800° C; $\mathcal{E} = 1.92$; $\dot{\mathcal{E}} = 0.26/\text{sec}$; delay 13 sec; EPE; 585 X.

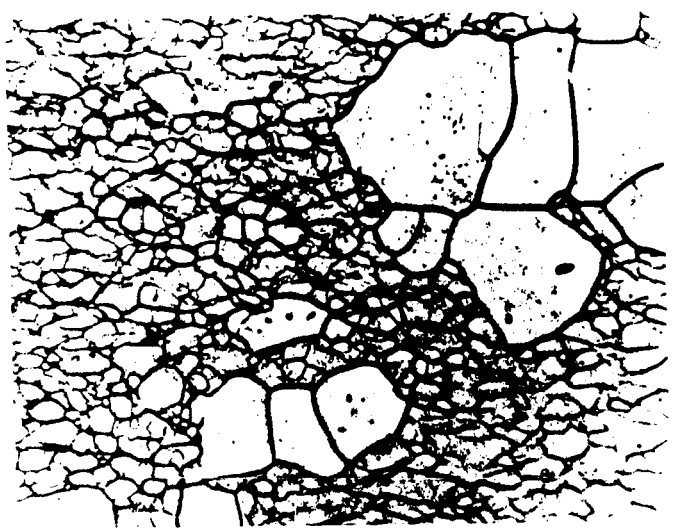


Fig. 80 - Silicon steel; 800° C; $\varepsilon = 1.75$; $\dot{\varepsilon} = 0.26/\text{sec}$; delay 35 sec; EPE; 585 X.



Fig. 81 - Silicon steel; 800°C; ε = 0.42; ε = 0.15/sec; delay 1 sec; ΤΕΜ; 11,400 X.



Fig. 82 - Silicon steel; 800° C; $\varepsilon = 0.60$; $\dot{\varepsilon} = 0.075/\text{sec}$; delay 5 sec; TEM; 11,400 X.



Fig. 81 - Silicon steel; 800° C; $\varepsilon = 0.42$; $\dot{\varepsilon} = 0.15/\text{sec}$; delay 1 sec; TEM; 11,400 X.

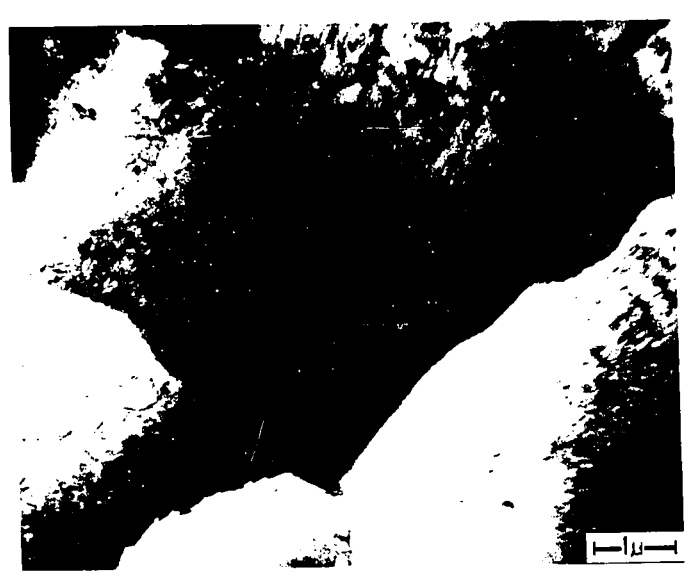


Fig. 82 - Silicon steel; 800° C; $\varepsilon = 0.60$; $\dot{\varepsilon} = 0.075/\text{sec}$; delay 5 sec; TEM; 11,400 X.



Fig. 83 - Silicon steel; 800° C; $\varepsilon = 0.60$; $\dot{\varepsilon} = 0.075/\text{sec}$; delay 35 sec; TEM; 11,400 X.



Fig. 83 - Silicon steel; 800° C; $\mathcal{E} = 0.60$; $\dot{\mathcal{E}} = 0.075/\text{sec}$; delay 35 sec; TEM; 11,400 X.



Fig. 84 - Silicon steel; 800° C; $\varepsilon = 0.76$; $\dot{\varepsilon} = 0.15/\text{sec}$; delay 40 sec; TEM; 2,850 X.



Fig. 85 - Silicon steel; 800° C; $\varepsilon = 0.76$; $\dot{\varepsilon} = 0.15/\text{sec}$; delay 40 sec; TEM; 11,400 X.

Fig. 84 - Silicon steel; 800° C; $\mathcal{E} = 0.76$; $\dot{\mathcal{E}} = 0.15/\text{sec}$; delay 40 sec; TEM; 2,850 X.



Fig. 85 - Silicon steel; 800° C; $\mathcal{E} = 0.76$; $\dot{\mathcal{E}} = 0.15/\text{sec}$; delay 40 sec; TEM; 11,400 X.

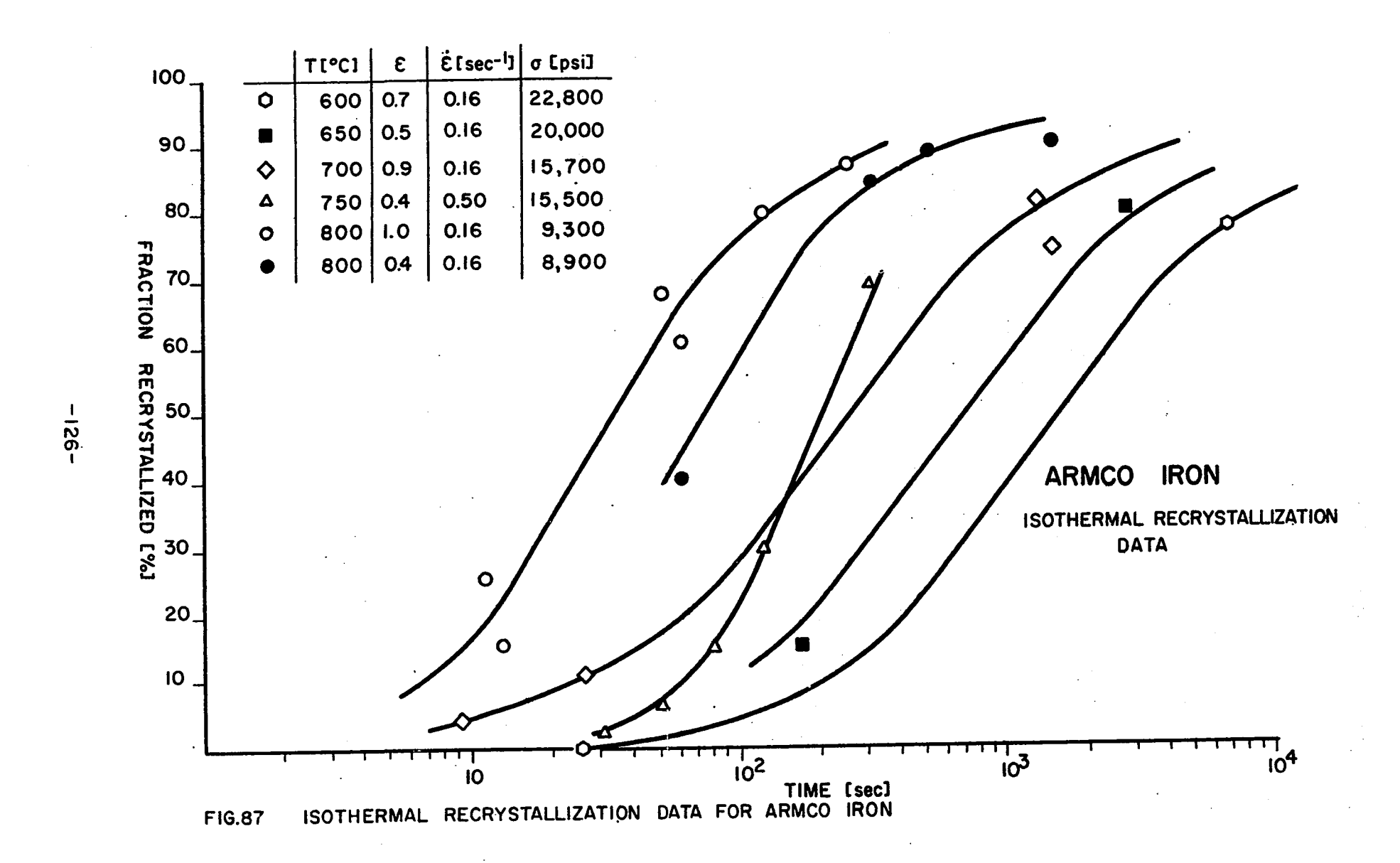


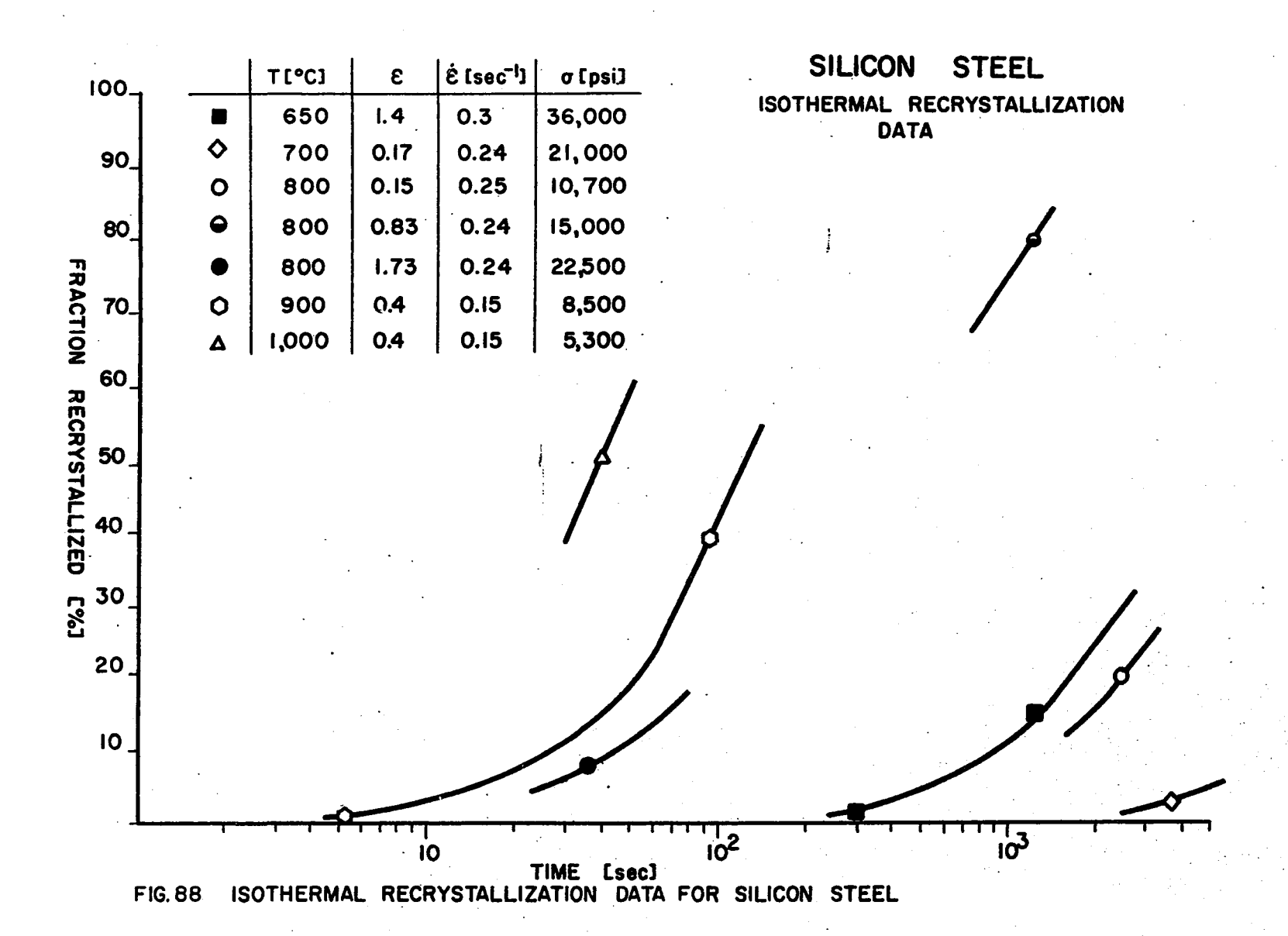
Fig. 86 - Silicon steel; 800° C; $\mathcal{E} = 0.76$; $\dot{\mathcal{E}} = 0.15/\text{sec}$; delay 40 sec; TEM; 28,600 X.



(

Fig. 86 - Silicon steel; 800° C; $\mathcal{E} = 0.76$; $\dot{\mathcal{E}} = 0.15/\text{sec}$; delay 40 sec; TEM; 28,600 X.





measurements on longitudinally sectioned specimens. The curves in the above-mentioned figures also show that at the same working and holding temperatures, recrystallization in Armco iron begins after shorter delays than in silicon steel. The curves are based on counts made on only 32 samples, and so they can only be used for an indication of the effect of temperature on recrystallization times.

Some examples of the metallographic evidence for recrystallization after hot compression are shown in Figs. 70,72-75, 77-80 and 89-91. Recrystallized grains were formed within a few seconds after the conclusion of the hot compression cycle, as can be seen in Fig. 73 at low magnifications, and in Fig. 75 at high magnifications. As the deformation temperature was decreased, the time lapse between the end of deformation and the onset of recrystallization increased. An indication of the effect of working temperature on the speed of recrystallization can be obtained from Figs. 89 to 91. Approximately the same fraction of recrystallized grains was produced by a time lapse of 10 minutes at 650°C as after 25 minutes after deformation at 560°C to the same strain.

5.5 MEAN SUBGRAIN SIZE AND MISORIENTATION

Mean_Subgrain Size. Variations in the subgrain sizes reported by different investigators for hot worked iron are considerable. Most of the values published, however, resulted from investigations carried out over a relatively narrow range of temperatures, strains and strain rates. A short survey of the previous work is given in Table VIII. As can be seen from these references, no systematic study of subgrain size and misorientation in iron or steel has yet been published.

The results obtained from the present investigation are listed

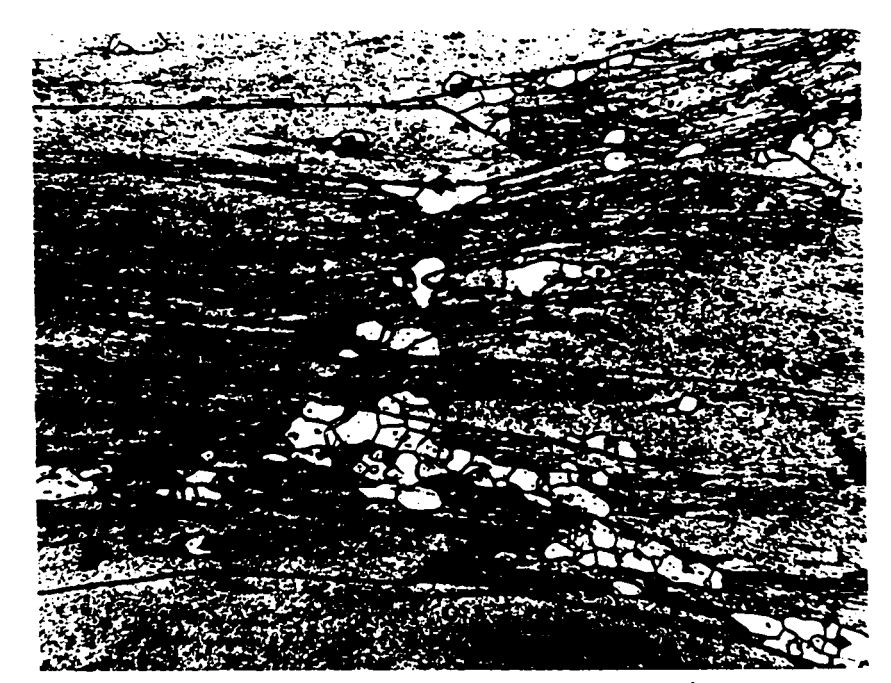


Fig. 89 - Silicon steel; 560°C; \mathcal{E} = 1.67; $\dot{\mathcal{E}}$ = 0.42/sec; delay 25 min; EPE; 220 X.



Fig. 90 - Silicon steel; 650°C; \mathcal{E} = 1.64; $\dot{\mathcal{E}}$ = 0.33/sec; delay 10 min; EPE; 220 X.



Fig. 89 - Silicon steel; 560°C; \mathcal{E} = 1.67; $\dot{\mathcal{E}}$ = 0.42/sec; delay 25 min; EPE; 220 X.

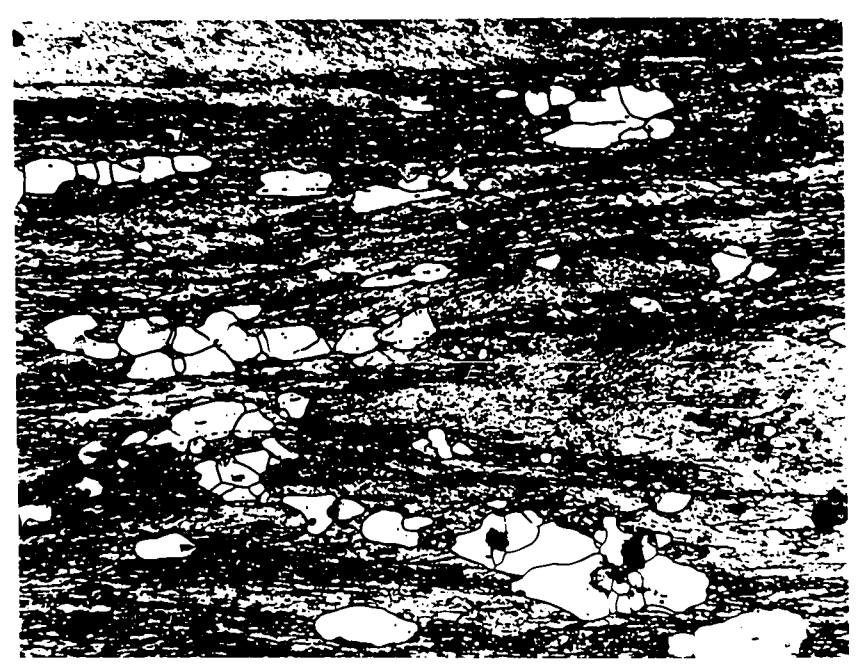


Fig. 90 - Silicon steel; 650°C; \mathcal{E} = 1.64; $\dot{\mathcal{E}}$ = 0.33/sec; delay 10 min; EPE; 220 X.

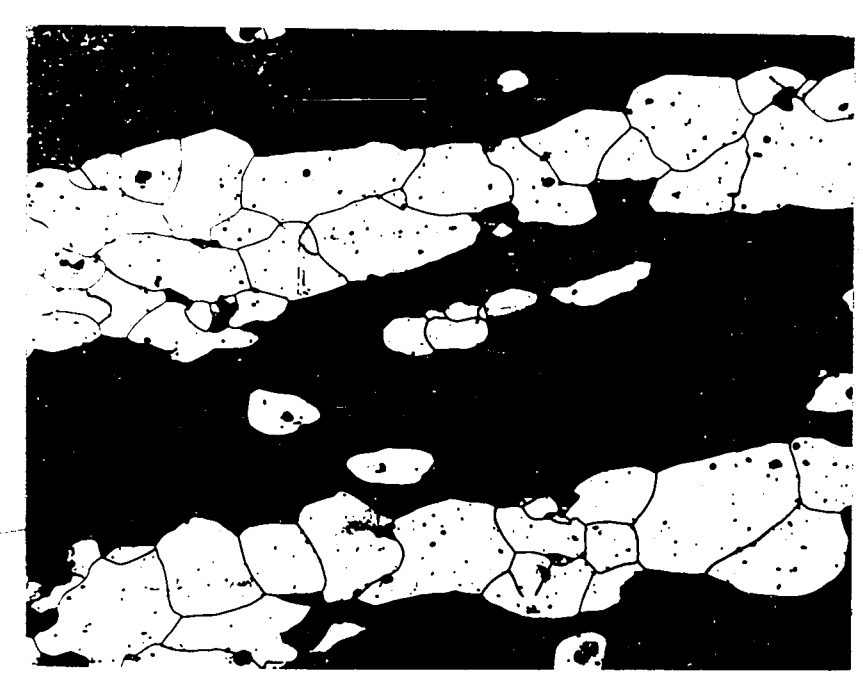


Fig. 91 - Silicon steel; 650° C; $\mathcal{E} = 1.29$; $\dot{\mathcal{E}} = 0.26/\text{sec}$; delay 25 min; EPE; 220 X.

 \bigcirc

Fig. 91 - Silicon steel; 650° C; $\mathcal{E} = 1.29$; $\dot{\mathcal{E}} = 0.26/\text{sec}$; delay 25 min; EPE; 220 X.

Table VIII. Subgrain Sizes Determined in Iron Deformed at High Temperatures

I NVESTI GATOR	MATERI AL	MODE OF HOT DEFORMATION	T [°c]	ε	<i>Ė</i> [sec ⁻¹]	DELAY [sec]	METHOD OF DE- TERMINATION OF "d"	MEAN "d" [んし]	MISORIENT- ATION Θ°
BALL ¹²⁵)	Iron 99.97%	Tension	-77 to + 500	to 0.28	4x 10 ⁻⁵	43,200	X-Ray	1.2 to 2.9	6° to 22°
REYNOLDS and TEGART ¹⁷)	Iron High Purity	Torsion	750 813 856	to frac- ture	4.6x 10 ⁻¹	1 to 15	Optical	1 to 2 2 to 5 5 to 10	Not given
CRUSSARD and TAMHANKAR ¹²)	Armco 99.96%	Tension and Creep	550 to 750	to frac- ture	4x 10 ⁻¹ to 4	Not given	X-Ray	Not given	6° to 15°
KEH and WEISSMANN ⁶¹)	Iron % not given	Tension and Creep	200 500		Not g	iven	2.0 4.0	Not given	
HIRANO, COHEN, AVERBACH and UJIIYE ¹⁴)	Iron 99.97%	Compression and Creep	742 to 885	0.2	to 2x 10-3	Not given	TEM	10.0	Not given
BARRETT, NIX and SHERBY 13)	3% Si iron	Creep	643	to 0.2	8.3x 10 ⁻⁶	Not given	TEM	2.0 18.0	Not given
GAROFALO, ZWELL, KEH and WEISSMANN ¹⁵)	Iron 50 ppm impuri- ties	Greep	600	0.22	Not given	Not given	X-Ray TEM	12.0 5.0	24 min of arc 15 min of arc

in Table IX for Armco iron and in Table X for silicon steel. Given in these tables are the values of the average subgrain "diameter" (d), as determined by optical microscopy, using both the comparison and the planimetric procedures, and by transmission electron microscopy. From the data in the two tables it can be seen that the optical observations of substructure lead to somewhat smaller (d) values than transmission electron microscopic observations in specimens which have been deformed at the higher stresses. Conversely, in specimens deformed at the lower stresses, optical microscopy leads to somewhat larger values of subgrain size than transmission electron microscopy. The scatter of the values obtained from optical examination is also considerably higher than that of the transmission electron microscopy values and so the optical results seem to be less reliable.

Subgrain Misorientation. Evaluation of the diffraction patterns gave information about the stability of misorientation with strain and with changes in strain rate and temperature in the steady-state region. The values shown in Tables IX and X were obtained by measuring only one component of misorientation, as already mentioned in section 4.5. This component represented the rotation about an axis parallel to the beam and the average component resulting from the measurements was estimated to be of the same order as the average component normal to the axis of the beam. It can be seen from Tables IX and X that, over the ranges investigated, the average misorientations do not change significantly with temperature, strain or strain rate, and remain of the order of a few degrees for both materials tested.

Table IX. Experimental Mean Subgrain Size and Misorientation (Armco iron)

T	ε	έ	DELAY	MI CRO-	log Z	6	MEASUR	MEASURED VALUES "d"			MISORIENT	ATI ON
				HARD-	_		TEM			Θ _{max} .	Θ _{avg.}	$\theta_{ ext{experimental}}$
			}	NESS				COUNTING				CAPCIZMENCUL
[°c]		[sec ⁻¹]	[sec]	[DPH]*)	**)	[ksi]	[m]	[m]	METRIC [~]	[Deg	rees]	·
600	0.6	0.16	5	(152)	15.7	-	2.7	-	-	4.0	3.5	4 - 3
600	0.6	0.16	10	(151)	15.7	22.70	3.0	-	-	3.0	3.0	3 - 3
600	0.6	0.16	10	155	15.7	-	-	2.8	2.5	-	- '	-
600	0.6	0.16	300	148		-	2.9	-	-	3.0		-
600	0.9	0.25	10	146	15.9	24.00	2.8	- .	-	4.5	4.5	42 - 42
600	0.9	0.075	25	(151)	-	-	-	3.0	2.5	-	-	-
600	1.1	0.16	1,500	(135)	-	-		3.5	2.5	-	-	1.
600	1.3	0.16	13	(158)		24.00	2.7	3.5	2.5	7.0	6.8	7-7-6월
650	0.6	0.13	1	149	14.7	19.85	3.1	_	-	3.0	2.5	2-2½-3
700	0.7	0.16	5	138	14.0	15.70	3.4	-	-	2.5	2.5	2월 - 2월
700	0.9	0.16	10	140	14.0	-	-	4.4	4.0	-	-	- '
700	0.9	0.075	10	(138)	13.7	14.78	3.4	4.3	5.6	-		<u>-</u>
700	1.5	0.23	5	154	-	17.00	3.2	-	-	4.0	4.0	4
700	1.5	0.27	15	153	-	-	-	9.1	5.0	-	-	-
700	1.5	0.12	25	148		-	-	6.7	4.7	-	-	-
750	0.5	0.25	1	129	13.5	14.20	3.9	6.7	6.7	2.2	2.2	2.2 - 2.2
750	0.6	0.40	1	(130)	13.7	-	-	3.6	3.3	-	-	-
750	0.7	0.25	1	(130)	13.5	-	· -	7.9	-	-	-	-
750	0.7	0.075	50	(126)		-		5.6	5.6	-	-	-
800	0.4	0.20	1	120	12.8	9.35	4.2	-	-	_	-	-
800	0.4	0.31	1	(120)	12.9	-	3.9	6.3	5.6	5.0	4.8	4-4-4½-5-5-5
800	0.6	0.075	15	(118)	-	-	-	5.8	6.7	-	-	-
800	0.6	0.13	1	122	12.6	-	4.3	6.4	5.6	3.0	3.0	3 - 3 - 3
800	0.6	0.12	<u>15</u>	117	-		<u>-</u> -	6.5	5.6		-	_

^{*)} Values in parentheses were taken from interpolations in Fig. 68.

^{**)} Values of log Z are given only for delay times up to 10 sec at 600° to 750°C, and for delay times up to 1 sec at 800° to 1,000°C.

Table X. Experimental Mean Subgrain Size and Misorientation (Silicon steel)

Т	ε	έ	DELAY	MICRO-	log Z	િ		MEASURED VALUES "d"			MI SORI ENTATI ON		
		 		HARD- NESS] . i}		TEM	OPTICAL COUNTING	LLY PLANI-	w _{max} .	Θ _{avg} .	[©] experimental	
[°c]		[sec ⁻¹]	[sec]	[DPH]*)	**)	[ksi]	[m]	[m]	METRIC [[]	[Deg	rees]		
650	0.5	0.09	2	228	17.9	25.80	3.1	-	-	2.0	1.8	2-1.8-1½	
650	1.3	0.25	5	225	-	-	-	2.9	2.5	-	-	-	
650	1.3	0.09	25	(227)	-	-	-	2.7	2.5	-	-	-	
650	1.3	0.25	1,200	(193)	-	-	-	3.6	4.0		-	-	
650	1.6	0.50	5	(236)	-	-	2.2	3.0	2.5	4.0	-	-	
650	1.6	0.25	10	(235)	-	-	-	3.2	2.8	-	-	-	
650	1.6	0.25	300	212		-		3.6	4.0		<u> </u>		
750	0.4	0.06	1	(220)	15.8	14.80	4.2	-	-	-	-	-	
750	0.4	0.25	2	221	16.5	19.00	4.0	-	-	-	-	-	
750	0.6	0.05	1	216	15.8	-	-	3.9	4.0	-	-	-	
750	0.7	0.075	2	219	16	16.75	4.0	4.0	4.0	2.0	2.0	2 - 2	
750	1.8	0.25_	10	216	-	20.70	3.3	3.4	3.0	-		-	
800	0.4	0.15	1	214	15.4	14.35	4.2	5.6	5.6	4.0	2.2	1½-2-2-4	
800	0.6	0.20	1	216	15.6	14.50	4.7	-	-	~	-	-	
800	0.6	0.075	35	205	-	-	5.0	-	-	3.5	-	-	
800	0.8	0.15	10	(211)		-	-	5.1	4.0	-	-	. -	
800	0.8	0.15	40	205	-	- .]	5.9	-	-	3.5	-	· -	
800	1.4	0.075	1	(213)	15.2	[-]	-	4.8	4.7	-	-	-	
800	1.5	0.25	15	(210)	_	-	-	4.9	5.0	-	-	-	
800	1.9	0.15	13	211	-	18.60	3.8	5.6	5.6	3.5	3.5	3½- 3½- 3½	
800	1.8	0.25	18	(210)			-	5.1	5.0	-	-		

continued

Table X. (continued)

T	3	Ė	DELAY	MICRO-	log Z	6		RED VALUES			I SORI ENT	
				HARD- NESS			TEM	OPTICAL COUNTING	PLANI -	O _{max.}	Θ _{avg.}	$\Theta_{ ext{experimental}}$
[°c]		[sec ⁻¹]	[sec]	[DPH]*)	**)	[ksi]	[<i>m</i>]		METRIC [ル]		rees]	
900	0.23	0.10	1	(203)	13.9	_	-	7.9	8.0	-	-	-
900	0.3	0.20	1	204	14.2	9.07	6.0	7.7	6.7	2.8	2.2	15-2-2-25-2.8
900	0.3	0.17	5	(202)	-	-	-	9.0	7.9	-	-	-
900	0.5	0.24	1	201	14.3	9.50	6.3	10.0	7.9	3.2	2.4	2-2-3.2
900	0.5	0.20	5	199	-	-	-	8.8	6.7	-	-	-
900	0.5	0.10	90	192	-	-	-	11.2	14.4	-] -	.
900	0.6	0.06	1.	203	13.7	7.75	7.1	11.7	7.9	-	-	-
900	0.6	0.10	11	202	13.9	8.00	6.0		<u>- </u>	3.8	3.8	3.8
1,000	0.3	0.05	1	187	12.4	4.62	8.9	12.5	11.2	4.0	2.6	2-2-2.8-4
1,000	0.3	0.15	1	194	12.9	5.30	8.2	15.9	15.7	-	_	-
1,000	0.4	0.06	1	192	12.5	-	-	15.4	11.2	-	-	-
1,000	0.4	0.15	1	192	12.9	5.30	8.1	-	-	-	-	-
1,000	0.5	0.15	1	196	12.9	5.30	8.7	15.3	11.2	, -	-	-
1,000	0.5	0.10	1	187	12.7	4.60	8.7	-	-	3.0	2.5	2-2½-3
	0.6	0.15	40	183	_		-	18.3	18.9	-	-	•

^{*,**)} See Table IX above.

5.6 MICROHARDNESS RESULTS

The hardening of metals during deformation at elevated temperatures is very difficult to determine. Hardness values of undeformed Armco iron have been measured and recorded 120) at temperatures ranging from 0 to $900^{\circ}\mathrm{C}$, with particular attention being paid to the hardness changes associated with the phase transformation. It is much more difficult, however, to perform hot hardness tests during deformation, and the hot hardness after deformation would be in error due to the occurrence of recovery. More commonly, hardness is measured at room temperature, and this method is used to evaluate the hardening of metals by cold deformation, or the softening associated with recovery. Similarly, the amount of work-hardening in hot deformed material can be evaluated by the increase in the room temperature hardness, measured before and after hot deformation. These results can be quoted in terms of the "residual hardness percent" $^{75)}$, which is the hardness increment due to hot deformation, expressed as a percentage of the hardness increment which would be obtained on cold deformation to the same strain.

The microhardness values determined in this investigation were measured at room temperature, following quenching from the working temperature. The results are given in Fig. 68.

5.6.1 MICROHARDNESS DEPENDENCE ON SUBGRAIN SIZE

The dependence of the yield strength on grain size is given by the well-known equation proposed by ${\rm HALL}^{121}$ and ${\rm PETCH}^{122}$) and discussed by others 123,124). Recent investigations of substructural strengthening 59) have revealed that the flow stress can also be expressed as a linear

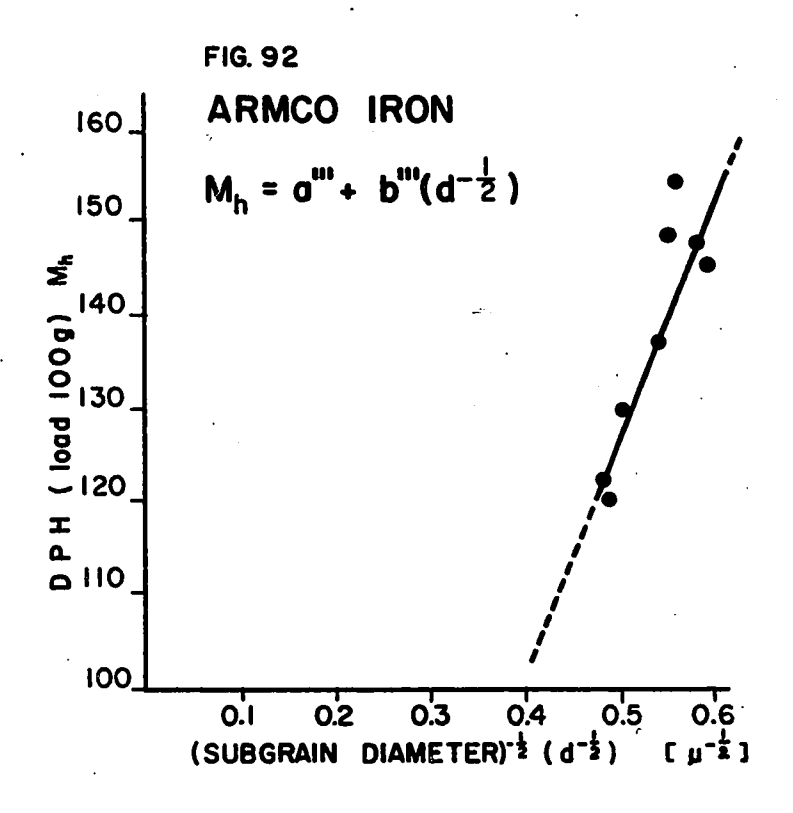
function of the square root of the <u>subgrain</u> size. This relationship seems to hold for a wide range of ferrous cold-drawn materials. Accordingly, the dependence of the hot-worked microhardness on subgrain size was investigated, with the following results.

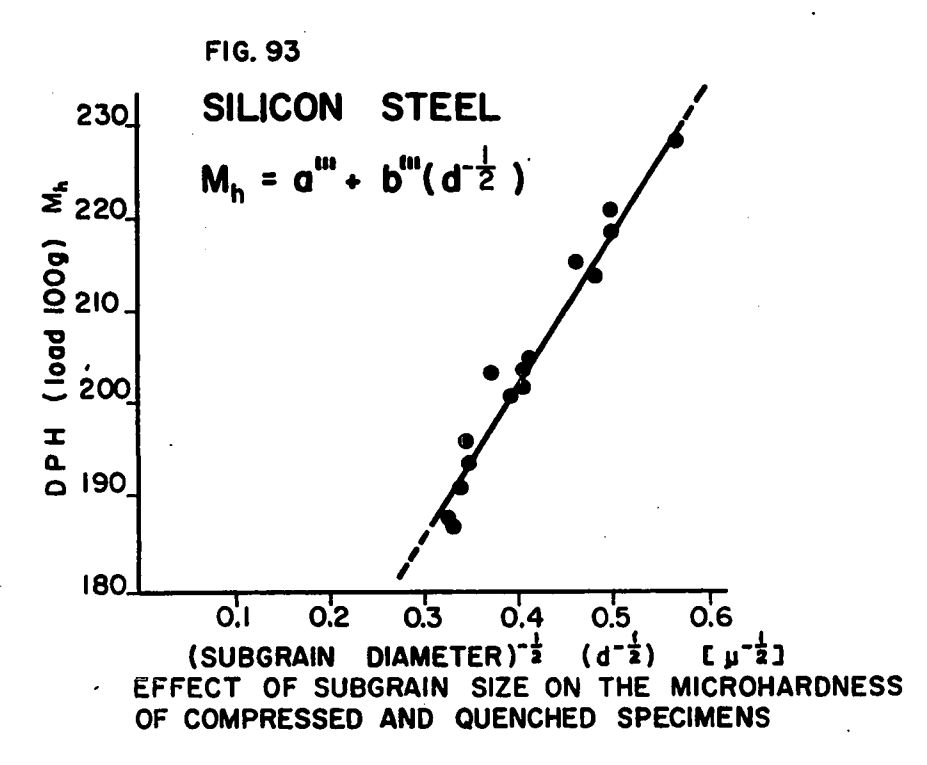
It can be seen from Figs. 92 and 93, in which the micro-hardness is plotted against the square root of the subgrain "diameter", that a straight line fit is obtained, with some experimental scatter.

A relationship of the HALL-PETCH type is thus satisfied and the micro-hardness (M_D) can be expressed by the following equation:

$$M_h = a''' + b''' (a^{-\frac{1}{2}})$$
 (23)

where: d = the average subgrain "diameter";
a''',b''' = constants.





6. DISCUSSION

6.1 TRUE STRESS-TRUE STRAIN CURVES

In the paragraphs which follow, the main features of the true stress-true strain curves obtained by hot compression will be discussed. The curves were drawn after correction of the raw data for friction and for the temperature increase due to compression, and represent flow curves for homogeneous, isothermal deformation. The corrected curves generally exhibit two stages: the transient, and the steady-state stage. The former region is represented by the rising part of the stress-strain curve, the latter by the horizontal part.

The initial slope of the curves indicates Transient Region. the rate of work hardening at the beginning of deformation. The slope becomes steeper as the temperature of deformation is decreased and as the strain rate is increased. With increasing strain the slope decreases, gradually becoming zero as steady-state compression sets in. It should be noted that no pronounced stress peaks are evident between the transient and steady-state regions, such as are observed on hot torsion stressstrain curves. The present curves, and those for the hot compression of low carbon 4) and medium carbon steels 4,30) at similar strain rates and temperatures, are alike in this respect. However, some of these curves presented in the above-mentioned references do exhibit just perceptible stress peaks at the higher temperatures and at very low strain rates. This feature suggests the occurrence of dynamic recrystallization during compression under these conditions, whereas the smoothly progressing curves represent deformation involving dynamic recovery alone.

Steady-State Region. As soon as an equilibrium between the rates of work hardening and of dynamic recovery is established, the flow stress remains constant with further increase in strain. The present data show that the lower limit of strain at which the steady-state region is established does not vary appreciably with temperature. In both materials investigated, steady-state compression sets in at true strains ranging from $\mathcal{E}=0.3$ to $\mathcal{E}=0.6$, depending on the strain rate. The steady-state is established earlier at lower than at higher strain rates. The present results indicate that, whilst temperature has a small effect on the onset of the steady-state, the influence of strain rate is substantial. This is only in partial agreement with $STUWE^{62}$, who considered that neither the strain rate nor the temperature has much effect on the strain coordinate of this point.

Under the same conditions of strain rate and temperature, the stress required for the steady-state compression of 2.8% silicon steel is substantially higher than that for Armco iron. The effect of an addition of 0.26% Mn to Armco iron on the steady-state flow stress, especially at higher temperatures, is, however, negligible (compare Fig. 15b and 18b). These seemingly contradictory results can be explained as follows. The addition of 2.8% Si to iron results in a 5.47 atomic percent alloy. Thus the flow stress increase observed can simply be attributed to solid solution strengthening, which is apparently fairly marked, even at 800°C. The addition of 0.26% Mn represents an atomic proportion of 0.267 a/6. This is probably too small an addition to be detected by the present technique.

On some of the corrected curves, the stress does not remain

constant with strain, but increases after a strain of about 0.8. This could be due to the following causes:

- (a) The presence of more friction than allowed for in the calculations. The rise in stress could be due to the large increase in the contact area between the anvil and the specimen at higher strains, leading to lubrication break-down. This hypothesis is supported by the observation that steady-state deformation ends at approximately the same strains as those at which barreling becomes pronounced.
- (b) The disruption of steady-state straining by an irreversible microstructural change. The rise in the flow stress could, for example, be due to the development of a preferred orientation. In the absence of recrystallization, a pronounced hot worked texture could lead to a restriction in the combinations of slip systems available to the deformation.

It should also be noted that, at the lower temperatures and higher strain rates, some of the true stress-true strain curves never attain a steady state, but continue to show work hardening. Such a continuous increase in flow stress can be seen in silicon steel at 650°C and a strain rate of 0.5/sec (Fig. 19b), and also in Armco iron at 800°C and a strain rate of 0.9/sec (Fig. 18b). This observation could be due to the abovementioned strain rates being too high to permit the establishment of steady-state compression at the strains attained. In addition the apparent work hardening could also be caused by a malfunction of the constant strain rate controller. A continuous increase in flow stress would, in this case, be associated with increasing, instead of constant, true strain rates.

6.2 MATERIAL CONSTANTS AND ACTIVATION ENERGIES FOR HOT COMPRESSION

The flow stress, strain rate and temperature data obtained from the corrected true stress-true strain curves were correlated using equation (17), and the values of the material constants were determined. The hyperbolic sine equation was found to be valid over the full range of experimental temperatures and strain rates.

In previous work, hot torsion data for carbon steels in the \(\mathbb{r}\)-region \(\frac{19}{2} \), and for austenitic chrome-nickel steels \(\frac{20}{2} \) were expressed and correlated in terms of this equation \(\frac{85}{2} \). Recently hot extrusion data for commercially pure aluminum \(\frac{86}{2} \) were found to fit the above relationship as well. It can therefore be concluded that strain rates can be correlated with flow stresses over a wide range of hot working temperatures by the use of the (sinh) relationship.

The above-mentioned equation involves four material constants (A, \mathcal{L}, n') and ΔH , which characterize the process of hot compression. The determination of these constants has already been described in section 5.2 and the values obtained will now be discussed.

Constants (A, n' and ∞). The constant (A) depends on impurity content and has a value about two orders of magnitude higher for 2.8% silicon steel than for Armco iron (Table VII). The values of the material constants (n') and (∞) determined in the present investigation do not differ substantially from those reported previously for other iron-based materials deformed by torsion in the austenitic region (Table XI). No comparable values of the material constants have been uncovered either for silicon steel, or for Armco iron deformed in the ferritic region.

Table XI. Experimental Values of the Material Constants \mathscr{L}_{p} , \mathscr{L} , and n'

		MODE OF				
MATERIAL	PHASE STUDIED	HOT WORKI NG	\mathcal{L}_{r} [kg.cm] ⁻¹	& [psi] ⁻¹	n'	REFERENCE
Soft iron	r	Torsion	0.050	*) _{1.075x10} -4	4.70	85
0.25% C steel	r	Torsion	0.050	*) _{1.075x10} -4	4.60	85
0.85% C stee1) }	Torsion	0.057	*) _{1.220x10} -4	4.55	85
1.20% C stee1	r	Torsion	0.058	*) _{1.250x10} -4	4.55	85
18%Cr 8%Ni steel) r	Torsion	0.042	*)9.050x10 ⁻⁵	4.30	85
25% Cr steel	«	Torsion	0.070	*) _{1.50 ×10} -4	3.45	85
Armco iron	£	Compression	-	1.17 x10 ⁻⁴	4.60	Present
2.8% Si steel	&	Compression		1.15 x10 ⁻⁴	4.30	investi- gation

These values of (\mathscr{L}) were calculated from the reported values of (\mathscr{L}_p) by the present author.

Activation Energies. Most of the data reported to date concerning steel activation energies apply to deformation in the austenitic region, as shown in Table XII. On examination of the differences shown in the table, SELIARS and TEGART⁸⁵⁾ suggested that the higher activation energies were probably connected with recrystallization. This explanation is reasonable, since activation energies for the recrystallization of zone-melted iron are reported to range up to 88 kcal/mole¹⁰⁹⁾. The creep activation energies in the γ -region reported in Table XII do not differ substantially from those for hot torsion, but are lower than those for creep in the α -region.

In the creep of non-ferrous metals, e.g. cadmium 129), aluminum 129) and tantalum 11), most investigators have concluded that the activation energy is approximately that of self-diffusion. This conclusion was extended to the hot torsion of austenitic steels 12) and to the creep of ferritic steels 5,7). It is commonly believed that the diffusion rates in the ferromagnetic range are lower than those estimated from the extrapolation of data determined in the paramagnetic temperature range 131,132,141,142). Hence the activation energy for self-diffusion is higher in the ferromagnetic region, as has been shown in a number of recent investigations 131,141,142). Furthermore, ISHIDA et al⁵⁾ found that over the Curie transformation range (775 to 1,045°K), the activation energy increases abruptly with decreasing temperature and decreases again below the Curie temperature.

In order for a comparison to be made between deformation and self-diffusion activation energies, a comprehensive review of published values of the latter is presented in Table XIII. The self-diffusion

Table XII. Activation Energies for the Hot Deformation of Various Steels

				·		
MATERIAL	PHASE STUDI ED	MODE OF HOT WORKING	ACTIVATION ENERGY FOR CREEP [kcal/mole]	ACTIVATION ENERGY FOR HOT WORKING [kcal/mole]		
Soft iron (0.05% C)	Y	Torsion	61. 2 ^{#)} .	67.0 ⁸⁵⁾ 64.0 ¹⁹⁾ 77.0 ²⁰⁾		
0.25% C stee1	y	Torsion	73.6 ^{#)}	72.5 ⁸⁵⁾ 69.0 ¹⁹⁾ 82.0 ²⁰⁾		
0.79% C steel	y	-	102.6 ^{#)}	-		
0.85% C steel	r	Torsion	-	81.0 ⁸⁵⁾ 78.0 ¹⁹⁾ 97.0 ²⁰⁾		
1.20% C steel	y	Torsion	61.4 ^{#)}	93.0 ⁸⁵⁾ 91.0 ¹⁹⁾ 110.0 ²⁰⁾		
18%Cr 8%Ni steel	y	Torsion	75.0 ⁸⁵⁾	99.0 ⁸⁵⁾ 84.0 ¹⁹⁾ 97.0 ²⁰⁾		
25% Cr steel	£	Torsion	-	85.0 ⁸⁵⁾ 73.0 ¹⁹⁾ 79.0 ²⁰⁾		
Armco iron	L	-	*) _{78.0} 7)	-		
36%Ni 10%Cr steel	y	Torsion	67 to 73.0 ¹²⁾	84.0 ¹²⁾		
Armco iron	y	Torsion	-	65.0 ¹²⁾		
Armco iron	L	-	*) ₈₉ to 93 ¹²⁾	•		
Iron (composition not given)	L	-	68 to 78 ⁹¹⁾			
Armco iron	L	Compression	•	66.0 (Present work)		
2.8% Si steel	L	Compression	-	80.0 (Present work)		

^{#)} These data were calculated or collected by SELLARS and TEGART 85) from references 9 and 19.

^{*)} For temperatures below 0.5Tm.

Table XIII. Activation Energies for Self-Diffusion in Various Irons and Steels

		•	_	
MATERIAL	PHASE STUDIED	TEMPERATURE RANGE [°C]	ACTIVATION ENERGY FOR SELF-DIFFUSION (kcal/mole)	REFERENCE
Soft iron	r	970 - 1,357	74.2	Data
Soft iron	y	1,064 - 1,393	67.9	collected
Soft iron	<i>y</i> -	1,064 - 1,393	64.5	by ¹³¹⁾
Soft iron	2+3	720 - 900	73.2	"
Soft iron	/3	809 - 905	59.7	lı lı
Soft iron	2+3	650 - 850	67.1	11
Soft iron	L+B	775 - 892	64.1	ff 、
Soft iron	ß	796 - 895	67.2	11
Soft iron	ß	809 - 905	57.2	11
Soft iron	y	1,063 - 1,393	64.5	Investigated
Soft iron	ß	809 - 905	57.2	by ¹³¹)
Soft iron	£	700 - 750	60.0	11
3.8% Si steel	æ	1,050 - 1,350	52.3-53.5	130)

activation energy for 3.8% silicon steel 130) quoted in this table is surprisingly low, which may be ascribed to the different methods used by the authors for the determination of their data. For the silicon steel work, YOUNG and MYKURA 130) used a mass transfer method, whereas in their iron investigations, BUFFINGTON et al 131) applied tracer techniques. The activation energy for self-diffusion in silicon steel could therefore be higher than that shown in Table XIII.

The activation energy of 66 kcal/mole for Armco iron determined in the present work is in the range of self-diffusion activation energies shown in Table XIII. It is also very close to the values published for the hot torsion of low carbon steel in the y-range 12,19,85), as shown in Table XII. The position of the lowest point off the fitted line at the bottom of the graph in Fig. 28 suggests a slight change in the Armco iron activation energy at 800°C. This is thought to be associated with the transition into the paramagnetic state, and is in agreement with the above-mentioned investigations concerned with changes in self-diffusion behavior during the phase transformations in from.

No data were uncovered with which to compare the activation energy resulting from the hot compression of silicon steel. ROSSARD²⁰⁾, and ROSSARD and BLAIN¹⁹⁾, however, concluded that the 4% silicon steel they used exhibited a hot working behavior similar to that of 25% Cr steel, which implies similar activation energies for both materials. They also reported that the hot torsion activation energy for their 25% Cr ferritic steel ranged from about 70 kcal/mole to 79 kcal/mole. SELLARS and TEGART⁸⁵⁾ calculated the activation energy for 25% Cr steel using ROSSARD's experimental data and found it to be as high as 85 kcal/mole.

The present investigation gave a value of 80 kcal/mole for the activation energy of hot compression of 2.8% silicon steel. It was also observed that the hot working behavior of ROSSARD's 4% silicon steel was similar to that of the present steel. This is demonstrated in Fig. 27, in which can be seen the excellent fit of the hot torsion data for the 4% silicon steel with the family of lines representing the present results. The data of ROSSARD and BLAIN were obtained from hot torsion tests 19 , and the hot torsion torques and angular velocities were converted into equivalent uniaxial stresses and strain rates, and evaluated by the application of the material constant (\mathcal{L}) obtained for the 2.8% silicon steel used in these experiments. The value of the activation energy calculated from the present data is thus comparable with the activation energy for 25% Cr ferritic steels. It also agrees with the activation energy for creep of 2.42% silicon iron, which was found to be 81.5 kcal/mole 142 .

The position of the last experimental point above the fitted line in Fig. 29 suggests a slight increase in activation energy with decreasing temperature in silicon steel. This is unlikely and would contradict the general observation (133) that the activation energy remains constant or increases with temperature. This discrepancy, which has also been discussed in a previous investigation (86), is probably associated with the increased friction due to lubrication break-down at high strains, as already discussed in section 6.1.

6.3 SUBSTRUCTURE FORMATION DURING HIGH TEMPERATURE COMPRESSION

So far little attention has been paid to the substructural changes during the hot working of steel in the ferritic region. Most

of the previous investigators have been concerned with creep behavior 12,13,15,16), although some work has been done in hot torsion 17,18,21) and hot tension 125). Three general types of substructural configurations have been observed:

- (a) banded dislocation substructures,
- (b) polygonized tilt boundaries perpendicular to the active slip planes,
- (c) equiaxed substructures.

In the present investigation it was observed that, during hot compression, a cell structure begins to form at small plastic strains.

The cell walls consist of complex dislocation networks which are not in general simple tilt or twist boundaries. Straining at higher temperatures leads to larger and more perfectly formed subgrains, with a lower interior dislocation density. All three of the above-mentioned types of substructure were observed. The first and the second configurations mentioned above, however, were mostly confined to the transient region and were not frequently detected.

Banded Substructure. Substructural bands were only observed in a few grains. Observations at higher magnifications indicated that the bands consist of arrays of dislocation pits. Similar observations have been reported by BARRETT et al¹³⁾ and LYTTON et al¹⁶⁾, who found that the configurations are slip-band traces which occur in regions where only a few systems operate simultaneously. One of the above authors¹⁶⁾ also pointed out that the directions of the slip traces are in agreement with the directions of the maximum resolved shear stresses.

The present observations suggest further that at a constant strain rate the spacing of the slip bands increases slightly with the temperature at which they are formed. The average slip band spacing, at the same temperature and strain rate, is larger in Armco iron than in silicon steel. This feature, however, was not noted in the investigations quoted above, as they were performed within a small range of temperatures and strain rates.

There was one other feature observed which is worth mentioning. In the present work, slip band traces were observed less often as the temperature of hot working increased. This is associated with some kind of degeneration of the banded configuration due to the higher mobility of dislocations at higher temperatures. With the aid of thermal activation, the dislocations which are confined in bands are able to rearrange themselves by climb and cross-slip into a substructure having lower energy. Delay before quenching at the hot working temperature has the same effect on the rearrangement of the dislocation bands.

Extended Tilt Boundaries. The other form of substructure observed in the transient region was the low-angle tilt boundary, which was formed by polygonized segments. This type of substructure, however, was seldom observed, and was localized near grain boundaries, while the slip bands described above, were generally found inside the grains. The most likely reason for the difference is that more vacancies were available for climb in the grain boundary areas. Although grain boundaries act as sinks for vacancies at lower temperatures, at higher temperatures, they are believed to emit vacancies ¹²⁶. An alternative interpretation has been advanced by LYTTON et al¹⁶, who proposed that polygonized groups of edge dislocations are formed to relieve bending stresses at grain boundary shear faults.

Equiaxed Subgrains. In the present work, the formation of

equiaxed cells was observed early in the transient region. This is in contrast to the observations of BARRETT et al¹³⁾ on the creep of silicon iron. They observed that the formation of an equiaxed substructure occurred gradually throughout primary creep. The reason why the equiaxed substructure was not observed early in primary creep by the above-mentioned investigators may have been due to the low temperatures (596 to 743°C) and the low strains ($\mathcal{E} = 0.2$) at which their experiment was carried out. The maintenance of a steady-state substructure will be discussed in greater detail in section 6.4.1 below.

Comparison of Optical and Electron Microstructures. Tables IX and X show that more scatter in the values of mean subgrain size was obtained when these were determined optically than when measured by transmission electron microscopy. In optical micrographs, separate subgrains cannot always be distinguished, which is attributed to the non-uniform etching of sub-boundaries. Counting subgrains per unit area is thus uncertain and so is the determination of the mean subgrain size. On the other hand, transmission electron micrographs exhibit the whole circumference of the subgrain in the observed section and thus offer more reliable results.

6.4 RECOVERY AND RECRYSTALLIZATION

The softening of metals during hot working has traditionally been associated with recrystallization (see, for example, A.H. COTTRELL 134). One reason for this assumption is that most hot worked metals, when examined at room temperature are recrystallized. Recent investigators 2,21,85,86,121) have shown, however, that in high stacking fault

energy metals and alloys, dynamic recovery rather than recrystallization is the restoration process during hot working. In these metals, recrystallization takes place only after forming is complete, and while the specimens are cooling to room temperature or are being isothermally annealed 33). In the paragraphs which follow, the phenomena of dynamic recovery during hot working, static recovery after hot working and recrystallization after hot working, as observed in the present investigation, will be discussed.

6.4.1 DYNAMIC RECOVERY DURING HOT COMPRESSION

In the present investigation, recrystallization was absent during hot compression. This result was demonstrated by rapid quenching following hot compression, so that the as-compressed structure was preserved virtually unchanged. The experiments also clarified the role of recovery and polygonization in the softening process associated with hot compression. The observed substructural phenomena exhibited the following main features, which will now be discussed.

During steady-state compression, the subgrain diameter is not affected by strain, as already mentioned in section 5.3.2 above. This is attributed to the equilibrium between the rate of dislocation generation and the rate of internal annihilation as well as to the process of repolygonization. At constant strain rate and deformation temperature, a stable dislocation density is established. Hence the spacing in the dislocation networks which form the walls of the subgrains remains unchanged, and so does the flow stress. The substructures observed in hot compression are similar to those formed during steady-state creep 13,91), hot torsion 12,17,19),

and hot extrusion^{2,86,135)}. The results of the above investigators, however, did not demonstrate the constancy of the steady-state subgrain size over as wide a range of strains as do the present results. This is because of the strain non-uniformity connected with the mode of deformation (torsion, tension), or because of the limited strain range used (extrusion). The former reason has already been discussed in the section 1.1 above.

Another characteristic of the steady-state network configuration during hot compression is the stability of its geometry with strain. The subgrains remain equiaxed. This implies a process of relocation of the networks assisted by a limited amount of sub-boundary migration. If the sub-boundaries were unable to rearrange themselves continuously during steady-state compression, the subgrains would become elongated in the direction of flow. Elongated subgrains, however, were not detected at all in the present investigation. This observation is in agreement with the substructural changes occurring during aluminum extrusion reported by JONAS and co-workers ^{72,86}. It is in conflict with STÜWE's theory of hot working, in which the sub-boundaries are not considered to be disturbed by the dislocation flux ⁶², so that the subgrains must be drawn out in approximately the same manner as the grains. The latter theory is thus presumed to be in error regarding this point.

It is also of interest to note that the misorientation between adjacent subgrains also remains constant during steady-state compression. The average value varies from 1.8 to 6.8 degrees, most of the observed misorientations being in the range of 2.5 to 3.5 degrees, and is unaffected by strain. This observation, however, conflicts with the

increase of misorientation with strain proposed by McLEAN¹²⁸⁾. When McLEAN's equation is used for hot compression, it predicts misorientations ranging up to 50 degrees for the strains involved in the present work. Such misorientations were never detected, and the constancy of misorientation during steady-state compression is further substantiated by the fact that the dislocation density remains constant in this regime.

The behavior of subgrains during hot compression, which has been discussed above, supports the model for steady-state hot deformation proposed by JONAS et al⁷²⁾ and McQUEEN et al⁸⁶⁾ which has already been introduced in section 2.4.2. This model explains the maintenance of the equiaxed substructure by the relocation of the dislocation networks through the continuous disintegration and reformation of the sub-boundaries at the equilibrium spacing. The term "repolygonization" proposed by the above-mentioned investigators for this process is thus seen to apply to the substructural changes occurring during hot compression as observed in the present work.

6.4.2 STATIC RECOVERY AFTER HOT COMPRESSION

Little attention has so far been paid to the phenomenon of static recovery after hot working, as compared with that given to recovery after cold working. There are several reasons for this. For one thing, until recently, little was known about the hot working process. Furthermore, recrystallization is still considered as the dominant process controlling softening after hot working. However, static recovery after hot working is also important, because it is inevitable, unless the work piece is quenched immediately after hot working. Also, knowledge of the factors affecting the rate of recovery after hot working

can enable investigators to extrapolate to zero time the property values determined during static recovery and thus to better approximate the behavior during the working process. Sometimes the intermediate properties between consecutive hot working operations are of interest and they can also be determined if the rate of property change with time is known.

To date no investigations have been uncovered concerning static recovery after the steady-state hot compression of steels in the ferritic region. In the present work static recovery has been investigated by measuring the recovered microhardness as a function of delay time after the conclusion of hot working. The results, however, can only be used for tentative conclusions for the following reasons:

- (a) The number of specimens investigated for the purpose of static recovery was not considered sufficient for authoritative conclusions.
- (b) The scatter of the microhardness readings was high, although the measurements were performed with care, following the recommendations of previous investigators 108,136 .
- (c) The kinetics of the process are complicated, since four variables have to be considered (the instantaneous value of the property, the activation energy, the temperature and the time).

To simplify the conditions in the present work, isothermal annealing was used instead of cooling, so that one of the variables was made constant. Furthermore, the activation energy was assumed to remain constant during the short time period after compression which was of interest. This enabled the application of the simple exponential equation (5), which was introduced in section 2.4.1 above. The time dependence of the microhardness and the metallographic observations will now be discussed.

The rate of static recovery after steady-state compression increases with increasing hot working temperature and strain rate. Static recovery after compression at 1,000°C leads to almost full softening after about 40 seconds. Also recrystallization sets in almost immediately at The observed dependence of the recovery rate upon this temperature. temperature is somewhat similar to the annealing behavior of cold worked metals, except that in annealing equally strained samples after cold working, the driving force at each temperature is constant, as all the deformation was performed at the same temperature. In the case of annealing after cold working, the recovery rate is also dependent on the amount of work hardening, which increases with the strain, and not with the ZENER-HOLLOMON parameter, as in hot working. For this reason the occurrence of fairly fast recovery following steady-state hot working is somewhat unexpected on first analysis. This is because the amount of work hardening (and therefore the driving force for recovery) is very low compared with that for cold working. The fact that noticeable recovery occurs can be attributed to two factors. First, the low general dislocation density after hot working means that the nucleation of new crystals takes place much more slowly than after cold working to the same strain. This gives the recovery process much more time to operate at equal annealing temperatures. Also, the rate of recovery after hot working is presumably considerably enhanced by the excess vacancies produced by the deformation. The generation of vacancies in greater quantity at high deformation temperatures than at low temperatures has been described by TAKAMURA 137). By contrast, in annealing after cold working, a time lapse is inevitably permitted before the annealing takes

place. During this period, the excess vacancies generated by the deformation are probably eliminated. Thus static recovery after cold working takes place in the presence of lower vacancy supersaturations than static recovery immediately after hot working.

Microscopic observation of the effect of static recovery on the substructure in the period of isothermal annealing clearly indicated changes in the networks. As the delay time increased, the mean subgrain diameter increased slightly, but the subgrains still remained equiaxed. This observation is in reasonable agreement with the following two investigations. A small change in subgrain size was reported by ENGLISH and BACKOFEN³³⁾ in hot compressed 3 1/4% silicon iron over the period of time during which recrystallization was taking place. A slight increase in subgrain size was also noted during recovery after cold working by LESLIE et al^{77,109)}.

6.4.3 RECRYSTALLIZATION AFTER HOT COMPRESSION

In section 6.4.1 it was mentioned that recrystallization was not detected during hot compression under the conditions of the present experiment. However, recrystallization did take place during isothermal annealing after compression and followed static recovery. This is in agreement with the annealing behavior of cold worked iron of commercial purity, where recrystallization also begins in the recovered matrix 138). It also agrees, at least at lower temperatures, with the results for the recrystallization of hot compressed 3 1/4% silicon iron 33).

As in the case of static recovery after hot compression, the amount of data obtained is not considered sufficient for the detailed

description of isothermal recrystallization. For this reason, the conclusions, which will now be discussed briefly, are to be considered as tentative.

The recrystallization data which were determined in the annealing period following hot compression are represented in Figs. 87 and 88. The data for 50% recrystallization taken from these figures can be plotted and extrapolated to higher deformation temperatures and shorter annealing times, as shown in Fig. 94. Although extrapolation over large distances has to be interpreted with care, the plot does suggest that, at higher temperatures than those used in the present work, recrystallization should start within a few milliseconds of the completion of deformation, or even during hot working itself. Support for this extrapolation can be obtained from the investigation of ENGLISH and BACKOFEN 33). Some of the isothermal recrystallization data presented by these investigators are also shown in Fig. 94.

It is not possible, at the present time, to determine whether recrystallization actually occurs during deformation at high temperatures, or only very rapidly after the completion of straining. The possibility of recrystallization during hot working is opposed to the opinion of some previous investigators $^{21,85,127)}$ who have concluded that high stacking fault energy metals, such as Al, &-Fe, Zn, Mg, Cd and Sn, do not recrystallize during creep or hot working. On the other hand, the occurrence of concurrent recrystallization in &-Fe during hot torsion has been supported by ROBBINS et al²³⁾.

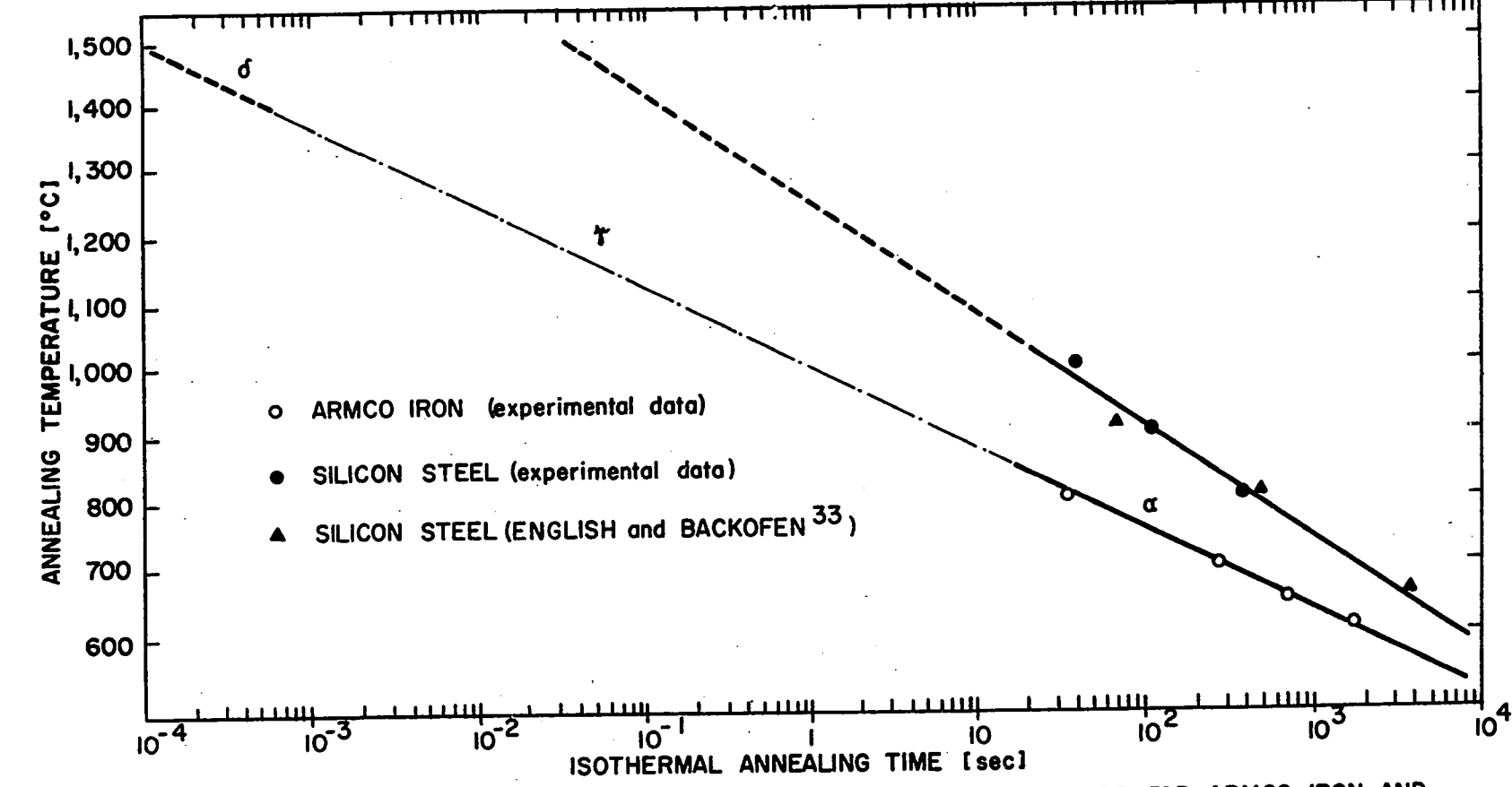


FIG. 94 TIME OF HALF RECRYSTALLIZATION AS A FUNCTION OF TEMPERATURE FOR ARMCO IRON AND SILICON STEEL

6.5 SUBGRAIN SIZE AS A FUNCTION OF STRESS, STRAIN RATE AND TEMPERATURE

In this section the applicability of the strain rate equation (17) to the present data will be discussed and the experimental functions relating subgrain diameter to flow stress, strain rate and temperature will be presented.

In section 5.2 it was shown that the relationship between the observed stress/strain rate/temperature data can be represented by equation (17). When the ZENER-HOLLOMON parameter (Z) is substituted into equation (17), the following relation between (Z) and the stress function is obtained:

$$Z = A \left[\sinh (66) \right]^{n'}$$
 (24)

Data for the two experimental materials plotted in terms of this equation are shown in Fig. 95. A straight line fit is obtained for each material, showing that the data are well represented by equation (24). The slope of the line is the exponent (n') of equations (17) and (24), and is referred to as a material constant in this work (see section 5.2.1 above).

The state of the substructure, however, does not enter into equation (17) or (24) directly for a number of reasons $^{135)}$. First, until recently, the detailed configuration of hot working or creep substructures, and its variation with strain, strain rate and temperature, was not known. Furthermore, it has been maintained for some time that the steady-state substructure geometry is uniquely related to the steady-state flow stress, or alternatively to the ZENER-HOLLOMON parameter $Z = \left[\dot{\mathcal{E}} \exp\left(\frac{\Delta H}{RT}\right)\right]$. Thus, if a substructure term were included in equation (17) or (24), a substitution could be made in terms of the stress or (Z) equivalent of the substructure term, so that the final equation would still be given

in terms of $(\dot{\mathcal{E}}, 6, and T)$ alone.

It is also of interest that when the strain rate equation is written in the form Z = f(6),(24), it provides a good guideline for finding appropriate functions relating the subgrain size to both the flow stress, and to (Z). The determination of these functions will now be described in detail.

Subgrain Size in Terms of Stress. Having determined the mean subgrain diameter for different conditions of hot compression (see Tables IX and X), the following relationship was found to hold between the mean subgrain diameter and the steady-state flow stress:

$$d^{-1} = a_1' + b_1' \log \sinh (66)$$
 (25)

where a_1' and b_1' are constants. This relationship is represented graphically for both materials in Fig. 96.

Some other functions, expressed by the following equations, were also found to fit the stress data:

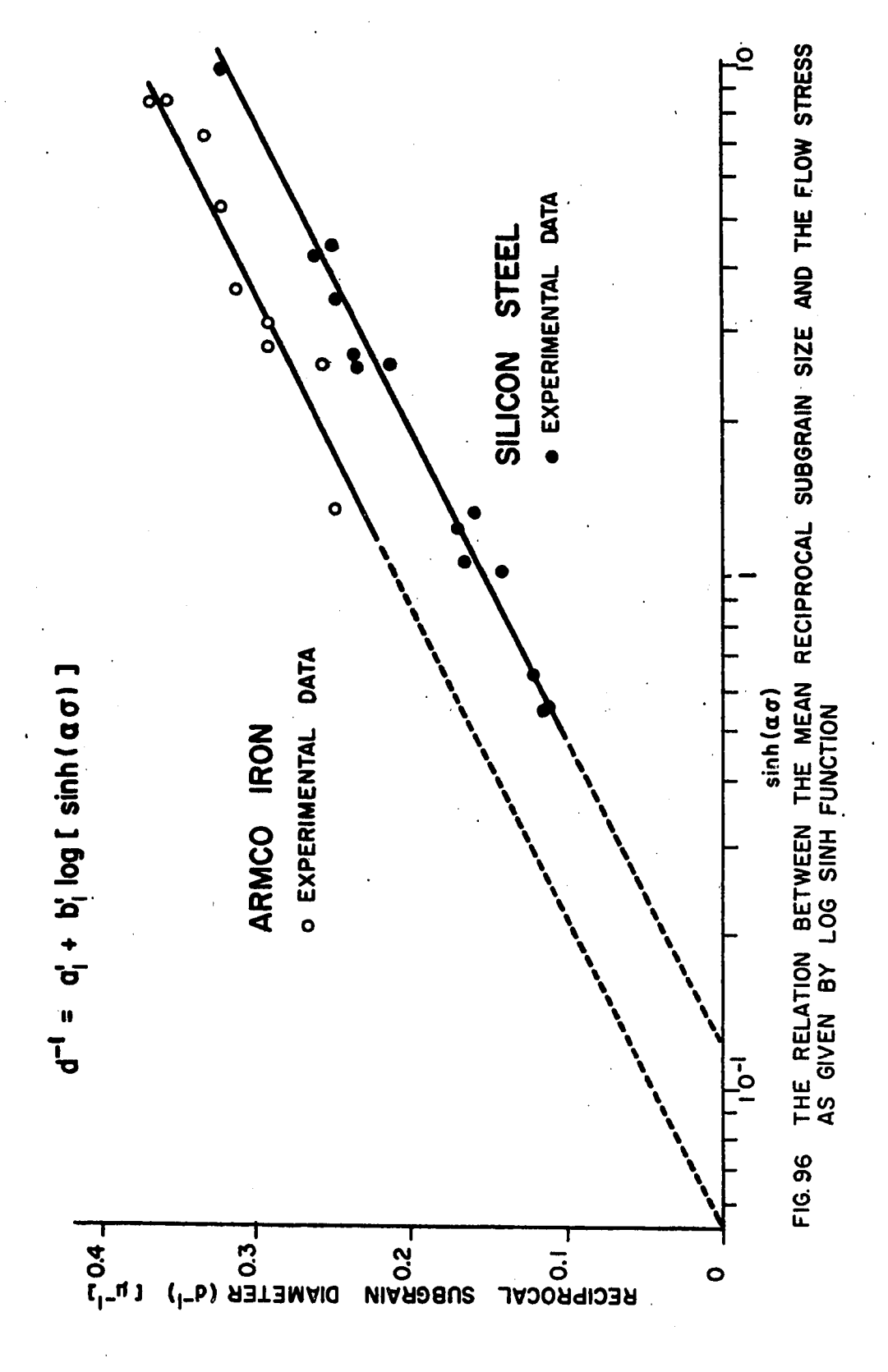
- (a) the simple linear equation: $d = d_0 kG$ (26)
- (b) the reciprocal diameter/stress equation:

$$d^{-1} = a_2^1 + b_2^1 6 (27)$$

- (c) the power equation: $d^{-1} = b_3^* 6^n$, and (28)
- (d) the power sinh equation:

$$d^{-1} = b_{4}^{1} \left[\sinh (\mathcal{L}6) \right]^{N}$$
 (29)

In the above equations, (d_0) , (k), (a_2') , (b_2') , (b_3') , (b_4') , (\mathcal{L}) , (n) and (N) are constants, and their values are listed in Table XIV Selow. The equations are represented in Figs. 97 to 100, and equations (25), (27)



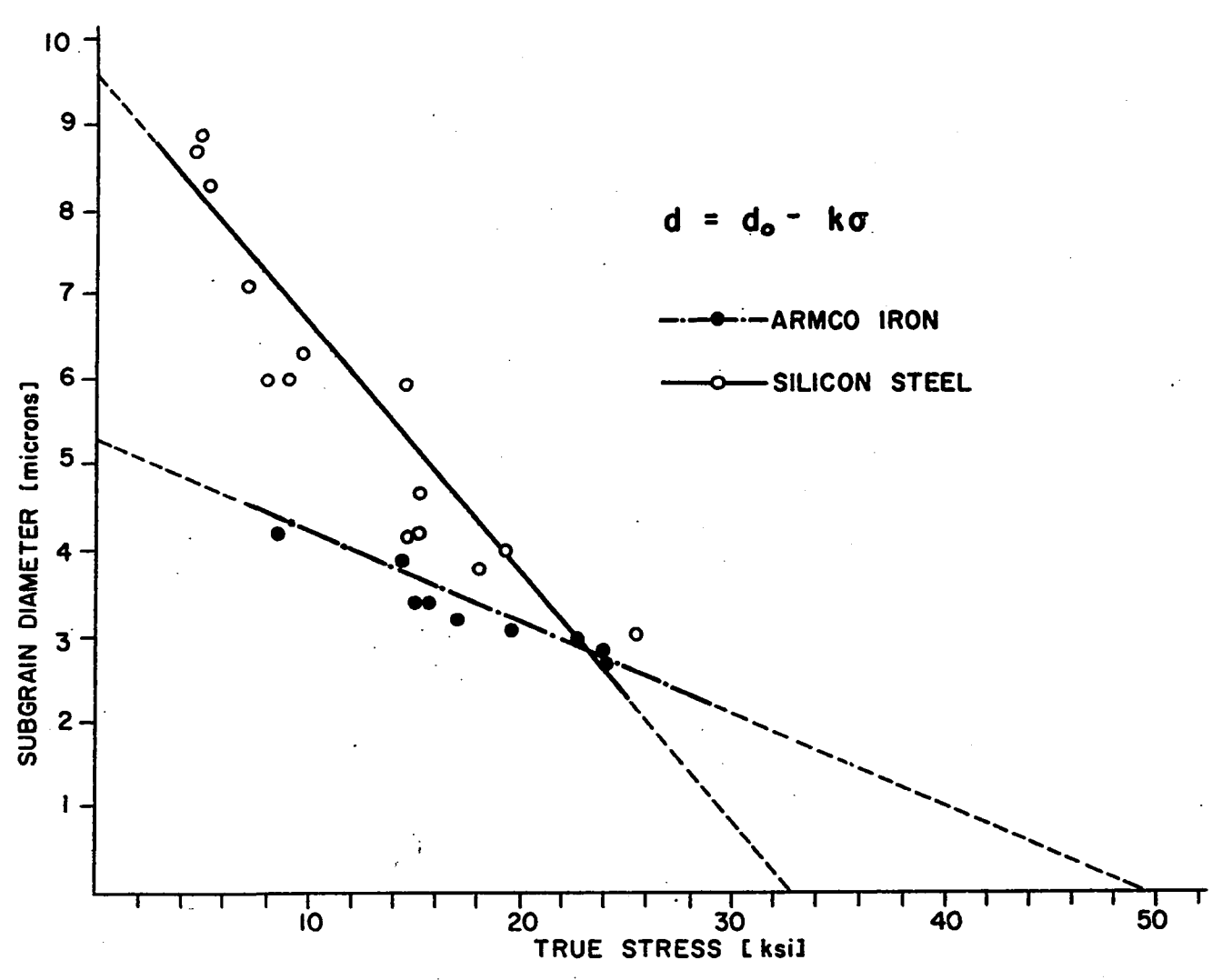
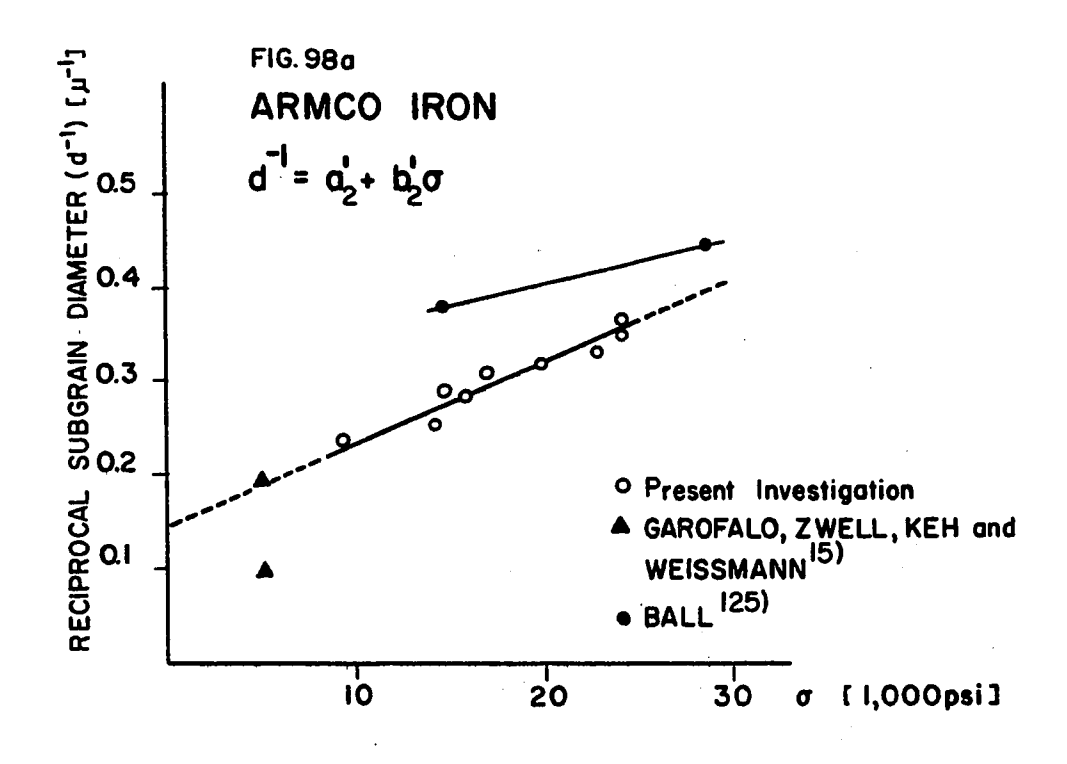
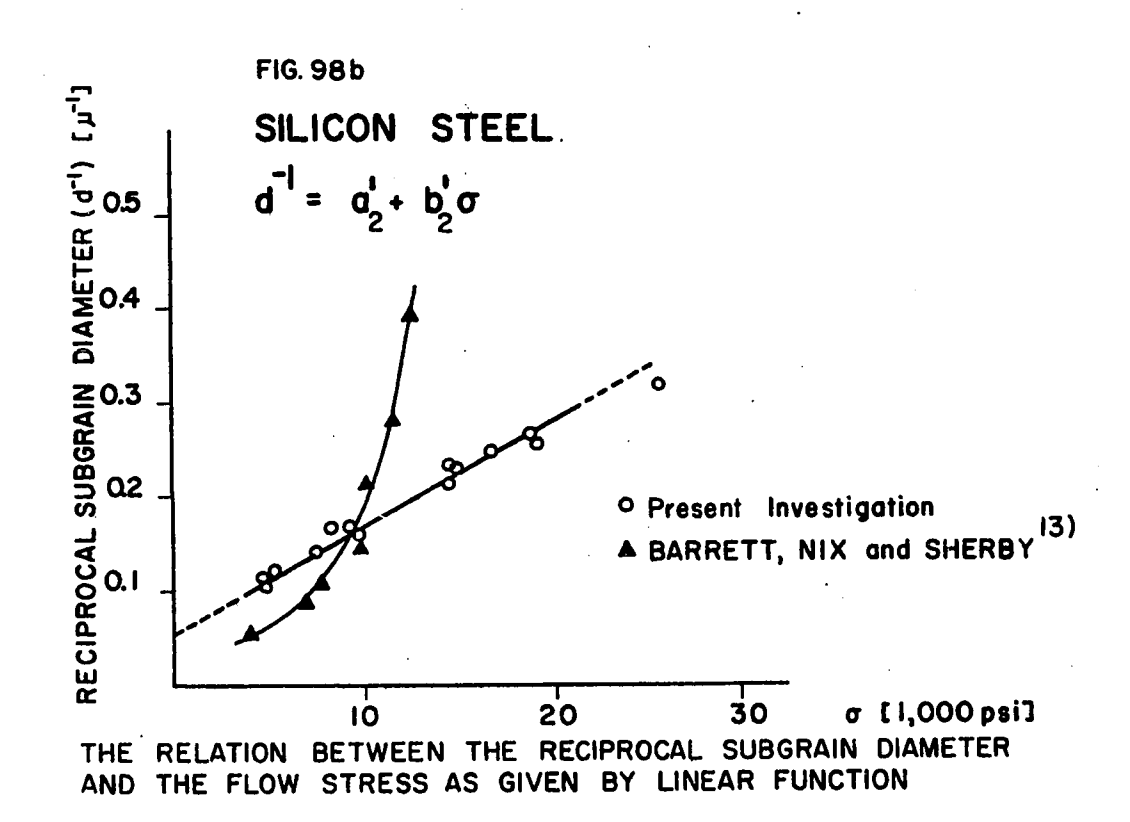
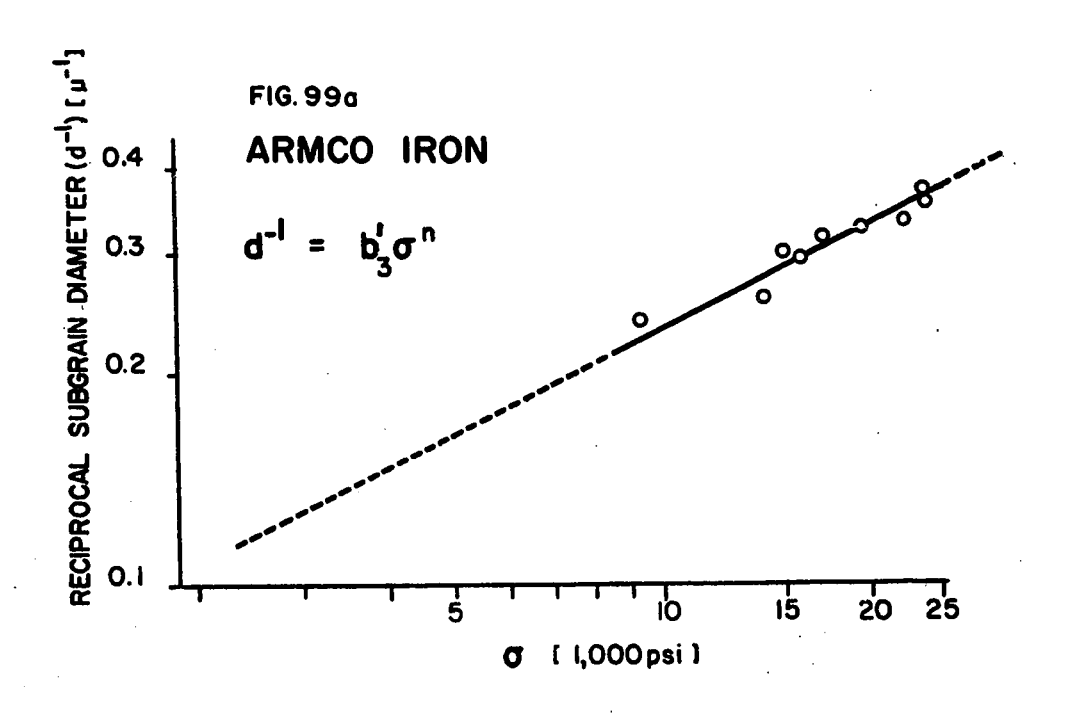
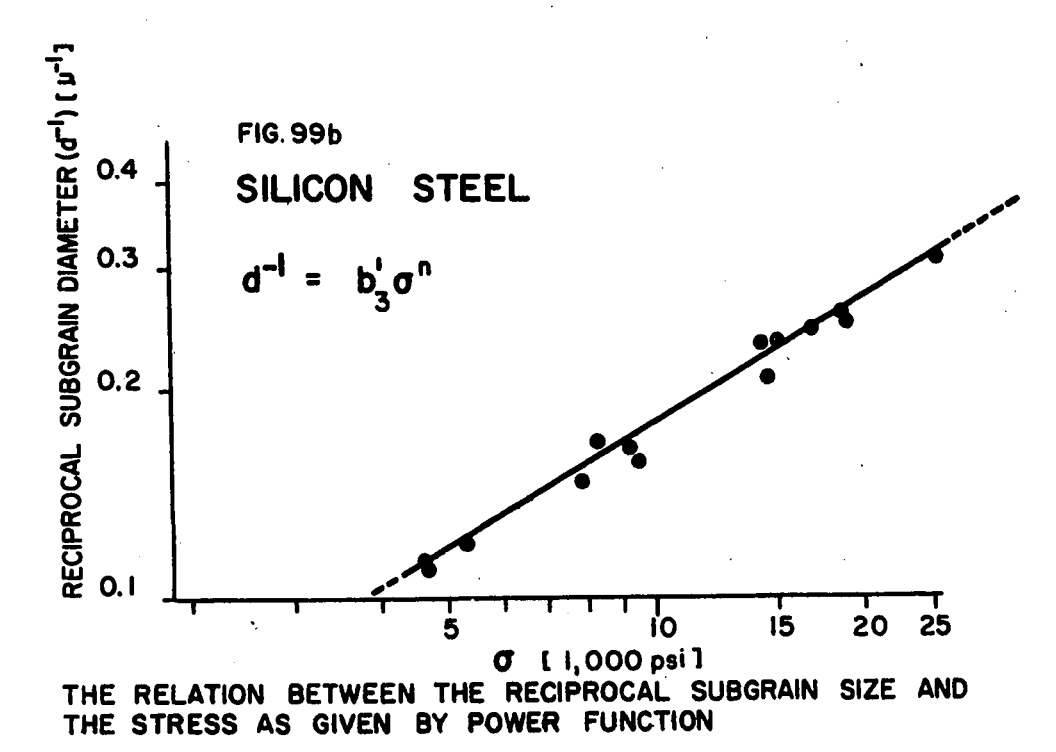


FIG. 97 SUBGRAIN SIZE/FLOW STRESS RELATIONSHIP IN ARMCO IRON AND SILICON STEEL









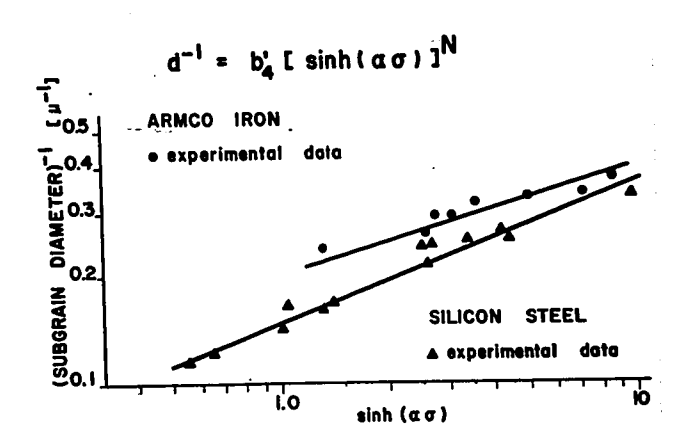


Fig. 100 - The dependence of the reciprocal subgrain size on stress

and (28) are compared graphically in Fig. 101. The subgrain size equations will now be compared and their applicability to the present work and to creep and high speed hot working will also be discussed.

The simple linear equation was used by GAROFALO^{91,140)} for the correlation of steady-state creep data of austenitic stainless steel. From the application of GAROFALO's equation to the present results (Fig. 97), it can be seen that the fit is limited to the intermediate range of stresses and does not apply at high and low stresses. The graph shows that at the higher stresses attainable in hot working, the subgrain size predicted by this equation becomes negative, so that the relation cannot apply. Similarly, at the lower stresses obtained in high temperature creep, the maximum subgrain diameter predicted by equation (26) is limited to 6 and 10 microns, for the two materials. This is in conflict with many creep results. For example, in 3% silicon steel, steady-state subgrain sizes of about 20 microns have been observed at a temperature of 643°c¹³⁾.

The reciprocal diameter/stress equation (27) which is represented in Figs. 98a and 98b, does not imply negative subgrain sizes at high stresses as does the above-mentioned simple linear equation (26). However, it intercepts the vertical axis at (d⁻¹) values of 0.14 and 0.06 (microns)⁻¹, i.e. subgrain sizes about 7 and 16 microns. For the reasons discussed in the foregoing paragraph, it cannot apply in the high temperature creep region. In contrast to equations (26) and (27), the power equation (28) fits the hot working data and also apparently predicts a satisfactory fit for both creep and high speed hot working data, as does equation (29).

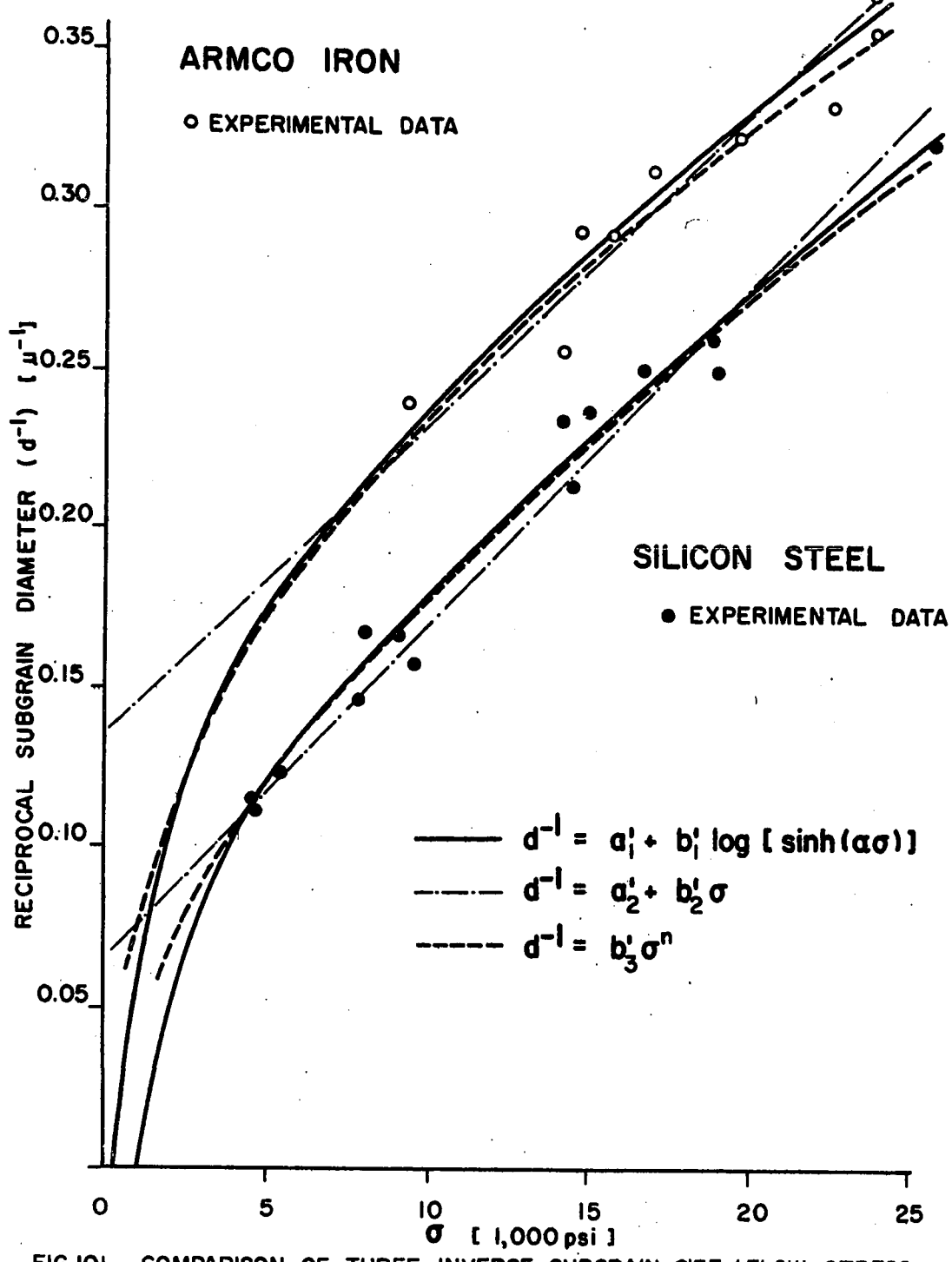


FIG.101 COMPARISON OF THREE INVERSE SUBGRAIN SIZE / FLOW STRESS RELATIONSHIPS FOR ARMCO IRON AND SILICON STEEL

Returning to the (log sinh) equation (25), introduced above and proposed in this dissertation, it can be seen that the equation can be extrapolated back into the creep stress range in agreement with the observed values of subgrain size. This is because the (log sinh) term approximates a logarithmic law at low stresses and a linear law at high stresses.

At low stresses, where [sinh (&6)] $\approx (\&6)$, equation (25) takes the following form: $d^{-1} = a'_1 + b'_1 \log \mathcal{L} + b'_1 \log \mathcal{L}$

or
$$d^{-1} = a_1'' + b_1' \log 6$$
 (30)

where $a_{1}' = a_{1}' + b_{1}' \log \mathcal{L}$.

Thus

At high stresses, [sinh (66)] \approx [$\frac{1}{2}$ exp (66)], and equation (25) becomes:

$$d^{-1} = a'_{1} + b'_{1} \log[\frac{1}{2} \exp(\mathcal{K}G)],$$
or
$$d^{-1} = a'_{1} + b'_{1}G$$
(31)

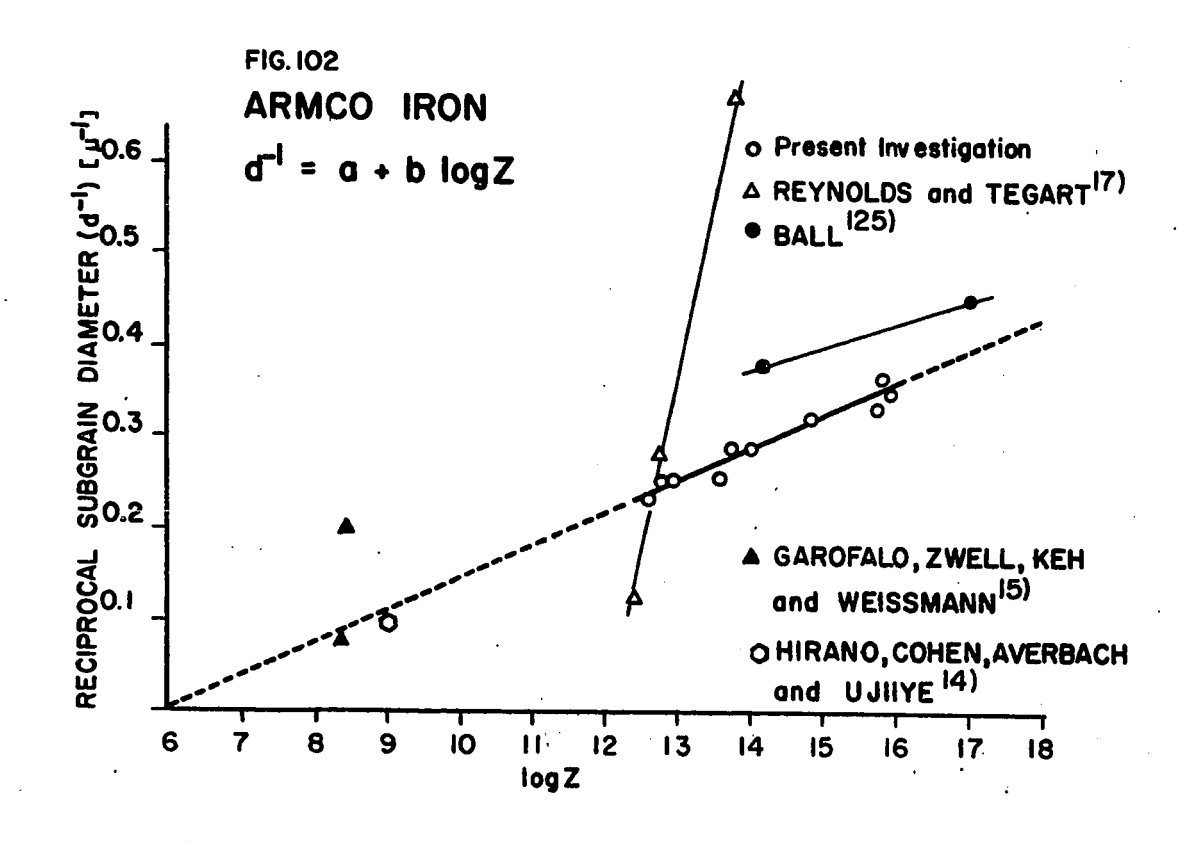
where $a_1'' = (a_1' - 0.3 b_1')$ and $b_1'' = 0.434 b_1' & ...$

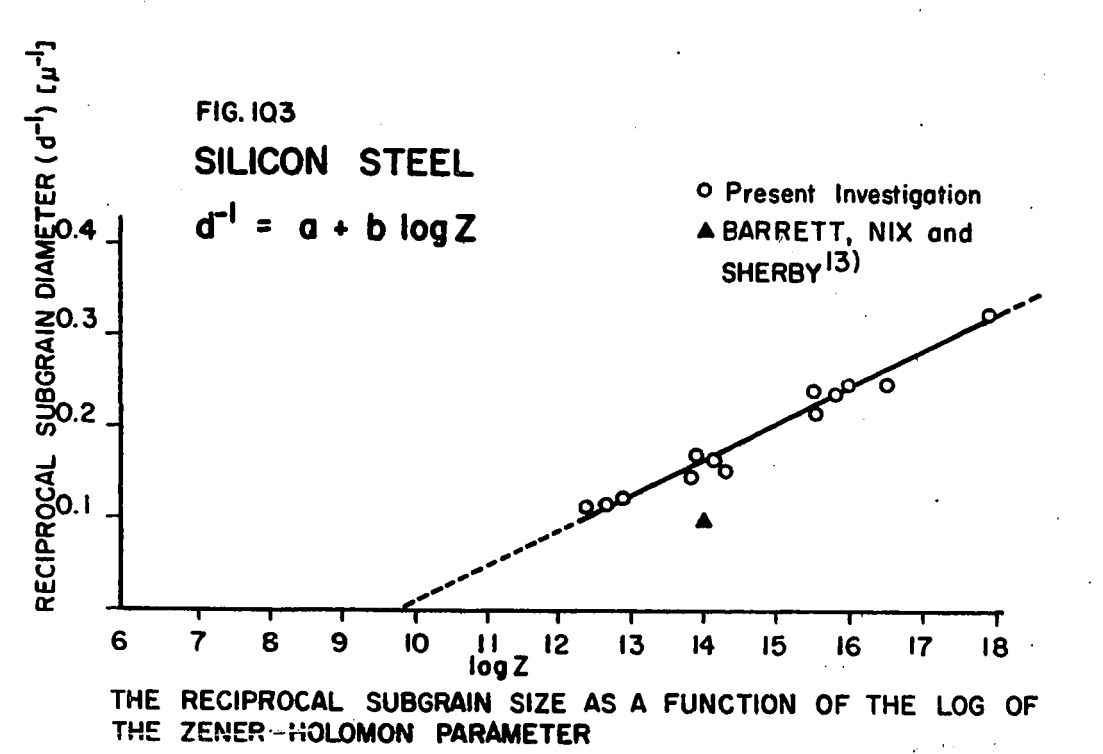
Thus it can be seen that at high stresses, equation (25) and equation (27) are similar in form.

Subgrain Size as a Function of (Z). The reciprocal subgrain size function of (Z) corresponding to equation (25) can be obtained by substituting equation (24) into equation (25), and solving for (d^{-1}) . $d^{-1} = a + b \log Z$

(32)

where (a) and (b) are new constants related to (a_1^{\prime}) and (b_1^{\prime}) in equation (25) in the following way: $a = a_1' - \frac{b_1'}{n!} \log A$, and $b = \frac{b_1'}{n!}$. Figs. 102 and 103 show that a good fit is obtained when the experimental subgrain diameters are plotted against the logarithm of the ZENER-HOLLOMON parameter, as required by equation (32). Inspection of equation (32)





indicates that (d⁻¹) approaches zero at (log Z) values about 6 for Armco iron and 10 for silicon steel. In low strain rate-high temperature creep, however, lower values of (Z) than this can apply, so that the values of the "constants" (a, a'₁, b and b'₁) for creep are probably somewhat lower than those listed for hot working in Table XIV. This means that equations (25) and (32) represent the data in the hot working range of (Z) and (G) fairly well, but do not extrapolate into the creep range as well as equation (24).

A better fit in the creep range can be obtained by the use of the following equations, proposed recently in a paper based on this dissertation (135):

$$d^{-1} = p(Z)^{q};$$
 (33)

$$d^{-1} = b_4' \left[\sinh (\mathcal{C} \mathcal{G}) \right]^N; \qquad (29)$$

In this case (A) and (n') in equation (24) are equal to $\lceil \frac{b_4}{p} \rceil \frac{1}{q}$ and $(\frac{N}{q})$ respectively. The latter equation has already been introduced above and a graphical representation of the former is shown in Fig. 104. It can be seen that this equation applies to both hot working and creep. More data concerning mean subgrain size during steady-state creep are needed, however, to enable a definite choice to be made between equations (25) and (32) or (29) and (33).

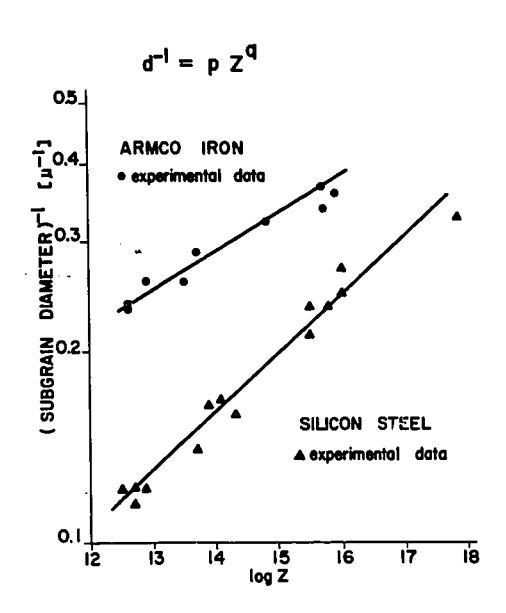


Fig. 104 - The dependence of the reciprocal subgrain size on the ZENER-HOLLOMON parameter

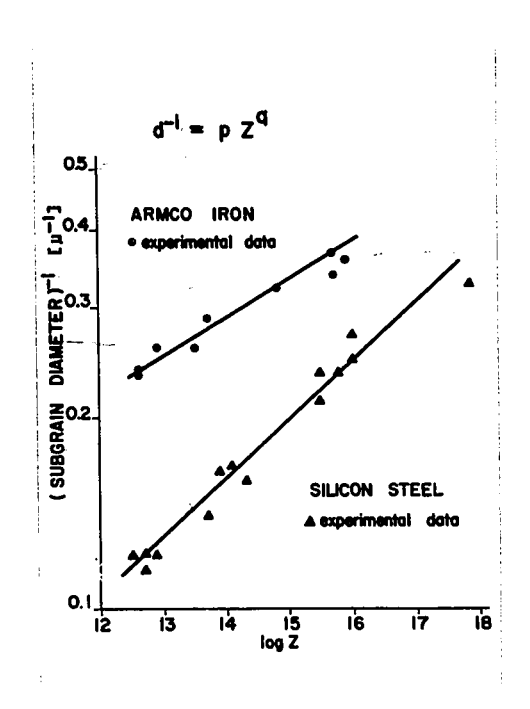


Fig. 104 - The dependence of the reciprocal subgrain size on the ZENER-HOLLOMON parameter

Table XIV. Experimental Values for the Constants in Equations 25 to 29, 32 and 33.

CONSTANT	NUMBER OF EQUATION, [FIGURE]	ARMCO IRON	SILICON STEEL
a	32	-0.218	-0.389
ъ	[102, 103]	0.0367	0.0395
a'i	25	0.210	0.154
b <u>'</u> 1	[96]	0.168	0.170
a'2	27	0.145	0.055
b 1	[98a, 98b]	9x10 ⁻⁶	11.4×10 ⁻⁶
b	28	2.4x10 ⁻³	6.8x10 ⁻⁴
n	[99a, 99b]	0.50	0.60
р	33	0.047	0.010
q	[104]	0.057	0.089
b	29	0.21	0.16
N	[100]	0.263	0.385
ď	26	5.3	9.6
k	[97]	1.06x10 ⁻⁴	2.93×10 ⁻⁴

6.6 THE INTRODUCTION OF SUBSTRUCTURE PARAMETERS INTO THE STRESS/STRAIN RATE/TEMPERATURE EQUATION

The experimentally determined stress dependence of the equilibrium subgrain size was discussed in the previous section, in which two alternative functions were proposed:

$$d^{-1} = a_1' + b_1' \log \sinh (26)$$
 (25)

$$d^{-1} = b_4' \left[\sinh \left(\mathcal{L} \delta \right) \right]^{N}$$
 (29)

These represent the hot deformation data obtained over the full range of experimental strain rates and temperatures. In the following paragraphs, based on a recent paper by JONAS, AXELRAD and UVIRA 135, a new strain rate equation containing explicit substructure parameters will be introduced. The equation which follows was proposed on the basis of the experimental evidence described in this dissertation:

$$\dot{\varepsilon} = A_1 S_d \left[\sinh \left(S_{\theta} 6 \right) \right]^m \exp \left(-\frac{\Delta H}{RT} \right)$$
 (34)

In this equation (A_1) is a constant related to the impurity content, (S_d) and (S_θ) are substructure parameters, the exponent (m) is related to the stress sensitivity of the strain rate, and (ΔH) and (R) have their usual meanings.

It is proposed that equation (34) is valid for steady-state conditions, and for transitions from one steady state to another, but that it applies only to cubic metals with reasonably high stacking fault energies, in which well-defined substructures are formed. A further restriction is that its validity is limited to homologous temperatures above 0.5 or 0.55 and to hot working strain rates below 10³ or 10⁴/second, at which mobile dislocations begin to approach the velocity of shear waves in the material.

The substructure parameters (S_d) and (S_0) are related to the average subgrain size, and to the average misorientation, respectively, and can be evaluated as follows. It is to be expected that when a series of samples suffers creep or hot working at the same applied

stress and temperature, the initial strain rate will decrease with decreasing initial (d). Two functions which describe such a dependence are:

$$S_{d} = K_{1} \exp \left(-K_{2}/d\right)$$
and
$$S_{d} = K_{3}(d)^{K_{4}}$$

where the constants $(K_{1,2,3,4})$ are related to the subgrain size dependence of the strain rate. It should be noted that the significant parts of the subgrain size parameter (S_d) are contained in the two exponents (K_2) and (K_4) , which can be calculated from the constants in equations (24), (25), (29) and (34). In these calculations, (S_0) is set equal to (\mathcal{C}) , as explained in reference (135), and then, it can readily be shown that the constants (K_2) and (K_4) are given by:

$$K_2 = \frac{2.3 (m-n')}{b_1^!}$$
 $K_4 = \frac{m-n'}{N}$

The values of (n'), (b') and (N) required in these relationships are given in Tables VII and XIV above. The exponent (m), however, can only be obtained from differential testing, and in the absence of differential hot working data, (m) has to be calculated from differential creep tests.

Once values for (K_2) or (K_4) have been obtained, equation (34) can be employed for the prediction of the new strain rates accompanying changes in the applied stress when the temperature and initial substructure are kept constant. It also specifies the initial strain rates obtained from two substructures of different (d)'s at the same flow stress and temperature. Hence it gives an estimate of the extent to which the sub-

sequent creep resistance of a metal can be enhanced by warm or hot working so as to produce a fine substructure.

6.7 <u>MICROHARDNESS MEASUREMENTS</u>

The dependence of the room temperature microhardness upon the subgrain size produced during hot working was described in section 5.6.1 and will now be discussed.

In both materials investigated, the room temperature microhardness is inversely proportional to the square root of the mean subgrain diameter. The dependence of microhardness upon subgrain size was found to be valid both when the workpiece was quenched immediately after hot compression, and also when it was subjected to isothermal static recovery. A similar dependence was found in hot extruded aluminum by WONG et ${\rm al}^{75)}$. It can be seen that the subgrain size/room temperature microhardness relationship of hot worked materials is similar to the relation between the lower yield point and the grain size proposed by HALL¹²¹⁾ and PETCH¹²²⁾. The relationship observed in the present work suggests that the sub-boundaries created during hot working present at room temperature almost as strong barriers to dislocation movement as grain boundaries do. This view was adopted by EMBURY et al 59, who came to a similar conclusion for the cell size/flow stress relationship of various cold worked metals. They found that the cell walls developed during cold deformation act analogously to grain boundaries, but may also possess long-range stress fields. The present conclusions are also supported by the work of BALL on the hot tension of polycrystalline iron at temperatures below 0.5 $T_{\rm m}$. In this work he concluded that,

although at high temperatures sub-boundaries are not such effective barriers to slip as grain boundaries, their effectiveness increases as the temperature decreases.

The other important feature of the compressed specimens was the increase in softening by dynamic recovery as the deformation temperature was increased. After the steady-state compression of Armco iron at 800°C, and of silicon steel at 1,000°C, the microhardnesses were only 20% and 5%, respectively, higher than those of the recrystallized specimens. The softening took place without recrystallization and was brought about by the occurrence of enhanced dynamic recovery. The enhancement of recovery during hot working has been previously demonstrated in hot worked aluminum both by torsion 139) and by extrusion 75).

6.8 ROOM TEMPERATURE PROPERTIES IN TERMS OF HOT WORKING STRAIN RATES AND TEMPERATURES

Equations (32) and (33) relate the mean size of the hot worked substructure to the imposed strain rate at a given temperature. The hot worked substructure, if preserved during cooling to room temperature, then controls the room temperature properties, such as microhardness. Having determined both these relationships, the room temperature microhardness can be correlated directly with the imposed strain rates and temperatures of hot working.

This correlation, however, is restricted by the condition that no recrystallization occurs during hot working and that the as-worked substructures are preserved during cooling to room temperature. It is only an approximation, of course, because of inevitable errors in the determination of the mean subgrain size and the microhardness. Thus for

a desired value of a room temperature property, the appropriate hot working strain rate and temperature can be estimated. Or, vice versa, the room temperature properties can be predicted approximately from the imposed hot working strain rate at a given temperature. In the present work, the microhardness $(M_{\mbox{H}})$ in DPH (load 100 g) can be predicted by the use of the following alternative equations:

$$M_{H} = a''' + b''' [a + b \log z]^{\frac{1}{2}}$$
 (35)

(resulting from equations (23) and (32)), or

$$M_{\rm H} = a''' + c (Z)^{\frac{1}{2}q}$$
 (36)

(obtained by combining equations (23) and (33)).

Here: (a)(a''),(b)(b''') and (q) are constants,

(c) is a constant =
$$b''' \times p^{\frac{1}{2}}$$
,

(p) is another constant from equation (33),

 $Z = \text{the ZENER-HOLLOMON parameter } (\dot{\mathcal{E}} \frac{\Delta H}{RT}).$

The above-mentioned restrictions concerning equations (35) and (36) can be partially removed if the change in mean subgrain size during static recovery is known. By adding the recovery/subgrain size relationship to the above equations, a new relationship can be obtained. The validity of this relationship extends over the period of isothermal static recovery after hot working to the moment when recrystallization sets in.

7 CONCLUSIONS

The main conclusions derived from the work described above are listed below in five sections, each dealing with a different aspect of the investigation. The conclusions are based on the hot compression of Armco iron and 2.8% silicon steel in the ferritic region at constant strain rates ranging from 5×10^{-2} to 1/sec. Most of the samples were quenched in water within one second of the end of deformation. Selected samples were held at the deformation temperature and isothermally annealed for times up to $1\frac{1}{2}$ hours before quenching.

TRUE STRESS-TRUE STRAIN CURVES

- 1. Unlike the curves obtained from hot torsion, true stress-true strain curves for hot compression do not exhibit pronounced peaks at the transition from transient to steady-state hot working.
- 2. The strain at the onset of the steady-state increases with strain rate at constant temperature; it is not substantially affected by temperature change at constant strain rate.
- 3. The flow stress of Armco iron in hot compression over the temperature range 600° C to 800° C is virtually unaffected by the addition of 0.26% Mn.

STRAIN RATE EQUATIONS AND MATERIAL CONSTANTS

- 1. The results show the applicability of the equation of SELLARS and TEGART⁸⁵⁾ to the hot compression of iron and steel. This equation, first proposed for the correlation of flow stress, strain rate and temperature during steady-state hot torsion, thus applies to hot compression as well.
- 2. The material constants (n') and (&) do not differ substantially from those reported for the hot torsion of low carbon steels in the austenitic

region.

- 3. The activation energy for the hot compression of Armco iron over the temperature range 600°C to 800°C is 66 kcal/mole, which is in agreement with the activation energies reported for the hot torsion of low carbon steels in the austenitic region. It is also similar to the activation energy for self-diffusion and is slightly lower than that for high temperature creep.
- 4. The activation energy for the hot compression of 2.8% silicon steel over temperatures ranging from 650°C to 1,000°C is 80 kcal/mole. This value is close to the activation energy reported by ROSSARD²⁰ and by ROSSARD and BLAIN¹⁹ for the hot torsion of 25% Cr ferritic steel.

SUBSTRUCTURAL RESULTS

- 1. The hot compression of Armco iron at temperatures below 800°C, and of 2.8% silicon steel below 1,000°C is governed by dynamic recovery alone. Recrystallization does not occur during the process.
- 2. Equiaxed subgrains begin to form in the transient region. During steady-state hot working, the equiaxed subgrains remain constant in size and shape and their geometry is independent of strain. These results confirm the theory of repolygonization proposed by JONAS and co-workers 86,135).
- 3. During steady-state hot compression, the mean subgrain size is related to the strain rate and temperature by the following equation:

$$d^{-1} = a + b \log Z.$$

It is also related to the flow stress as follows:

$$d^{-1} = a' + b' \log \sinh (\mathcal{L}G),$$

where (a), (a'), (b) and (b') are constants.

- 4. The determination of mean subgrain size by electrolytic etching and optical microscopy can give misleading results. This is attributed to the non-uniform etching of sub-boundaries. Transmission electron micrography offers a more reliable means of subgrain size measurement.
- 5. The misorientation of adjacent subgrains is not affected by strain during steady-state hot working.
- 6. The strain rate during transient and steady-state hot working can be expressed by the relation 135)

$$\dot{\mathcal{E}} = A_1 S_d \left[\sinh \left(S_0 \delta \right) \right]^m \exp \left(-\frac{\Delta H}{RT} \right),$$

where (S_d) and (S_0) are substructure parameters and (A_1) and (m) are constants. (S_0) , the misorientation parameter, is constant during hot working, and (S_d) , the subgrain size parameter has two alternative forms: $S_d = K_1 \exp(-K_2/d)$ and $S_d = K_3 (d)^{K_4}$, where $(K_{1,2,3,4})$ are constants.

RECOVERY AND RECRYSTALLIZATION AFTER HOT WORKING

- 1. The mean subgrain size slowly increases during isothermal static recovery following deformation.
- 2. Recrystallization follows static recovery during isothermal annealing and starts almost immediately after compression. The times for 50% recrystallization after steady-state compression range as follows: in Armco iron, from 35 sec at 800°C to 30 min at 600°C; in 2.8% silicon steel, from 40 sec at 1,000°C to 1½ hours at 650°C. These results suggest that, at higher temperatures, recrystallization can occur within milliseconds of the conclusion of deformation, or possibly during the deformation itself.

MICROHARDNESS RESULTS

1. The room temperature microhardness is inversely proportional to square root of the subgrain size, and can be expressed by an equation of the HALL-PETCH type, as follows:

$$M_{H} = a^{111} + b^{111} (d^{-\frac{1}{2}}),$$

where (a''') and (b''') are constants.

- 2. In contrast to the annealing behavior of cold worked iron, during hot working, almost complete softening is achieved without recrystallization. This is brought about by the occurrence of extensive dynamic recovery.
- 3. The rate of isothermal static recovery of microhardness after hot compression increases with deformation temperature and strain rate.

STATEMENT OF ORIGINAL WORK AND CONTRIBUTION TO KNOWLEDGE

The present investigation is the first to the author's knowledge, in which hot compression is treated and analyzed as a thermally activated process. This is also the first time that the stress/strain rate/temperature relationship for hot compression is shown to be similar to that for creep, and that the influence of the deformation variables on the hot worked substructures is examined in detail. The further contributions of this investigation to the understanding of hot working are the following:

- (a) The true stress-true strain curves for hot compression are plotted after correction for the effect of friction and temperature increase. The activation energies for hot compression are calculated and found to be similar to those of creep and of self-diffusion.
- (b) The properties of the hot worked substructure (mean subgrain size and misorientation) are shown to be independent of strain in the steady-state regime of deformation.
- (c) New functions are proposed to relate mean subgrain size during steady-state deformation to the flow stress, and to the ZENER-HOLLOMON parameter.
- (d) In a paper based on this investigation (135), a new strain rate equation containing explicit substructure terms is proposed.
- (e) Dynamic recovery is shown to be the principal softening mechanism during hot compression, and the results indicate that it can lead to final hardnesses almost as low as those of recrystallized materials. The room temperature properties of the unrecrystallized material are

demonstrated to be functions of the hot worked subgrain size, and hence of the deformation variables.

(f) The progress of recovery and recrystallization after hot working is described. The rate of isothermal static recovery after hot compression is shown to increase with deformation temperature and strain rate. The dependence of static recrystallization times on temperature is also described.

It should be added that equipment was designed and built to produce constant true strain rates at elevated temperatures, followed by rapid quenching. The original aspects of this apparatus are also described in the dissertation.

REFERENCES

- 1. D. McLEAN, Mechanical Properties of Metals. John Wiley & Sons, Inc., New York (1962).
- 2. H. J. McQUEEN, Internal Report PM-M-67-7, Dept. of Energy, Mines and Resources, Mines Branch, Ottawa (1967).
- 3. J.F. ALDER and V.A. PHILLIPS: J. Inst. Metals, 83, (1954-55), 80.
- 4. P.M. COOK: Proc. Conf. Properties of Mat. at High Rates of Strain. Inst. Mech. Eng., London (1957), 86.
- 5. Y. ISHIDA, C.Y. CHENG and J.E. DORN: Trans. AIME, 236 (1966), 964.
- C.R. BARRETT and W.D. NIX: Acta Met., <u>13</u> (1965), 1247.
- 7. O.D. SHERBY, R.L. ORR and J.E. DORN: Trans. AIME, 200 (1954), 71.
- 8. F. GAROFALO, W.F. DOMIS and F. VON GEMMINGEN: Trans. AIME, 230 (1964), 1460.
- 9. R. FELTHAM: Proc. Phys. Soc., 66B (1953), 865.
- 10. W.D. KLOPP, W.R. WITZKE and P.L. RAFFO: Trans. AIME, 233 (1965), 1860.
- 11. W.V. GREEN: Trans. AIME, 233 (1965), 1818.
- 12. C. CRUSSARD and R. TAMHANKAR: Trans. AIME, 212 (1958), 718.
- 13. C.R. BARRETT, W.D. NIX and O.D. SHERBY: Trans. Am. Soc. Metals, <u>59</u> (1966), 3.
- 14. K. HIRANO, M. COHEN, B.L. AVERBACH and N. UJIIYE: Trans. AIME, 227 (1963), 950.
- 15. F. GAROFALO, L. ZWELL, A.S. KEH and S. WEISSMAN: Acta Met., 9 (1961), 721.
- J.L. LYTTON, C.R. BARRETT and O.D. SHERBY: Trans. AIME, <u>233</u> (1965), 1399.
- R.A. REYNOLDS and W.J. McG. TEGART: J. Iron Steel Inst., <u>200</u> (1962), 1044.
- 18. J. L. ROBBINS, O.C. SHEPARD and O.D. SHERBY: J. Iron Steel Inst.,

- 199 (1961), 175.
- 19. C. ROSSARD and P. BLAIN: Publication IRSID-Série A, No. 174 (1957), I, II.
- 20. C. ROSSARD: Thesis (L'Université de Paris), Série A, No. 3512, No. d'ordre 4384.
- 21. D. HARDWICK and W.J.McG. TEGART: Mem. Sci. Rev. Met., <u>58</u> (1961), 869.
- 22. K. TAJIMA and K. KUGAI: Tetsu To Hagane, 42 (1956), 38.
- 23. J.L. ROBBINS, O.C. SHEPARD and O.D. SHERBY: Trans. Am. Soc. Metals, 60 (1967), 205.
- 24. A. NADAI and M.J. MANJOINE: J. Appl. Mech., 8 (1941), A-77.
- 25. K. INOUYE: Tetsu To Hagane, <u>41</u> (1955), 25.
- 26. K. INOUYE: Tetsu To Hagane, 41 (1955), 15.
- 27. S. GORCZYCA: Mem. Sci. Rev. Met., <u>57</u> (1960), 153.
- 28. N. SOKOLOV, P. SURKOV and D.I. GURFEL: Fiz. metal. metalloved., 20 (1965), 83.
- 29. H. KORNFELD and G. HARTLEIF: Archiv für das Eisenhüttenwesen, 17 (1944), 221.
- 30. W. LUEG and H.G. MÜLLER: Archiv für das Eisenhüttenwesen, 28 (1957), 505.
- 31. L.D. SOKOLOV: Doklady Akademii Nauk SSSR, <u>57</u> (1949), 459.
- 32. L.D. SOKOLOV: J. techn. phys. (USSR), 16 (1946), 437.
- 33. A.T. ENGLISH and W.A. BACKOFEN: Trans. AIME, 230 (1964), 396.
- 34. F.R.N. NABARRO, Z.S. BASINSKI and D.B. HOLT: Advanc. Phys., <u>13</u> (1964), 193.
- 35. F. KROUPA and V. VÍTEK: Can. J. Phys., 45 (1967), 945.
- 36. E.N. Da C. ANDRADE and Y.S. CHOW: Proc. Roy. Soc. London, <u>175</u> (1940), 290.
- 37. B. ŠESTAK and S. LIBOVICKÝ: Acta Met., 11 (1963), 1190.

- B. ŠESTÁK and S. LIBOVICKÝ: Proc. of the Conference held at the National Physical Laboratory, Teddington, Middlesex (1963), 158.
- 39. D. HULL: Acta Met., 9 (1961), 909.
- 40. J.B. COHEN, R. HINTON, K.LAY and S. SASS: Acta Met., 10 (1962), 894.
- 41. J. WEERTMAN and J. WEERTMAN, Elementary Dislocation Theory. Macmillan Co., New York (1964), 116.
- 42. L.J. TEUTONICO: Acta Met., 13 (1965), 605.
- 43. R.J. WASILEWSKI: Acta Met., 13 (1965), 40.
- 44. F.R.N. NABARRO and T.R. DUNCAN: Can.J. Phys., 45 (1967), 939.
- 45. A.W. SLEESWYK: Phil. Mag., 8 (1963), 1467.
- 46. B. ŠESTÁK, N. ZÁRUBOVÁ and V. SLÁDEK: Can. J. Phys., 45 (1967), 1031.
- 47. H. CONRAD and G. SCHOECK: Acta Met., 8 (1960), 791.
- 48. G.E. DIETER Jr., Mechanical Metallurgy. McGraw-Hill Book Co. Inc., New York (1961), 483.
- 49. A. SEEGER, Dislocations and Mechanical Properties of Crystals.

 Fisher, Johnston, Thomson, Vreeland, editors. John Wiley and Sons,
 Inc., New York (1957), 261.
- 50. P.B. HIRSCH, Dislocations in Solids. The Faraday Society, London (1964), 111.
- 51. T. E. MITCHELL, R.A. FOXALL and P.B. HIRSCH: Phil. Mag., 8 (1963), 1895.
- 52. B.L. MORDIKE and P. HAASEN: Phil. Mag., 7 (1962), 459.
- 53. N.P. ALLEN, B.E. HOPKINS and J.E. McLENNAN: Proc. Roy. Soc. London, 234 (1956), 245.
- 54. H. CONRAD: Proc of Conference on the Relation between Structure and Mechanical Properties of Metals, Teddington, Middlesex (1963), 476.
- 55. D.F. STEIN, J.L. LOW Jr. and A.U. SEYBOLT: Acta Met., 11 (1963), 1253.
- 56. D. McLEAN: Can J. Phys., 45 (1967), 973.

- 57. W. CARRINGTON, K.F. HALE and D. McLEAN: Proc. Roy. Soc. London, 259 (1961), 203.
- 58. D.G. BRANDON, R. ANDERSON and J. SPREADBOROUGH, Dislocations in Solids. The Faraday Society, London (1964), 262.
- 59. J.D. EMBURY, A.S. KEH and R.M. FISHER: Trans. AIME, 236 (1966), 1252.
- 60. A.S. KEH, Direct Observations of Lattice Defects in Crystals. Interscience, New York-London (1962), 213.
- 61. A.S. KEH and S. WEISSMANN, Electron Microscopy and Strength of Crystals. Thomas-Washburn, Intersience Publishers, New York (1963), 231.
- 62. H.P. STÜWE: Acta Met., <u>13</u> (1965), 1337.
- 63. H.P. STÜWE: Zeitschrift für Metallkunde, 56 (1965), 633.
- 64. C. ROSSARD: 7ème Colloque de Métallurgie (1963) Ecrouissage, Restauration, Recristallisation. Presses Universitaires, France, 112.
- 65. I.S. SERVI and N.J. GRANT: J. Inst. Metals, 80 (1951-52), 33.
- 66. J. BURKE, The Kinetics of Phase Transformations in Metals. Pergamon Press, New York (1965).
- 67. K.A. OSIPOV, Activation Processes in Solid Metals and Alloys. Edward Arnold (Publishers) Ltd., London (1964), 5.
- 68. J.G. BYRNE, Recovery, Recrystallization, and Grain Growth. The Macmillan Co., New York (1965).
- 69. R.E. REED-HILL, Physical Metallurgy Principles. D. Van Nostrand Co. Inc., Princeton, New Jersey (1964), 574-580.
- 70. G. SCHOECK, Mechanical Behavior of Metals. J.E. Dorn, McGraw-Hill Book Co. Inc., New York (1961), 57.
- 71. A.D. Le CL'IRE, Diffusion in Body-Centered Cubic Metals. Am. Soc. Metals, Metals Park, Ohio (1965), 3.
- 72. J.J. JONAS, H.J. McQUEEN and W.A. WONG, Deformation Under Hot Working Conditions. Iron Steel Inst., London (1967), to be published.

- 73. E.C.W. PERRY/AN: Trans. AIME, 203 (1955), 1053.
- 74. P.H. THORNTON and R.W. CAHN: J. Inst. Metals, 89 (1960-61), 455.
- 75. W.A. WONG, H.J. McQUEEN and J.J. JONAS: J. Inst. Metals, <u>95</u> (1967), 129.
- 76. P.A. BECK: Advanc. Phys., <u>3</u> (1954), 245.
- 77. W.C. LESLIE, J.T. MICHALAK and F.W. AUL, Iron and Its Dilute Solutions.
 Interscience Publishers, New York (1963), 119.
- 78. P. GORDON, Emergetics in Metallurgical Phenomena, Vol. I. W. M. Mueller, Gordon and Breach Science Publishers, New York (1965), 208.
- 79. J.T. MICHALAK and H.W. PAXTON: Trans. AIME, 221 (1961), 850.
- 80. R.W. CAHN, Physical Metallurgy. John Wiley & Sons Inc., New York (1965), 956.
- 81. A.H. COTTRELL, Dislocations and Plastic Flow in Crystals. Oxford Clarendon Press (1953), 188.
- 82. R.W. CAHN: Proc. Phys. Soc., A63 (1950), 323.
- 83. H. HU, Recovery and Recrystallization of Metals. L. Himmel, Interscience Publishers, New York (1963), 311.
- 84. H. CONRAD, Mechanical Behavior of Metals at Elevated Temperatures.

 J.E. Dorn, McGraw-Hill Co., New York (1961), 149.
- 85. C.M. SELLARS and W.J.McG. TEGART: Mém. Sci. Rev. Mét., <u>63</u> (1966), 731.
- 86. H.J. McQUEEN, W.A. WONG and J.J. JONAS: Can. J. Phys., <u>45</u> (1967), 1225.
- 87. G. SCHOECK, Mechanical Behavior of Metals. J.E. Dorn, McGraw-Hill Book Co. Inc., New York (1961), 79.
- 88. N.F. MOTT, Creep and Fracture of Metals at High Temperatures. Proceedings of a Symposium held at the National Physical Laboratory (1954), London, Her Majesty's Stationary Office (1956), 21.
- 89. J. WEERTMAN: J. Appl. Phys., 26 (1955), 1213.

- 90. J. WEERTMAN: Acta Met., 15 (1967), 1082.
- 91. F. GAROFALO, Fundamentals of Creep and Creep-Rupture in Metals. Macmillan Co., New York (1965).
- 92. W.D. NIX: Acta Met., 15 (1967), 1079.
- 93. N. LOIZOU and R.B. SIMS: J. Mech. Phys. Solids, 1 (1953), 234.
- 94. J. SEJOURNET: Lubricat. Eng., (1962), 324.
- 95. D.R. AXELRAD: Trans. Soc. Rheology, 9:1 (1965), 219.
- 96. D.R. AXELRAD: J. Sci. Instrum., <u>39</u> (1962), 640.
- 97. P.B. SEWELL, C. D. STOCKBRIDGE and M. COHEN: Can.J. Chem., <u>37</u> (1959), 1813.
- 98. C.E. MORRIS: Met. Progr., 56 (1949), 696.
- 99. R. PACKWOOD: Private communication.
- 100. E.C. BAIN and J.R. VILLELLA, Metals Handbook. Am. Soc. Metals, Metals Park, Ohio (1948), 399.
- 101. ASTM Standards (1964), Part 31, Designation E 112-63, section C, 225.
- 102. G. THOMAS, Transmission Electron Microscopy of Metals. John Wiley and Sons, Inc., New York (1964), 251.
- 103. R.H. ALDERSON and J.S. HALLIDAY, Techniques for Electron Microscopy. Blackwell Sci. Publicat., Oxford (1965), 478.
- 104. H.J.McQUEEN: Private communication.
- 105. G. VENTURELLO, C. ANTONIONE and F. BONACCORSO: Trans. AIME, 227 (1963), 1433.
- 106. C. ANTONIONE, G. DELLA GATTA and G. VENTURELLO: Trans. AIME, 230 (1964), 700.
- 107. A. ROSEN, M.S. BURTON and G.V. SMITH: Trans. AIME, 230 (1964), 205.
- 108. D. KIRK: Ph.D. Thesis. Dept. of Industrial Metallurgy, University of Birmingham, England (1958).
- 109. W.C. LESLIE, F.J. PLECITY and J.T. MICHALAK: Trans. AIME, <u>221</u> (1961), 691.

- 110. N.H. POLAKOWSKI: J. Iron Steel Inst., 163 (1949), 250.
- 111. M. COOK and E.C. LARKE: J. Inst. Metals, 71 (1945), 371.
- 112. T.A. READ, H. MARKUS and J.C. McCAUGHEY, Fracturing of Metals.

 Am. Soc. Metals, Metals Park, Ohio (1948), 228.
- 113. W. SCHROEDER and D.A. WEBSTER: J. Appl. Mech., <u>16</u> (1949), 289.
- 114. A.L. TITCHENER and M.B. BEVER: Progr. Metal Phys., 7 (1958), 247.
- 115. R.O. WILLIAMS: Trans. AIME, 224 (1962), 719.
- 116. H.C. FIEDLER: J. Iron Steel Inst., 205 (1967), 158.
- 117. J.E. HILLIARD and J.W. CAHN: Trans. AIME, 221 (1961), 334.
- 118. J.E. HILLIARD, Recrystallization, Grain Growth and Textures. Am. Soc. Metals, Metals Park, Ohio (1966), 268.
- 119. G.R. SPEICH and R.M. FISHER, Recrystallization, Grain Growth and Textures. Am. Soc. Metals, Metals Park, Ohio (1966), 563.
- 120. W. CHUBB: Trans. AIME, 203 (1955), J. of Metals, 189.
- 121. E.O. HALL: Phys. Soc. Proc. 64B (1951), 747.
- 122. N.J. PETCH: J. Iron Steel Inst., 174 (1953), 25.
- 123. A. CRACKNELL and N.J. PETCH: Acta Met., $\underline{3}$ (1965), 186.
- 124. J.C.M. LI: Trans. AIME, 227 (1963), 239.
- 125. C.J. BALL: J. Iron Steel Inst., 191 (1959), 232.
- 126. R.E. SMALLMAN: Modern Physical Metallurgy. Butterworths, London (1963), 99.
- 127. D. HARDWICK, C.M. SELLARS and W.J.McG. TEGART: J. Inst. Metals, 90 (1961-62), 21.
- 128. D. McLEAN: J. Inst. Metals, 80 (1951-52), 507.
- 129. C.R. BARRETT, A.J. ARDELL and O.D. SHERBY: Trans. AIME, 230 (1964), 200.
- 130. W.S. YOUNG and H. MYKURA: Acta Met., 13 (1965), 449.

- 131. F.S. BUFFINGTON, K. HIRANO and M. COHEN: Acta Met., 9 (1961), 434.
- 132. R.J. BORG, Diffusion in Body-Centered Cubic Metals. Am. Soc. Metals, Metals Park, Ohio (1965), 225.
- 133. J.E. DORN, Creep and Recovery. Am. Soc. Metals, Cleveland (1957), 225.
- 134. A.H. COTTRELL, An Introduction to Metallurgy. Edward Arnold (Publishers) Ltd., London (1967), 405.
- 135. J.J. JONAS, D.R. AXELRAD and J.L. UVIRA: Trans. Japan Inst. Metals, 8 (1968), to be published.
- 136. H. BÜCKLE: Metallurg. Reviews, Inst. Met., London, 4 (1959), 49.
- 137. J.I. TAKAMURA, Physical Metallurgy. R.W. Cahn, John Wiley and Sons, Inc., New York (1965), 721.
- 138. J. TALBOT, Recovery and Recrystallization of Metals. L. Himmel, Intersc. Publishers, New York (1963), 269.
- 139. D. HARDWICK and W.J.McG. TEGART: J. Inst. Metals, 90 (1961-62), 17.
- 140. F. GAROFALO, O RICHMOND, W.F. DOMIS and F. VON GEMMINGEN, Joint International Conference on Creep. London (1963): The Instit. Mech. Eng., 1.
- 141. S. KARASHIMA, H. OIKAWA and T. WATANABE: Acta Met., 14 (1966), 791.
- 142. S. KARASHIMA, H. OIKAWA and T. WATANABE: Trans. Japan Inst. Metals, 8 (1968), to be published.